



**University of
Sheffield**

Design of alkali-activated cements with maximised recycled content

Laura Stefanini

Supervised by:
Professor John L. Provis
Dr. Brant Walkley

A thesis submitted in fulfilment of the requirements for the degree of

Doctor of Philosophy

Department of Materials Science and Engineering
University of Sheffield

May 2023

Abstract

The cement industry is responsible for emitting over 8 % of global CO₂ emissions. It is widely accepted that new binders are needed in order to supplement Portland cement (PC) and reduce CO₂ emissions. Alkali-activated cements have many advantages over PC besides providing a low-carbon alternative, including the potential to valorise a wide range of industrial wastes and tailorable chemical/mechanical properties dependent on the type of precursors utilised. The fundamental reaction to produce an alkali-activated cement occurs between (calcium-)aluminosilicate precursors and an alkaline solution (activator), commonly based on sodium/potassium hydroxide and sodium/potassium silicates. The alkaline solution is considered the least sustainable component of the alkali-activation process, contributing to nearly half of the net CO₂ emissions. The function of the activator is to introduce the driving force needed for the dissolution of the Ca, Si, and Al present within the precursors and to promote their subsequent polycondensation through the alkaline liquid medium. The resulting products are C-A-S-H, C-(N-)A-S-H, and N-A-S-H gels.

Alkali-activated cements can be produced from a wide range of precursors; the most commonly used to date are ground granulated blast furnace slag (GGBFS) and fly ash. The availability of these materials is becoming more limited globally. GGBFS is already a valuable product as a supplementary cementitious material in traditional cement, whilst production of fly ash, a by-product from coal fired electricity generation, has been in steady decline for several decades as the world switches to more sustainable energy production. There is now a major drive to explore and characterise a wide range of current industrial by-products and wastes as novel precursors or partial replacements of conventional precursors for alkali-activated cements. The effort to utilise several waste sources, some limited geographically, is necessary to highlight the applicability of this technology globally as a key pathway to revolutionising the construction sector.

In this work four types of waste materials from industrial sources: i) five calcined waste clays from a kaolin mine (Imerys, UK); ii) basic oxygen furnace slag (BOFS) from a steelmaking plant (ArcelorMittal, Belgium); iii) stainless steel slag from an electric arc furnace (EAFS, Orbix, Belgium); and iv) copper slag (CS) from a refinement plant (Aurubis Beerse, Belgium), are characterised and investigated as potential precursors to form alkali-activated cements. Calcium aluminate cement (CAC) additions are also explored as additives to alkali-activated cements, specifically to take advantage of the well documented early-age properties of conventional CAC hydration. Enhancement of early-age properties may provide a route to ultimately reduce the activator dosage required to form satisfactory binders, further improving the sustainability of alkali-activated cements.

The search for alternative precursors specifically from waste sources necessitates a case-by-case approach to determine the suitability of each material for several distinct roles, e.g. as either an active binder forming material or filler material. A sequential methodology involving initial material characterisation, followed by binder formulation and assessment, allows for robust analysis of wastes as potential cement precursors. The data presented in this work provide a valuable source of information on the classification of certain waste materials and their behaviour in blended systems. The suitability of calcined clays from a kaolin mine side extraction process are found to be highly dependent on the resulting particle morphologies and amorphous phase fraction. Alkali-activation of 20 wt.% blends of the most suitable calcined clay with GGBFS shows satisfactory compressive strength values for high strength applications. Clays with poor mixing characteristics and low amorphous contents are deemed more suitable as filler materials. Portlandite present in weathered BOFS specimens is shown to be utilised by enabling replacement of costly sodium hydroxide and sodium silicate activators with sodium carbonate. EAFS exhibits poor reactivity, unsuitable for use as a precursor material. Heavy metal species within EAFS are found to be satisfactorily encapsulated and chemically stable within GGBFS blends. CS is characterised as a potential direct

replacement for GGBFS. CS is found to rapidly form a strong iron-rich gel phase when activated, complementing conventional C-A-S-H and N-A-S-H gel phases formed from traditional precursors. This work demonstrates the design of novel cements based on alkali-activation technology with tailorable properties dependent on the unique precursors utilised, to ultimately simplify the application of alkali-activation to new waste sources.

Acknowledgments

I would like to express my sincere gratitude to my supervisors, Professor John L. Provis and Dr. Brant Walkley. Your guidance and support have been invaluable in helping me complete this journey. Your insightful feedback and mentoring have helped me grow as both a researcher and a person. I especially appreciate the trust and freedom you gave me to pursue my research interests and my interest towards sustainability, which I will continue to pursue with enthusiasm. Thank you for inspiring me to make a positive impact.

Of course the second thank you goes to my babou for being an integral part of my success, without you none of this would have been possible! I could not have been luckier in meeting you during my first week in Sheffield. You have been my rock, my source of inspiration and encouragement, providing scientific stimulation and an essential source of strength. Your patience, love, understanding have been the greatest motivation, and now the next step awaits us, together.

Thank you to my family for your support throughout my PhD journey and in life. My mum's advice led me to Sheffield, where I have had the privilege of pursuing my academic goals. She has been my personal consultant and academic role model, always there to offer wise advice. My dad has also been a great source of inspiration, teaching me to be a good person and reminding me to always find joy and a laugh in life. Teresa, you might not know how much I think of you, and how fulfilling it is to see your progress in life. You are a great source of encouragement and emotions, hopefully we can provide each other stability and comfort during both good times and bad. Lastly, I cannot forget to mention Ettore, my little old brother, and nonna, who have been a constant source of love and encouragement. All of you have encouraged me to pursue my dreams and find my way in life on my own terms. Your unwavering belief in me has given me the confidence to overcome any obstacle. I am

Acknowledgments

deeply grateful for the unconditional love and support you have shown me throughout the years.

I am incredibly grateful for the support and love of my friends, including Marco, Imad, Ben, Tom, Gaone, Cass, Matt, Georgie, Michele, Katie, Theo, Minerva, Sasso, Toby, Chewie, and everyone else who has been there for me. I have felt loved and part of a family. You all have provided a much-needed break from work and have helped me to maintain a “healthy” work-life balance. Your love and emotional support have been crucial in helping me to maintain my motivation, stay focused on my research, and navigate the inevitable challenges that come with pursuing a PhD.

I am also grateful to my colleagues, the University of Sheffield, and ISL members, with a special thank you to Dan and Martin for their help and support in making lab work easier.

I want to express my gratitude to the Grantham Centre for Sustainable Futures, particularly to Deborah and Jana. Besides the financial support, the Grantham Centre has given me the unique opportunity to participate to COP27 and to enriching training programmes. Lastly, I would like to acknowledge the financial support received from Interreg NWE and express my gratitude to everyone who was part of the URBCON project.

Thank you all for believing in me and supporting me along the way.

Table of Contents

| | |
|---|----|
| Abstract..... | i |
| Acknowledgments | iv |
| Table of Contents | vi |
| List of Figures and Tables..... | ix |
| List of Figures | ix |
| List of Tables..... | xv |
| 1. Introduction..... | 1 |
| 1.1 Research background | 1 |
| 1.2 Objectives | 3 |
| 2. Literature Review | 5 |
| 2.1 Sustainable development in the construction industry | 5 |
| 2.2 History and origin of alkali-activated cements | 6 |
| 2.3 Physical and chemical difference between Portland cement and alkali- activated cements | 7 |
| 2.4 Alkali-activated cements | 10 |
| 2.4.1 Low-calcium systems..... | 11 |
| 2.4.2 High-calcium systems..... | 19 |
| 2.4.3 Blended and hybrid systems | 27 |
| 2.4.4 Alternative precursors | 30 |
| 2.5 Conclusions | 32 |
| 3. Materials and Methods | 33 |
| 3.1 Materials..... | 33 |
| 3.1.1 GGBFS characterisation..... | 33 |
| 3.1.2 Activators..... | 35 |
| 3.2 Testing methods..... | 36 |
| 3.2.1 Isothermal calorimetry | 36 |
| 3.2.2 Mini-slump tests..... | 36 |

| | | |
|--------|--|----|
| 3.2.3 | Setting time..... | 37 |
| 3.2.4 | Solvent exchange to stop hydration..... | 37 |
| 3.2.5 | X-ray diffraction (XRD) | 37 |
| 3.2.6 | Fourier-transform infrared spectroscopy (FTIR) | 38 |
| 3.2.7 | Scanning electron microscopy (SEM) | 38 |
| 3.2.8 | Mechanical properties..... | 38 |
| 3.2.9 | Solid state nuclear magnetic resonance (NMR)..... | 39 |
| 3.2.10 | Mercury intrusion porosimetry (MIP)..... | 39 |
| 3.2.11 | Leaching tests | 40 |
| 3.2.12 | X-ray fluorescence (XRF)..... | 41 |
| 3.2.13 | Particle size analysis (PSA)..... | 42 |
| 4. | Calcined Clays from Waste Sources in Alkali-Activated Cements | 43 |
| 4.1 | Introduction | 43 |
| 4.2 | Materials..... | 45 |
| 4.2.1 | Calcined clays characterisation..... | 45 |
| 4.2.2 | Pozzolanicity tests..... | 51 |
| 4.2.3 | Mix design and specimen preparation..... | 53 |
| 4.3 | Results and discussion | 54 |
| 4.3.1 | Alkali-activated blends of 70 wt. % GGBFS and 30 wt. % of calcined waste clays | 54 |
| 4.3.2 | Optimization of systems with clay C4..... | 62 |
| 4.4 | Conclusions..... | 76 |
| 5. | Non-Blast Furnace Slag in Alkali-Activated Cements..... | 78 |
| 5.1 | Basic oxygen furnace slag (BOFS) additions in alkali-activated cements with sodium silicate and sodium carbonate | 78 |
| 5.1.1 | Introduction..... | 78 |
| 5.1.2 | Materials and methods | 81 |
| 5.1.3 | Results and discussion..... | 85 |
| 5.1.4 | Conclusions | 93 |
| 5.2 | Electric arc furnace slag (EAFS) in alkali-activated cements..... | 95 |
| 5.2.1 | Introduction..... | 95 |

| | | |
|-------|---|-----|
| 5.2.2 | Materials and methods | 96 |
| 5.2.3 | Results and discussion..... | 101 |
| 5.2.4 | Conclusions | 114 |
| 5.3 | Copper slag (CS) and ternary blends in alkali-activated cements | 115 |
| 5.3.1 | Introduction..... | 115 |
| 5.3.2 | Materials and methods | 117 |
| 5.3.3 | Results and discussion..... | 122 |
| 5.3.4 | Conclusions | 141 |
| 6. | Hybrid Binders with Calcium Aluminate Cements (CAC) | 143 |
| 6.1 | Introduction | 143 |
| 6.2 | Materials and methods..... | 144 |
| 6.3 | Results and discussion | 147 |
| 6.3.1 | Isothermal calorimetry | 147 |
| 6.3.2 | Mini-slump test and setting times | 149 |
| 6.3.3 | X-ray diffraction..... | 150 |
| 6.3.4 | Fourier-transform infrared..... | 154 |
| 6.3.5 | Solid-state nuclear magnetic resonance | 156 |
| 6.3.6 | Scanning electron microscopy..... | 161 |
| 6.3.7 | Compressive strength..... | 164 |
| 6.4 | Conclusions | 166 |
| 7. | Conclusions..... | 168 |
| | References..... | 173 |
| | Publications, Conferences, and Awards..... | 228 |
| | Journal publications | 228 |
| | Conferences contributions | 229 |
| | Awards..... | 230 |

List of Figures and Tables

List of Figures

| | |
|---|----|
| Fig. 2.1: Schematic representation of the production of PC: from raw materials mining, to calcination, grinding, and final transportation | 8 |
| Fig. 2.2: Ternary diagram CaO-SiO ₂ -Al ₂ O ₃ showing precursor classes and their general compositions. Modified after [55] | 11 |
| Fig. 2.3: Schematic of N-A-S-H structure | 12 |
| Fig. 2.4: Reaction steps of alkali-activation of a low-calcium precursor. Modified after [48], [63] | 13 |
| Fig. 2.5: Structures of clay mineral groups 1:1 and 2:1 | 15 |
| Fig. 2.6: XRD patterns of kaolinite, metakaolin, and mullite, showing the transitions due to increased calcination temperature | 17 |
| Fig. 2.7: Schematic of C-S-H structure | 20 |
| Fig. 2.8: Schematic of C-A-S-H structure | 21 |
| Fig. 2.9: Reaction steps of the alkali-activation of GGBFS (as representative of high-calcium precursors). The reaction products and secondary products are identified. Modified after [118] | 22 |
| Fig. 2.10: Iron and steel making processes. Modified after [121] | 23 |
| Fig. 3.1: SEM image of GGBFS particles | 34 |
| Fig. 3.2: XRD pattern of GGBFS | 34 |
| Fig. 3.3: FTIR spectrum of GGBFS | 35 |
| Fig. 4.1: Particle size distributions for calcined waste clays and GGBFS..... | 46 |
| Fig. 4.2: XRD patterns of GGBFS and calcined clays C1 to C5 | 48 |

Fig. 4.3: SEM images of calcined clay samples C1 to C5.....49

Fig. 4.4: XRD pattern of C4 prior and after calcination.....50

Fig. 4.5: Results of R3 test for calcined clays, based on the total heat released from a formulated paste during 6 days at 20 °C [255].....52

Fig. 4.6: (a) Rate of heat evolution and (b) cumulative heat of alkali-activated blends of 30 wt. % calcined waste clays/70 wt. % GGBFS, at 20 °C54

Fig. 4.7: XRD patterns of alkali-activated blends with 30 wt. % of calcined waste clays after 28 days. Note that the phases marked as “CSH” will almost certainly contain alumina and thus are more precisely described as C-A-S-H, but a more concise form of the notation is used in the graphics57

Fig. 4.8: BSE images of alkali-activated blends of GGBFS and 30 wt. % calcined waste clays after 28 days of curing. EDS values are included for particles and characteristic features and calculated as an average of at least five points. (Error \pm 1%)59

Fig. 4.9: Compressive strength of alkali-activated blends of 30 wt. % calcined clays and GGBFS after 7 days and 28 days. Error bars represent the standard deviation among three replicate specimens.....61

Fig. 4.10: (a) Rate of heat evolution and (b) cumulative heat of alkali-activated blends of 20 wt. % C4 and 80 wt. % GGBFS, reacting at 20 °C.....63

Fig. 4.11: XRD patterns of alkali-activated GGBFS (0C4-a), and blends of 20 wt. % C4 and 80 wt. % GGBFS (20C4-b and 20C4-c). Note that the phases marked as “CSH” will contain alumina and thus are more precisely described as C-A-S-H, but a more concise form of the notation is used in the graphics65

Fig. 4.12: FTIR spectra of precursors and alkali-activated samples based on GGBFS with and without 20 wt. % C4, after 2 days and 28 days of curing.....67

Fig. 4.13: ²⁹Si MAS NMR spectra of precursors: (a) GGBFS and (b) calcined C4 69

Fig. 4.14: ²⁹Si MAS NMR spectra with fit and deconvolution of: (a) 0C4-a 2 days, (b) 0C4-a 28 days, (c) 20C4-c 2 days, (d) 20C4-c 28 days. The grey band represents the contribution of the unreacted GGBFS which is directly scaled from the raw GGBFS spectrum under the assumption of congruent dissolution70

Fig. 4.15: ²⁷Al MAS NMR spectra for precursors GGBFS and C4 and alkali-activated pastes.....72

Fig. 4.16: Differential pore volume of alkali-activated pastes based on GGBFS and 20 wt. % calcined clay C4, after 28 days of curing74

Fig. 4.17: Compressive strength of alkali-activated pastes based on GGBFS and 20 wt. % calcined clay C4. Error bars represent the standard deviation among three replicate specimens.....75

Fig. 5.1: Particle size distribution of precursors GGBFS, BOFS, and BOF6381

Fig. 5.2: BSE images of the raw precursors: (a) GGBFS, and (b) BOFS82

Fig. 5.3: XRD patterns of GGBFS, BOFS, and BOF6383

Fig. 5.4: Heat evolution rate of BOFS-GGBFS mixtures activated with (a) sodium silicate and (c) sodium carbonate; total heat cumulative of BOFS-GGBFS mixtures activated with (b) sodium silicate and (d) sodium carbonate, measured at 20 °C86

Fig. 5.5: XRD patterns of BOFS and GGBFS activated with sodium silicate after (a) 2 days, and (c) 28 days of curing, and activated with sodium carbonate after (b) 2 days, and (d) 28 days. Note that the phases marked as “CSH” will almost certainly contain alumina and thus are more precisely described as C-A-S-H, but a more concise form of the notation is used in the graphics89

Fig. 5.6: FTIR spectra of BOFS and GGBFS activated with (a) sodium silicate after 2 days and 28 days, and (b) activated with sodium carbonate after 2 days and 28 days of curing91

Fig. 5.7: Compressive strength of specimens based on BOFS and GGBFS and activated with sodium silicate and sodium carbonate, after 7 days and 28 days of curing. Error bars represent the standard deviation among three replicate specimens.....93

Fig. 5.8: Particle size distributions of GGBFS and EAFS used in this study.....96

Fig. 5.9: SEM images showing the morphology and particle size distribution of GGBFS and EAFS97

Fig. 5.10: XRD patterns of GGBFS and EAFS.....97

| | |
|---|-----|
| Fig. 5.11: FTIR spectra of precursors GGBFS and EAFS | 98 |
| Fig. 5.12: BSE image of a EAFS particle with EDS analysis (from top left: Mg, Al, Si, Ca, Cr, and Fe) | 99 |
| Fig. 5.13: Isothermal calorimetry data for samples 100G, 25E, 50E, 75E, and 100E, measured at 20 °C..... | 101 |
| Fig. 5.14: Fresh properties of the AACs based on GGBFS and EAFS: (a) flow diameter over time of the GGBFS-EAFS mixtures; (b) initial and final setting time increasing the replacement level of GGBFS | 103 |
| Fig. 5.15: XRD patterns of AACs based on GGBFS and EAFS at 2 days and 28 days of curing. Note that the phases marked as “CSH” will contain alumina and thus are more precisely described as C-A-S-H, but a more concise form of the notation is used in the graphics | 105 |
| Fig. 5.16: FTIR spectra of AACs based on GGBFS and EAFS at 2 days and 28 days of curing | 106 |
| Fig. 5.17: BSE images of alkali-activated pastes based on GGBFS and EAFS after 2 days and 28 days of curing. Compositions of particles numbered 1 to 5 are given in Table 5.7. | 109 |
| Fig. 5.18: Pore structure of the alkali-activated pastes after 2 days and 28 days: (a) cumulative pore volume and (b) differential pore volume | 111 |
| Fig. 5.19: Strength development of alkali-activated mortars based on GGBFS and EAFS: (left) compressive strength and (right) flexural strength. Error bars represent the standard deviation among six replicate specimens (left) and three replicate specimens (right) | 112 |
| Fig. 5.20: Particle size distributions of GGBFS, CS, and EAFS | 117 |
| Fig. 5.21: Morphology of solid precursors GGBFS, EAFS, and CS as observed by SEM..... | 118 |
| Fig. 5.22: XRD patterns of GGBFS, CS, and EAFS | 119 |
| Fig. 5.23: FTIR spectra of the precursors GGBFS, CS, and EAFS | 120 |
| Fig. 5.24: Heat evolution of alkali-activated pastes based on GGBFS, CS, and | |

| | |
|--|-----|
| EAFS at 20 °C..... | 123 |
| Fig. 5.25: Cumulative heat released by alkali-activated pastes based on GGBFS, CS, and EAFS at 20 °C..... | 125 |
| Fig. 5.26: (a) Mini-slump test and (b) setting times results for all alkali-activated pastes based on GGBFS, CS, and EAFS..... | 126 |
| Fig. 5.27: Comparison of setting times and heat evolution profiles for samples 100G and 100C..... | 127 |
| Fig. 5.28: XRD patterns of alkali-activated pastes based on GGBFS, CS, and EAFS after 2 days, 28 days, and 91 days. Note that the phases marked as “CSH” will contain alumina and thus are more precisely described as C-A-S-H, but a more concise form of the notation is used in the graphics | 128 |
| Fig. 5.29: FTIR spectra of AACs based on GGBFS, CS, and EAFS after 2 days and 28 days..... | 130 |
| Fig. 5.30: BSE images of samples 100G, 50C, 50C/15E, and 100C after 2 days and 28 days of curing | 133 |
| Fig. 5.31: Plot of (Al+Fe)/Si vs Ca/Si mass ratios obtained from EDS analysis of distinctive matrix regions for samples 100G, 50C, and 100C after 2 days and 28 days, along with precursor materials, GGBFS and CS..... | 135 |
| Fig. 5.32: Differential porosity of alkali-activated pastes based on GGBFS, CS, and EAFS after 2 days and 28 days of curing..... | 136 |
| Fig. 5.33: Strength development of alkali-activated mortars based on GGBFS, CS, and EAFS: (left) compressive strength and (right) flexural strength. Error bars represent the standard deviation among six replicate specimens (left) and three replicate specimens (right) | 138 |
| Fig. 6.1: Particle size distribution of GGBFS and CAC | 145 |
| Fig. 6.2: XRD patterns of precursor materials GGBFS and CAC..... | 146 |
| Fig. 6.3: (a) Heat evolution and (b) cumulative heat of alkali-activated and hybrid samples at 20 °C..... | 148 |
| Fig. 6.4: XRD patterns of alkali-activated and hybrid samples from 1 day to 28 | |

days of curing: (a) 0C-a, (b) 10C-a, (c) 10C-b, (d) 0C-c, and (e) 10C-c. Note that the phases marked as “CSH” will contain alumina and thus are more precisely described as C-A-S-H, but a more concise form of the notation is used in the graphics 153

Fig. 6.5: FTIR spectra of alkali-activated and hybrid samples after 2 days and 28 days 155

Fig. 6.6: ²⁹Si MAS NMR spectra of precursors (a) GGBFS and (b) CAC 156

Fig. 6.7: ²⁹Si MAS NMR spectra with fit and deconvolution, of: (a) 0C-a 2 days, (b) 0C-a 28 days, (c) 10C-a 2 days, (d) 10C-a 28 days (e) 10C-b 2 days, and (f) 10C-b 28 days. The grey band represents the contribution of the unreacted GGBFS which is directly scaled from the raw GGBFS spectrum under the assumption of congruent dissolution 158

Fig. 6.8: ²⁹Si MAS NMR spectra with fit and deconvolution of samples activated with 4M NaOH: (a) 0C-c 2 days, (b) 0C-c 28 days, (c) 10C-c 2 days, and (d) 10C-c 28 days. The grey band represents the contribution of the unreacted GGBFS which is directly scaled from the raw GGBFS spectrum under the assumption of congruent dissolution 159

Fig. 6.9: ²⁷Al MAS NMR spectra for (a) alkali-activated and hybrid specimens activated with activator mixtures a and b after 2 days and 28 days, (b) alkali-activated and hybrid specimens activated with 4M NaOH after 2 days and 28 days, and (c) precursor materials GGBFS and CAC 160

Fig. 6.10: BSE images of alkali-activated and hybrid samples after 2 days and 28 days of curing 162

Fig. 6.11: CAC particle (left) and EDS points (a) and (b) identified as gehlenite and CA (right)..... 163

Fig. 6.12: Bulk atomic ratio Ca/Si (as determined by SEM-EDS analysis) for alkali-activated and hybrid samples after 2 days and 28 days of curing 164

Fig. 6.13: Compressive strength of alkali-activated and hybrid samples after 7 days and 28 days. Error bars represent the standard deviation among three replicate specimens 165

List of Tables

| | |
|--|----|
| Table 3.1: Density and particle size analysis (d_{10} , d_{50} , and d_{90} values) of GGBFS..... | 33 |
| Table 3.2: Oxide composition (wt. %) of GGBFS as measured with XRF. Loss of ignition (LOI) at 1000 °C..... | 33 |
| Table 3.3: Heavy metal leaching limits (U1 and U2) established by NEN-7345:94 [242]..... | 41 |
| Table 4.1: Density and particle size analysis of calcined clays and GGBFS | 45 |
| Table 4.2: Oxide composition (wt. %) of calcined clays and GGBFS as measured with XRF. Loss of ignition (LOI) at 1000 °C..... | 46 |
| Table 4.3: Result of the pozzolanicity test for the calcined waste clays | 51 |
| Table 4.4: Mix proportions of alkali-activated blends using GGBFS and calcined waste clays C1 to C5 | 53 |
| Table 4.5: Initial and final setting times and mini slump test results for alkali-activated paste samples including 30 wt. % calcined clay and 70 wt. % GGBFS | 56 |
| Table 4.6: Initial and final setting times and mini-slump test results for alkali-activated blends of 20 wt. % C4 and 80 wt. % GGBFS..... | 64 |
| Table 4.7: Deconvolution results for ^{29}Si MAS NMR spectra of the alkali-activated blends. Estimated uncertainty in absolute site percentages is $\pm 2\%$ | 71 |
| Table 4.8: Total porosities measured for alkali-activated pastes based on GGBFS and 20 wt. % calcined clay C4, after 28 days of curing. Error bounds represent the standard deviation among 2 replicate specimens | 75 |
| Table 5.1: Density and particle size analysis of GGBFS, BOFS, and BOFS63 | 81 |
| Table 5.2: Oxide composition (wt. %) of GGBFS and BOFS as measured with XRF. Loss of ignition (LOI) at 1000 °C | 82 |
| Table 5.3: Mix proportions of the pastes based on BOFS and GGBFS | 84 |
| Table 5.4: Mini-slump test and setting times results for pastes based on BOFS and GGBFS | 88 |
| Table 5.5: Oxide composition (wt. %) of GGBFS and EAFS as measured with XRF | 96 |

Table 5.6: Mix proportions of the alkali-activated mortars based on GGBFS and EAFS100

Table 5.7: Compositional EDS analysis of particles of GGBFS and EAFS labelled 1 to 5 in Fig. 5.17, where 1 *a* and *b* are GGBFS particles; 2 *a*, *b*, *c*, and *d* are spinel phases embedded in the melilite solid solution; 3 *a*, *b*, and *c* calcium silicates; 4 *a* and *b* are merwinite particles; and particle 5 is an iron silicate.....110

Table 5.8: Total porosity of the pastes based on GGBFS and EAFS after 2 days and 28 days of curing.....111

Table 5.9: Results obtained from ICP and calculated following NEN-7345:94 test for samples 100G and 50E, and compared with limit U1113

Table 5.10: Oxide composition (wt. %) of GGBFS, CS, and EAFS as measured with XRF117

Table 5.11: Physical properties of solid precursors GGBFS, CS, and EAFS118

Table 5.12: Mix proportions of the alkali-activated mortars based on GGBFS, CS, and EAFS.....122

Table 5.13: Total porosity of alkali-activated pastes based on GGBFS, CS, and EAFS, measured by MIP after 2 and 28 days of curing137

Table 5.14: Results obtained from ICP and calculated following NEN-7345:94 test [242] for samples 100G and 50C, and 50C/50E, and comparison with limits U1 and U2. Values above these limits are underlined in the table140

Table 6.1: Density and particle size analysis of GGBFS and CAC145

Table 6.2: Oxide composition (wt. %) of GGBFS and CAC as measured with XRF145

Table 6.3: Mix proportions of hybrid pastes with GGBFS and CAC146

Table 6.4: Mini-slump tests and initial and final setting time results for hybrid mixtures based on GGBFS and CAC.....149

Table 6.5: Quantification of Qⁿ environments identified in ²⁹Si MAS NMR spectra of alkali-activated and hybrid samples based on GGBFS and CAC after 2 days and 28 days. Estimated uncertainty in site percentages is ±1%.....157

Chapter 1.

Introduction

1.1 Research background

Global climate change awareness and the limitation of resources worldwide have introduced a new primary requirement for new and current research to consider sustainable development. Since the Paris agreement [1], the transition towards sustainable models of technological development are a key concern, in a joint effort to save the planet, by maintaining global warming below 1.5 °C and mitigating global greenhouse gas emissions [2].

Cementitious materials and binders are the most widely utilised manmade materials in human history. In recent history, cementitious materials have overtaken traditional materials such as wood and stone in construction, and their importance is expected to increase even more in the foreseeable future. The recent dramatic growth in world population, which is forecast to increase, will be reflected in growing demand for concrete production to support urbanisation and infrastructure development, especially in developing countries [3]–[6]. Concrete demand is also strongly connected with the development of other foundation sectors, such as energy production, which underpins further economic growth [7].

Portland cement (PC) is the main binding material used in construction applications. The CO₂ emissions related to its production are enormous, including both inherent (due to the chemical reaction of decomposition of limestone) and process (requirement for high temperature to generate the active calcium silicate phases) contributions [8]. Beside carbon emissions, the construction industry is a huge consumer of raw materials that originate from mining operations which are inherently invasive and damaging to the local environment. An urgent revolution in this sector is required to provide a scientific alternative to reduce our reliance on PC and help promote a transition to a more sustainable construction sector [9], [10].

Most industrial processes generate large volumes of waste and by-products, some of which can be used as supplementary cementitious materials (SCMs), acting to reduce the volume of PC needed [11]. These same classes of wastes can be used as raw materials for the direct production of cementitious materials through alkali-activation technology, eliminating much of the intrinsic carbon cost associated with PC production.

Alkali-activated cements (AACs) are produced from the reaction of a powder precursor with an alkaline solution. The materials obtained are hardened three-dimensional connected networks with local structures ranging from completely amorphous to crystalline. This wide class of binders can be divided into two main categories: low-calcium binders, also called geopolymers, produced from aluminosilicate sources to form N-A-S-H gels with a higher degree of cross-linking Q^4 and secondary zeolites phases [12], [13], and high-calcium alkali-activated materials, which form C-A-S-H gels and secondary hydrotalcite and AFm-like phases similar to PC-based systems [14], [15]. The overall crosslinking is lower in high-calcium systems, however it still exceeds that seen in conventional PC systems [16]. Under the appropriate conditions, AACs have been shown to reach superior performances than conventional construction materials based on PC [17]. They can be designed to meet certain specifications for niche applications, exhibiting outstanding technical properties such as high strength, and superior chemical [18] and thermal resistances [19]. AACs can introduce a low-carbon pathway to supplement the construction industry with binders, firstly by removing the intrinsic CO_2 emissions involved during calcination, and secondly by opening up the possibility to use industrial waste sources as bulk precursor materials. The introduction of an alkaline solution does result in a significant carbon impact, however life cycle analyses on AACs report an overall reduction of CO_2 emission compared to PC production ranging from 30 % up to 80 % [20]. To maximise this environmental benefit, AACs have to be designed with geographical considerations in mind, utilising local waste components that will vary from region to region. This means that AAC design requires a case-by-case approach.

The most used precursors in alkali-activation are ground granulated blast furnace slag (GGBFS) and fly ash, both of which are becoming less available in certain regions and are already highly competitive resources, especially within the cement industry. The search for different types of precursors is needed to ultimately reduce the environmental impact of the construction industry through alkali-activated technology. In this study, we consider four possible waste candidates: waste clays from Imerys (UK), stainless steel slags, including basic oxygen furnace slag (BOFS) from ArcelorMittal (Belgium), and electric arc furnace slag (EAFS) from Orbix, (Belgium), and copper slag (CS) from Aurubis Beerse (Belgium). All four of these waste materials have been characterised and investigated as potential precursors for alkali-activated low-carbon binders.

1.2 Objectives

The initial objective of this work is to investigate the potential of four types of waste materials from industrial sources: calcined clays, BOFS, EAFS, and CS, and their detailed characterisation. This is followed by design and development of AACs, both mortars and pastes, targeting a maximisation of binder waste content up to a 75 wt. % replacement of conventional alkali-activated material precursor (in this case GGBFS). The study also aims to investigate the use of calcium aluminate cement (CAC) in the production of hybrid binders to obtain enhanced early-age properties and reduce the initial activator dosage required.

These new AACs are tested and validated through isothermal calorimetry to determine reaction kinetics; setting time and workability are evaluated to study the fresh properties of AACs; microstructural analysis is determined via X-ray diffraction (XRD), Fourier-transform infrared (FTIR) spectroscopy, scanning electron microscopy (SEM) coupled with energy-dispersive X-ray spectroscopy (EDS), mercury intrusion porosimetry (MIP), and solid state nuclear magnetic resonance (NMR); leaching tests are carried on to analyse the leachability of heavy metals from

AACs. These are compared to previously reported AACs, to assess their performance and early-age behaviour. This methodology enables the suitability of each material to be determined for several distinct roles, such as an active binding phase, an additive, or filler material. The study provides valuable information on the behaviour of waste materials in blended systems and aims to ultimately simplify the application of alkali-activation to new waste sources.

Overall, the project work described in this thesis further elucidates the necessary characterisation methods required to completely ascertain the suitability of new waste classes within alkali-activation technology, whilst ultimately tackling the overarching goal of minimising the consumption of primary resources and reducing the overall CO₂ emissions during the production of high-performance cementitious materials.

Chapter 2.

Literature Review

2.1 Sustainable development in the construction industry

Sustainable development is defined by the United Nations as “technological advancement which meets current demands without compromising the ability of future generations to meet their own needs,” [21] encompassing the fair utilisation of natural resources available to industry. Construction materials are critical resources in the global economy, with worldwide cement production reaching 4.1 billion tonnes in 2022 [22]. This level of production equates to between 5-7 % of global CO₂ emissions across all sectors [23], [24]. The United Nations forecasts a rise in global population, up to 9.7 billion people by 2050 [25], driving further urbanisation especially in developing nations. The continued need for new buildings and infrastructure to sustain such population growth will increase demand for primary construction materials such as concrete and cement. Concrete needs to fulfil certain mechanical criteria, such as good strength, resilience, and durability for most commercial applications, on top of more recent socio-economic pressures that demand affordability and consideration towards reuse to satisfy the requirements of the evolving world. This presents a major challenge for the construction industry, which now has to move away from the current status quo to help support sustainable social and economic development. The main strategies to increase the sustainability of the construction industry [26], [27] include:

- (i) Increasing the energy efficiency of cement plants, replacing fossil fuels with alternative fuels, and implementing CO₂ capture and storage (CCS) or CO₂ capture utilisation and storage (CCUS).
- (ii) Maximising the PC clinker replacement with low-carbon SCM in concrete.

- (iii) Develop alternative low-carbon binders not based on Portland clinkers, which require new standards.
- (iv) Waste valorisation, reducing natural resource consumption and recycling of used concrete.

The first solution regarding energy efficiency is generally applicable to all major industries and has been implemented in some form in most industrial settings. The other strategies are more pertinent to the construction sector, however not all these strategies have the same impact on reducing CO₂ emissions.

Developments in alternative low-carbon binders and waste valorisation strategies hold significant promise for achieving sustainable construction and may offer greater potential for reducing the environmental impact of the construction industry. Waste valorisation and recycling are crucial for reducing natural resource consumption and minimising the environmental impact of construction and other industries. The development of alternative low-carbon binders not based on Portland clinkers has garnered significant interest in the scientific community. Moving forward, it will be important to continue exploring and implementing these strategies to ensure that the construction industry is able to meet the growing demand for infrastructure while also supporting sustainable social and economic development.

2.2 History and origin of alkali-activated cements

The first patented work on alkali-activated materials dates back to 1895 when Whiting combined blast-furnace slag with caustic soda producing a useful binding material, reporting slaked lime additions to improve the quality of the product [28]. In 1908, Hans Kühl [29] also patented the production of cements formed by combining a vitreous slag with alkaline sources, such as lime, sodium carbonate, and sulfates, mixed with water, achieving performance comparable to the best Portland cement. In the 1940s, Purdon [30] expanded on the work by studying several combinations of blast furnace slags and chemical activators, identifying the enhanced

tensile and flexural strength of slag-alkali cements. As a result, these materials were commercialised under the name “Purdocement”. In 1965, Glukhovsky [31] and his team at the Kiev Civil Engineering Institute proved that low-calcium aluminosilicate sources could also be used as binders in alkali-activation technology. The investigation of various precursor materials and activators in the 1970s by the same group, now led by Krivenko, further advanced the knowledge of alkali-activation technology and its applications [32]. In the same decade, Davidovits [33] introduced “geopolymers”, binders made by mixing low-calcium clays with alkaline solutions [34]. The United States Army recognised the potential of alkali-activated materials for military applications in a report in 1985 [35], which further spurred the commercialisation of “Pyrament” as a repair medium with good strength and durability properties [36]. Since the 1990s, research and development in alkali-activation technology has expanded rapidly to become a significant field of scientific interest. Commercialisation however, is still limited to a few companies in several countries, including Australia [37], China, the United States, Brazil, India, Ukraine, and Russia [38]. Standardisation and regulatory efforts are underway by RILEM (with TC 294-MPA “Mechanical properties of alkali-activated concrete” and TC 283-CAM “Chloride transport in alkali activated materials”) and the scientific community [39] to create a framework for the general implementation of alkali-activation technology.

2.3 Physical and chemical difference between Portland cement and alkali-activated cements

PC is traditionally manufactured, as shown in Fig. 2.1, by calcining various raw materials sourced from open-face quarries, mining, and dredging operations [40]. These raw materials, consisting mainly of limestone (CaCO_3) as well as clays, shale, and sand, acting as sources of silica and alumina, with small amounts of iron ore and bauxite, are mixed and heated in a rotary kiln at temperatures of 1450 °C. The

materials are initially preheated to $\sim 900\text{ }^{\circ}\text{C}$ using the kiln exhausts to decompose limestone into quicklime (CaO), which releases CO_2 gas. At $1450\text{ }^{\circ}\text{C}$, CaO reacts with other materials and additives in the kiln to produce a solid clinker composed mainly of tricalcium silicate or alite (C_3S ¹), dicalcium silicate or belite (C_2S), tricalcium aluminate (C_3A), and tetracalcium aluminoferrite (C_4AF). After cooling and stabilisation, the resulting clinker is typically ground into a fine powder with added gypsum ($\text{CaSO}_4 \cdot 2\text{H}_2\text{O}$) to improve its final wet properties.

The initial decomposition of limestone generates 0.78 tonnes of CO_2 gas per tonne of CaO produced [39], which constitutes the inherent CO_2 emission in PC production that accounts for approximately 60-70 % of the total emissions [8], [41]. Combustion of carbon-based fuels during cement production generates extrinsic emissions estimated to be around 0.31 tonnes of CO_2 per tonne of cement produced [42]. The use of low-carbon fuels and other technological improvements can help reduce these extrinsic emissions, however, little room for further improvement exists. As long as PC is required, the elimination of inherent emissions related to traditional CaO production from limestone will not be possible.

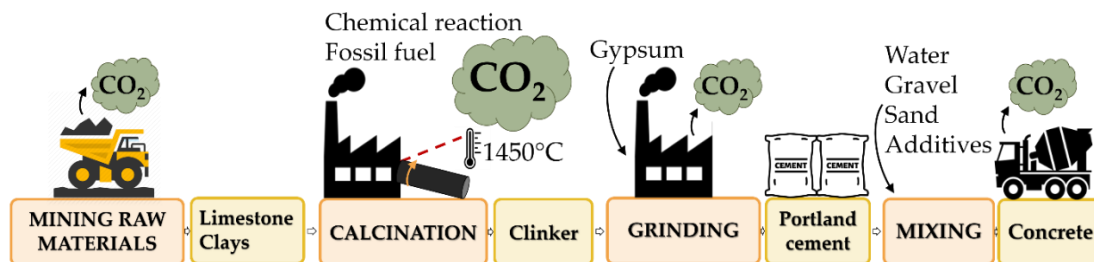


Fig. 2.1: Schematic representation of the production of PC: from raw materials mining, to calcination, grinding, and final transportation

¹ Cement phases are expressed in cement oxide notation as follows:

| Oxide | CaO | SiO ₂ | Al ₂ O ₃ | Fe ₂ O ₃ | MgO | Na ₂ O | K ₂ O | CO ₂ | H ₂ O |
|----------|-----|------------------|--------------------------------|--------------------------------|-----|-------------------|------------------|-----------------|------------------|
| Notation | C | S | A | F | M | N | K | c | H |

Alternative cements, such as alkali-activated materials, have a major advantage over PC in terms of lower CO₂ emissions during production. The high temperature clinkerisation step and the inherent emissions from decarbonising limestone can be avoided with these materials. Alkali-activated materials are reported to be economically and technically feasible for precast ready mixes in locations where the activator and precursor materials are readily available [37], [39]. The main challenge for global upscaling of these materials is the availability of the activator solution. Sodium silicate is one of the most widely used activator solutions, but its synthesis generates considerable CO₂ emissions that diminish the overall environmental benefit of alkali-activation technology. At current production levels, sodium silicate is unable to serve as a viable source for even a mere 0.1 % replacement of PC based materials [43].

Detailed life-cycle analyses (LCAs) comparing alkali-activated cements to PC have been reported [44]–[47], raising serious debate on the most suitable approach to analyse these materials. Factors such as geographical and economic considerations, as well as the baseline PC material used for comparison, further add to the complexity and validity of such assessments. With the wide range of mix designs, precursor materials, and activating solutions available, there exist scenarios whereby alkali-activated materials can have significant environmental benefits, whilst others may result in little to no net emission reduction. The most optimistic calculations on environmental benefits of AACs published by Duxson *et al.* and Weiszäcker *et al.* [48], [49] report a 80 % reduction in global warming impact compared to PC production, although it was found that using metakaolin-based precursors in alkali-activated concretes had a similar impact as PC concretes [46]. Most studies report intermediate values of emission reduction ranging from 40-50 % [50]–[52]. Inefficient mix designs may have a negative effect, although generally speaking the chemical synthesis of activator solutions is considered to be the least sustainable aspect of alkali-activation technology [45], [46]. The production process of sodium silicate is particularly detrimental on the LCA impact [53]. Alkali-activation technology does, however, offer a pathway to valorise not only low purity raw materials but also low purity

activator solutions, eliminating the need for further energy intensive refinement processes [53]. Undoubtedly, research in the field of alkali-activation technology needs to address the challenge of designing and formulating well-behaving and highly efficient alkali-activated concretes that reduce overall emissions to levels below those of current PC production.

2.4 Alkali-activated cements

Alkali-activation is a term given for the reaction that occurs between powder precursors and an alkaline source in liquid media. The function of the alkaline activator is to introduce the chemical driving force needed for the dissolution of Ca, Si, and Al species present within the precursor materials by increasing the pH of the mixture. The activator promotes the subsequent polycondensation reaction between dissolved species that involves the nucleation and growth of gel phases within the liquid media. The primary gel phases formed are known as C-A-S-H and N-A-S-H, both consisting of tetrahedral aluminate bound between silicate tetrahedra, and play a fundamental role in the initial stages of gel formation [39], [48], [54].

The resulting hardened binders have a highly complex microstructure consisting of unreacted particles, porosity, hardened gel phases, and new continuously forming gel. The gel structure is chemically disordered, similar to calcium silicate hydrates (C-S-H) formed as a hydration product in PC, with the main difference being the degree of crosslinking due to tetrahedral Al replacing Si in the network. When this occurs, a negative charge is generated on the tetrahedrally coordinated Al. To maintain electroneutrality, cations such as Na⁺ and K⁺ sit within pore sites and in the interlayer acting as stabilising agents within the gel structure.

The mix design involving the selection of precursors and activator solutions can result in distinctive microstructural characteristics that will be discussed in-depth further within this review. The nature of alkali-activation allows for a wide range of precursors to be utilised; Fig. 2.2 illustrates a ternary CaO-SiO₂-Al₂O₃ diagram with

the chemical compositions of the main groups of raw materials used in alkali-activation.

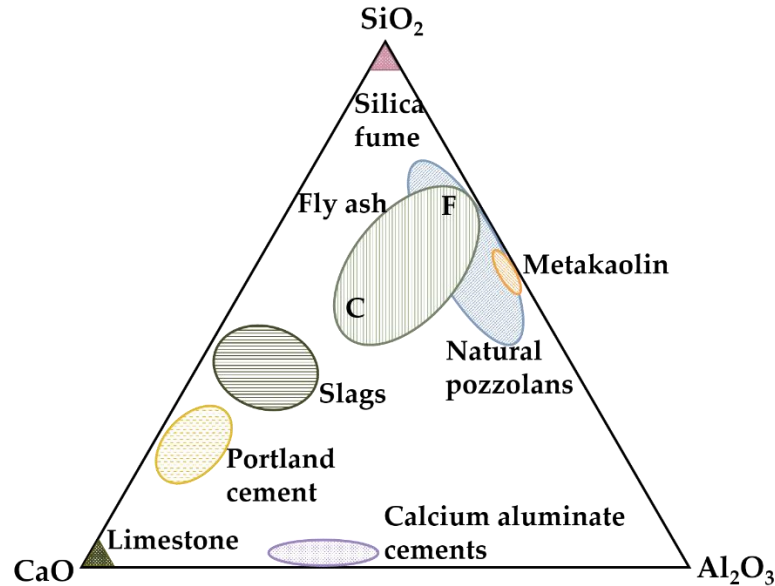


Fig. 2.2: Ternary diagram CaO-SiO₂-Al₂O₃ showing precursor classes and their general compositions. Modified after [55]

There are two primary categories of alkali-activated materials that can be classified according to the presence of Ca in the precursors. Low-calcium alkali-activated materials (or geopolymers), which mainly consist of N-A-S-H gels, are typically created using common aluminosilicate precursors such as fly ash and metakaolin [34], [56]. Conversely, C-A-S-H gels are formed in high-calcium systems and usually originate from metallurgical slag precursors.

2.4.1 Low-calcium systems

When aluminosilicate precursors are mixed with an alkaline activator in low-calcium systems, they generate N-A-S-H gel. The N-A-S-H gel structure is disordered and highly cross-linked (Fig. 2.3). The gel consists of Q⁴ polymerised silicate networks with Al tetrahedra that share oxygen atoms with neighbouring Si tetrahedral, as Al-

O-Al bonds between tetrahedra are forbidden according to Löwenstein's rule. The negative charge of Al tetrahedra within the framework is balanced by alkali cations [57], [58]. The composition and short-range order on length scales of up to 5-8 Å resemble zeolitic systems, with crystalline nanostructures embedded amongst amorphous binding gel. Similarities are seen between the hydrothermal synthesis of zeolites and the polycondensation reaction during alkali-activation of low-calcium materials [59], [60]. This allows fundamental chemical models on reaction pathways to be applied across both systems [61], enabling the engineering of hybrid geopolymer-zeolite composite materials for various applications [62].

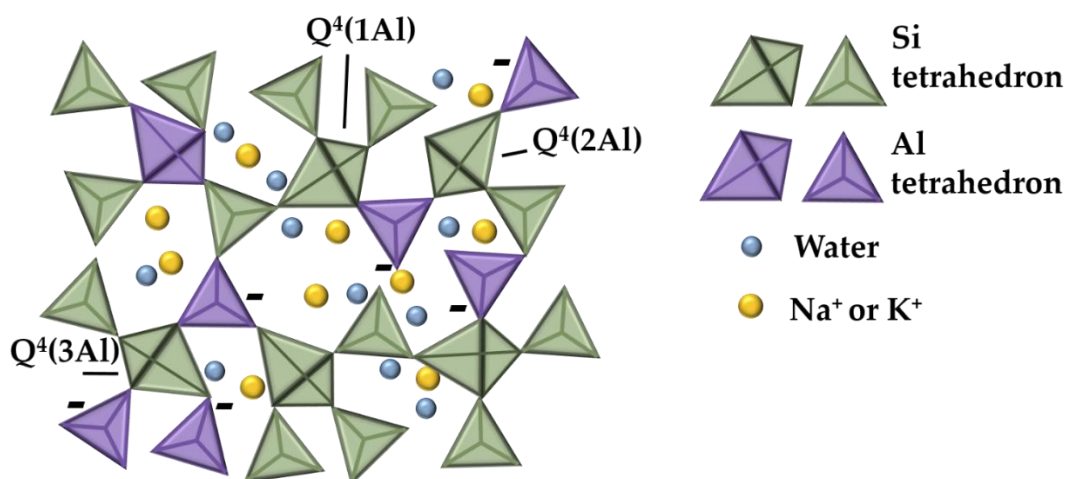


Fig. 2.3: Schematic of N-A-S-H structure

Alkaline hydrolysis promotes the dissolution of solid precursors, resulting in the release of monomeric Al and Si species. Dissolved monomers rearrange to form dimers, trimers, and so on, until the solution becomes supersaturated with respect to aluminosilicate gel, N-A-S-H, and starts to nucleate and further grow via polycondensation reactions. The resulting gel consists of highly cross-linked polymeric networks and continues to react until maximum connectivity is achieved [63], [64]. Specific to NaOH-activated systems, the gel chemistry is described to evolve in two stages; an initial Al-rich gel (gel 1 in Fig. 2.4) forms due to higher reactivity and therefore rapid dissolution and availability in alkaline medium of Al,

which is subsequently replaced by Si units (forming gel 2) as Si concentration increases. [65] The rearrangement process leads to the formation of N-A-S-H. The interactions of dissolved Al and Si are responsible for determining the final features and behaviour of the resulting aluminosilicate binder. For silicate-activated systems, the activity of silicate species within the activator solution is a crucial factor in controlling the rate of structural rearrangement and densification [66].

Zeolites are frequently formed as secondary reaction products in low-calcium alkali-activated cements. Various zeolitic by-products have been reported in the literature depending on reaction parameters such as curing temperature, pH, water/SiO₂ ratio, Si/Al ratio, and SiO₂/Na₂O ratio [67].

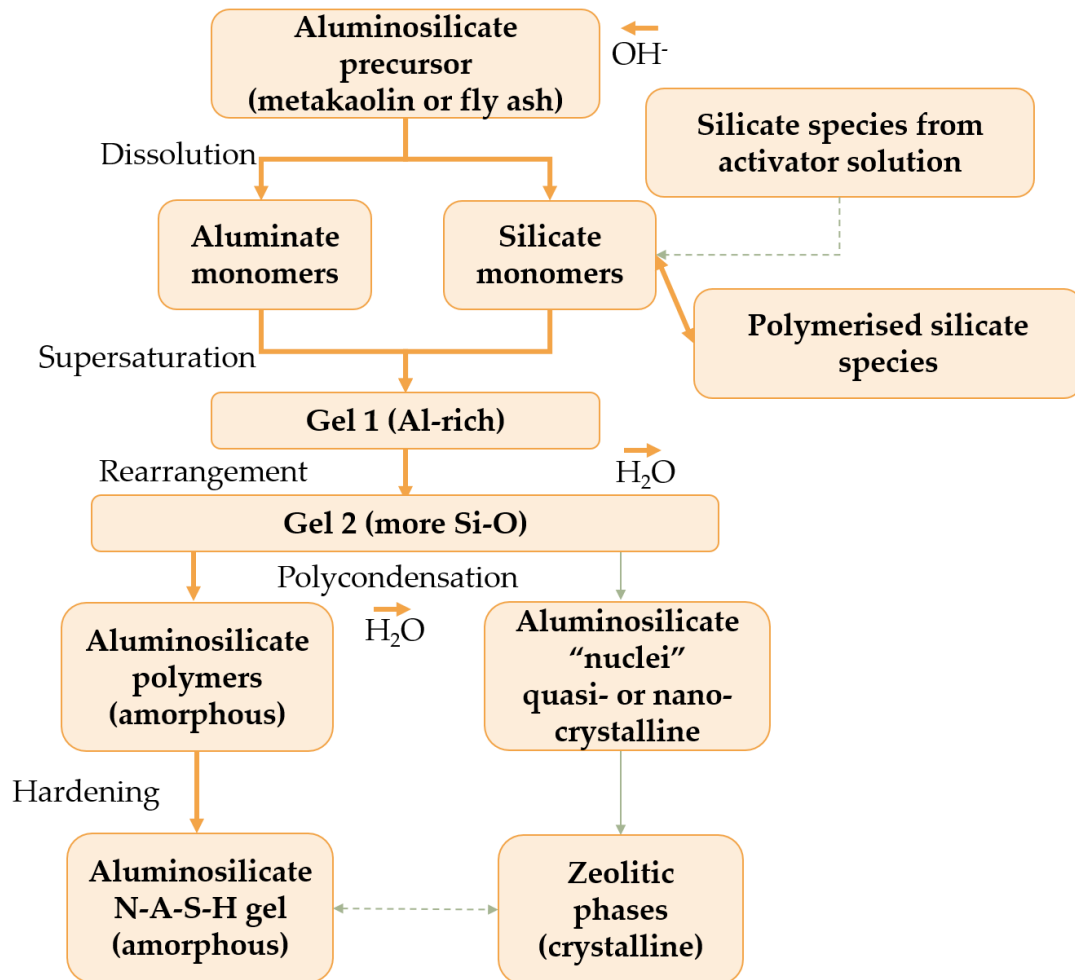


Fig. 2.4: Reaction steps of alkali-activation of a low-calcium precursor. Modified after [48], [63]

Multiple characterisation methods are required to fully elucidate the physical and chemical properties of these systems, that are highly dependent on compositional and processing factors. Fresh properties and early-stage setting can be studied with calorimetric techniques, ultrasonic pulse velocity, and rheological studies. FTIR spectroscopy is widely utilised to investigate chemical bonding present primarily regarding functional groups. Solid-state NMR spectroscopy is a powerful tool that can be used to garner a more fundamental understanding of the three-dimensional structure of alkali-activated materials by investigating both Si and Al environments, as well as Na, H, O, and Ca in the amorphous phases. Deconvolution analysis of ^{29}Si NMR spectra can provide in-depth structural data of gel phases [68] that can be linked to thermodynamic models regarding gel formation [69]. N-A-S-H gel exhibits good mechanical properties, high thermal stability, and corrosion resistance. In contrast with the high-calcium binders, only a small amount of residual water enters into the gel structure. Water is predominately concentrated within macroscopic pores that facilitates dehydration via thermal treatment without negatively impacting the gel structure [70].

2.4.1.1 *Clays*

Natural clays are considered to be one of the most abundant and widely available aluminosilicate sources on earth. Calcined clays can potentially act as suitable precursor materials in alkali-activation technology, however, their current reported use at large scale in construction is still limited [71].

The structure of clay materials is usually composed of alternating tetrahedral and octahedral sheets stacked together to form distinct repeating layers. Each tetrahedral sheet is composed of SiO_4^{4-} tetrahedral units that share basal oxygens with neighbouring tetrahedra to give a pseudo-hexagonal network. Octahedral sheets are composed of Al^{3+} in six-fold coordination. Al^{3+} can be substituted by other trivalent cations such as Fe^{3+} , and rarely by Mg^{2+} and Fe^{2+} . In this case, all oxygens are shared with neighbouring octahedra, with hydroxyl groups found in the interlayer or in the vacancies due to the stacking of the tetrahedral and octahedral sheets. The stacking

of the tetrahedral-octahedral (T-O) sheets will determine the classification of the clay mineral in question, as shown in Fig. 2.5. Group 1:1 includes minerals with one tetrahedral and one octahedral sheet stacked together to form a T-O layer. Kaolinite, serpentine, and halloysite are the most common examples of group 1:1 minerals. Group 2:1 is composed of minerals with one octahedral sheet stacked between two tetrahedral sheets to give a T-O-T layer, and include: illite, smectite, vermiculite, and micas [72]. An interlayer can exist between each stack, as in the case of chlorite, whereby a brucite- or gibbsite-like interlayer hydroxide sheet forms a 2:1:1 structural arrangement [73].

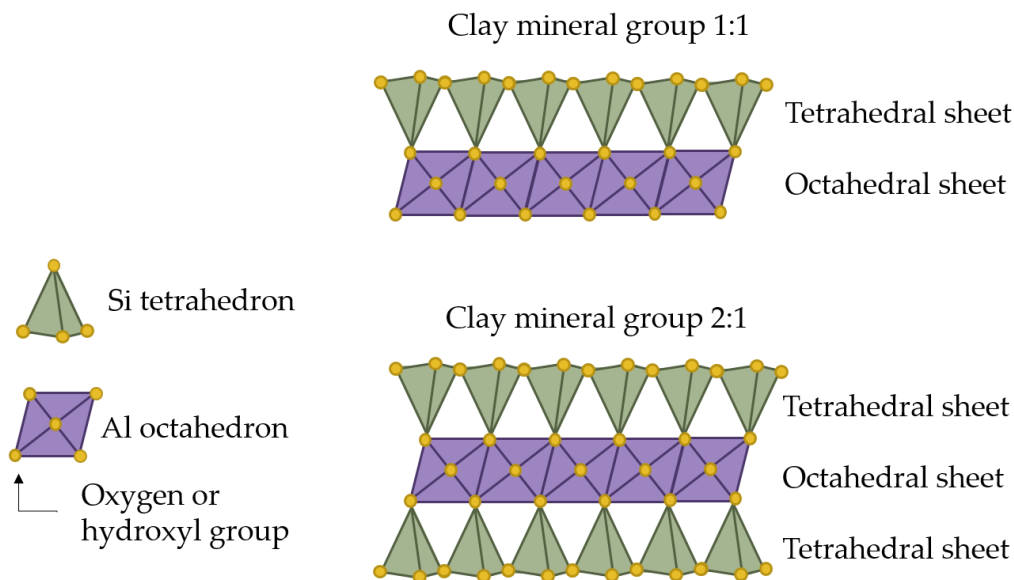


Fig. 2.5: Structures of clay mineral groups 1:1 and 2:1

The use of untreated clays in cement as SCMs is reported to negatively affect workability and not provide major benefits [74]. The stable crystalline structure of clays does not exhibit significant pozzolanic activity, whilst the high surface area and consequent electrostatic charge of platelet-like particle morphologies necessitates increased water to binder ratios [75]. Calcination of clays via heat treatment promotes structural transformations that increase the reactivity of the clay material and increase pozzolanic activity. This occurs via the removal of structurally bonded

water (dehydroxylation), which in the case of kaolinite is present in the form of hydroxyl groups between T-O layers, at temperatures of 500-900 °C. When these terminal hydroxyl groups are continuously removed, the structure initially collapses to form a disordered metastable phase called metakaolin, with further dehydroxylation resulting in complete amorphisation [76]. The dehydroxylation temperature is specific for each individual clay [76], [77] and is controlled by physical factors such as particle size and degree of crystallinity, as well as chemical factors such as concentration of hydroxyl groups [71]. The dehydroxylation temperature indicates the starting transformation temperature above which amorphisation occurs, however, increasing the temperature further may initiate recrystallization into high-temperature stable phases, such as mullite ($3\text{Al}_2\text{O}_3 \cdot 2\text{SiO}_2$) or corundum (Al_2O_3) in the case of metakaolin. The recrystallization temperature is again specific for each clay, varying from 850 °C for illitic clays, up to 1000 °C for kaolinite [78], [79]. Optimisation of the calcination time and temperature is important to allow for complete dehydroxylation and resulting amorphous phase formation without any recrystallization into high temperature structures.

Kaolin, illite, and montmorillonite (smectite group) are the three most abundant natural clays in the earth's crust. Out of these clays, kaolin has been demonstrated to exhibit the best potential use as an aluminosilicate precursor due to the wide calcination temperature range, avoidance of particle coarsening/sintering during calcination, and high pozzolanic activity after calcination [80]–[82]. Kaolin has a large temperature range between initial dehydroxylation and high temperature recrystallization, underpinned by the direct exposure of surface hydroxyl groups on the Al octahedral sheet [81]. Alkali-activation may also offer a pathway for the valorisation of partial or non-kaolinitic clays, or clays with low purities that are considered as waste materials.

2.4.1.2 *Metakaolin*

Kaolinite is currently extracted from pure kaolinite deposits, as a by-product from mine-tailings, and from paper industry waste. Metakaolin is the calcination product

of kaolinite, a metastable partially amorphous transition phase with high reactivity, generated at temperatures between 550–800 °C, below the temperature of recrystallization to mullite (Fig. 2.6). During calcination, kaolinite loses its layered and ordered structure, the resulting structural strain of the dehydroxylated aluminium octahedra and the high Al-O-Al bond energies increase the reactivity of metakaolin [83], [84]. One of the main limitations to widespread utilisation of metakaolin as a cement binder is its fine particle size and platelet-like particle morphology [85]. The platelet-like particle morphology can cause dispersion issues and impact workability, requiring increased water to be added to the mix. The replacement of metakaolin calcined using rotary kilns with metakaolin synthesised via flash calcination has been shown to improve the performance of the raw material. The resulting spherical particles reduce water demand [86]–[88] and increase pozzolanic activity with greater surface area [89].

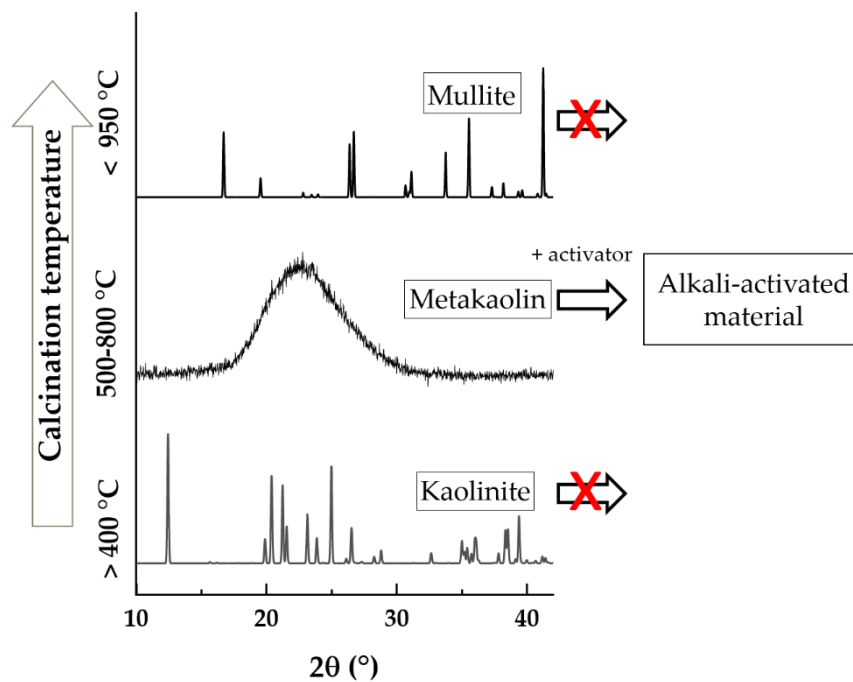


Fig. 2.6: XRD patterns of kaolinite, metakaolin, and mullite, showing the transitions due to increased calcination temperature

Alkali-activated concretes based on metakaolin can exhibit good performance [86], [90], however the more beneficial way of utilising metakaolin lies in blending it with other binding materials such as slag or fly ash [91], [92]. When blended with other cementitious materials, metakaolin is able to react at ambient temperature with portlandite (Ca(OH)_2), formed during cement hydration, in the presence of water to create additional C-S-H gel [92].

2.4.1.3 *Copper slag (low-calcium and iron-rich metallurgical slag)*

Global production of copper was reported to be around 24.8 million tonnes in 2022 [93], with 2.20 tonnes of CS produced for every tonne of copper [94], [95].

CS is a by-product generated during the matte smelting and refining of copper [96]. During the smelting process, copper ore is heated and melted to separate impurities, such as Fe and S, present in the unrefined ore. Two distinct molten phases are generated during this process. Silica is added to react with impurity oxides to create strongly bonded silicates that are the main constituent of CS. In contrast, sulphides tend to form a matte phase as they have a lower tendency to form anion complexes. Direct addition of silica ensures complete isolation of copper from the matte, which occurs when the concentration of SiO_2 is near the saturation limit [95].

CS is primarily composed of Fe and Si, but may also contain other trace elements depending on the composition of the ore, the type of furnace used during smelting, and the metallurgical refinement process employed. CS is a hard, black, glassy material with densities ranging from 2.8-3.8 g/cm^3 . When air-cooled, CS develops several good mechanical properties for utilisation as an aggregate, such as robustness, abrasion resistance, high thermal stability, and high friction due to highly angular particle morphologies [94]. Its vitreous nature, however, can impact its frictional properties and skid resistance [94], and thus its performance as an aggregate particularly when used in road construction. CS has been utilised as a fine and coarse aggregate in both conventional and alkali-activated concretes [95], [97], [98]. The typical oxide composition varies within the range of: Fe_2O_3 (35-60 %), SiO_2

(25-40 %), CaO (1-10 %), Al₂O₃ (3-15 %), CuO (0.3-2 %), and MgO (0.7-3.5 %) [95], [99], [100]. The main crystalline mineral phases found in CS are fayalite and magnetite [101]. Minor phases reported include a partially amorphous fraction formed during the rapid cooling of the molten slag, composed of glassy Si and Fe. It is this highly reactive glass phase that determines the pozzolanic properties of CS, which can be exploited in alkali-activated mixes studied in this work. Whilst crystalline iron silicate phases are very slow to dissolve in alkaline media, the amorphous phase can completely dissolve rapidly. The amorphous phase fraction in CS represents a very important factor in assessing their suitability for alkali-activation [102]. Formation of iron-rich gel phases has been reported for AACs containing CS [103], however the structure and reaction mechanism is not yet fully understood. The amorphous nature of both the precursor and reaction products means that the efficacy of conventional structural analysis techniques, such as X-ray diffraction, is limited. The high iron content also restricts the use of solid-state NMR, a technique commonly employed in cement and alkali-activation research to investigate the binding aluminosilicate network [102]. Most reported investigations into CS systems involve more exotic techniques such as ⁵⁷Fe Mössbauer spectroscopy [104]–[106] or XANES [107] to elucidate important structural information. Alkali-activation of iron-rich slags with sodium silicate has been reported to result in the dissolution of Fe³⁺ and Fe²⁺ from the slag. Dissolved Fe²⁺ ions form octahedral layers, whilst dissolved Fe³⁺ forms silicate-like networks with tetrahedral coordination, whereby Na⁺ cations act as charge balancing species, similarly to the behaviour of Al in C-A-S-H or N-A-S-H. There is, however, some disagreement in the literature regarding the tetrahedral coordination of Fe³⁺ in the silicate network, with certain studies reporting Fe³⁺ to be in 5-fold coordination [107].

2.4.2 High-calcium systems

GGBFS is by far the most investigated Ca-rich precursor in alkali-activation. The gel products obtained from the alkali-activation of GGBFS are termed C-A-S-H, calcium silicate aluminate hydrates, similar to the hydration product of PC, known as C-S-H.

The molecular structure of C-A-S-H resembles C-S-H, whereby CaO sheets are interlayered with aluminosilicate chains, forming a tobermorite-like dreierketten structure as highlighted in Fig. 2.7.

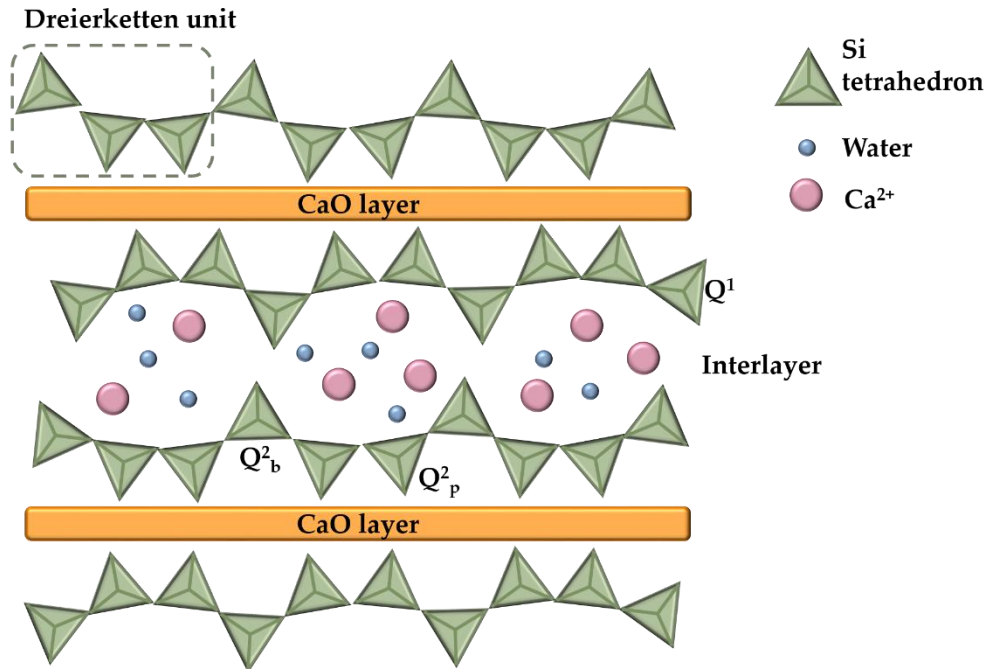


Fig. 2.7: Schematic of C-S-H structure

The 2-D structural comparison between C-A-S-H and C-S-H can be seen by comparing Fig. 2.7 and Fig. 2.8. The atomic short-range order appears alike, however, at increasing length scales, C-S-H exhibits nano-crystallinity, whereas C-A-S-H shows ordering only up to 15 Å giving rise to a highly disordered nano-scale tobermorite-like structure [108]. The degree of polymerisation (or crosslinking) of C-A-S-H is higher than C-S-H, aided by the inclusion of Al, which can replace Si in the network, resulting in very densely packed structures. Lower Ca/Si ratios of approximately 1 are found in C-A-S-H along with higher Al contents (with Al/Si ratio of 0.1-0.2) than in C-S-H [109]–[112]. C-A-S-H structures have been described as coexistence of both the 11 and 14 Å tobermorite-like phases [112] and taking into account the inherent limitation of the crosslinked and non-crosslinked structures of the various tobermorite-like units, a structural model was developed, enabling the

calculation of the chain length, Al/Si ratio, and degree of crosslinking for these structures, which cannot be adequately described using traditional models for non-crosslinked tobermorite-like C-S-H gels [16].

C-A-S-H structure varies depending on the activator used: NaOH activated slags result in a more ordered gel structure and higher Ca/Si ratio than silicate-activated slag [113]. Alongside the main products, intermediate gels (C,N)-A-S-H, with partial replacements of Ca with Na, or with Na partially adsorbed on C-A-S-H can be formed according to the chemistry of the activator solution and precursor materials [110], [114].

Additional reaction products seen can include layered double hydroxides (LDH) with a hydrotalcite-like structure, and zeolites that vary in composition depending on the precursors used.

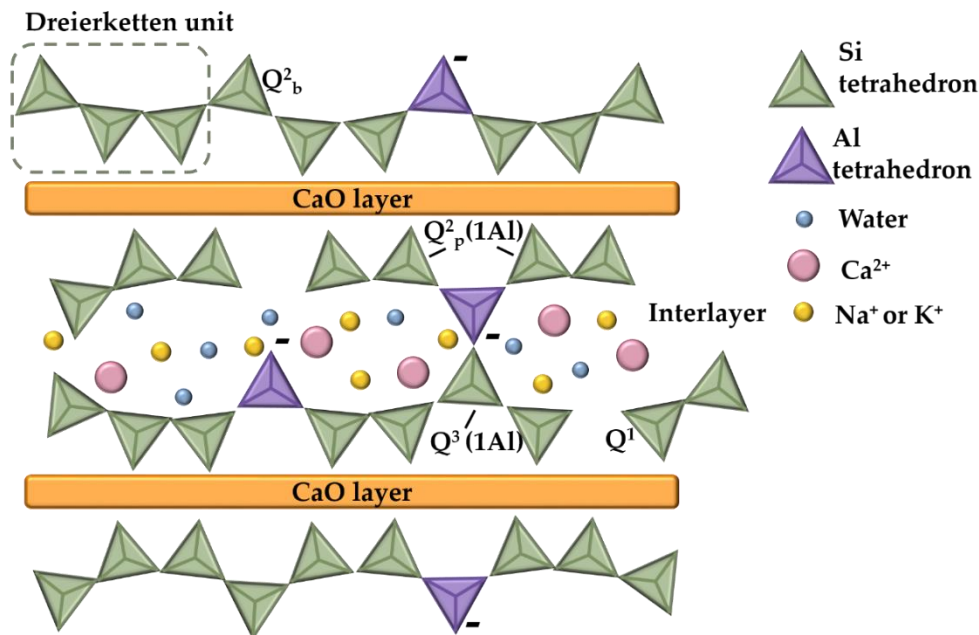


Fig. 2.8: Schematic of C-A-S-H structure

For alkali-activated slags, C-A-S-H is usually not the sole reaction product. Mg and Al-rich LDH lamellar structures, of which hydrotalcite is the naturally occurring

phase, with general structure $Mg_{1-x}Al_x(OH)_2(CO_3)_x \cdot nH_2O$ are seen when the MgO content of GGBFS is above 5% [110], [115]. AFm-like phases are formed as a secondary product of NaOH-activated slags [110], [116]. Strätlingite, a silicate-containing AFm-like phase, can be found when using precursors with high Al content are activated with silicates [117], whilst zeolites such as gismondite and garronite are seen for GGBFS with low MgO and high Al_2O_3 contents (Fig. 2.9). The structural water found in C-A-S-H binds to the network and acts as a strong space-filling molecule, contributing to strength.

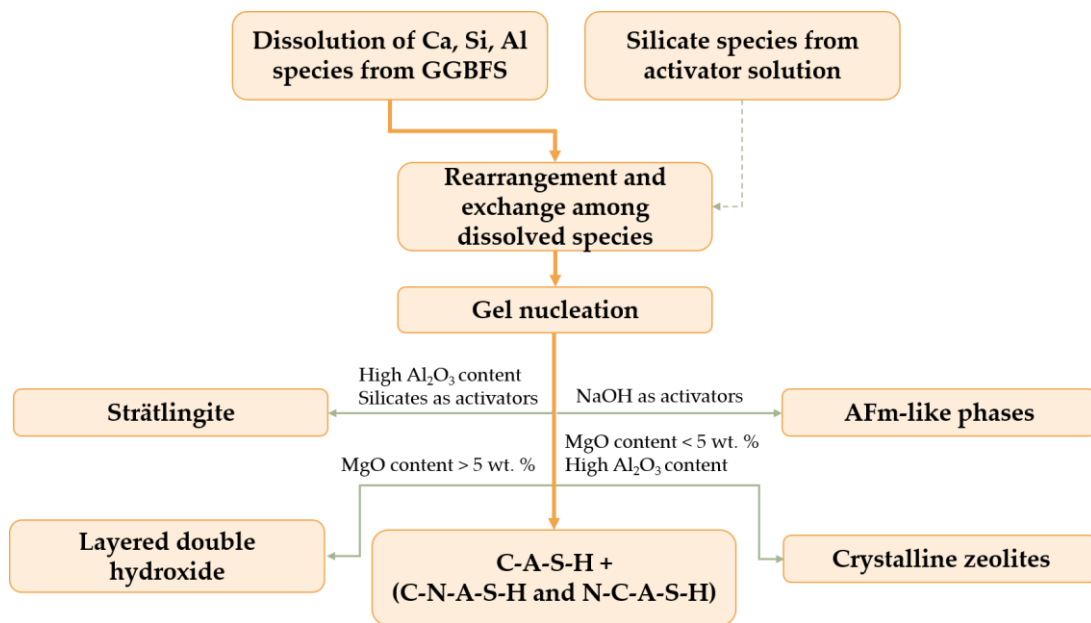


Fig. 2.9: Reaction steps of the alkali-activation of GGBFS (as representative of high-calcium precursors). The reaction products and secondary products are identified. Modified after [118]

The nature of the activating solution has a significant effect on C-A-S-H composition. For silicate-activated systems, the lower Ca/Si ratio values result in a more disordered C-A-S-H structure than in NaOH-activated systems. This is due to the higher availability of Si in the pore solution provided by the activator.

2.4.2.1 GGBFS

As of 2021, global crude steel production was estimated to be around to 1.96 billion tonnes [119]. Large scale production of iron and steel generates large quantities of

waste materials, 90 % of which are slags [120]. This amounts to roughly 400 kg of slag per tonne of steel generated via traditional methods including blast furnace and basic oxygen furnace, and 200 kg of slag per tonne of steel produced via an electric arc furnace from scrap steel [120]. The large quantity of slag produced should support its consideration as a sustainable resource, however in some cases, utilisation of such slags is not possible. The classification of iron and steel slag depends on the type of furnace in which they are produced. The main factors affecting the characteristics of slags, such as composition, mineralogy, and other properties, are the initial raw mineral ores and the cooling process used after refinement. The steelmaking process begins using a blast-furnace to obtain melted pig iron from iron ore. From the separation of melted pig iron, blast-furnace slag (BFS) is obtained, which is usually rapidly quenched, ground, and granulated to obtain GGBFS.

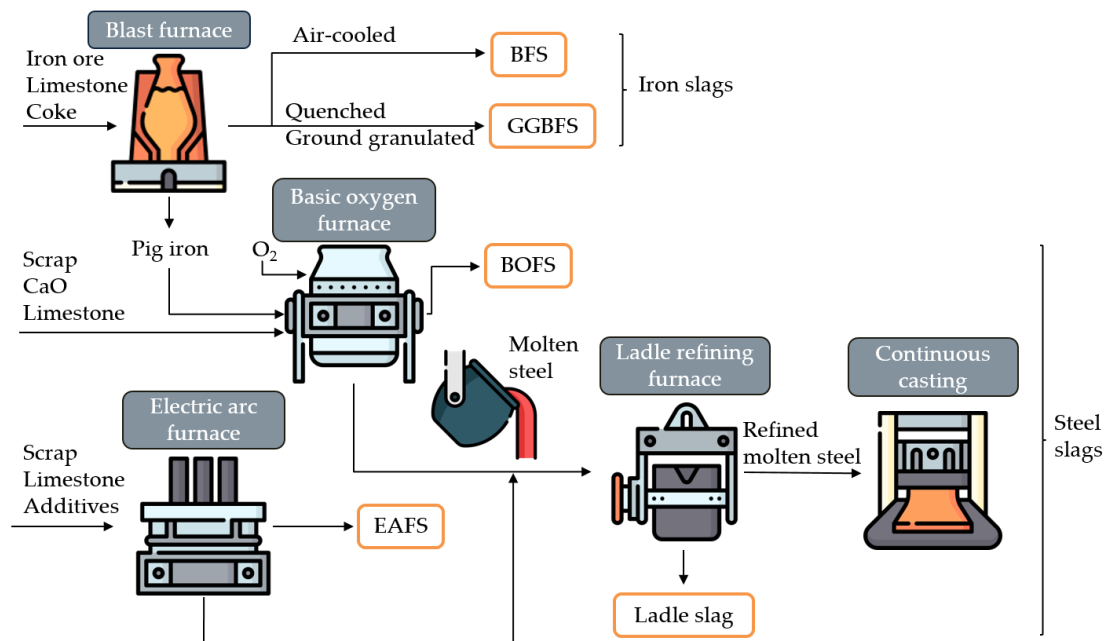


Fig. 2.10: Iron and steel making processes. Modified after [121]

GGBFS has been extensively investigated as both an SCM for conventional clinker-based cement and as an alkali-activated material. Its composition is often described as a mixture of poorly crystalline phases based on CaO , Al_2O_3 , SiO_2 , and MgO with

traces of other elements such as Cr, Ti, S, and Mn. GGBFS formed from quick cooling of molten slag has a glassy and partially amorphous structure that is highly reactive. Slow cooling of molten slag melts leads to the appearance of crystalline phases of Ca-Al-Mg silicates, such as gehlenite C_2AS and åkermanite C_3MS_2 , resulting in poor reactivity and cementing properties [122]. Slags with a glass-like structure consisting of a CaO/SiO_2 ratio between 0.5-2.0 and an Al_2O_3/SiO_2 ratio between 0.1-0.6 are considered optimum for alkali-activation [123].

The presence of MgO in varying amounts can influence the strength of the alkali-activated binder. High MgO content in the slag results in faster reaction rates and consequently can increase compressive strength at early ages [124]. This is due to the formation of hydrotalcite-group phases in addition to the C-A-S-H phase, that have good mechanical properties. High MgO content can also increase binder resistance to carbonation, as the formation of the hydrotalcite structure prevents the detrimental effect of carbonation penetrating further into the bulk [125], whilst also restricting chloride ingress. Both these factors significantly increase the durability of the binder. As MgO content in the slag has a positive influence on the properties of the alkali-activated material, special consideration must be given to identify the optimal MgO content [126] needed in order to improve the general performance of the binder [117].

2.4.2.2 *Steel slags: BOFS and EAFS*

Steel slags, disregarding the different production routes shown in Fig. 2.10, have some common characteristics. Both BOFS and EAFS are generated from the addition of lime (or dolomite) into the furnace, with their function to prevent the oxidation of the molten metal and to aid in removing impurities.

BOFS is a by-product generated during the conversion of molten iron into crude steel using a basic oxygen furnace. During this process, also known as the Linz-Donawitz process, scrap and fluxing agents such as CaO and dolomitic lime are added to the furnace, whilst high-pressure oxygen is injected through a lance, causing impurities

to be oxidized and removed [127]. The resulting molten steel is then poured into moulds to form various steel products, whilst the by-product BOFS is separated and cooled. An alternative two-step process is used to produce steel from scrap metal. The first stage generates EAFS, whilst the final refinement stage produces ladle slag. Here an electric arc furnace is filled with limited amounts of steel scrap (termed “cold” steel), limestone (or dolomite), and other additives. When graphite electrodes are lowered into the steel charge, an arc is generated, which causes the melting and purification of steel at around 1550 °C. As the metal melts, oxygen is blown into the vessel oxidising the impurities, which combine with limestone to form EAFS [128].

The composition and characteristics of steel slags are highly variable and depend on the starting materials, cooling conditions, and the steelmaking plant in question [121]. Average densities for steel slag range from 2.8-3.6 g/cm³. The high Fe content is reported to provide high abrasion and corrosion resistance as an aggregate [129]. Most steel slags consist of crystalline oxides: CaO, FeO, Fe₂O₃, SiO₂, MgO, and Al₂O₃, and often also MnO and P₂O₅, arranged in complexes of calcium silicates, aluminosilicates, aluminoferrites, and RO phases (solid solutions of CaO, MgO, MnO, and SiO₂) [100], [130], [131]. The CaO content varies between 40-55 %, SiO₂ between 12-28 % [131], whilst the FeO content varies from sample to sample. Generally speaking the FeO content in BOFS is higher than EAFS [127], however, there are exceptions to this trend.

Several publications have shown that steel slags can be used as aggregates in concretes: fine aggregates [132], [133], coarse aggregates [134], for roads and pavements [135], [136], for infrastructure and special applications in high strength and self-compacting concretes [137], and also as aggregates in alkali-activated concretes [138]–[140]. In some cases, increased performance is reported when compared to natural aggregates due to their increased hardness and abrasion resistance [141]. LCA studies on steel slags as aggregates report an improved environmental benefit when replacing natural aggregates [140], [142].

The main issues in the usage of both BOFS and EAFS as aggregates are potentially severe volumetric expansion of aggregates due to the presence of free lime and MgO [100], and leaching of toxic heavy metal complexes, such as Cr, V, Mo, and Ba [143]. Applications of steel slags as SCMs or precursors for alkali-activation are also limited [144] by the relatively low, if any, content of hydraulic phases such as alite, belite, and aluminoferrites, and their limited pozzolanic activity. There exist several treatments of steel slags to improve their properties; long weathering is usually a requirement prior to the usage of steel slags as aggregate [100], [145]. Accelerated environmental carbonation causes a stabilisation of expansive phases through the formation of nano-crystalline calcite in the external layers, directly reducing the free lime content. Potential leaching of heavy metals is also minimised by the conversion of toxic metal complexes to more stable forms in this process, effectively immobilising these within the aggregate [146]. The formation of stable heavy metal phases can also be controlled through the modification of the cooling process, tailored to form stable solid spinel phases with low solubility, in which Cr is strongly bound [147], [148]. Silica additions to fluid slag during the deslagging period can also result in an inert EAFS product through the formation of highly stable gehlenite matrices [149].

Effective encapsulation/immobilisation of slag products that contain high quantities of toxic elements and that are considered to be susceptible to leaching can be achieved through alkali-activation [150]. Various processing pathways may be considered to increase slag reactivity, such as re-melting and quenching of steel slags to promote the formation of amorphous phases [151] or other chemical and mechanical activation pathways, such as mechanical grinding of slag into fine powder [152], thermal excitation [153], [154], and the addition of phosphoric acid to reduce the CaO content [155].

Several studies report the inclusion of steel slags in alkali-activated materials to improve workability due to particle fineness and low reactivity, allowing a reduction in the water required for the mix [156], [157]. EAFS is reported in many cases to act

as a filler material rather than an active component in the alkali-activation process [158]–[160], whilst additional treatments such as carbonation curing have been reported necessary to achieve satisfactory results [161]. Inclusion of BOFS as an SCM [129], [162], [163] and as a precursor material in alkali-activation are reported to be more successful, conditional on the use of appropriate activator solutions [164], [165].

Overall, steel slags have a high potential environmental benefit in reducing carbon emissions and removing the need for landfill when used as a substitute for cement and as a construction material. Steel slags may be an environmentally friendly alternative to natural aggregates by eliminating the negative environmental impacts associated with mining specifically for such aggregate materials. Other metallurgical slags are currently being studied as potential raw materials in alkali-activation to reduce the demand for blast furnace slag. They generally do not show the same properties as steel slags, as although they exhibit pozzolanic activity, they lack hydraulic properties due to the lack of lime [94].

2.4.3 Blended and hybrid systems

There exists great interest within the alkali-activation field in enhancing binder performance by forming a coexistence of both N-A-S-H (low-Ca) and C-A-S-H (high-Ca) gels and exploiting both their unique properties. C-A-S-H gels provide high chemical binding of water and therefore a reduction in the permeability of the system, whilst N-A-S-H gels have elevated chemical and thermal resistance due to free water within the structure.

The optimal conditions in which these two gel types can co-precipitate are strongly influenced by pH and the content of dissolved Al. At high pH, reactive Ca from C-S-H can dissolve and reprecipitate to form portlandite, whilst C-S-H obtained in alkaline media with additions of reactive Al results in increased cross-linking of the network and the crystallisation of strätlingite-like phases [166], [167]. Investigations into the controlled synthesis of C-S-H gel from PC, and N-A-S-H gels, have demonstrated that C-S-H gel forms at $\text{pH} > 11$, whilst N-A-S-H gel is detected at pH

>12.5 [168]. N-A-S-H gels are modified by high Ca concentrations in high pH solutions to form C-(N)-A-S-H gels [169], and ultimately C-A-S-H. The high alkalinity in this case leads to ion exchange, whereby Na is replaced by Ca, suggesting that N-A-S-H phases may suffer from some chemical instability at high pH in the presence of reactive Ca [170]. Distinct compositional regions representing the two gels were detected by SEM-EDS revealing that the elemental composition within each gel phase is consistent. This indicates that, under appropriate conditions, the two gel phases can coexist and reach a state of thermodynamic stability [170], [171]. However, due to the influence of several factors, including the blending ratio, raw material composition, reactivity, and the activator solution used, it remains challenging to accurately predict the structure of resulting gel phases.

The blended binders based on calcined clays and GGBFS strongly depend on the alkalinity of the activator, on its modulus, and the degree of intermixing between precursors [172]. For highly alkaline systems, the formation of C-S-H is inhibited or slowed due to the quick reaction of the aluminosilicate source on the surface of GGBFS particles, and the low solubility of Ca^{2+} that starts to precipitate as portlandite instead of forming C-S-H phases. In moderately-alkaline conditions, the dissolution of Ca^{2+} from the GGBFS tends to form C-S-H phases at early ages, whilst the aluminosilicate sources react later to form N-A-S-H gels at later ages. This gives rise to a coexistence of the two gel phases in the initial stages of reaction [172]–[174].

A deeper understanding of the behaviour of alkali-activated blended systems can provide a foundation for future binder design, allowing the incorporation of materials from diverse sources, to ultimately obtain high-performance binders with minimal environmental cost.

2.4.3.1 *Hybrid binders*

Hybrid binders represent one possible approach to decrease the amount of alkaline solution needed for the activation of the raw materials in alkali-activation. This class of binders are generated by incorporating a limited amount of traditional

cementitious materials, up to a maximum of 30 wt. %, in the production of an alkali-activated material [175], [176]. Hybrid binders have generated significant interest from both industry and academia as a practical approach towards increasing the utilisation of AACs in the market, without completely dismantling traditional cement production [177]. The dominant chemistry in the case of hybrid binders comes from the solid precursor, with secondary C-S-H playing a minor role.

Research on gel coexistence has highlighted mutually beneficial reaction pathways in hybrid binders. The alkaline content and presence of soluble silica in the activator solution are known to affect the hydration of PC, whilst precursors, such as fly ash, show accelerated activation in the presence of PC. Heat released during hydration favours chemical reactions that induce ash dissolution, setting, and hardening [178], [179].

Additives like PC [179], [180], portlandite ($\text{Ca}(\text{OH})_2$) [181], and CaO [182] have been successfully used in alkali-activation to enhance binder properties [183], including compressive and flexural strength, and early age behaviour [184]. These additives also allow for a reduction in liquid activator concentration by increasing the pH of the system via their dissolution [179], [185]. The reduced activator demand is considered to be highly desirable, along with the potential to valorise a variety of industrial wastes.

2.4.3.2 *Hybrid binders with calcium aluminate cements*

CACs are hydraulic materials containing high amounts of alumina, usually between 40 and 85 wt. % [186]. CACs are known for their rapid strength development (up to 90% of final strength in 24 hours), thermal resistance, and resistance to chemical attack, making them desirable for specialist concrete applications such as refractory materials. CAC manufacture involves fusing or sintering a measured mixture of limestone and bauxite, and potentially accounts for lower CO_2 emissions with respect to PC production, but is considerably more expensive [187]. CAC has been studied extensively as a cement in its own right, with known hydration products that exhibit

rapid setting times and exceptionally early strength development [188]. Monocalcium aluminate ($\text{CaO}\cdot\text{Al}_2\text{O}_3$, or CA in cement shorthand notation) is the main phase of CAC which quickly reacts with water at ambient temperatures to form metastable hexagonal calcium aluminate hydrates (CAH_{10} and CA_2H_8). These phases are associated with initial strength development, but their chemical stability is strongly dependent on temperature, time, and the water/cement ratio. The main limitation on the use of CAC in structural construction applications is due to a process known as conversion, whereby the metastable hexagonal aluminate hydrates convert to stable cubic aluminate hydrate (C_3AH_6) accompanied by the formation of AH_3 gel and the expulsion of water. This consequently increases the porosity of the binder, resulting in volume change and a dramatic loss of strength [186], [189].

The addition of reactive silica in various forms, such as fly ash [190], [191], GGBFS [192], micro-silica [193], and sodium silicate [194], can lead to the formation of strätlingite (C_2ASH_8), reducing or inhibiting the formation of cubic aluminate hydrate. Strätlingite is a stable crystalline compound which is recognised to give better mechanical properties than cubic aluminate hydrate [195].

The behaviour of CAC in moderately and highly alkaline environments has been investigated in some studies [196], [197], as has its effect on the alkali-activation of precursors including GGBFS [198], metakaolin [199], natural pozzolans [200], [201], red clay brick wastes [202], and fly ash [203], for the formation of hybrid binders. Most of these studies did not observe the typical hydration products of CAC (CAH_{10} , C_2AH_8 , AH_3); highly alkaline conditions and high temperatures favour instead the formation of cubic aluminate hydrate from the outset, and if sources of silica are present, katoite-type phases are preferentially formed over strätlingite, which is not favoured in highly alkaline environments.

2.4.4 Alternative precursors

Besides the precursors explored previously in this review, alkali-activation technology has the potential to exploit and valorise novel waste materials from

diverse streams. The requirements for precursor materials are significantly different, and can be considered less stringent than in conventional cement manufacture. Any type of aluminosilicate can potentially be activated, allowing for the utilisation of various unconventional waste materials. There exists a large variety of waste materials which are either pozzolanic or have intrinsic binding properties (latent hydraulic) which can be used to produce binders [38]. The major factors to consider when evaluating the viability of new waste sources is the annual volume output and long term stability of production, along with geographical considerations [204]. These factors are fundamental in allowing alkali-activated technology to become a competitive alternative to conventional cement manufacture. Other precursors, not currently under mainstream investigation, are other types of slags [205]–[208], such as phosphorus slags. Elemental phosphorus can be extracted from the phosphate ore, generating a calcium silicate-rich slag which has already been investigated for alkali-activation [209]. Other metallurgical slags include silicate-rich slags obtained from the pyrometallurgical industry, which extracts metals such as Ni [210], FeNi [211], [212] Zn [213] and Pb [214], Mn (silicomanganese slag [215], [216]), and Ti (titaniferous slag [217]) from the respective ores. Biomass ashes obtained from rice husk [218], palm oil fuel [219], [220], and sugar cane bagasse [221] have been investigated as alternative precursors due to their high amorphous silica content and similarities to fly ash. Wastes from other industrial activities, such as red mud [222] obtained from alumina extraction in the Bayer process, construction and demolition waste [223], ceramic waste [202], glass waste [224]–[226], and several types of mine tailings [227] have also have been investigated. Additionally, certain classes of urban wastes can be valorised or stabilised through alkali-activation, such as ashes from municipal solid waste (MSW) incineration [228]–[231] and sediments from water treatment plants [232], [233].

2.5 Conclusions

Alkali-activation technology offers a sustainable solution with numerous advantages over PC, including the potential to utilise a wide range of industrial wastes as precursors. This study explores the potential of four waste materials from industrial sources including calcined clays, BOFS, EAFS, and CS as potential precursors to form AACs and hybrid binders with CAC. The waste materials are characterised, and novel binders are formulated. The suitability of each material is assessed, demonstrating the potential for designing novel cements based on alkali-activation technology with tailorable properties dependent on the unique precursors utilised. The data presented in this work provide a valuable source of information on the classification of certain waste materials and their behaviour in blended systems, which can ultimately simplify the application of alkali-activation to new waste sources.

Chapter 3.

Materials and Methods

3.1 Materials

Characterisation of GGBFS and the activator solutions utilised in this study are detailed in this chapter. Characterisation of the alternative raw materials used is given in their relevant chapters: calcined waste clays in section 4.2.1, BOFS in section 5.1.2, EAFS in section 5.2.2, CS in section 5.3.2, and CAC in section 6.2.

3.1.1 GGBFS characterisation

GGBFS used in this study is provided by Ecocem, (Belgium). The density and particle size of the GGBFS used in this study are shown in Table 3.1 while the oxide composition obtained with X-ray fluorescence (XRF) is shown in Table 3.2. In each of the following chapters, the control formulation is produced using GGBFS as a baseline material, which is then replaced with alternative materials to assess their impact on the final alkali-activated cements.

Table 3.1: Density and particle size analysis (d_{10} , d_{50} , and d_{90} values) of GGBFS.

| Sample | Density | Particle size analysis (μm) | | |
|--------|----------------------------|--|----------|----------|
| | (g/cm^3) | d_{10} | d_{50} | d_{90} |
| GGBFS | 2.9 | 3.8 | 12.7 | 31.0 |

Table 3.2: Oxide composition (wt. %) of GGBFS as measured with XRF. Loss of ignition (LOI) at 1000 °C

| Sample | CaO | SiO ₂ | Al ₂ O ₃ | MgO | SO ₃ | TiO ₂ | Fe ₂ O ₃ | MnO | LOI |
|--------|------|------------------|--------------------------------|-----|-----------------|------------------|--------------------------------|-------|-----|
| | (%) | (%) | (%) | (%) | (%) | (%) | (%) | 2 (%) | (%) |
| GGBFS | 43.5 | 36.4 | 10.5 | 7.0 | 1.4 | 0.5 | 0.3 | 0.3 | 0.2 |

Fig. 3.1 shows an SEM image of GGBFS particles which appear angular and irregular.

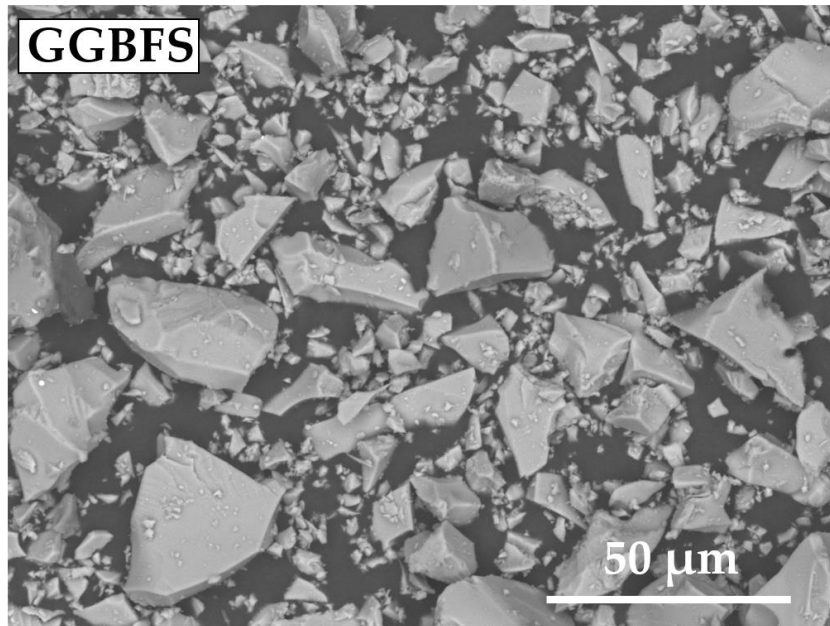


Fig. 3.1: SEM image of GGBFS particles

The XRD pattern of GGBFS shown in Fig. 3.2 indicates an amorphous structure with a broad feature due to diffuse scattering centred at $30^\circ 2\theta$, and a distinct lack of any crystalline phases.

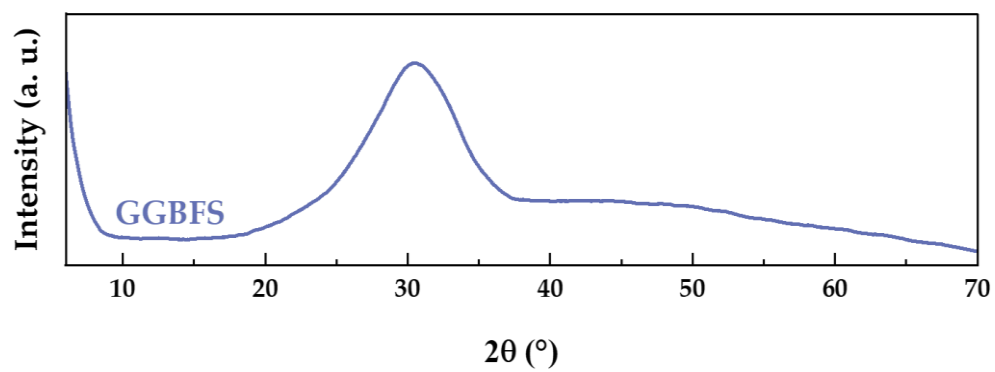


Fig. 3.2: XRD pattern of GGBFS

Fig. 3.3 displays the FTIR spectrum of GGBFS. Two main absorption bands are seen at $\sim 1000\text{-}900\text{ cm}^{-1}$ and at $\sim 500\text{ cm}^{-1}$ corresponding to Si-O-T (T = tetrahedral Si, Al) asymmetric stretching vibrations (ν_a) and Si-O symmetric stretching vibrations (ν_s), respectively [234], along with a minor resonance at $\sim 700\text{ cm}^{-1}$ attributed to the Si-O out of plane bending vibration (δ_a). The broadness of these peaks is indicative of the highly amorphous structure consisting predominantly of silicates. A small signal at $1500\text{-}1400\text{ cm}^{-1}$ can be attributed to atmospheric carbonation.

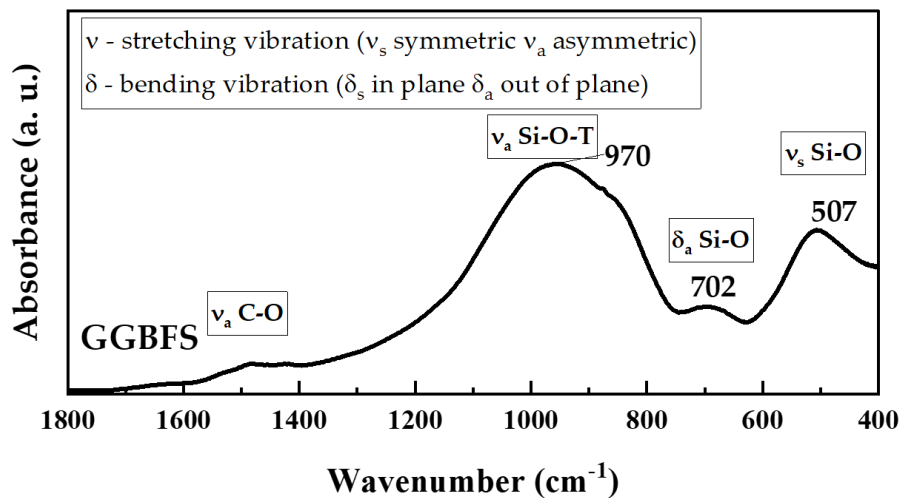


Fig. 3.3: FTIR spectrum of GGBFS

3.1.2 Activators

Sodium hydroxide (NaOH) pellets (purity > 98 %, Sigma-Aldrich) and a commercial sodium silicate solution (PQ Corporation), with a solids content of 44.1% and a modulus (molar ratio $\text{SiO}_2/\text{Na}_2\text{O}$) of 2.07, were used to synthesis the alkaline activator solutions. In section 5.1 Na_2CO_3 is also used (purity 99.5 %, Sigma-Aldrich).

3.2 Testing methods

3.2.1 Isothermal calorimetry

Isothermal calorimetry provides fundamental information about the reaction kinetics and steps of reaction of AACs. The heat generated during the reaction of alkali-activation is associated with the dissolution, degree of reaction, and the extent of gel formation, which are all exothermic processes.

The reaction kinetics of pastes were determined via isothermal calorimetry using a TAM Air Conduction Calorimeter (TA Instruments, USA) at 20 °C. For the systems described in Chapters 4 and 6, 20 g of fresh paste were transferred into a glass vial after mechanically mixing for ~ 2 min; whilst, to prepare the mixtures discussed in Chapter 5, 10 g of solid precursors were weighed, transferred into a glass vial, and initially dry-mixed; the alkaline solution was added using a pipette and manually mixed for ~ 30 s to allow a more complete recording of the initial peak. The vial was sealed and promptly loaded into the calorimeter along with a reference vial filled with water as described by Wadsö [235]. The thermal behaviour was monitored and recorded for ~ 200 h. The results are presented as heat release per gram of solid binder, i.e. precursor and solid activators combined.

3.2.2 Mini-slump tests

A mini-slump test was conducted on fresh mixtures after 30 min to determine the workability. A slump cone with a height of 57 mm, and internal top and bottom diameters of 19 and 38 mm respectively was used. For each slump test, the slump cone was placed on a flat sheet and gradually filled with the fresh mixture. The cone was then lifted as slowly as possible (< 1 cm/s) [236] and the mean value of the flow diameters measured in two perpendicular directions recorded as the spread. The results relative to section 5.2 and 5.3 were conducted at Ghent University on alkali-activated pastes after 5 min, 30 min and 60 min from the beginning of mixing using

a slump cone of dimensions 40 mm in height, 38 mm top inner diameter, and 60 mm bottom inner diameter. Before each measurement the pastes were manually remixed.

3.2.3 Setting time

The Vicat method was used to evaluate initial and final setting times of fresh alkali-activated pastes, with experiments performed in an automatic Matest VICATRONIC apparatus (Impact Test Equipment, UK) equipped with a 1.13 mm needle, following as closely as possible the standard testing procedure EN 196-3 [237] considering the nature of the materials being tested. Fresh pastes were poured into a conical frustum mould with a height of 40 mm, top internal diameter of 60 mm, and bottom internal diameter of 70 mm. The initial setting time was determined as the moment in which the separation between the needle and the base plate reached 6 ± 3 mm. The final setting time was recorded once a maximum penetration depth of 0.5 mm into the specimen was achieved.

3.2.4 Solvent exchange to stop hydration

Solvent exchange to stop the hydration was used prior XRD, FTIR, SEM, NMR, and MIP analysis. Small fragments of samples were immersed in isopropanol [238] for at least 36 h and then dried in an oven at 35 °C. Once dry, the samples were either crushed and sieved (for XRD, FTIR, and NMR) or mounted in a cup for SEM sample preparation.

3.2.5 X-ray diffraction (XRD)

XRD patterns of raw materials and hardened alkali-activated pastes were examined to identify crystalline phase assemblage and obtain information on the amorphous content which exhibits distinctive features for the presence of C-A-S-H gel structure. XRD patterns were obtained using a PANalytical X'Pert³ (PANalytical, USA) diffractometer operating in Bragg-Brentano geometry with a Cu K α radiation source at 45 kV and 40 mA, fitted with a PIXcel-Medipix3 detector. Samples were analysed

over the 2θ range of 5 - 70 °, using a step size of 0.02 °. Phase identification was carried out using ICDD PDF+4 (ICDD, USA) and HighScore plus (Malvern Panalytical, UK).

3.2.6 Fourier-transform infrared spectroscopy (FTIR)

FTIR analysis was performed using a PerkinElmer Frontier FTIR spectrometer (PerkinElmer, USA) coupled with a triglycine sulfate detector. 2 mg of precursor material were mixed and ground together with 200 mg of KBr. The mixed powder was transferred to a 13 mm pellet die and pressed with 10 tonnes of force to form a transparent pellet which was subsequently tested in the spectrometer. FTIR spectra were collected between 4000 and 400 cm^{-1} with a resolution of 2 cm^{-1} . A blank sample consisting of 200 mg of KBr is regularly measured to establish the background line. This measurement is repeated approximately every hour or sooner if there are changes in humidity levels.

3.2.7 Scanning electron microscopy (SEM)

SEM was conducted using Hitachi TM3030 instrument coupled with the EDS software QUANTAX 70 (Bruker, USA). Powder specimens were prepared by placing a small amount of powder material on a carbon dot adhered to a 12.5 mm Al SEM pin stub. Loose powder was removed using compressed air. Hardened paste fragments were mounted in epoxy resin, left to cure overnight, and demoulded ready for polishing. Samples were ground using SiC sandpaper in ascending grits and polished with 3 and 1 μm diamond suspensions. Polished samples were carbon coated prior to SEM analysis.

3.2.8 Mechanical properties

The compressive strength of alkali-activated mixtures was determined after 7 and 28 days on 50 mm cubes according to the relevant sections of ASTM C109 [239] considering the difference in the nature of the materials. Fresh pastes were poured into moulds and sealed. After 24 hours (or as soon as possible thereafter) the cube specimens were demoulded, resealed, and stored in a curing chamber at 20 ± 1 °C

until testing age. The strength values for the mixtures at each testing age are reported as the mean value of three tests.

In sections 5.2 and 5.3 the compressive and flexural strengths were determined on mortar prisms with dimensions 40 x 40 x 160 mm, according to EN 1015-11 [240], at 1, 3, 7, and 28 days at Ghent University. Specimens were kept sealed in a curing chamber (20 ± 1 °C; 95 % relative humidity) until the day of testing. The compressive and flexural strengths for each curing age are reported as the mean value of six (compressive) or three (flexural) measurements performed on the mortars.

3.2.9 Solid state nuclear magnetic resonance (NMR) spectroscopy

Solid state single pulse ^{27}Al and ^{29}Si magic angle spinning (MAS) NMR spectra were conducted in the Department of Chemistry at the University of Sheffield and acquired on a Bruker Avance III HD 500 spectrometer at 11.7 T (B_0) using a 4.0 mm dual resonance CP/MAS probe, yielding a Larmor frequency of 130.32 MHz for ^{27}Al and 99.35 MHz for ^{29}Si . ^{27}Al MAS NMR spectra were only qualitatively interpreted and collected using 1.7 μs nonselective ($\pi/2$) excitation pulse, a spinning speed of 12.5 kHz, 5 s relaxation delay, and a total of 512 scans. ^{29}Si MAS NMR spectra were acquired using a 5.5 μs nonselective ($\pi/2$) excitation pulse, a spinning speed of 12.5 kHz, 60 s relaxation delay, on a total of 256 scans. Gaussian curves were used to deconvolute the ^{29}Si MAS NMR spectra, fitting the minimum number of peaks and maintaining consistent the peak position and full width at half maximum (FWHM) of each resonance. The chemical shifts are compared to an external standard of 1.0 M $\text{Al}(\text{NO}_3)_3$ for all ^{27}Al spectra and to pure tetramethylsilane (TMS) for ^{29}Si spectra. All analysis was performed using Bruker Top Spin 4.0.

3.2.10 Mercury intrusion porosimetry (MIP)

The porosity of samples was analysed via MIP tests. Prior to analysis the specimens were crushed into 10 mm pieces and immersed in isopropanol for two days in order to stop the hydration process. Preserved specimens were then dried at 35 °C and stored under vacuum at ambient temperatures for one week. MIP measurements

were carried out using an AutoPore V (Micrometrics, UK) porosimeter. ~ 10 mm pieces were selected to give a total charge of 2.2 ± 0.2 g. The mercury/material contact angle was set to 130° [241]. The analysis was conducted with a gradual reduction of pressure (up to 50 μ Hg) and a surface tension of mercury of 0.485 N/m was used in the calculations. Pore size and volume were measured at 200 MPa.

3.2.11 Leaching tests

The leaching of heavy metals for cast monoliths was studied for a period of 91 days immersed in water following the procedure described in NEN-7345:94 [242] (tank test). Three cylindrical monoliths were prepared for every composition, each with a diameter of 10 mm and height of 50 mm. Samples were cured for 28 days under sealed conditions, and then immersed into distilled water in a closed vessel with a liquid/solid volume ratio of 5. Prior to immersion, both bases of the monoliths were covered with epoxy resin to avoid contact with water. Extractions of leachate occurred after 1 h, 24 h, then 3 days, 7 days, 14 days, 28 days, 56 days, and 91 days from the beginning of the test for each sample. Each leachate was passed through 0.2 μ m filter paper and sent for ICP analysis to an external laboratory. After each leachate extraction, distilled water is newly added to each sample.

The fraction of leachate (E_i) is calculated as:

$$E_i = \frac{C_i \cdot V}{A} \quad (1)$$

where C_i is the concentration of the component in fraction i , V is the volume of the eluate, and A is the exposed surface area of the specimen, which in this case is the lateral surface area of the cylinder monoliths only.

The cumulative leaching value is then calculated for each component as:

$$\varepsilon_n = \sum_{i=1}^N E_i \quad (2)$$

for each of the n elements of potential concern, where N is the number of extractions ($N = 8$ in this case).

The materials are classified as a function of cumulative leaching value for each leachate in three following categories according to the limiting concentrations U1 and U2 as shown in Table 3.3:

Category 1 (C1): ε_n is lower than U1 for each heavy metal present in the sample. These materials do not present any environmental restriction in their use. Category 2 (C2): ε_n is between U1 and U2 for some of the heavy metals present in the sample, but not exceeding U2 for any element. These materials do not face any environmental restriction in their use, but after their service life it is compulsory to remove the contaminant elements with concentrations higher than U1. Category 3 (C3): ε_n is higher than U2 for one or more elements. These materials have a limited utilisation. Table 3.3 shows the values of U1 and U2 for selected relevant elements, according to NEN-7345 [242].

Table 3.3: Heavy metal leaching limits (U1 and U2) established by NEN-7345:94 [242]

| | As | Ba | Cd | Co | Cr | Cu | Hg | Mo | Ni | Pb | Sb | Se | V | Zn |
|------------------------------|-----|-------|-----|-----|-----|-----|-----|----|-----|-----|-----|----|------|------|
| U1 (mg/m²) | 40 | 600 | 1 | 25 | 150 | 50 | 0.4 | 15 | 50 | 100 | 3.5 | 3 | 250 | 200 |
| U2 (mg/m²) | 300 | 45000 | 7.5 | 200 | 950 | 350 | 3 | 95 | 350 | 800 | 25 | 20 | 1500 | 1500 |

3.2.12 X-ray fluorescence (XRF)

The XRF measurement, used to obtain the chemical composition, was conducted on a PANalytical Zetium machine operated using PANalytical SuperQ software. The PANalytical WROXI (wide-ranging oxides) calibration was used to determine the oxide concentrations in weight percent. The measurements were made on 40 mm fused beads, prepared with a Claisse LeNeo Fluxer machine. The fused beads were prepared by mixing in a platinum crucible 10 g of lithium tetraborate (with 0.5% LiI) flux with 1 g of powder sample. The sample in the crucible was then heated in 5 steps before being poured into a platinum mould and cooled following a standard procedure: 1) 4 min at 1065°C, 2) 3 min at 1065°C rocking at 10 rpm and an angle of

15°, 3) 6 min at 1065°C rocking at 30 rpm and an angle of 40°, 4) 1 min at 1000°C, 5) 4 min at 1000°C rocking at 25 rpm and an angle of 45°.

3.2.13 Particle size analysis (PSA)

The detailed particle size distribution for each of the raw materials was measured applying a light scattering technique using a Malvern Mastersizer 2000 particle size analyser in isopropanol.

Chapter 4.

Calcined Clays from Waste Sources in Alkali-Activated Cements

This section is based on: L. Stefanini, D. Ansari ¹, B. Walkley, J. L. Provis, “Characterisation of calcined waste clays from kaolinite extraction in alkali-activated GGBFS blends” – under review.

¹*Imerys, United Kingdom*

The experimental investigation, data interpretation, and writing of the original draft of this chapter were carried out by L. Stefanini, whilst B. Walkley and J. L. Provis supervised the work and revised the draft. D. Ansari provided the materials, and specifically the calcination of the clays and the modified Chappelle test presented in this chapter were performed by Imerys.

4.1 Introduction

Clay minerals are considered to be abundant, predominating in soils and sedimentary rocks found throughout the earth’s crust. Clays are easily sourced from various locations globally and are generally not considered to be a limited resource. Quality and suitability of clays for use as a primary resource for given applications is, however, highly dependent on the specific mineral composition, particle morphology, and particle size. Careful selection and testing of clay sources is necessary to ensure desired behaviour as a raw resource for any given process. Calcined clays are extensively used as SCMs in concrete owing to their pozzolanic

properties [243], and can be also used as a primary raw material in alkali-activation [244]–[246].

Kaolinite is one of the most common aluminosilicate mineral clays. Metakaolin, the anhydrous calcined form of kaolinite, is the most widely investigated type of calcined clay [80], [81], due to the availability of sources with consistent elemental compositions without significant impurities, and high pozzolanic reactivity. Alkali-activation technology can potentially accommodate residues from the primary extraction of kaolinite deposits, and metakaolin sources that do not satisfy purity requirements for use as conventional SCMs, providing pathways to valorise clays that are currently considered to be waste materials [204].

Literature on metakaolin based AACs has highlighted technical issues ranging from poor workability [247] to high water demand [85], [248]. These problems are attributed to the inherent platelet-like morphology of kaolinite giving rise to high particle surface area and strong electrostatic interactions during mixing. Increasing water content to overcome these effects can lead to substantial drying shrinkage and cracking [75], [249]. Changes in mix design, aimed at minimising capillary porosity, can help reducing shrinkage [250]. Blends with high-Ca precursors have also been shown to improve resulting microstructures, with the formation of both C-A-S-H and N-A-S-H phases [251]. Such gel coexistence carries several advantages in terms of increased mechanical properties, improved durability, and greater achieved densities. Only limited studies exist on the alkali-activation of non-kaolinitic clays [252].

The utilisation of calcined waste clays, sourced from the extraction of kaolin, in mixed blends with a well-studied Ca-rich precursor like GGBFS is investigated. The inclusion of calcined waste clays as a possible replacement for GGBFS may provide a pathway to achieve tailored systems with coexisting C-A-S-H and N-A-S-H phases.

4.2 Materials

4.2.1 Calcined clays characterisation

Blends of GGBFS and calcined waste clays were used as precursors for alkali-activation. The GGBFS used was provided by Ecocem (Belgium) and the calcined waste clays were sourced by Imerys (UK), as a by-product of kaolinite extraction from a mine located in Cornwall. Clays were previously calcined in a muffle furnace during 1 h at either 750 or 800 °C as indicated in Table 4.1. The densities of precursors, for all precursor materials are shown in Table 4.1 and Fig. 4.1. Both C1 and C2 exhibit multi-modal particle size distributions. C3 and C5 show similar unimodal distributions, whilst C4 has the largest average (d_{50}) particle size.

Table 4.1: Density and particle size analysis of calcined clays and GGBFS

| Sample | T calcination | Density (g/cm ³) | Particle size analysis (µm) | | |
|--------|---------------|---------------------------------|-----------------------------|----------|----------|
| | (°C) | | d_{10} | d_{50} | d_{90} |
| GGBFS | - | 2.95 | 3.75 | 12.7 | 31.0 |
| C1 | 800 | 2.59 | 2.72 | 10.5 | 263 |
| C2 | 750 | 2.60 | 3.62 | 48.4 | 282 |
| C3 | 800 | 2.61 | 7.85 | 26.2 | 77.0 |
| C4 | 750 | 2.69 | 19.8 | 68.1 | 152 |
| C5 | 800 | 2.69 | 8.15 | 24.5 | 66.0 |

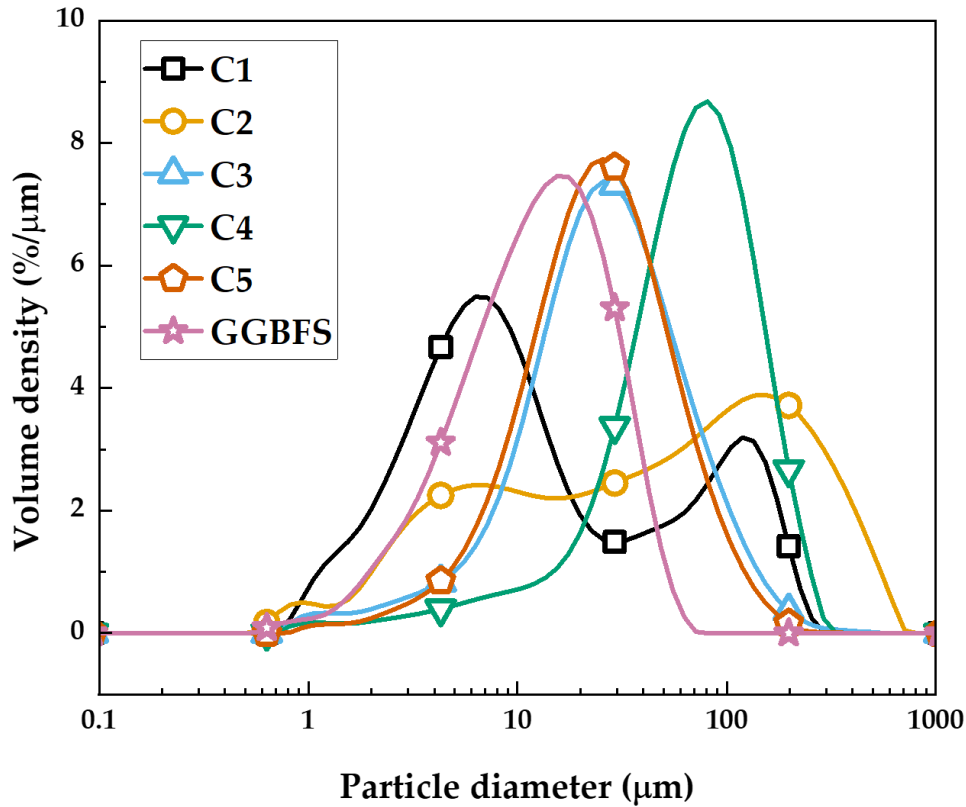


Fig. 4.1: Particle size distributions for calcined waste clays and GGBFS

The chemical oxide compositions of the calcined waste clays obtained by XRF are shown in Table 4.2. C1, C2, and C3 share a similar composition with a Si/Al ratio of approximately 2.2 to 2.3, whereas C4 and C5 exhibit a higher Si/Al ratio exceeding 3. This elevated ratio could be attributed to a greater proportion of quartz within the samples.

Table 4.2: Oxide composition (wt. %) of calcined clays and GGBFS as measured with XRF. Loss of ignition (LOI) at 1000 °C

| Sample | SiO ₂ (%) | Al ₂ O ₃ (%) | CaO (%) | MgO (%) | Na ₂ O (%) | K ₂ O (%) | Cr ₂ O ₃ (%) | Fe ₂ O ₃ (%) | TiO ₂ (%) | LOI |
|--------|-------------------------|---------------------------------------|------------|------------|--------------------------|-------------------------|---------------------------------------|---------------------------------------|-------------------------|-----|
| GGBFS | 36.4 | 10.5 | 43.5 | 7.0 | - | - | 1.4 | 0.3 | 0.5 | 0.2 |
| C1 | 51.3 | 40.5 | 0.1 | 0.6 | 0.9 | 3.6 | 1.2 | 1.7 | 0.1 | - |
| C2 | 54.4 | 41.5 | 0.1 | 0.2 | 0.2 | 1.2 | 1.2 | 1.5 | 0.8 | - |
| C3 | 52.5 | 39.6 | - | 0.4 | 0.3 | 3.7 | 1.2 | 2.2 | 0.2 | - |
| C4 | 66.6 | 23.6 | 0.1 | 0.4 | 0.4 | 5.0 | 1.3 | 2.4 | 0.2 | - |
| C5 | 56.4 | 31.4 | - | 0.7 | 0.6 | 6.4 | 1.2 | 2.9 | 0.4 | - |

The XRD patterns of the raw materials are presented in Fig. 4.2. GGBFS is amorphous with a characteristic broad peak between 25-35° 2 θ . The main phases identified across all calcined waste clays are muscovite ($\text{KAl}_2(\text{AlSi}_3\text{O}_{10})(\text{OH})_2$, PDF#00-058-2034), quartz (SiO_2 , PDF#01-087-2096), K-rich alkali-feldspars ($\text{K}_2\text{O}\cdot\text{Al}_2\text{O}_3\cdot 6\text{SiO}_2$, PDF#00-019-0932), traces of kaolinite ($\text{Al}_2\text{Si}_2\text{O}_5(\text{OH})_4$, PDF#04-013-3074), and an amorphous phase fraction distinguished by a very broad low intensity signal. C3, C4, and C5 have similar phase fractions of muscovite, quartz, and alkali-feldspar. C2 contains large quartz particles, small muscovite particles, and traces of anatase (TiO_2 , PDF 01-086-1155), confirmed by the multimodal size distribution shown in Fig. 4.1 and SEM powder analysis shown in Fig. 4.3. C1 is the only sample to contain residual traces of kaolinite. The predominant crystalline phase in C1 is muscovite combined with its partially dehydroxylated form. Overlap between the main quartz peak (~ 27 °) and the indexed muscovite pattern makes it difficult to determine whether quartz is in fact present in trace amounts. The main phases identified across all calcined waste clays are muscovite ($\text{KAl}_2(\text{AlSi}_3\text{O}_{10})(\text{OH})_2$, PDF#00-058-2034), quartz (SiO_2 , PDF#01-087-2096), K-rich alkali-feldspars ($\text{K}_2\text{O}\cdot\text{Al}_2\text{O}_3\cdot 6\text{SiO}_2$, PDF#00-019-0932), traces of kaolinite ($\text{Al}_2\text{Si}_2\text{O}_5(\text{OH})_4$, PDF#04-013-3074), and an amorphous phase fraction distinguished by a very broad low intensity signal. C3, C4, and C5 have similar phase fractions of muscovite, quartz, and alkali-feldspar. C2 contains large quartz particles, small muscovite particles, and traces of anatase (TiO_2 , PDF 01-086-1155), confirmed by the multimodal size distribution shown in Fig. 4.1 and SEM powder analysis shown in Fig. 4.3. C1 is the only sample to contain residual traces of kaolinite. The predominant crystalline phase in C1 is muscovite combined with its partially dehydroxylated form. Overlap between the main quartz peak (~ 27 °) and the indexed muscovite pattern makes it difficult to determine whether quartz is in fact present in trace amounts.

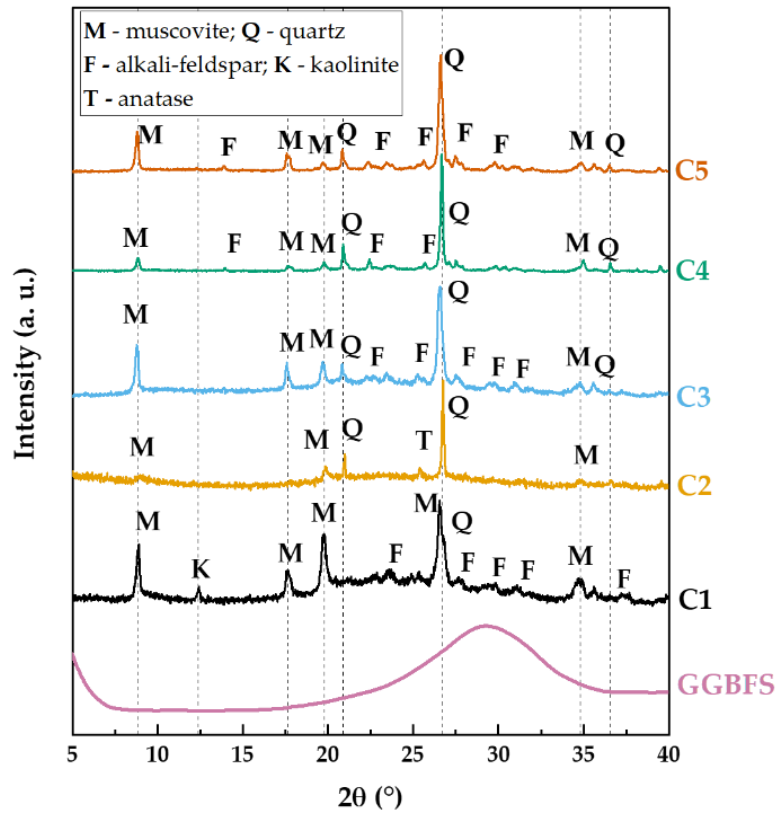


Fig. 4.2: XRD patterns of GGBFS and calcined clays C1 to C5

The differences in particle size distribution and particle morphology between the calcined waste clay samples are highlighted in SEM images in Fig. 4.3. C1 is composed of predominately small platelet-like particles with a minor fraction of large particles present. C2 powder shows a similar multi-modal distribution with distinct fine and coarse particle sizes. C3 and C5 have similar particle sizes but show distinct differences in morphology. C5 has uniform platelet-like particles, whilst C3 consists of plate shaped grains of various dimensions. C4 has the largest particle sizes among the calcined waste clays and exhibits regular equiaxed particle morphologies.

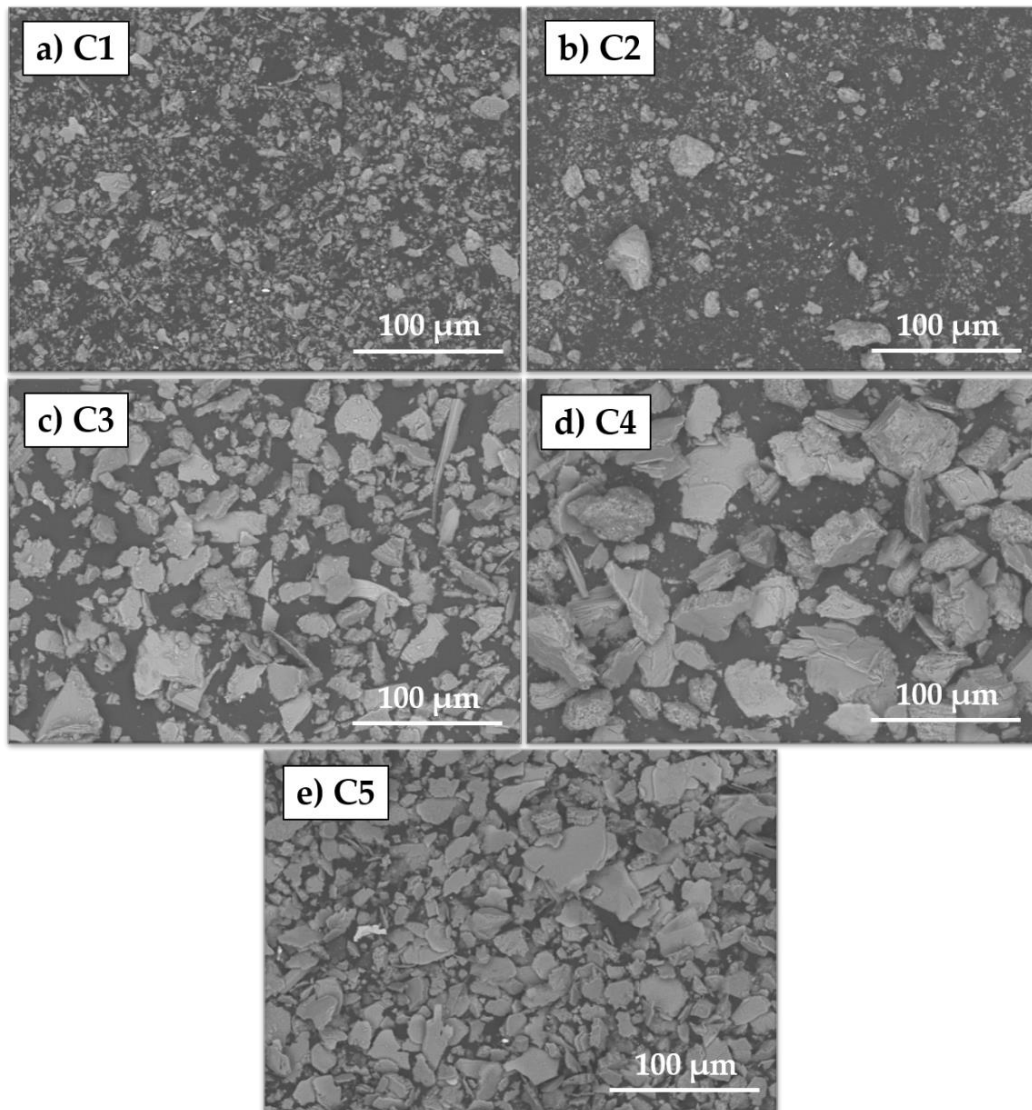


Fig. 4.3: SEM images of calcined clay samples C1 to C5

Fig. 4.4 shows the XRD patterns of C4 before and after calcination. The kaolinite content present in the uncalcined sample is dehydroxylated to form amorphous metakaolin in the calcined sample. The crystallinity of muscovite is partially affected by calcination at 750-800 °C, the peak intensities are reduced when compared with the uncalcined sample. Dehydroxylation of muscovite is not well understood, albeit full conversion to dehydroxylated muscovite is likely to be completed at higher

temperatures $> 800\text{ }^{\circ}\text{C}$; the conversion of muscovite into an amorphous phase is reported to be minimal [81].

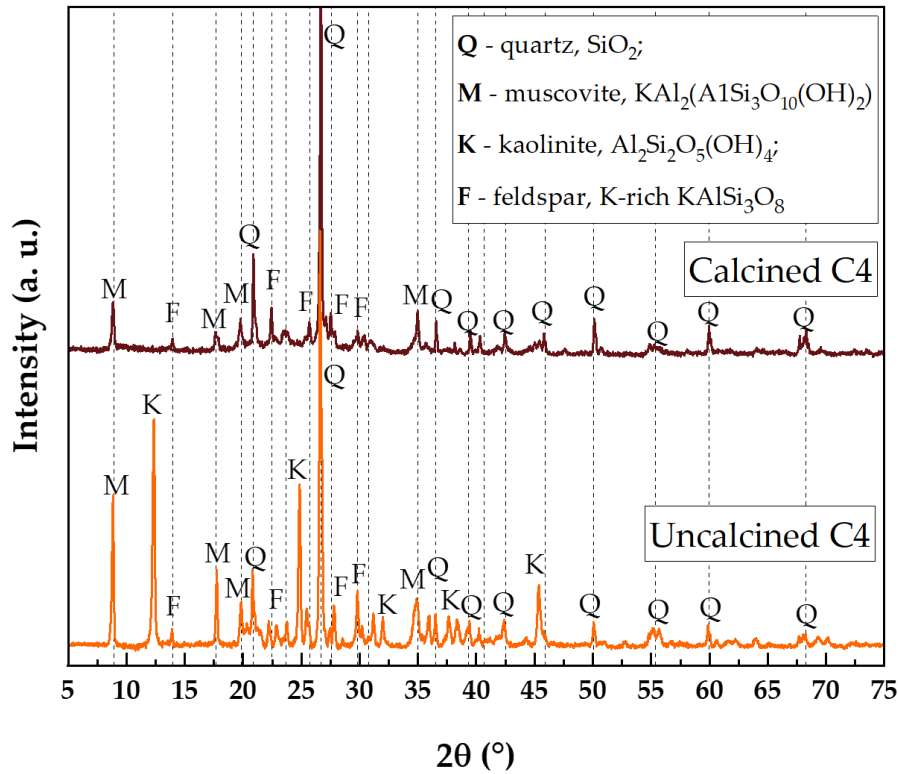


Fig. 4.4: XRD pattern of C4 prior and after calcination

The quartz present in C4 remains unaffected post-calcination. The chemical composition and structural parameters of the alkali-feldspar $(\text{K,Na})_2\text{O}\cdot\text{Al}_2\text{O}_3\cdot 6\text{SiO}_2$ phase present are not known. The combination of varying concentrations of K and Na within the structure and the newly formed phase from the dehydroxylation of muscovite both influence the phase peak positions in the XRD data, making it difficult to obtain structural parameters without more detailed compositional data. It was not possible to satisfactorily determine the phase fractions of the crystalline/amorphous phases via Rietveld refinement due to the aforementioned ambiguities in compositional and structural parameters.

4.2.2 Pozzolanicity tests

Pozzolanic reactivity of calcined clays refers to their ability to react with portlandite that is formed during the hydration of cementitious materials. Tests were based on a modified Chapelle test [253], [254], measuring the amount of calcium hydroxide (Ca(OH)_2) fixed by the reaction of 1 g of metakaolin and 2 g of portlandite at 90°C for 16 hours. The portlandite content free in solution at the end of the reaction was extracted using sucrose and subjected to acid titration to determine its exact concentration. According to this test, the pozzolanic activity of a metakaolin source should not be less than 700 mg $\text{Ca(OH)}_2/\text{g}$ metakaolin [253]. The results for the calcined waste clays are shown in Table 4.3.

Table 4.3: Result of the pozzolanicity test for the calcined waste clays

| Sample | mg $\text{Ca(OH)}_2/\text{g}$ |
|--------|-------------------------------|
| C1 | 1011 |
| C2 | 567 |
| C3 | 967 |
| C4 | 576 |
| C5 | 943 |

Three out of five samples are within this range, whilst the others are significantly below. Most surprising is the drop in pozzolanic reactivity seen in C4 compared to C3 and C5, even though all three samples show similar phase assemblage (Fig. 4.2) and particle morphologies (Fig. 4.3).

R3 tests [255] were performed to compare with pozzolanic activity data from the modified Chapelle test. The R3 test correlates pozzolanic activity with total heat released by the reaction of calcined waste clay, portlandite, and limestone pastes mixed with alkali-sulfates. Samples are hydrated for 6 days at 20°C as stated in the original R3 development work [255]. The results for the calcined waste clays are shown in Fig. 4.5. C1 shows the highest reactivity, whilst C2 has the lowest recorded

activity, in agreement with the modified Chapelle test data. The most noticeable difference is the similar activity between C3, C4, and C5 samples.

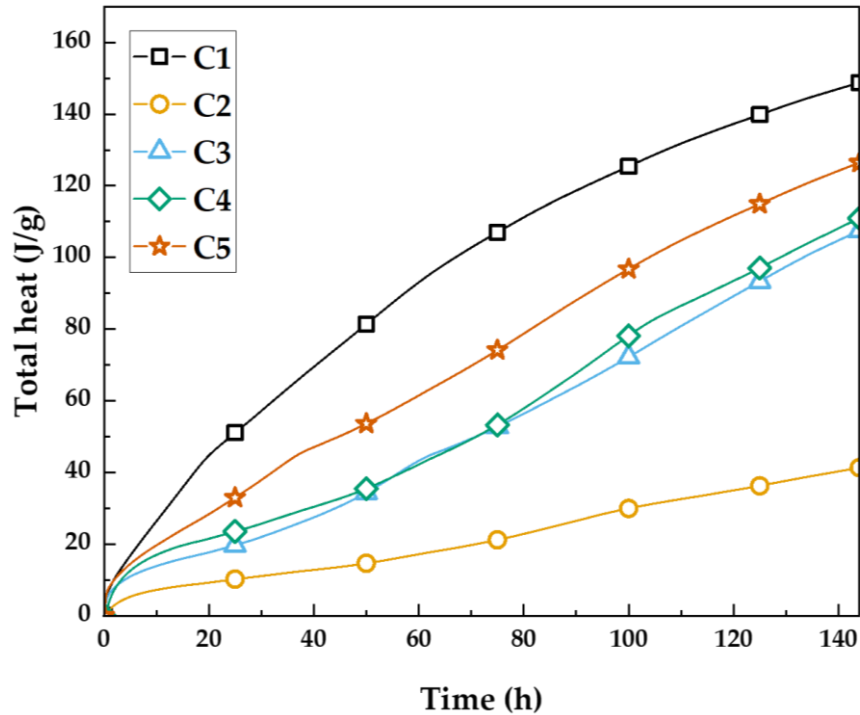


Fig. 4.5: Results of R3 test for calcined clays, based on the total heat released from a formulated paste during 6 days at 20 °C [255]

The pozzolanic reactivity of calcined clays is not a direct measure of their reactivity in alkali-activation, whereby portlandite is absent. These tests are included in this work as potential indication of reactivity of calcined clays with the activator solution, as there is no specific direct test for classifying their reactivity in alkali-activation. Reactive Si and Al in calcined clays may interact with alkaline solutions similarly to the interaction with portlandite. The following results will suggest that a potential link between the reactivity of calcined clays in both alkali-activation and as SCM scenarios could exist, however in alkali-activation it is crucial to consider other factors, such as clay particle size, morphology, and mix design (including activator type, concentration, and blends with other solid precursors).

4.2.3 Mix design and specimen preparation

Alkali-activated pastes were initially prepared by mixing GGBFS with 30 wt. % of each calcined waste clay to obtain five specimens with the same water/binder ratio and activator solution. The activator used for this study was a solution of sodium silicate with a modulus of 1.3 and 5.7 wt. % Na₂O with respect to the precursors, the amount of which was set to give a constant water/binder ratio (w/b) of 0.4 for all five mixes, where the binder is defined as the sum of the solid precursors plus dissolved solids in the activator. The second part of this work investigated the effect of the activator solution, varying the modulus (molar ratio of SiO₂/Na₂O) from 0.9 to 1.2 and the alkali-dosage (wt. % Na₂O respect to the precursors) from 4.7 to 5.2 wt. %, on blends based on 20 wt. % C4 and 80 wt. % GGBFS. The control formulation was designed on solely GGBFS to give the same overall Si/Al and Na/Al molar ratios as the waste calcined clay and GGBFS blend with lower activator dosage, designated type “a”. A w/b of 0.38 was maintained constant across all three mixes. Binder formulations are given in Table 4.4.

Table 4.4: Mix proportions of alkali-activated blends using GGBFS and calcined waste clays C1 to C5

| Sample | Precursors (wt.%) | | Activator solution | | w/b (mass ratio) | Si/Al (molar ratio) | Na/Al (molar ratio) |
|--------|----------------------|-------|---|--|------------------------|---------------------------|---------------------------|
| | Calcined clay | GGBFS | Modulus (SiO ₂ /Na ₂ O molar ratio) | Alkali-dosage (wt. % Na ₂ O) | | | |
| 30C1 | 30 (C1) | 70 | 1.3 | 5.7 | 0.4 | 4.0 | 0.6 |
| 30C2 | 30 (C2) | 70 | 1.3 | 5.7 | 0.4 | 4.0 | 0.6 |
| 30C3 | 30 (C3) | 70 | 1.3 | 5.7 | 0.4 | 4.1 | 0.6 |
| 30C4 | 30 (C4) | 70 | 1.3 | 5.7 | 0.4 | 5.9 | 0.9 |
| 30C5 | 30 (C5) | 70 | 1.3 | 5.7 | 0.4 | 4.8 | 0.7 |
| 0C4-a | - | 100 | 0.6 | 4.0 | 0.38 | 5.9 | 0.8 |
| 20C4-b | 20 (C4) | 80 | 0.9 | 4.7 | 0.38 | 5.9 | 0.8 |
| 20C4-c | 20 (C4) | 80 | 1.2 | 5.2 | 0.38 | 6.1 | 0.9 |

4.3 Results and discussion

4.3.1 Alkali-activated blends of 70 wt. % GGBFS and 30 wt. % of calcined waste clays

4.3.1.1 Isothermal calorimetry

Isothermal calorimetry experiments were carried out to determine the reaction kinetics of blended mixes. Fig. 4.6 (a) shows the heat flow developed by the five alkali-activated mixtures with different calcined waste clays. The general reaction occurs in two stages, identified by the appearance of two exotherms in the calorimetry data. The first stage (I) takes place from the onset of the reaction lasting up to ~ 5 h. The intensity of this initial exotherm is similar across all mixes except for 30C2 and 30C5, reaching a maximum around 1 h. The initial exotherm for the 30C2 mix has a lower intensity and is slightly delayed compared to the other mixes, whilst the initial exotherm for 30C5 appears earlier in time. This initial heat release is associated with wetting and dissolution of precursor material and an initial formation of reaction gel products.

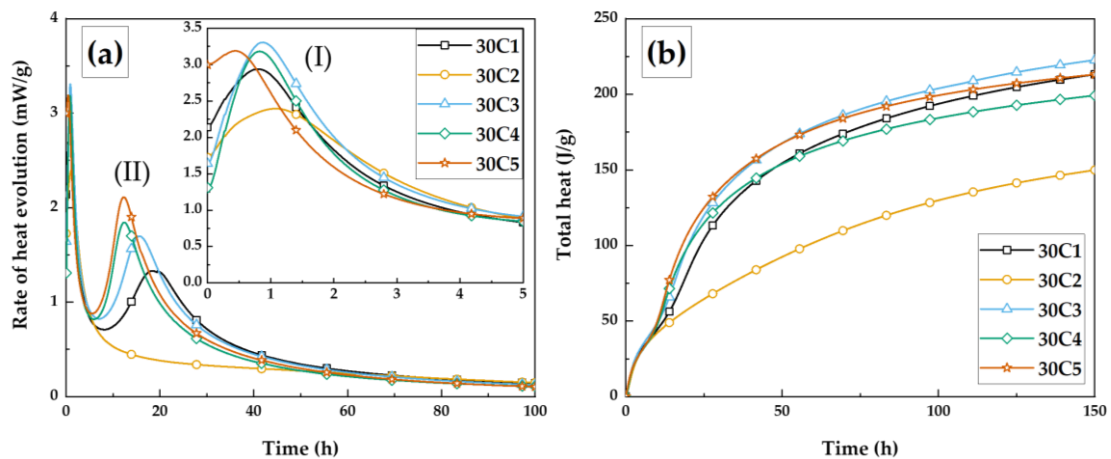


Fig. 4.6: (a) Rate of heat evolution and (b) cumulative heat of alkali-activated blends of 30 wt. % calcined waste clays/70 wt. % GGBFS, at 20 °C

This stage is followed by a dormant period during which the rate of heat evolution is low. The dormant period appears brief for all mixtures except 30C2 which is noted to have the lowest pozzolanic reactivity (Table 4.3). The second reaction stage (II) is attributed to polycondensation, further nucleation and growth of gel reaction products, from 5 to 60 h. Both 30C5 and 30C4 exhibit an intense exotherm at similar reaction times, whilst the exotherm intensity is slightly reduced and delayed with respect to time for both 30C3 and 30C1 mixes. This second exotherm is not seen in the 30C2 mix, suggesting a clear lack of reactivity attributed to minimal gel polycondensation. The intensity and timing of this second exotherm follows the general trend in pozzolanic reactivity seen in the R3 test (Fig. 4.5). Except for C1, the more reactive calcined waste clays show more intense second exotherms at shorter reaction times. The lower than expected heat release recorded for 30C1 is attributed to the formation of microstructural clusters that can hinder ideal reaction kinetics and is further discussed in the following sections. After deceleration of the second exotherm, the reaction enters into a steady state in which minimal heat is continuously released as the reaction proceeds.

Fig. 4.6 (b) illustrates that after a reaction time of 150 h, the total heat evolved for 30C1, 30C3, 30C4, and 30C5 is similar, whilst the total heat release by the 30C2 mix was approximately half that of the other mixes. Over time, it becomes apparent that the total heat evolution curve for the 30C1 mix surpasses that of the 30C4 mix as particle agglomeration becomes less of a limitation to reaction, enabling the higher pozzolanic reactivity of the C1 material to be fully realised.

4.3.1.2 Setting time and mini-slump tests

Table 4.5 displays the initial and final setting times for all mixtures containing 30 wt. % of calcined waste clays and 70 wt. % of GGBFS. The range of initial and final setting times values across all calcined waste clay mixes is quite narrow, spanning from 80 to 170 min. The 30C5 mixture exhibited the fastest initial and final setting times of 80

min and 120 min, respectively, which is relatively short, but acceptable for most applications [256].

Table 4.5: Initial and final setting times and mini slump test results for alkali-activated paste samples including 30 wt. % calcined clay and 70 wt. % GGBFS

| Sample | Setting time (min) | | Mini-slump diameter (mm) |
|--------|--------------------|-------|-----------------------------|
| | Initial | Final | |
| 30C1 | 100 | 140 | 75 |
| 30C2 | 110 | 150 | 105 |
| 30C3 | 120 | 160 | 97 |
| 30C4 | 120 | 170 | 132 |
| 30C5 | 80 | 120 | 100 |

Mini-slump test results indicate a range from 75 mm (30C1) to 132 mm (30C4), noting that the original cone base diameter, i.e. the zero slump measurement, is 60 mm. The inclusion of metakaolin in cement mixes has been reported to decrease workability [257]. This effect may arise from the distinct morphology of metakaolin particles and is believed to be the main factor affecting workability in the calcined waste clay mixes reported here. In case of platelet-like particles, the high surface area to volume ratio may increase the opportunity for inter-particulate forces, such as van der Waals forces, to form agglomerates upon particle collisions [72]. Particles with platelet-like morphologies may have stronger forces acting on their edges and corners that may disrupt the uniformity of the double layer, increasing the electrostatic interactions between particles [258]. Conversely, the large and relatively equiaxed particles of C4, have a lower surface area to volume ratio that is beneficial for workability. The more uniform distribution of electrostatic forces around individual particles prevents agglomeration by increasing inter-particle repulsion, minimising electrostatic interactions during mixing. On the other hand, the smaller particle size of C1 is reflected in a substantial reduction in flow characteristics of the 30C1 mix.

4.3.1.3 X-ray diffraction

Fig. 4.7 displays the XRD patterns of alkali-activated blends of GGBFS with 30 wt.% calcined waste clays. The formation of multiple new phases during alkali-activation is evident upon comparison with the XRD patterns of both unreacted calcined waste clays and raw GGBFS shown in Fig. 4.2. The presence of calcite (CaCO_3), which displays a prominent peak at approximately $29^\circ 2\theta$, hydrotalcite-group phases characterised by distinct broad peaks around $11^\circ 2\theta$, and C-S-H (or C-A-S-H) identified by broad peaks at approximately 29° and $50^\circ 2\theta$, can be observed in all of the alkali-activated blends investigated.

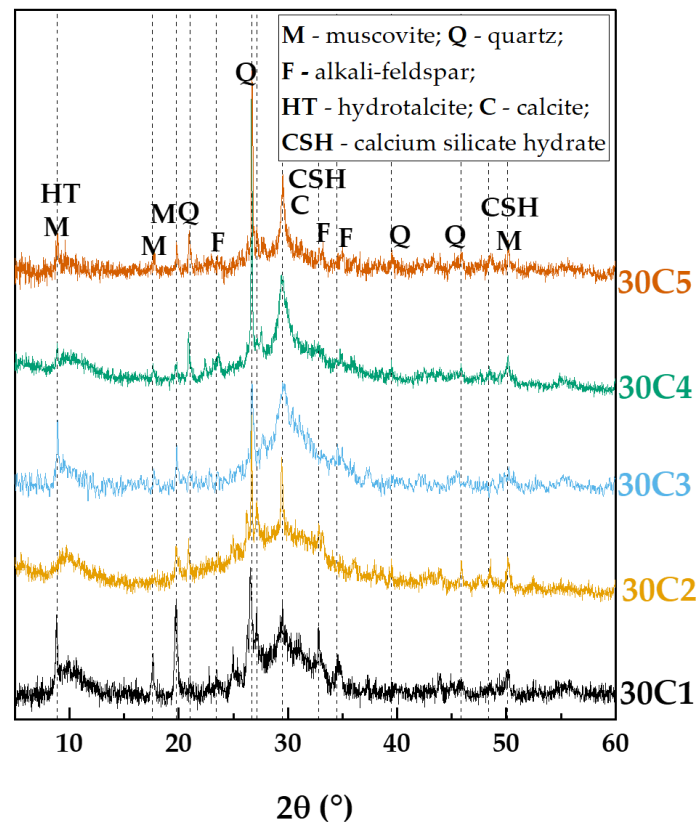


Fig. 4.7: XRD patterns of alkali-activated blends with 30 wt. % of calcined waste clays after 28 days. Note that the phases marked as “CSH” will almost certainly contain alumina and thus are more precisely described as C-A-S-H, but a more concise form of the notation is used in the graphics

The main difference between the calcined waste clays is seen in the 30C2 pattern which exhibits a markedly reduced intensity of the broad C-A-S-H peak. The low gel phase fraction is expected, as evidenced by the suppression of the secondary polycondensation exotherm in the calorimetry data shown in Fig. 4.6. Secondary phases of muscovite, quartz, and alkali-feldspar seen in the XRD patterns are remnant components present in the unreacted calcined waste clays.

4.3.1.4 Scanning electron microscopy

Backscattered electron (BSE) images of alkali-activated blends of 70 wt. % GGBFS and 30 wt. % calcined waste clays after 28 days are shown in Fig. 4.8. The brightest Z-contrast particles seen in all samples are identified as unreacted GGBFS due to the presence of Ca, as seen in the EDS spot analysis corresponding to one such particle. Ca is not expected to be present in significant quantities in the calcined waste clay particles. Unreacted GGBFS is surrounded by a gel matrix phase, consisting of predominantly C-(A)-S-H gel, that also encapsulates the unreactive mineral phases present in the calcined waste clays.

Each sample shows distinctive particles with varying Z-contrast, representative of the differing composition of each mineral phase. Fig. 4.8 (a) shows a large agglomerate of small clay (C1) particles within the gel matrix. The presence of high remnant porosity in this agglomerate indicates poor particle wetting by the activator solution, which if found throughout the specimen would result in less dissolution and polycondensation reactivity. This lack of reactivity is observed as lower heat evolution during the reaction, as shown in Fig. 4.6. These observations highlight the disparity between pozzolanic reactivity (Table 4.3), determined under near ideal conditions, and mix reaction kinetics (Fig. 4.6), which are heavily influenced by the completeness of wetting of agglomerated particles, and thus the relative ability to reach homogenous mixing. These porous regions are expected to be relatively mechanically weak and vulnerable to crack formation and propagation compared to the bulk binder. Therefore, it is crucial to take extra precautions to ensure complete

mixing, particularly in cases where small particle sizes and high electrostatic interactions promote cluster formation.

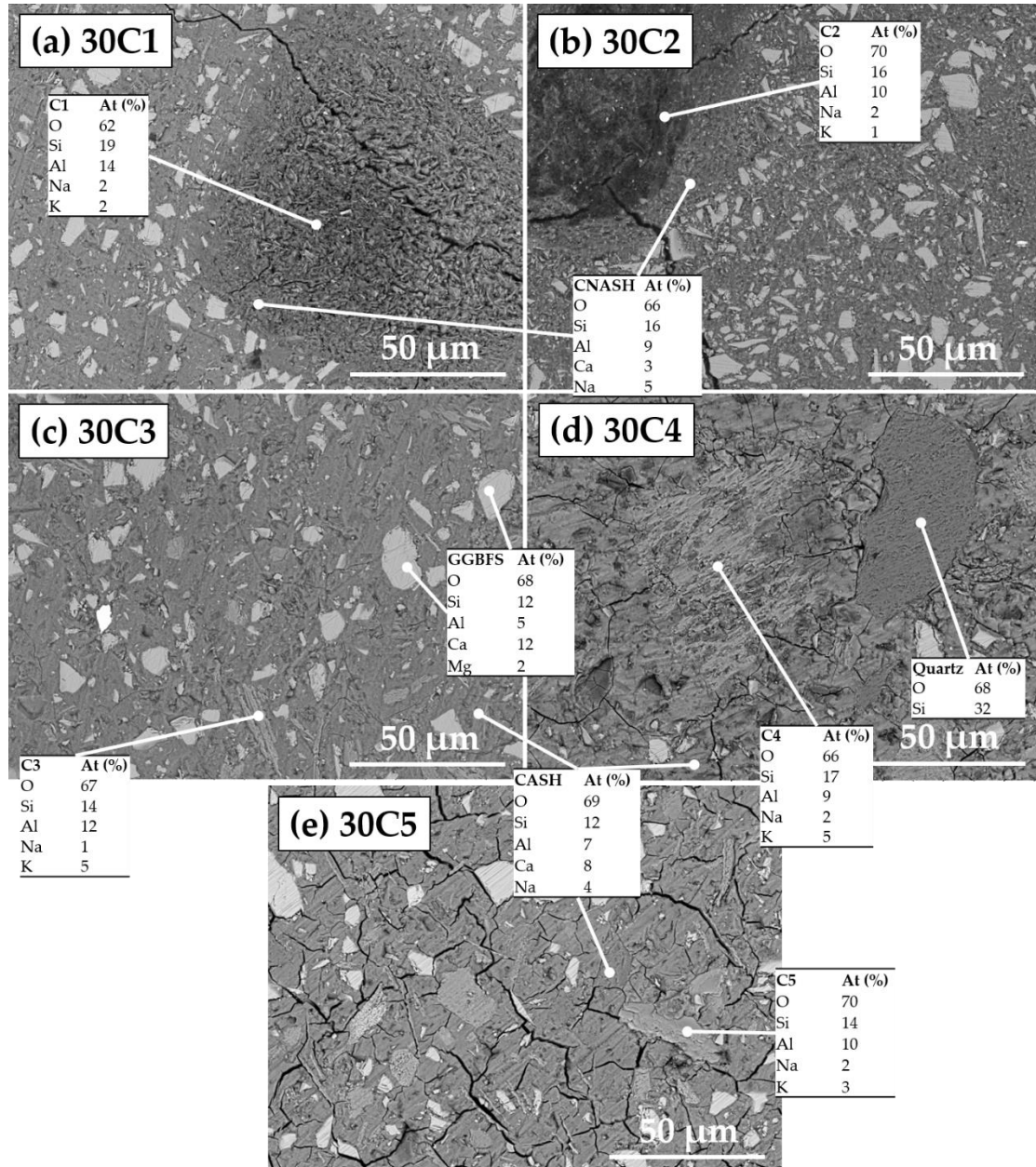


Fig. 4.8: BSE images of alkali-activated blends of GGBFS and 30 wt. % calcined waste clays after 28 days of curing. EDS values are included for particles and characteristic features and calculated as an average of at least five points. (Error $\pm 1\%$)

In the case of 30C2, a clear reduction in overall gel phase fraction is seen by the large number of both fine and coarse unreacted GGBFS particles throughout the matrix in

Fig. 4.8 (b). The interparticle spacing between GGBFS particles is substantially smaller than is seen in the other samples, indicating a lack of enhanced gel formation as observed from the complete suppression of the secondary exotherm in the 30C2 calorimetry data (Fig. 4.6). Around both agglomerate phases identified in Fig. 4.8 (a and b), a C-(N)-A-S-H phase is slowly forming. Unreacted clay-derived mineral particles can be distinguished in the 30C3, 30C4, and 30C5 microstructures surrounded by a dense gel matrix (Fig. 4.8 (c, d, e)). However, sample 30C5 presents cracking which may be due to drying during the vacuum conditions. The varying Z-contrast of the mineral particles combined with EDS analysis allow for identification of the unreactive mineral phases present, with the most prominent being elongated muscovite and alkali-feldspar particles seen in Fig. 4.8 (c), and a large quartz particle in Fig. 4.8 (d)], consistent with the XRD data discussed in section 4.3.1.3.

4.3.1.5 *Compressive strength*

The compressive strength results for the alkali-activated blends, as seen in Fig. 4.9, can be categorised into two general groups: group (I) including both 30C1 and 30C2 which achieve compressive strengths of < 40 MPa after 7 days, and group (II) including 30C3, 30C4, and 30C5 which develop similar compressive strengths of around 60 MPa after 7 days. All samples show an increase in compressive strength from 7 to 28 days, with 30C5 attaining a maximum compressive strength of 80 MPa. Out of the group (II) samples, 30C4 shows the lowest compressive strength gain from 7 to 28 days. The lack of significant compressive strength development can be ascribed to the partial filler behaviour of the C4 clay component, which allows for initially greater dissolution of the highly reactive GGBFS. This promotes the number of gel nucleation sites and further gel precipitation to obtain high early age strength. The improved flow and dispersion characteristics of group (II) calcined waste clays, as seen in the mini-slump tests (Table 4.5), contributes to the development of a dense microstructure that underpins higher compressive strengths. The partial amorphous content in these calcined waste clays is believed to react during alkali-activation to provide a greater volume fraction of binder phases. In group (I), the lower

compressive strength of 30C1 in spite of the high pozzolanic reactivity of the C1 clay is explained in terms of the poor mixing and dispersion issues highlighted by lower workability (Table 4.5) and visible microstructural defects in Fig. 4.8 (a). The poor pozzolanic reactivity of C2 has a detrimental effect on the achieved compressive strength of 30C2 due to reduced gel phase formation. Clearly the dispersion and homogenisation of precursors during mixing is a key factor in producing optimised blends, which if overlooked, can result in the discrepancies between high initial precursor reactivity and low compressive strengths seen here.

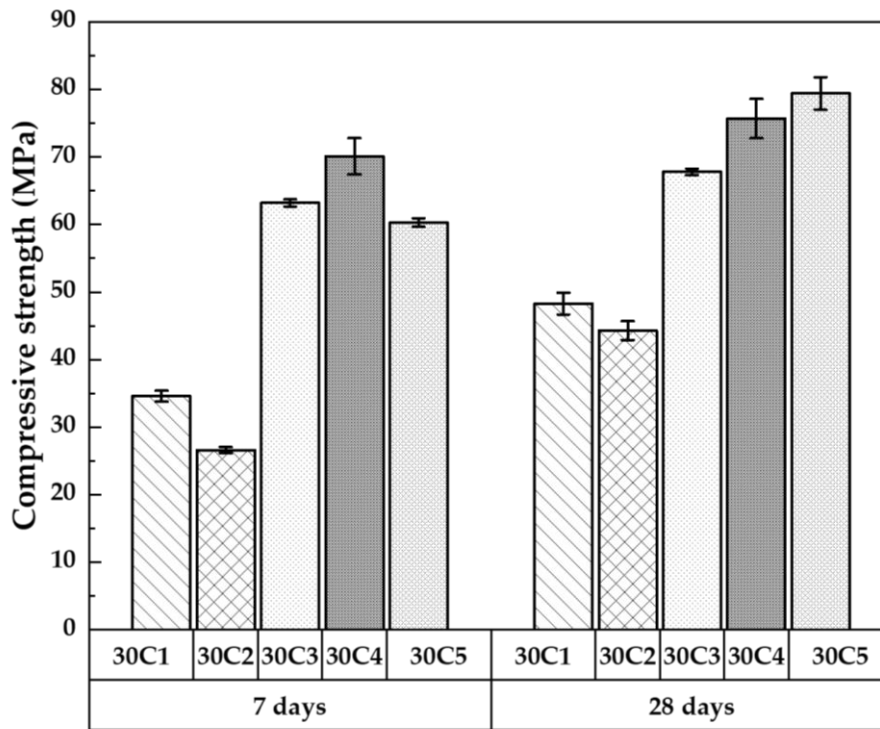


Fig. 4.9: Compressive strength of alkali-activated blends of 30 wt. % calcined clays and GGBFS after 7 days and 28 days. Error bars represent the standard deviation among three replicate specimens

4.3.2 Optimization of systems with clay C4

The current expectation from the concrete industry is that calcined clay replacement fractions in cements do not greatly exceed 20 wt. % due to operational limitations, excessive shrinkage and porosity, and strength reduction [259]. Thus, 20 wt. % replacement of GGBFS with calcined waste clay C4 was selected for further investigation of the effect of varying the modulus of sodium silicate activator solutions compared to an unblended GGBFS-based system. The mix designs are described in Table 4.4.

4.3.2.1 *Isothermal calorimetry*

The heat evolution profiles of alkali-activated pastes based on 20 wt. % C4 / 80 wt. % GGBFS varying the modulus of the activator solution, are shown in Fig. 4.10 (a). The large exotherm seen before 5 h in all mixes is identified as the pre-induction period representing wetting of the solid precursors followed by initial particle dissolution and gel formation [260]. This first stage (I) is followed by an induction or dormant period characterised by a low but non-zero rate of heat release in which the dissolution process continues [260].

The presence of an induction period in slag-rich AACs is characteristic of sodium silicate activated systems rather than systems activated purely by sodium hydroxide [261]. The 0C4-a sample has a relatively short induction period of ~ 10 h followed by a second exotherm with a maximum rate of heat release recorded at 15 h. This second reaction stage (II) is again (as discussed in section 4.3.1.1) associated with the precipitation, nucleation, and growth of reaction gel products during polycondensation [260], [262]. Sample 0C4-a shows reaction acceleration and deceleration all within the space of 24 h.

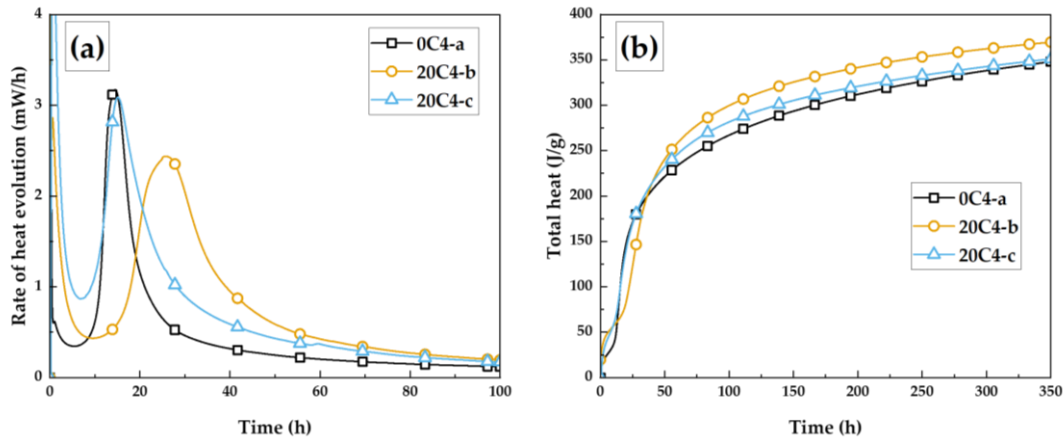


Fig. 4.10: (a) Rate of heat evolution and (b) cumulative heat of alkali-activated blends of 20 wt. % C4 and 80 wt. % GGBFS, reacting at 20 °C

Data obtained for the 20C4-b and 20C4-c mixes show profiles with two distinct exotherms, similar to 0C4-a. The initial exotherms are more intense with a higher activator modulus due to increasing the concentration of reactive Si species, and slightly broader implying a longer dissolution period of the less reactive C4 component. The second stage exotherms of 20C4-c and 0C4-a are remarkably similar in intensity, albeit with a broader acceleration deceleration period for 20C4-c concluded within 48 hours, suggesting that the increase in modulus between activators “a” and “c” may compensate for the lower reactivity of the calcined clay than GGBFS. The 20C4-b sample exhibits a much longer induction period of ~ 16 hours before the second exotherm. The second stage is again slightly depressed in intensity and broader, reaching a steady state after 50 h for both 0C4-a and 20C4-c, explained by the reduced availability of initial reactive gel-forming species present within the system when replacing GGBFS with C4.

Observations on reaction kinetics of these binders are agreement with previous studies on sodium silicate activated slags [124], [260] and GGBFS systems activated by mixtures of sodium hydroxide and sodium silicate [125] that report two exotherms separated by an induction period. The inclusion of calcined waste clay prolongs the overall dissolution period, highlighted by a general broadening of the

exotherms. It is interesting to notice in Fig. 4.10 (b) that after ~ 50 h of reaction the total heat released by both 20C4-b and 20C4-c-a is in fact larger than 0C4-a.

4.3.2.2 *Setting time and mini-slump tests*

The blended systems 20C4-b and 20C4-c exhibit faster initial and final setting times than 0C4-a as shown in Table 4.6. This could be simply explained on the basis of increasing activator concentration. However, the inclusion of C4, known to contain an amorphous metakaolin fraction, may also enable synergistic effects between its reactive metakaolin component and the Ca-rich GGBFS to accelerate the reaction and lower the setting time [263].

Table 4.6: Initial and final setting times and mini-slump test results for alkali-activated blends of 20 wt. % C4 and 80 wt. % GGBFS

| Sample | Setting time (min) | | Mini-slump |
|--------|--------------------|-------|------------|
| | Initial | Final | mm |
| 0C4-a | 200 | 280 | 92 |
| 20C4-b | 145 | 265 | 129 |
| 20C4-c | 125 | 180 | 132 |

Mini-slump results show an increase in workability of around 40 % with C4 inclusion and increased activator concentration. This effect can be explained by the morphology of the C4 particles, predominantly large and equiaxed particles ($d_{50} \sim 68 \mu\text{m}$) which are much larger than the GGBFS particles ($d_{50} \sim 12 \mu\text{m}$) and undergo greater dispersion during mixing (Fig. 4.1). It is known that smaller particles have an increased tendency to flocculate due to high surface area and increased weak physical interactions; the resulting dispersion problems are usually alleviated by either an increase in water content or the addition of a superplasticizer [264].

4.3.2.3 X-ray diffraction

Fig. 4.11 shows the XRD patterns for the AACs based on GGBFS and calcined clay C4.

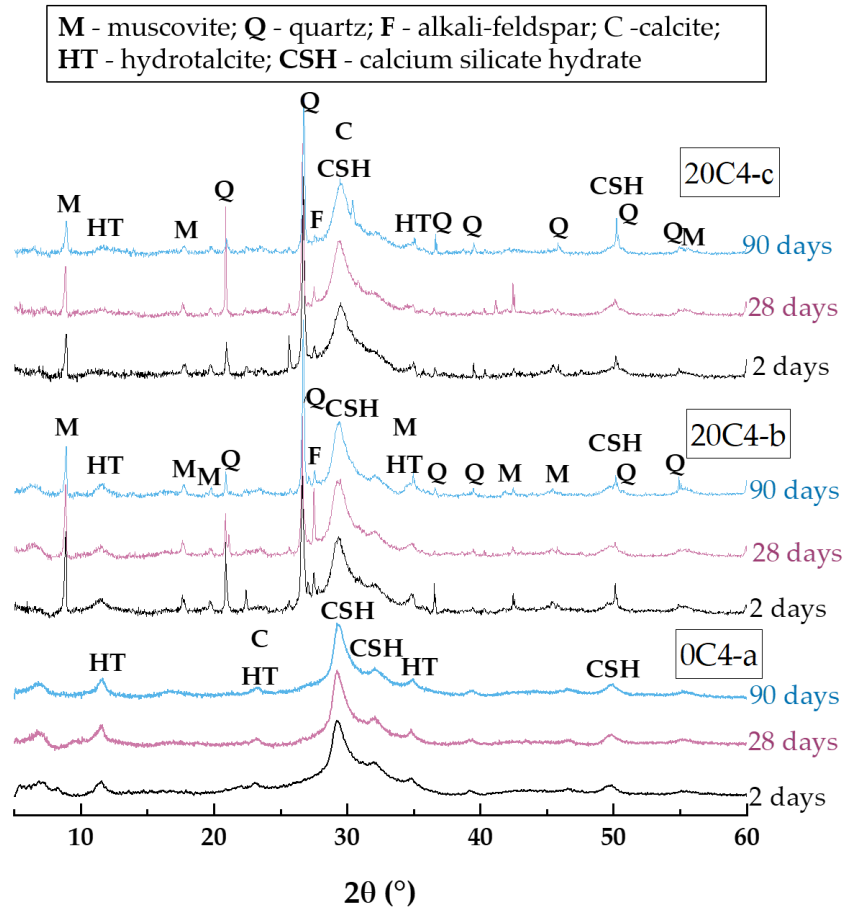


Fig. 4.11: XRD patterns of alkali-activated GGBFS (0C4-a), and blends of 20 wt. % C4 and 80 wt. % GGBFS (20C4-b and 20C4-c). Note that the phases marked as “CSH” will contain alumina and thus are more precisely described as C-A-S-H, but a more concise form of the notation is used in the graphics

The pattern for 0C4-a shows a distinct amorphous hump centred $\sim 29^\circ 2\theta$ indicative of C-A-S-H gel formation [265]. The minor crystalline phase identified is a hydrotalcite (HT) which has been studied extensively in alkali-activated slag systems [15], [266], [267]. The formation of hydrotalcite involves the dissolution of Mg^{2+} present within GGBFS, and precipitation with recrystallisation. The inclusion of

hydrotalcite is known to impart beneficial properties on overall binder behaviour including resistance to carbonation and chloride ingress [125], [268].

The primary crystalline phases of the precursor calcined waste clay C4 – muscovite (M) and quartz (Q) – are present throughout the 20C4-b and 20C4-c patterns obtained after 2, 28, and 90 days. Again, the broad response at $\sim 29^\circ 2\theta$ highlights the formation of C-S-H/C-A-S-H gel after alkali-activation. The formation of hydrotalcite in the 20C4-b mix is seen after 2 days, but hydrotalcite formation is barely detected in the 20C4-c pattern. The higher activator modulus is expected to limit the degree of XRD-observable hydrotalcite formation, with much smaller hydrotalcite precipitates (nanoscale) favoured in higher modulus environments [269].

4.3.2.4 *Fourier-transform infrared spectroscopy*

FTIR spectra of raw GGBFS, calcined clay C4, and the alkali-activated pastes 0C-a, 20C4-b, and 20C4-c after 2 and 28 days, are displayed in Fig. 4.12. The GGBFS absorption spectrum shows a major absorption band with a peak at $\sim 970\text{ cm}^{-1}$ relating to asymmetric silicate (Si-O-T, with T = tetrahedral Si, Al) bond stretching vibrations, whereby the stretching of the Si tetrahedron in question results in a simultaneous contraction of adjacently bonded tetrahedral Si or Al, i.e. opposite atomic motion [270]. The absorption band $\sim 700\text{ cm}^{-1}$ is due to symmetric Si-O-Si bond stretching along with the final absorption band $\sim 540\text{ cm}^{-1}$ indicative of Si-O-T bond bending [271], [272]. C4 has a main band with centred around 1052 cm^{-1} indicative of bonding vibrations Si-O-T seen in quartz, but also in metakaolin, which is responsible for the broadness of this band [273]. Other bands at 776 cm^{-1} , attributed to the Al-O bending of AlO_6 octahedral sites within metakaolin [274], 546 cm^{-1} , and 478 cm^{-1} can be attributed to crystalline quartz and muscovite [275].

Looking at the absorption spectra obtained for the alkali-activated specimens, the first absorption band $\sim 3454\text{ cm}^{-1}$ is due to H-OH bond stretching from weakly bonded water molecules trapped on the surface or in pores within the samples, along with the corresponding H-OH bond bending at $\sim 1655\text{ cm}^{-1}$ [272], [276]. The bands

between 1490-1410 cm^{-1} are related to C-O bond stretching [277], [278]; in particular the absorption peak $\sim 1489 \text{ cm}^{-1}$ corresponds to aragonite or vaterite [191], [279]. These phases were not detected in the XRD data as discussed above, but which may be present in trace amounts due to atmospheric carbonation of the samples during preparation and/or analysis. Again, the major absorption band between 1200-900 cm^{-1} is associated with asymmetric Si-O-T bond stretching. This particular band is the most significant in understanding the formation of reaction products [168], [201]. It should be noted that for all binders formed after alkali-activation, this band shifts to lower wavenumbers and becomes narrower when compared to the unreacted precursors GGBFS and C4. Incorporation of Al tetrahedra within the gel structure is seen by a shift towards lower wavenumbers due the change in local environment and bond vibrations. In the discussion that follows, the remaining symmetrical Si-O-T bond stretching $\sim 700 \text{ cm}^{-1}$ and Si-O-T bond bending $\sim 460 \text{ cm}^{-1}$ vibration bands are considered to include contributions from substituted Al.

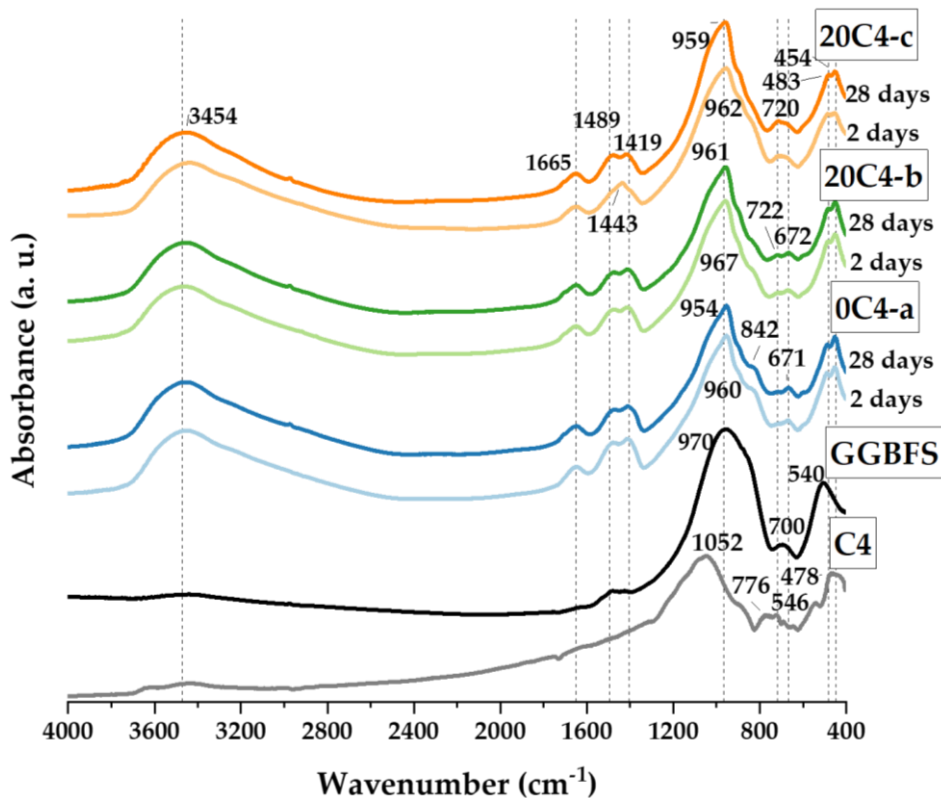


Fig. 4.12: FTIR spectra of precursors and alkali-activated samples based on GGBFS with and without 20 wt. % C4, after 2 days and 28 days of curing

Increasing the curing times to 28 days resulted in narrowing of the band at $\sim 950 \text{ cm}^{-1}$ and a shift to lower wavenumbers compared with the 2 day samples [280]. This is reported in the literature to arise from increased incorporation of Al within the silicate structure. The bands in question contain contributions from Al-O-Si linkages, of which the Al-O bonds are less stiff than Si-O [281], that result in perturbations of local Si-O bonding [282]. The C4 component is acting as an Al source, gradually increasing the number of Si-O-Al bonds within the gel structure over time.

4.3.2.5 *Solid state nuclear magnetic resonance spectroscopy*

The ^{29}Si MAS NMR spectra of the precursors (GGBFS and calcined waste clay C4) are shown in Fig. 4.13. The GGBFS spectrum exhibits a single broad resonance with maximum intensity at $\sim -75 \text{ ppm}$ (Fig. 4.13 (a)) suggesting a wide distribution of tetrahedral Si environments $\text{Q}^n(\text{mAl})$ and chemical shifts. The overall chemical shift and shape indicate that low cross-linked species and/or high degrees of Al substitution dominate the GGBFS structure. This is in agreement with the glassy, highly-depolymerised nature of the precursor and with previous studies [125], [283][284]–[286]. The GGBFS spectrum can be adequately simulated with a single peak centred at -74.7 ppm as seen in Fig. 4.13 (a); it is not claimed that this is representing a single site environment, but it is a useful description of the GGBFS contribution to the spectra of hardened binders.

The complex spectrum for C4 in Fig. 4.13 (b) is a combination of resonances attributed to quartz, muscovite, and K-rich feldspar. The narrow resonance at -106.6 ppm is attributed to quartz SiO_2 (Q^4) whilst the broader resonance at -110 ppm can be attributed to a partially amorphous phase obtained as a result of clay calcination at $750 \text{ }^\circ\text{C}$ [80]. The main resonance bands for muscovite are found at -87 ppm , -91.2 ppm , and -95.5 ppm [287] along with the resonance bands of various forms of KAlSi_3O_8 alkali-feldspar reported in the range -97 ppm to -103 ppm , assigned here as resonances at -99 and -102.6 ppm [287]–[289]. Dehydroxylation of muscovite has been reported to provide a shift of the muscovite resonances towards the feldspar region

[287]. Only partial dehydroxylation of the muscovite phase may occur after calcination at 750 °C, meaning that both muscovite and the dehydroxylated phase will be present. [290], [291].

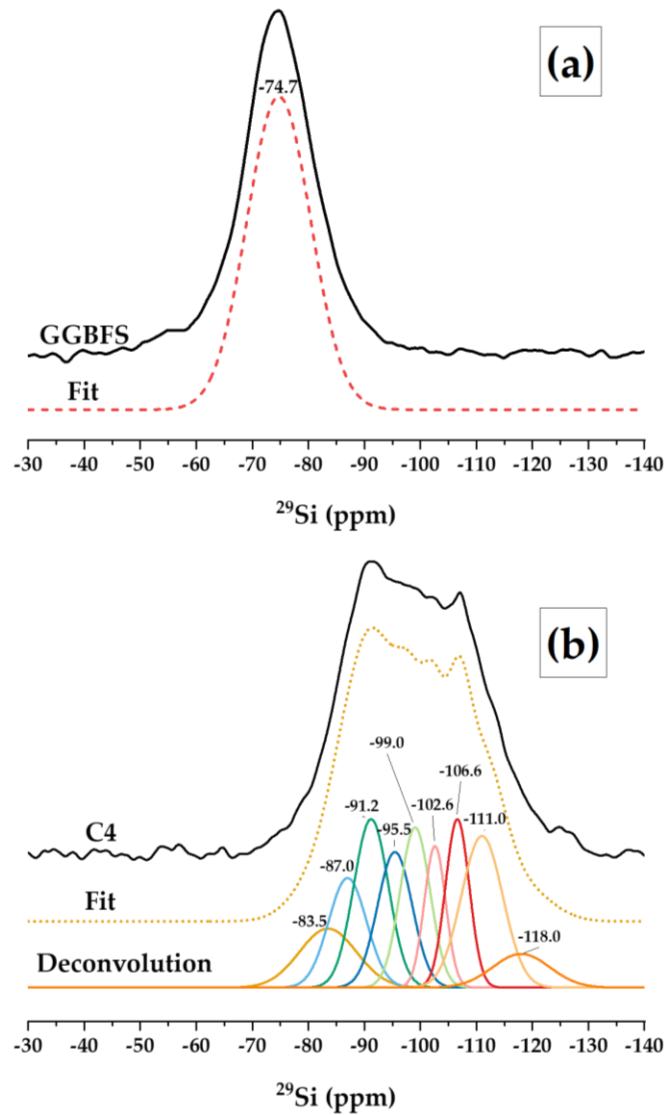


Fig. 4.13: ^{29}Si MAS NMR spectra of precursors: (a) GGBFS and (b) calcined C4

The deconvolution curves for the ^{29}Si MAS NMR spectra for alkali-activated GGBFS, 0C4-a, and blended 20C4-C after 2 and 28 days can be seen in Fig. 4.14. Five main

resonance bands are identified for all spectra, centred at -76 ppm, -78 ppm, -81.5 ppm, -84 ppm, and -89 ppm which are assigned to $Q^1(I)$, $Q^1(II)$, $Q^2(1Al)$, Q^2 , and $Q^3(1Al)$ environments, respectively [284], [292], [293]. $Q^1(I)$ and $Q^1(II)$ represent two non-equivalent Q^1 environments, depending on the charge balancing ions [292]. The resonances identified are consistent with the formation of C-A-S-H gels [169]. Table 4.7 gives the deconvolution results of the ^{29}Si MAS NMR spectra using Gaussian curve fitting as reported in the literature [16], [116], [294]. It is assumed that GGBFS undergoes congruent dissolution into the sodium silicate activator solution [16], [295], and so its spectral contribution is described by linearly scaling the intensity of the GGBFS spectrum without adjustment to its shape or position.

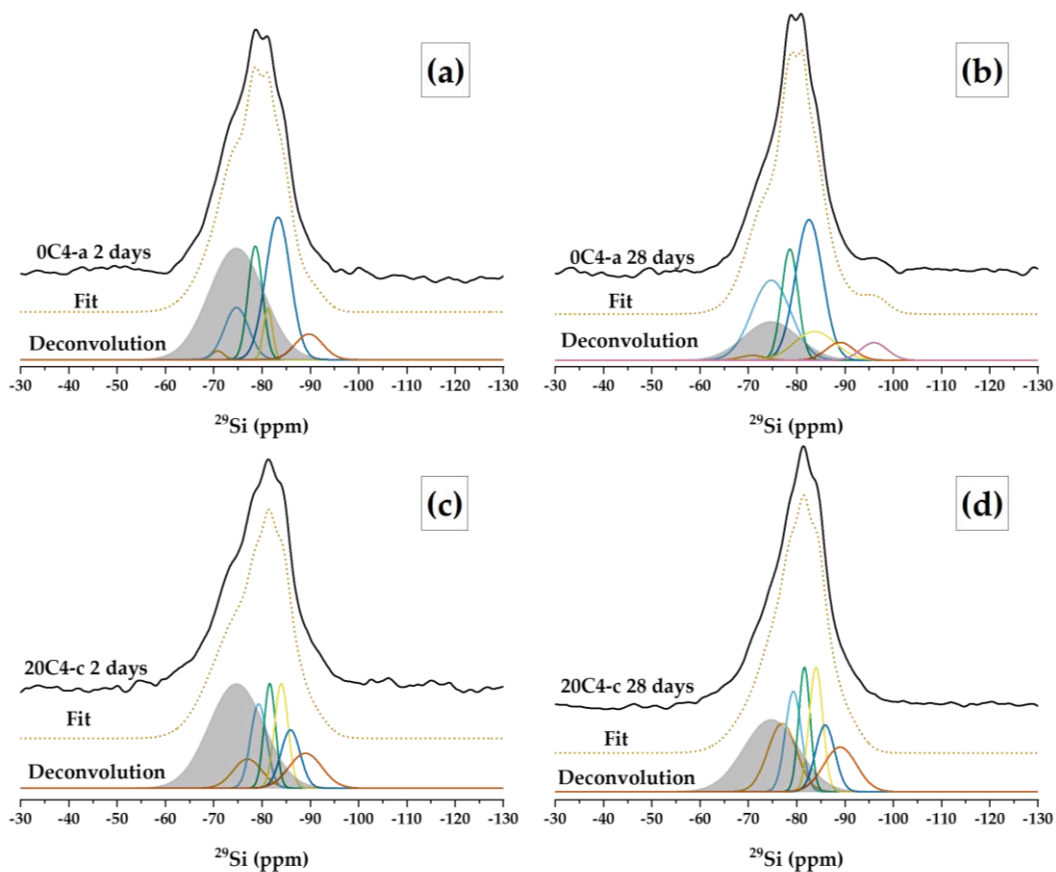


Fig. 4.14: ^{29}Si MAS NMR spectra with fit and deconvolution of: (a) 0C4-a 2 days, (b) 0C4-a 28 days, (c) 20C4-c 2 days, (d) 20C4-c 28 days. The grey band represents the contribution of the unreacted GGBFS which is directly scaled from the raw GGBFS spectrum under the assumption of congruent dissolution

The deconvolutions shown in Fig. 4.14 highlight a reduction in the residual GGBFS fraction in both 0C4-a and 20C4-C mixtures, along with greater C-A-S-H and reaction product formation with increased curing time from 2 to 28 days [280]. The initial degree of reaction for 0C4-a is slightly lower than that of 20C4-c at early ages, as indicated in the calorimetry data in Fig. 4.10 (b), although 0C4-a undergoes sustained greater reaction from 2 to 28 days as shown by the larger difference in the remnant slag phase. This difference in reaction behaviour between GGBFS and the C4-GGBFS blend is expected based on the known effects of C4 inclusion. The inert quartz phase fraction acts as a filler whilst increasing the number of nucleation sites and the available interparticle space for the polycondensation reaction to proceed. The fast generation of binding phases results in high early strength, however the lack of reactivity (chemical stability) of certain mineral phases limits the degree of reaction in the following 2 to 28 day period [296].

Table 4.7: Deconvolution results for ^{29}Si MAS NMR spectra of the alkali-activated blends. Estimated uncertainty in absolute site percentages is $\pm 2\%$

| Sample | Isotropic chemical shift, δ_{iso} (ppm) | | | | | | | | Unreacted GGBFS |
|----------------------|---|--------------------|---------------------|----------------------|----------------|---|-----|----------------------|--------------------|
| | Reaction products | | | | | | | Q ⁴ (3Al) | |
| | Q ⁰ | Q ¹ (I) | Q ¹ (II) | Q ² (1Al) | Q ² | Q ³ (1Al) or Q ⁴ (4Al) | | | |
| | -71 | -76 | -78 | -81.5 | -84 | -85.5 | -89 | -91 | -74.7 |
| 0C4-a 2 days | 1% | 26% | 10% | 3% | 21% | - | 4% | - | 36% |
| 28 days | 1% | 23% | 14% | 2% | 29% | 9% | 4% | 3% | 16% |
| 20C4-c 2 days | - | 8% | 12% | 11% | 13% | 11% | 11% | - | 34% |
| 28 days | - | 14% | 13% | 13% | 15% | 11% | 12% | - | 22% |

Highly cross-linked Si sites such as Q⁴(4Al) or Q⁴(3Al) could overlap with the regions assigned to Q³(1Al) at -89 ppm [292], [297]. It is not unreasonable to assume that the amorphous fraction identified in C4 from the comparison of its calcined and uncalcined XRD patterns (Fig. 4.4) could react to form highly cross-linked N-A-S-H gels, in addition to the C-A-S-H gel formed by reaction of the GGBFS. This process is hinted at by the increase in resonance intensity at about - 89 ppm in 20C4-c [283].

There are no significant bands corresponding to traces of the remnant clay C4 (Fig. 4.13 (b)).

Fig. 4.15 shows the ^{27}Al MAS NMR spectra of the precursors GGBFS and C4. The broad resonance with a maximum intensity at ~ 63 ppm attributed to tetrahedral Al environments [286] is seen in the GGBFS spectrum. The broadness of the band is indicative of local disorder and asymmetry consistent with the amorphous nature of GGBFS as highlighted in the XRD data (Fig. 4.2) [280], [285].

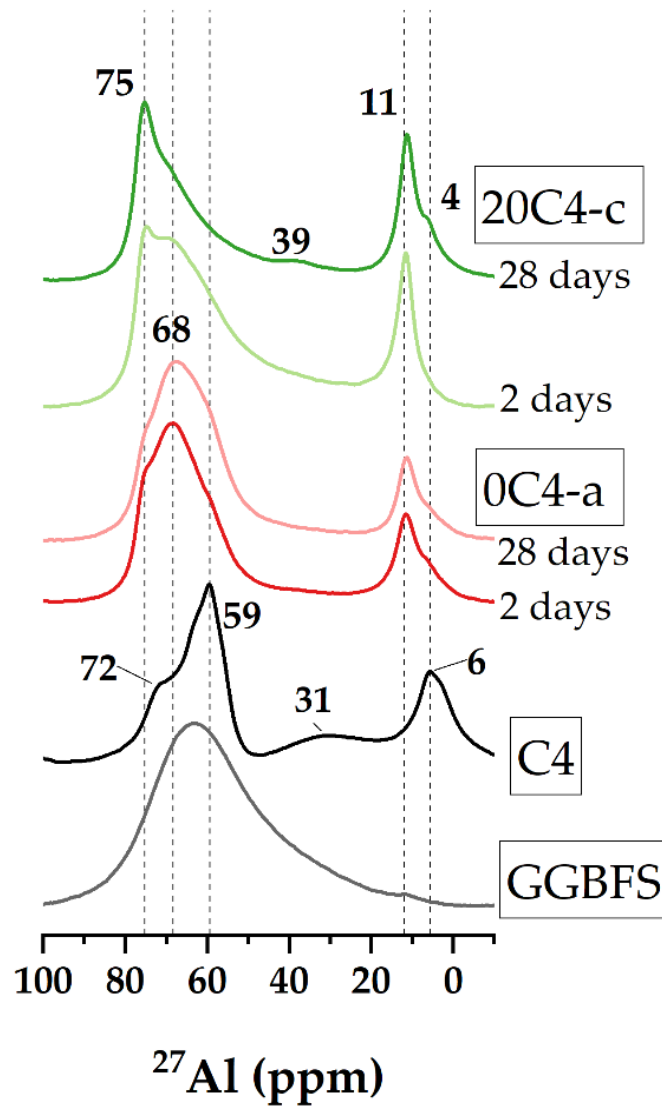


Fig. 4.15: ^{27}Al MAS NMR spectra for precursors GGBFS and C4 and alkali-activated pastes

Three distinct environments are identified in the ^{27}Al MAS NMR spectrum of the calcined waste clay C4. Two resonances at 72 ppm and 59 ppm within the tetrahedral Al(IV) region are associated to well defined Al tetrahedra found in alkali feldspar and muscovite. The resonance at ~ 6 ppm in the region below 20 ppm is associated with Al(VI) in octahedral coordination which only present in muscovite [298]. Beside the presence of Al in these well-defined coordination states, there is a weak broad signal between ~ 30 -40 ppm that can be attributed to distorted tetrahedral environments of Al(V), and most likely also a broad feature underlying the sharper peaks in the Al(IV) region. The appearance of these broad bands is consistent with the amorphous content of C4 formed after calcination [299].

Fig. 4.15 presents the ^{27}Al MAS NMR. The resonances seen at chemical shifts of 11 ppm are attributed to the formation of hydrotalcite-group compounds which contain Al(VI) in octahedral coordination. The resonances observed in the range 80-60 ppm are associated with the formation of C-A-S-H gels [292], [294]. The narrow resonance band at ~ 75 ppm seen in the 0C4-a spectrum increases in intensity with longer curing times, representing an increase short-length ordering of C-A-S-H and greater degree of polymerization as the reaction proceeds [266]. This resonance is associated with Al in a well-defined Al(IV) coordination and incorporated in bridging tetrahedra, whereby Al tetrahedra are bonded to $\text{Q}^2(1\text{Al})$ Si sites.

Two main resonances are distinguishable in the 20C4-c spectrum at 75 ppm and 68 ppm. These bands also become more intense and slightly narrower with longer curing, because of increased incorporation of Al and crosslinking of the network in the form of Al(IV) bonded to $\text{Q}^3(1\text{Al})$ sites [198], [284], [294]. This may also hint at the partial formation of N-A-S-H, i.e., Q^4 sites, along with C-A-S-H, as discussed above.

4.3.2.6 Mercury intrusion porosimetry

Pore size distributions of AACs are often classified into gel pores with diameters between 10 to 50 nm, capillary pores with diameters between 50 nm and 10 μm , and air voids above 10 μm [300].

Fig. 4.16 displays the pore size distributions of the alkali-activated pastes based on 20 wt. % of calcined clay C4 and 80 wt. % of GGBFS after 28 days of curing.

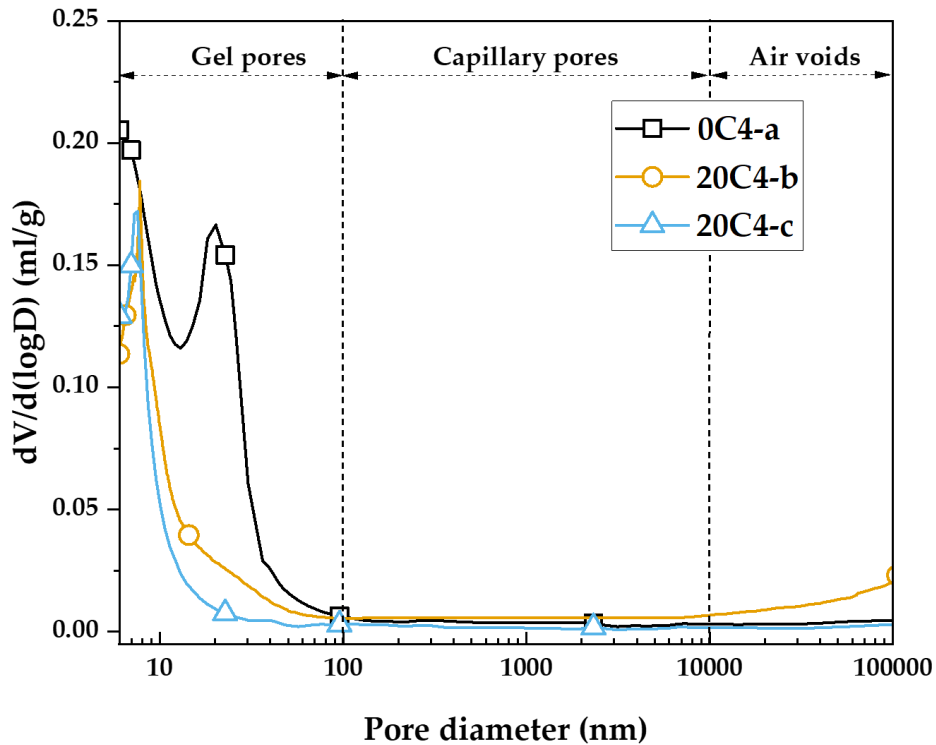


Fig. 4.16: Differential pore volume of alkali-activated pastes based on GGBFS and 20 wt. % calcined clay C4, after 28 days of curing

The predominant type of porosity seen in alkali-activated pastes is within the gel pore size range. 0C4-a has a well-defined peak in this region, whilst 20C4-b and 20C4-c show remarkably limited porosity within the analysed range, although may contain pores below the size range that can be accessed in these MIP experiments. No notable capillary pores are detected in any of the pastes.

Table 4.8 shows the measured values of total porosity for all paste samples. Samples containing C4 exhibit lower total porosity than the GGBFS sample. This suggests that 20C4-b and 20C4-c have formed dense binders due to effective particle dispersion with enhanced flow, and due to the higher modulus of the activating solution used. The partial formation of N-A-S-H gel coexisting with the large amounts of C-A-S-H

formed by the GGBFS may also result in a dense binder. Literature on gel coexistence has reported that this can lead to minimisation of porosity with improved material performance [39], [173], [251], [301].

Table 4.8: Total porosities measured for alkali-activated pastes based on GGBFS and 20 wt. % calcined clay C4, after 28 days of curing. Error bounds represent the standard deviation among 2 replicate specimens

| Sample | Total porosity (vol. %) |
|--------|-------------------------|
| 0C4-a | 21.07 ± 0.75 |
| 20C4-b | 8.89 ± 0.69 |
| 20C4-c | 5.31 ± 0.11 |

4.3.2.7 Compressive strength

The compressive strength results for alkali-activated pastes based on GGBFS and calcined clay C4 are shown in Fig. 4.17.

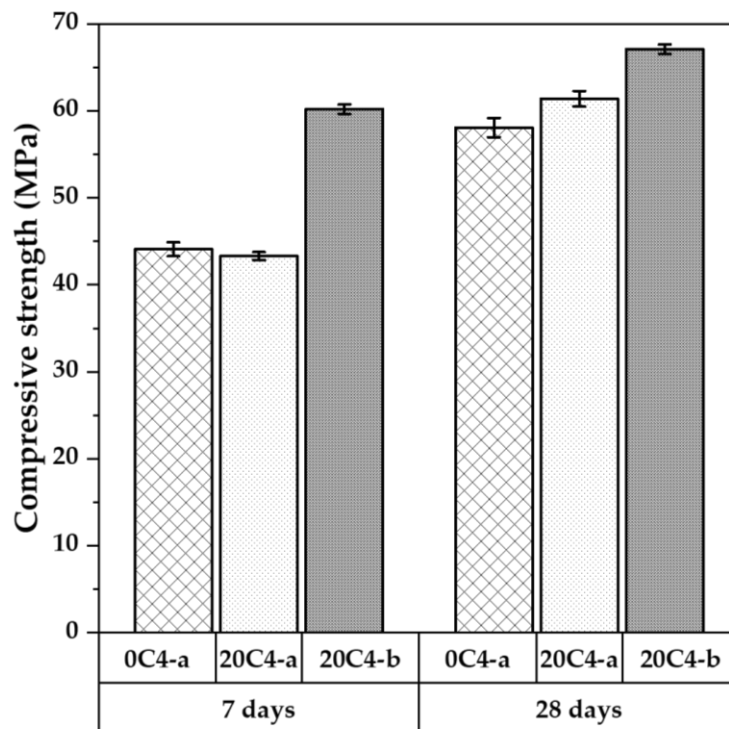


Fig. 4.17: Compressive strength of alkali-activated pastes based on GGBFS and 20 wt. % calcined clay C4. Error bars represent the standard deviation among three replicate specimens.

Compressive strength of the 20C4-b samples showed similar values (43 MPa after 7 days and 61 MPa after 28 days) to the 0C4-a sample. The two mixes in question were designed to reach the same Si/Al and Na/Al molar ratios by adjusting the modulus and Na₂O dosage of the activator solution, as C4 clay has a larger Al component than GGBFS. The 20C4-c sample, with increased activator concentration with respect to the other formulations, recorded the highest 7-day strength which exceeded 60 MPa, although only a minor increase was obtained after 28 days (67 MPa). Increasing the modulus of the activator solution from 0.9 to 1.3 makes a larger concentration of soluble silica in the liquid media available for the polymerisation of both Al and Si species. This results in the formation of an enhanced gel structure, reflected in the mechanical properties especially at early ages [251].

4.4 Conclusions

Calcined clays from waste sources, with low metakaolin content and low purity, were blended with GGBFS and alkali-activated with sodium silicate, and their properties investigated.

Careful investigation of physical properties including particle size, morphology, and phase assemblage is necessary to validate pozzolanic reactivity. In this study the R3 test was more reflective of the behaviour of the clay in an alkali-activated system than the modified Chapelle test. It was shown that calcined clays have a strong effect on the fresh properties, especially on the workability of blended pastes. The morphology of clay is a key factor in the mix design, and it is fundamental to understand how this can affect blended systems.

Good workability can translate in a well-behaving binder with a dense microstructure, low porosity, and high strength. A 20 wt. % calcined waste clay replacement level maintained similar compressive strength whilst achieving a denser binder. The quartz, muscovite, and alkali-feldspar contained in the calcined clays

appear to remain stable throughout alkali-activation, whilst the reaction of the amorphous phase fraction (the calcination product of the kaolinite that is present) resulted in the formation of a cross-linked binder gel.

This work has highlighted a complete methodology of characterising the behaviour of waste clay sources in alkali-activation and provides a basis for design optimisation to accommodate clay inclusions in novel binder systems.

Chapter 5.

Non-Blast Furnace Slags in Alkali-Activated Cements

5.1 Basic oxygen furnace slag (BOFS) additions in alkali-activated cements with sodium silicate and sodium carbonate

This section is based on: [L. Stefanini](#), B. Walkley, J. L. Provis, “Basic oxygen furnace (BOF) slag as an additive in sodium carbonate-activated slag cements” - under review.

The experimental investigation, data interpretation, and writing of the original draft of this chapter were carried out by L. Stefanini, whilst B. Walkley and J. L. Provis supervised the work and revised the draft.

5.1.1 Introduction

The iron and steel making industries are at the core of many developed and developing economies worldwide. As both industries have seen continuous growth, this has been inextricably linked with continued CO₂ emissions, consumption of primary raw materials, and large-scale generation of solid wastes [302]. Crude steel is produced either from pig iron through the basic oxygen furnace process (primary route) or starting from scrap and directly reduced iron through the electric arc furnace process. In 2018 global steel production reached 1,800 million tonnes, resulting in over 300 million tonnes of steel slags. Globally about 70 % of steel is produced through the basic oxygen furnace route which generates BOFS as a by-

product [303]. The construction industry has a great positive impact on economic growth, however contributes significantly to global CO₂ emissions and raw resource consumption [24], [304], [305], and there exists a strong drive to improve the sustainable development of both steelmaking and construction sectors [42]. Alkali-activation technology may provide a solution for both sectors [118], enabling the large-scale valorisation of steelmaking wastes [306] through their use in the production of high performance low-carbon binders [17] further contributing to the circular economy [307].

The main oxides within BOFS are CaO, SiO₂, Fe₂O₃, Al₂O₃, and MgO, present as mineral phases including calcium silicates, aluminosilicates, aluminoferrites, and the “RO” phase, which is a solid solution of CaO, FeO, MgO, and MnO commonly found in steel slags [164], [308], [309]. BOFS can vary substantially in mineral composition between sources, and generally exhibits poor hydraulic properties [121], [308]. The high content of free lime (up to 40 %) is the main limitation on the use of BOF in construction applications, as free lime is known to cause volumetric expansion of concretes upon its hydration into portlandite, which can potentially initiate structural failure [310]. BOFS has been used in asphalt [311], [312] and road pavements [313], as well as an aggregate for traditional concrete [132] and alkali-activated metakaolin [139] with minimal treatment. It also has use as a liming material in agriculture to improve the quality of soil [314]. Despite these various uses, most BOFS is discarded as landfill [302]. The reported utilisation of BOFS as a SCM, a mineral admixture, or as a precursor in alkali-activation technology is relatively limited. An investigation into the hydration properties of BOFS by Wang *et al.* [130] reported very slow reaction kinetics, that could be accelerated by increasing the fineness of BOFS particles, increasing the curing temperature, and utilising an alkaline solution. Fine BOFS has been successfully blended as an SCM in PC based materials without a significant reduction in performance [315]. Kourounis *et al.* [144] found BOFS inclusion in conventional cement systems to improve workability, while generally lowering final compressive strength. Work on using BOFS in AACs,

blended with GGBFS and fly ash, has been reported by only a few authors using strong activator solutions of NaOH [164] and high curing temperatures [316].

The performance and final application of alkali-activated materials is strongly influenced by characteristics of the solid precursors, including morphology, particle size, mineral composition, and amorphous fraction. The other main factor is the type and concentration of the activator solution [87], [124], [317], [318]. The activator type has a strong influence on the environmental impact of the resulting binder. Commonly used activators such as sodium/potassium silicates and sodium/potassium hydroxides have been reported to contribute a large fraction of the total CO₂ emitted from the alkali-activation process. [45]. Sodium carbonate may represent a more readily available, sustainable, and cheaper solution with respect to sodium silicate, reaching about a third of the cost and total CO₂ emitted. However, sodium carbonate activated slag cements tend to suffer from delayed hardening, requiring up to 5 days, and low early strength [319], [320]. The delay in hardening and strength development is strictly related to the lower alkalinity of the system, which is required for the complete dissolution of slag particles. For systems with pH < 12, only the dissolution of Ca from GGBFS is favoured, which is consumed by CO₃²⁻ to form carbonate salts such as calcite and gaylussite. The pH slowly increases when the CO₃²⁻ concentration is reduced, and after this happens, the reaction proceeds analogous to that in NaOH-activated slag, forming primarily a C-A-S-H gel [321]. Additives such as MgO [322], CaO [323], and calcined LDH phases [324] can be utilised to enhance early age properties, or the sodium carbonate can be blended with sodium silicates to improve early strength development [260].

In this study, seven binders were produced using 20 wt. % and 30 wt. % of BOFS as a replacement for GGBFS and activated with either sodium silicate or sodium carbonate solutions. The reaction kinetics during formation of these binders are analysed via isothermal calorimetry, and the setting time and workability assessed. The resulting phase assemblages in the hardened binders are determined via XRD and FTIR, and the compressive strength evaluated, benchmarked against

conventional systems. An optimisation of this system using a controlled fine BOFS fraction is also proposed to increase the strength of sodium carbonate-BOFS/GGBFS cements.

5.1.2 Materials and methods

Two types of precursor materials were used: GGBFS supplied by Ecocem (Belgium) and weathered BOFS supplied by ArcelorMittal (Belgium). The BOFS was used as received, with particle sizes ranging up to 500 μm , and a fine fraction (BOF63) obtained crushing using a ball mill and sieving to achieve a similar particle size distribution to GGBFS. Particle size and density values are presented in Table 5.1, and the particle size analysis illustrated in Fig. 5.1.

Table 5.1: Density and particle size analysis of GGBFS, BOFS, and BOFS63

| Sample | Density (g/cm^3) | Particle size analysis (μm) | | |
|--------|---------------------------------------|--|----------|----------|
| | | d_{10} | d_{50} | d_{90} |
| GGBFS | 2.9 | 3.8 | 12.7 | 31.0 |
| BOFS | 2.7 | 22.5 | 88.9 | 258 |
| BOF63 | 2.6 | 2.9 | 11.8 | 36.5 |

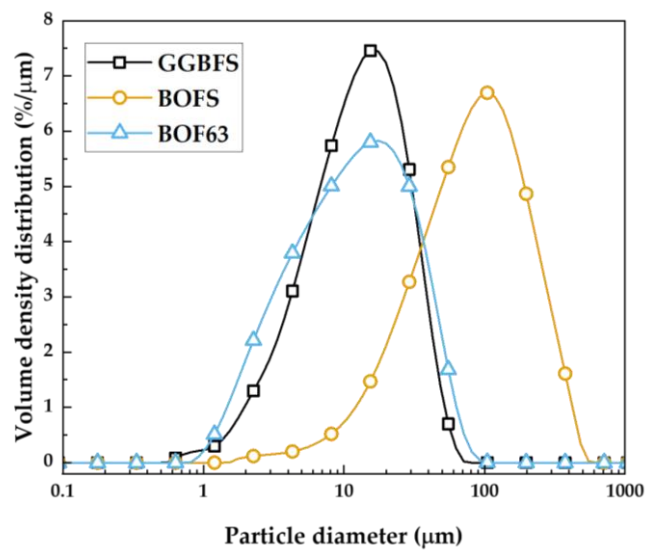


Fig. 5.1: Particle size distribution of precursors GGBFS, BOFS, and BOF63

The oxide composition is shown in Table 5.2. The loss of ignition (LOI) value of 8.1 wt. % for BOFS is relatively high due to the conditions of weathering and carbonation to which the sample was exposed.

Table 5.2: Oxide composition (wt. %) of GGBFS and BOFS as measured with XRF. Loss of ignition (LOI) at 1000 °C

| Sample | CaO (%) | SiO ₂ (%) | Al ₂ O ₃ (%) | MgO (%) | SO ₃ (%) | TiO ₂ (%) | Fe ₂ O ₃ (%) | MnO (%) | P ₂ O ₅ (%) | V ₂ O ₅ (%) | LOI (%) |
|--------|---------|----------------------|------------------------------------|---------|---------------------|----------------------|------------------------------------|---------|-----------------------------------|-----------------------------------|---------|
| GGBFS | 43.5 | 36.4 | 10.5 | 7.0 | 1.4 | 0.5 | 0.3 | 0.3 | - | - | 0.2 |
| BOFS | 43.4 | 9.7 | 1.9 | 3.6 | 0.3 | 0.7 | 27.5 | 2.5 | 1.6 | 0.8 | 8.1 |

SEM images representing the precursor particles are shown in Fig. 5.2. The GGBFS precursor consists of small (mostly < 20 µm) angular particles, while the BOFS precursor consists of much larger heterogeneous aggregated particles (many of which are > 100 µm) composed of smaller sub-units of differing morphologies.

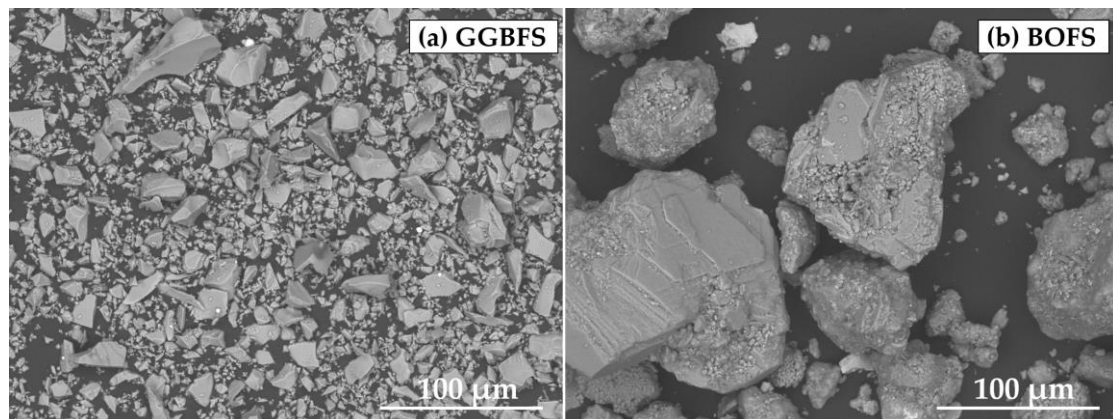


Fig. 5.2: BSE images of the raw precursors: (a) GGBFS, and (b) BOFS

The XRD patterns of the GGBFS, BOFS, and BOFS63 are presented in Fig. 5.3. The major crystalline phases identified in the XRD pattern of BOF slag include portlandite (P, Ca(OH)₂, PDF# 00-044-1481) and calcite (C, CaCO₃, PDF# 00-005-0586), along with the minor phases srebrodolskite (S, Ca₂Fe₂O₅, PDF#00-047-1744), wüstite (W, FeO PDF#00-006-0615), hydrous calcium-iron carboaluminates that evidently result from weathering of the slag (Fc, C₈AFcH₂₃, PDF#00-045-0572) and a solid

solution of CaO, FeO, MgO, and MnO (known as RO phase PDF#00-053-0926) commonly found in steel slags [164], [308], [309]. The major crystalline phases of the fine fraction of BOFS (BOF63) comprise portlandite and calcite, however with differing phase fractions. The intensities of the major portlandite peaks are greater than those of calcite, with all other minor crystalline phases suppressed; this may indicate that several crystalline constituents of the BOFS were largely contained in coarser particles which were removed by the crushing and sieving process applied here.

The XRD pattern of GGBFS indicates an amorphous structure with a broad feature due to diffuse scattering centred at $30^\circ 2\theta$, and a distinct lack of any crystalline phases.

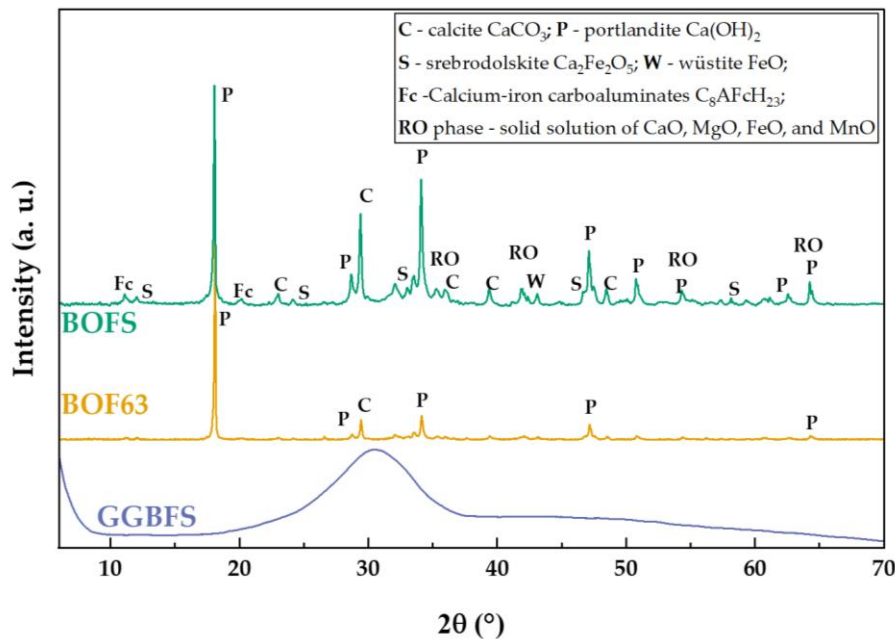


Fig. 5.3: XRD patterns of GGBFS, BOFS, and BOF63

Alkali-activated pastes were prepared by mixing GGBFS with 0 wt. %, 20 wt. %, and 30 wt. % of BOFS. Two types of activator solution were prepared. Type “a” was made by initially mixing NaOH pellets with water and adding sodium silicate solution on cooling of the solution, to obtain a modulus (molar ratio $\text{SiO}_2/\text{Na}_2\text{O}$) of 0.56, then

combined with the precursors to form a paste with an alkali-dosage of 4 g Na₂O per 100 g solid precursor and a water/binder mass ratio (w/b) of 0.38, where the binder is defined as the sum of the solid precursors plus dissolved solids in the activator. Type “b” was prepared by dissolving sodium carbonate in water, then mixed with the precursors at a dose of 8 g Na₂CO₃ per 100 g solid precursor and with w/b of 0.38. Each combination of precursors was activated with both activator types “a” and “b”. An optimised formulation was prepared with 20 wt. % of BOF63, activated with sodium carbonate, type b, and recorded as 20BOFb*. The details of all the formulations are shown in Table 5.3.

Table 5.3: Mix proportions of the pastes based on BOFS and GGBFS

| Sample | Precursors (wt. %) | | | Activator solution | | | w/b (mass ratio) |
|----------------|--------------------|------|-------|---|--|---|------------------------|
| | GGBFS | BOFS | BOF63 | Modulus (SiO ₂ /Na ₂ O molar ratio) | Alkali-dosage (wt. % Na ₂ O) | Na ₂ CO ₃ ^a | |
| 0BOFa | 100 | - | - | 0.56 | 4.0 | - | 0.38 |
| 20BOFa | 80 | 20 | - | 0.56 | 4.0 | - | 0.38 |
| 30BOFa | 70 | 30 | - | 0.56 | 4.0 | - | 0.38 |
| 0BOFb | 100 | - | - | - | 5.0 | 8.00 | 0.38 |
| 20BOFb | 80 | 20 | - | - | 5.0 | 8.00 | 0.38 |
| 30BOFb | 70 | 30 | - | - | 5.0 | 8.00 | 0.38 |
| 20BOFb* | 80 | - | 20 | - | 5.0 | 8.00 | 0.38 |

^a represented as g Na₂CO₃/100 g precursor

The precursors were dry blended for 60 s prior to addition of the alkaline activator solution. Pastes were mixed for 4 min at low speed (140 ± 5 rpm), then for 4 min at high speed (285 ± 5 rpm). The pastes were poured into 50 mm cubic moulds and sealed for at least 24 hours, then cured until reaching the specific testing age under laboratory conditions of 20 ± 1 °C.

5.1.3 Results and discussion

5.1.3.1 Isothermal calorimetry

Fig. 5.4 (a) and (c) show the heat evolution rates of BOFS-GGBFS blends activated with sodium silicate (modulus 0.56) and with sodium carbonate, respectively. Five stages can be identified in the heat evolution profile of AACs: pre-induction, induction, acceleration, deceleration, and diffusion period. The pre-induction period during the initial hour of reaction is associated with the dissolution and wetting of particles. This pre-induction signal is not clearly distinguishable within the data in Fig. 5.4(a) due to its rapid early onset and the delay in recording the early data points using isothermal calorimetry with external mixing. The induction period follows, characterised by very low heat release, in which dissolution of the precursors proceeds and the initial formation reaction products through precipitation-polycondensation occurs. The induction period terminates after a considerable amount of heat is released, signalling the initial acceleration stage. The 0BOFa sample exhibits an acceleration period after ~ 17 h. This behaviour is consistent with previous studies of similar systems [260]. Inclusion of BOFS resulted in a progressive shortening of the induction stage, which became ~ 12.5 h for 20BOFa, and ~ 8 h for 30BOFa. The acceleration peak in these two systems is also reduced in intensity compared to the pure GGBFS mixture. The acceleration-deceleration process is complete within 48 hours for all three samples. Fig. 5.4 (c) illustrates the heat evolution for the mixtures activated with sodium carbonate. 0BOFb shows an initial pre-induction peak during the first hour, followed by a second signal centred around 3 h which can be associated with initial formation of carbonate species [322]. This is followed by a long induction period, interrupted at ~ 35 h by the appearance of low intensity convoluted signals associated with the conversion of formed carbonates, e.g. gaylussite, to stable calcite [260]. The acceleration period occurs around ~ 80 h, forming a wide peak between 80-125 h corresponding to the delayed condensation and precipitation of C-A-S-H gels. Extended induction periods in sodium carbonate activated slag binders have been observed in several previous studies [319], [320],

[325]. The profiles of 20BOFb and 30BOFb in Fig. 5.4 (b) similarly include minor peaks after 2-3 h, associated with initial carbonate formation. The subsequent induction period is reduced in duration, ~ 12 h for 20BOFb and ~ 5 h for 30BOFb, compared to 0BOFb. The high intensity and convoluted shape of the initial peak in the 20BOFb* profile differs from that seen in 20BOFb due to the higher reactivity of the smaller particles within the fine BOF63 precursor.

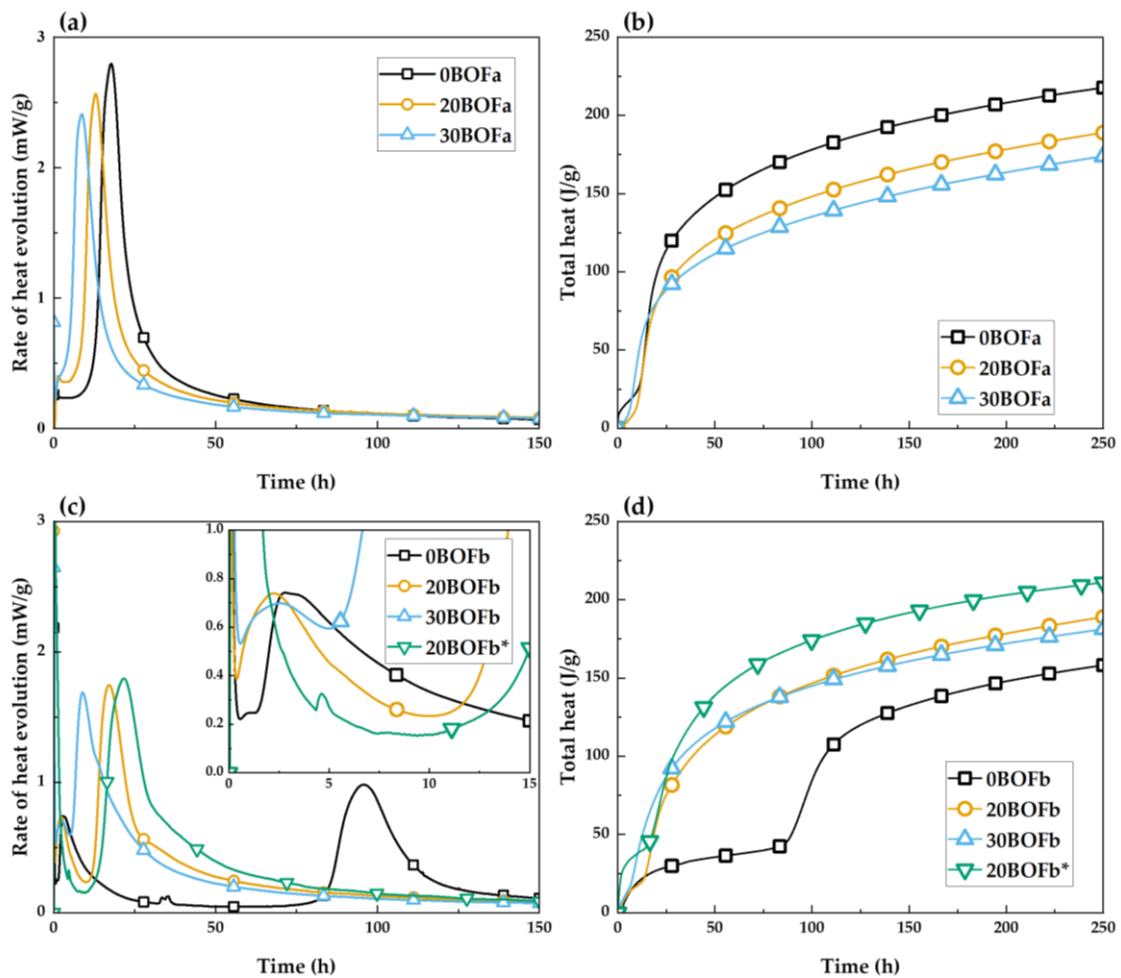


Fig. 5.4: Heat evolution rate of BOFS-GGBFS mixtures activated with (a) sodium silicate and (c) sodium carbonate; total heat cumulative of BOFS-GGBFS mixtures activated with (b) sodium silicate and (d) sodium carbonate, measured at 20 °C

The cumulative heat is shown in Fig. 5.4 (b) for all mixtures activated by activator type “a” based on sodium silicates, and Fig. 5.4 (d) for those with sodium carbonate.

The 0BOFa mixture exhibits the greatest overall heat release after 250 h, with increasing additions of BOF reducing the total heat evolution by 10 % and 15 % for 20BOFa and 30BOFa respectively. Interestingly, the converse trend is seen using sodium carbonate as the activator. 20BOFa and 20BOFb show similar profiles after an initial 100 h, and release similar amounts of heat (188.8 J/g and 188.9 J/g after 250 h). The combination of highly reactive GGBFS and the limited reactivity of portlandite in the high alkalinity systems, compared with the complete reaction of portlandite and reduced reactivity of GGBFS in the sodium carbonate environment, result in a similar cumulative contribution to the reaction kinetics and evolved heat. The cumulative heat of 20BOFb* reaches ~ 211 J/g, very close to the 217 J/g of 0BOFa, however the slope of the curve appears reduced at this point. After 250 h, 30BOFb has released more heat than 30BOFa, which may mean that the reactivity of portlandite gives a greater contribution to the exothermic profile.

5.1.3.2 *Mini-slump and setting times*

Table 5.4 shows the mini-slump results of the fresh mixtures. Inclusions of BOFS are seen to increase the workability of the systems activated by sodium silicate via the inclusion of larger particles and a consequent reduction in surface area. The lower reactivity of BOFS, with respect to GGBFS, and the limited solubility of portlandite in high alkalinity systems may also act to increase workability. The same trend is seen in mixtures activated with sodium carbonate, where the lower flow diameter of these samples than the silicate-activated mixes is consistent with the added silicates having a plasticising effect by dispersing the precursor particles [326].

Inclusion of BOFS results in an increasing trend in both initial and final setting times (Table 5.4) for systems activated with sodium silicate, underpinned by the lower reactivity of BOFS compared to GGBFS. Mix 0BOFb has a setting time of over 3 days,

as indicated in the heat evolution profile (Fig. 5.4 (b)), corroborating that the strength bearing phases do not form during the initial days of reaction [325], [327]. The presence of BOFS is thus noted to be responsible for achieving setting times within a reasonable timeframe. Increasing the BOFS content from 20 wt. % to 30 wt. % results in a slight increase in setting time, suggesting that in a sodium carbonate activated system containing some BOFS, the formation of hydration products of GGBFS is not inhibited by the formation of carbonate salts. The reduction of particle size of BOFS (as in 20BOFb*) results in shortened setting times, meaning that the portlandite contained in BOFS is reacting more promptly from finer BOFS particles.

Table 5.4: Mini-slump test and setting times results for pastes based on BOFS and GGBFS

| Sample | Mini-slump (mm) | Setting time (min) | |
|---------|--------------------|--------------------|----------|
| | | Initial | Final |
| 0BOFa | 92 | 200 | 280 |
| 20BOFa | 99 | 265 | 345 |
| 30BOFa | 116 | 270 | 320 |
| 0BOFb | 79 | ~ 3 days | ~ 4 days |
| 20BOFb | 88 | 280 | 355 |
| 30BOFb | 91 | 310 | 415 |
| 20BOFb* | 90 | 260 | 305 |

5.1.3.3 X-ray diffraction

Fig. 5.5 illustrates the XRD patterns of samples activated with type “a” activator (sodium silicate at MR 0.56) and type “b” activator (sodium carbonate) after 2 and 28 days of curing. In the 2-day 0BOFa pattern seen in Fig. 5.5 (a), the crystalline phases identified are calcium silicate hydrates (C-A-S-H), calcite (C, CaCO_3 PDF #01-086-0174) due to atmospheric carbonation [285], and a hydrotalcite-group phase (HT, $\text{Mg}_4\text{Al}_2(\text{CO}_3)(\text{OH})_{12}\cdot 3\text{H}_2\text{O}$ PDF #01-089-0460) partially carbonated for activator “b”. These reaction products have all previously been identified in alkali-activated GGBFS [15], [113], [328]. The 28-day 0BOFa pattern shows an increase in C-A-S-H peak intensity and a reduction in the full width at half maximum (FWHM),

indicating increased short-range ordering and a higher degree of polymerisation, as expected with increasing curing time. C-A-S-H, calcite, and the hydrotalcite-group (hydroxylated) phase are identified in the 2-day patterns of 20BOFa and 30BOFa, along with AFm-like phases including calcium hemicarboaluminate (Hc, $C_4Ac_{0.5}H_{12}$, PDF #00-041-0221) and monocarboaluminate (Mc, C_4AcH_{11} PDF#00-041-0219). These phases can be formed in conditions of low MgO content and/or surplus Al. The presence of carbonates helps the stabilisation of these AFm-like phases; the formation of Hc and Mc phases is promoted by available CO_3^{2-} present in the BOFS as calcite, and may also be influenced by the presence of an analogous AFm-like phase, Fc, in the weathered BOFS (Fig. 5.3). Remnant precursor peaks identified as portlandite (P, $Ca(OH)_2$ PDF#00-044-1481) show that there is incomplete reaction of the BOFS in high alkalinity environments, with potentially lower reaction kinetics due to its coarse particle size.

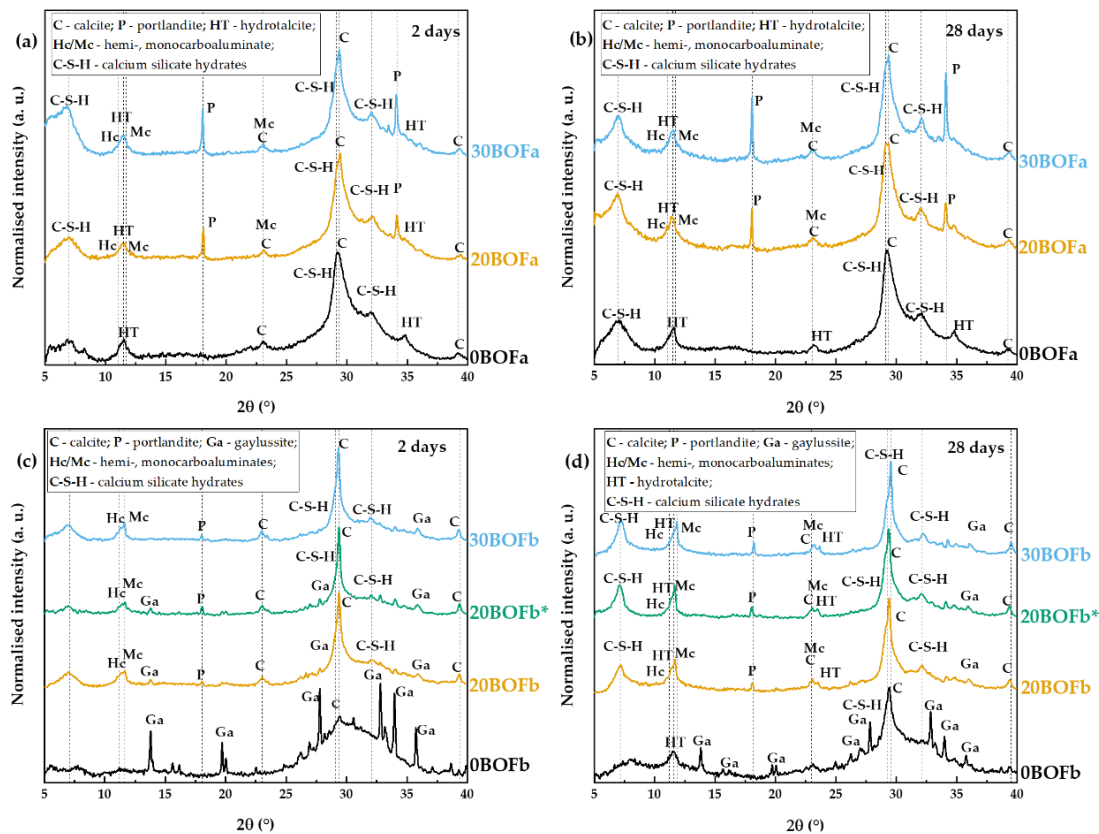


Fig. 5.5: XRD patterns of BOFS and GGBFS activated with sodium silicate after (a) 2 days, and (c) 28 days of curing, and activated with sodium carbonate after (b) 2 days, and (d) 28 days. Note that the phases marked as “CSH” will almost certainly contain alumina and thus are more precisely described as C-A-S-H, but a more concise form of the notation is used in the graphics

In contrast, the two main crystalline phases identified in the 2-day 0BOFb pattern shown in Fig. 5.5 (b) are gaylussite ($\text{Ca}, \text{Na}_2\text{Ca}(\text{CO}_3)_2 \cdot 5\text{H}_2\text{O}$, PDF #00-021-0343) and calcite, which are reported in sodium carbonate activated systems [260], [321], [322]. There is minimal formation of C-A-S-H gel and hydrotalcite-group phase present after 2 days (carbonated). These phases do appear after curing for 28 days, with minor Hc/Mc phases accompanied by a reduction in gaylussite phase fraction. This follows the mechanism proposed by Bernal *et al.* [321], whereby (i) CO_3^{2-} released by the activator reacts with the Ca^{2+} from the dissolution of GGBFS to initially form gaylussite and calcite; (ii) as the reaction proceeds, gaylussite releases Na^+ and converts to calcite; (iii) the reduction of CO_3^{2-} concentration promotes precipitation of C-S-H instead of CaCO_3 whilst increasing OH^- concentration gives a highly alkaline pore solution, (iv) the reaction proceeds similarly to that of NaOH activated slag after 4 days. Identification of secondary carbonate phases in the 2-day 0BOFb XRD pattern supports the interpretation of the 0BOFb calorimetric peaks seen in Fig. 5.4 (a) at 3 h and 35 h as the formation of these carbonate phases, with the subsequent peak after ~ 4 days due to the polycondensation and precipitation of C-A-S-H and hydrotalcite-group phases [260], [321].

The 2-day 20BOFb, 30BOFb, and 20BOFb* XRD patterns in Fig. 5.5 (b) shows the appearance of several reaction products, identified as C-A-S-H, hydrotalcite, Hc, Mc, calcite, and minor traces of gaylussite. The portlandite phase fraction is diminished compared to that seen in Fig. 5.5 (a) and (c), confirming the favoured reactivity of portlandite in systems of lower alkalinity. Portlandite provides an increase in pH via the release of OH^- , which then promotes the dissolution of GGBFS and formation of C-A-S-H gel from dissolved Si and Al species. The formation of AFm-like phases, Mc and Hc, is beneficial in promoting gaylussite dissolution by acting as a carbonate sink, also resulting in precipitation of both amorphous and crystalline CaCO_3 polymorphs [323], [324]. The phase evolution from 2 to 28-day in XRD patterns of 20BOFb, 20BOFb*, and 30BOFb seen from Fig. 5.5 (b) to (d) shows minimal change, especially no change in the peak intensity of the portlandite phase suggesting a cessation of further reaction.

5.1.3.4 Fourier-transform infrared spectroscopy

FTIR spectra of samples activated with sodium silicate and with sodium carbonate are shown in Fig. 5.6 (a) and (b) respectively. Similar bands are found for all samples, indicating that reaction products with comparable nature have formed. The H-OH bending band is seen at 1660 cm^{-1} , associated with partially bonded water after hydration [329]. Bands located in the range $1489\text{--}1419\text{ cm}^{-1}$ and at $\sim 870\text{ cm}^{-1}$ indicate the presence of carbonates, specifically the C-O asymmetrical stretching and asymmetrical bending vibrations. The existence of these bands is consistent with the present of partially crystalline calcium carbonate in different polymorphs, and gaylussite, with specific peaks located at 1450 cm^{-1} , 874 cm^{-1} , 855 cm^{-1} , 713 cm^{-1} , and 668 cm^{-1} [330]–[332] [325]. AFm-like phases such as hydrotalcite, Mc, and Hc may also contribute to these bands. [332]. The band shift observed for 0BOFb at $1489\text{--}1419\text{ cm}^{-1}$ in Fig. 5.6 (b) with increasing curing time supports the mechanism by which a high initial concentration of gaylussite is formed, which over time is converted to calcite and other polymorphs of CaCO_3 [324]. A reduction of the intensity of the carbonate bands with curing time is seen in all samples.

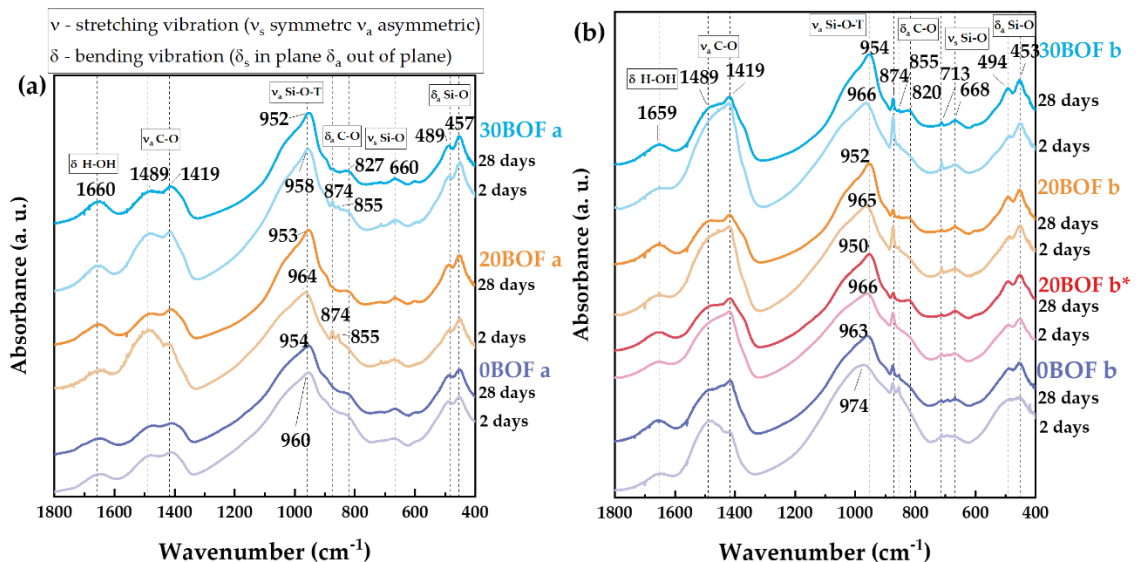


Fig. 5.6: FTIR spectra of BOFS and GGBFS activated with (a) sodium silicate after 2 days and 28 days, and (b) activated with sodium carbonate after 2 days and 28 days of curing

The band associated with formation of silicate binding phases appears at 970-950 cm^{-1} , assigned to the asymmetric stretching vibration mode of the Si-O-T (T = tetrahedral Si, Al) bonds. This band location is in agreement with the C-A-S-H structure formed by the activation of slag in alkaline media [168], [333], appearing narrower and sharpened for all samples with increasing curing time as a result of increased structural order of the gel phase as the reaction evolves [280]. The 2-day cured 0BOFb has a broad and rounded peak, due to the delay in C-A-S-H gel formation which was identified in the XRD analysis (Fig. 5.5) above. A shift of this band towards lower wavenumbers is also recorded in all samples as the crosslinking and the degree of polymerisation of the structure increase due to the incorporation of Al, from 2 to 28 days [171], [325]. At $\sim 700 \text{ cm}^{-1}$ and between 500-400 cm^{-1} are the regions associated with symmetric stretching vibration of Si-O bands, and deformation of SiO_4 tetrahedra, respectively. These last bands also become narrower as the reaction proceeds.

5.1.3.5 Compressive strength

The compressive strength results for blended GGBFS-BOFS systems are shown in Fig. 5.7. 0BOFa reaches 44 MPa and 56 MPa after 7 and 28 days respectively. After 7 days 0BOFb exhibits a compressive strength of 33 MPa, whereby the strength bearing phases (C-A-S-H gels) have formed after the initial 4 days of reaction.

All other mixtures have strength values between 20-35 MPa after 7 days. The respective compressive strength gains for mixtures including BOF between 7 and 28 days are greater than for 0BOFa. 20BOFa and 20BOFb obtain similar strength values, between 25-32 MPa after 7 days and 39-44 MPa after 28 days. The strength values of 20BOFb* are comparable to 0BOFb (45 and 46 MPa after 28 days, respectively). Further replacement of GGBFS by BOFS (30 wt. %) results in a slightly inferior compressive strength (up to 30-35 MPa). All the studied alkali-activated cements made with BOFS inclusions could potentially qualify for structural applications in normal concretes. It is demonstrated that the use of waste BOFS in GGBFS blends can

achieve desirable fresh and mechanical properties when utilising sodium carbonate as a low-cost activator.

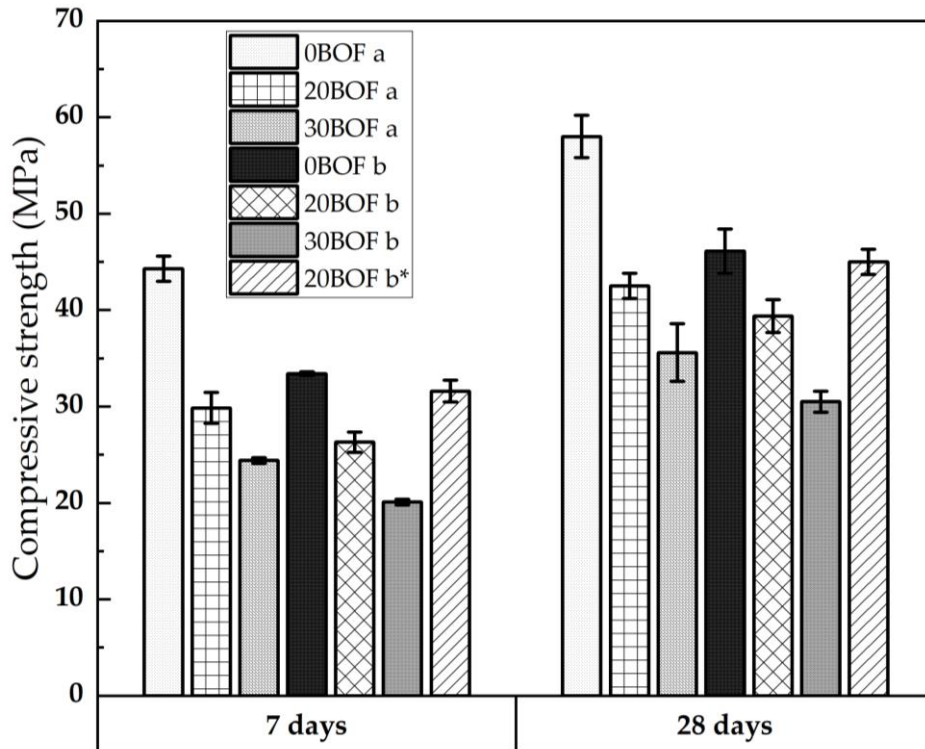


Fig. 5.7: Compressive strength of specimens based on BOFS and GGBFS and activated with sodium silicate and sodium carbonate, after 7 days and 28 days of curing. Error bars represent the standard deviation among three replicate specimens

5.1.4 Conclusions

This work has investigated the use of weathered BOFS as a partial replacement for GGBFS in alkali-activated cements produced using two different activator solutions: sodium silicate with modulus of 0.56, and sodium carbonate.

The reaction kinetics governing the formation of C-A-S-H are accelerated with weathered BOFS inclusion, by exploiting the fast reactivity of portlandite. Sodium carbonate activated-GGBFS has a 4-day induction period, reduced to ~ 10 h with 20 wt. % BOFS. The two-component system including 20 wt. % BOFS with GGBFS, and different activator solutions, resulted in comparable heat evolution.

Workability is affected by the activator type and by BOFS inclusion: The presence of sodium silicate results in higher workability due to a plasticising effect, and BOFS inclusions also increase workability due to the coarser particles and lower reactivity with respect to GGBFS. Setting times also increase with BOFS inclusion when using silicate activators, but BOFS addition accelerates the setting of sodium carbonate activated GGBFS which otherwise does not set until 3 days.

XRD analysis showed that in sodium silicate-activated systems, which have higher relative alkalinity, not all of the portlandite from the weathered BOFS reacted, whereas in sodium carbonate-activated systems the reaction of portlandite is nearly complete, providing an immediate increase in the pH and allowing GGBFS to react and form C-A-S-H gels in the initial stages of reaction. The typical delay observed in the sodium carbonate-activated slag system, via formation of carbonate salts, is therefore avoided. This is also confirmed also through the analysis of FTIR data, which showed that the only sodium carbonate-based system where C-A-S-H did not form appreciably at early age was that containing only GGBFS activated with sodium carbonate.

Specimens made with 20 wt. % BOFS inclusion obtain compressive strength values of up to 39-45 MPa after 28 days. These values are only slightly lower when compared to specimens made with solely GGBFS and are more than acceptable for several structural applications. Weathered BOFS can be used, without any treatment, as a valuable additive in the acceleration of the reaction of GGBFS. Reducing particle size can further increase the reaction of BOFS, and ultimately increase the strength of a sodium carbonate-activated BOFS-containing cement to be comparable with a GGBFS-sodium silicate cement. Additions of BOFS offer a new avenue for reduction of the activator dose in these cements, and the usage of sodium carbonate as an activator for GGBFS, providing a useful valorisation pathway for materials with otherwise very restricted potential applications.

5.2 Electric arc furnace slag (EAFS) in alkali-activated cements

This section is based on: S. Ghorbani, L. Stefanini, Y. Sun, B. Walkley, J. L. Provis, G. De Schutter, and S. Matthys, "Characterisation of alkali-activated stainless steel slag and blast-furnace slag cements," *Cement and Concrete Composites*, vol. 143, no. 105230, 2023, doi: <https://doi.org/10.1016/j.cemconcomp.2023.105230>.

The experimental investigation, data interpretation, and writing of the original draft of this chapter were carried out by L. Stefanini in collaboration with S. Ghorbani, whilst B. Walkley, J. L. Provis G. De Schutter, and S. Matthys provided supervision and revised the draft. Specific tests, such as mini-slump tests, MIP analysis, and compressive and flexural strength testing were conducted at Ghent University by S. Ghorbani.

5.2.1 Introduction

The increasing demand for GGBFS as a SCM in blends with PC has provided further impetus to explore other waste products, specifically from the steelmaking industry, as potential AACs [334]. However, the inconsistency in waste compositions [335], [336] and the presence of heavy metals are major limitations to the valorisation of steel slags; the leaching of toxic chromium compounds contained in stainless steel slags has been noted as being of particular concern [337], [338]. Global stainless steel slag production is reported to have been around 52 million tonnes in 2019, with EAFS being a substantial fraction of this output [335]. EAFS has been successfully used as an aggregate in cement-based materials [160], [339], for road pavements [340], and as a non-conventional SCM or filler material for PC [156], [341]. EAFS, when used as an SCM, has been reported to modify fresh properties such as paste rheology and setting time [156], [157], [342], albeit with reduced mechanical properties arising from the low reactivity of the EAFS [343].

This study aims to investigate the use of EAFS as a potential precursor replacement for AACs, or as a filler material, to reduce the amount of GGBFS required by these mixtures. The fresh, microstructural, and mechanical properties are characterised, along with leachability tests to check the stability of heavy metals in the AAC.

5.2.2 Materials and methods

In this study, the precursors GGBFS, provided by Ecocem (Belgium), with density $\rho = 2.89 \text{ g/cm}^3$, and EAFS type Fillinox 3000 provided by Orbix (Belgium) with $\rho = 3.25 \text{ g/cm}^3$, were used to produce AACs. The XRF results identifying the chemical compositions of the solid precursors are given in Table 5.5. Apart from the presence of Cr_2O_3 in EAFS, the main distinction between the two precursors is the disparity in concentrations of Al_2O_3 , MgO , and SO_3 .

Table 5.5: Oxide composition (wt. %) of GGBFS and EAFS as measured with XRF

| Sample | SiO_2 (%) | CaO (%) | Al_2O_3 (%) | Fe_2O_3 (%) | MgO (%) | SO_3 (%) | MnO (%) | Cr_2O_3 (%) | Others |
|--------|-----------------------|---------------------|--------------------------------|--------------------------------|---------------------|----------------------|---------------------|--------------------------------|--------|
| GGBFS | 36.4 | 43.50 | 10.5 | 0.3 | 7.0 | 1.4 | 0.3 | - | 0.6 |
| EAFS | 28.0 | 44.2 | 6.3 | 2.0 | 4.4 | 0.5 | 2.7 | 9.9 | 2.0 |

The particle size distributions of the precursor materials are shown in Fig. 5.8.

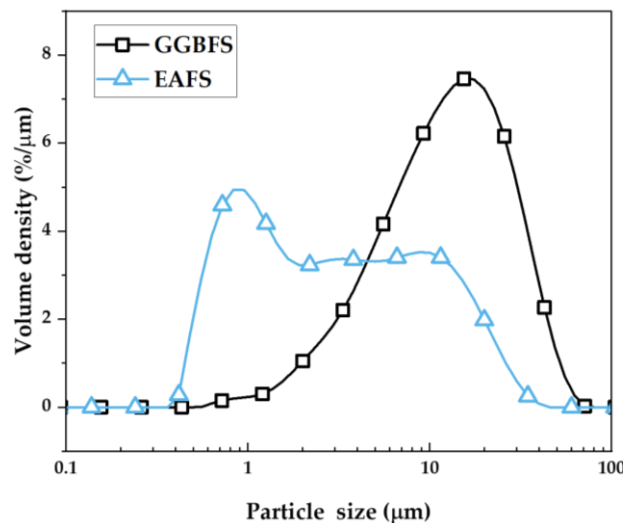


Fig. 5.8: Particle size distributions of GGBFS and EAFS used in this study

The GGBFS has d_{10} , d_{50} , and d_{90} values of 2.9 μm , 12.7 μm , and 31.0 μm , respectively, compared to 0.8 μm , 3.0 μm , and 15.6 μm respectively for EAFS. The obtained particle size distributions for GGBFS show a singular distribution, whereas the distribution for EAFS is multi-modal. SEM images of GGBFS particles show a range of particle sizes < 100 μm with angular morphologies, whilst EAFS consists of a combination of large particulates \sim 100 μm and fine grains < 1 μm (Fig. 5.9).

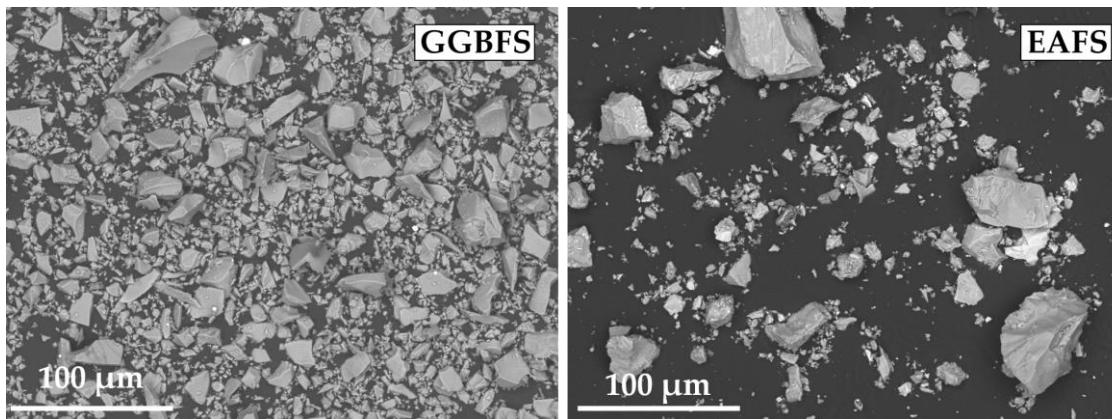


Fig. 5.9: SEM images showing the morphology and particle size distribution of GGBFS and EAFS

The XRD patterns of the solid precursors are displayed in Fig. 5.10.

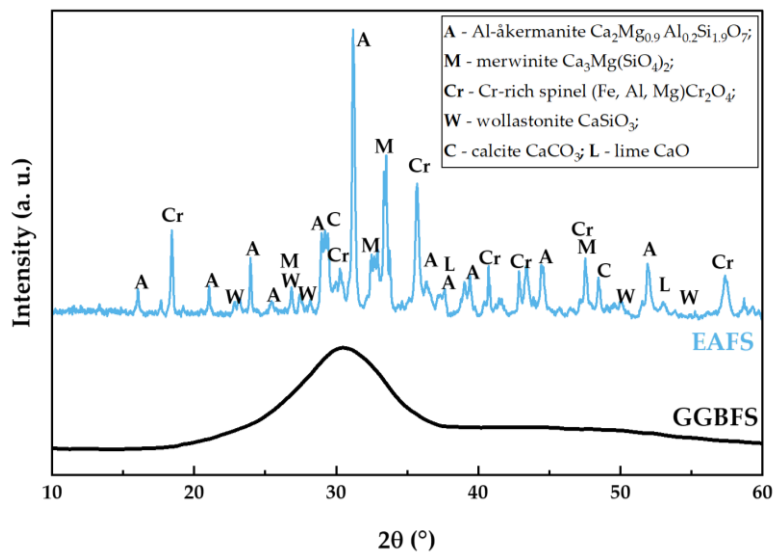


Fig. 5.10: XRD patterns of GGBFS and EAFS

The GGBFS pattern does not show any crystalline phase. A broad amorphous hump between 25 and $35^\circ 2\theta$ is recognizable. Phase identification of the crystalline phases in the EAFS XRD pattern indicate the presence of melilite (specifically, åkermanite with a partial Al substitution, $\text{Ca}_2\text{Mg}_{0.9}\text{Al}_{0.2}\text{Si}_{1.9}\text{O}_7$, PDF# 04-014-4688), and merwinite ($\text{Ca}_3\text{Mg}(\text{SiO}_4)_2$, PDF# 01-086-6219) as the main mineral phases. Less intense peaks corresponding to a mixed spinel phase $(\text{Fe}, \text{Mg}, \text{Al})\text{Cr}_2\text{O}_4$ (PDF# 04-016-2691), calcite (CaCO_3 , PDF# 01-086-4272), a minor amount of wollastonite (CaSiO_3 , PDF# 00-027-0088), and traces of free lime (CaO , PDF# 00-037-1497), were identified.

FTIR spectra of the raw materials are presented in Fig. 5.11. The GGBFS spectrum shows two main broad absorption bands with centre at 970 cm^{-1} and at 507 cm^{-1} corresponding to Si-O-T (T = tetrahedral Si, Al) asymmetric stretching vibrations and Si-O symmetric stretching vibrations, respectively [234]. A minor band found at $\sim 700\text{ cm}^{-1}$ is attributed to Si-O bending vibrations. The broadness of the bands is correlated with the amorphous structure of GGBFS.

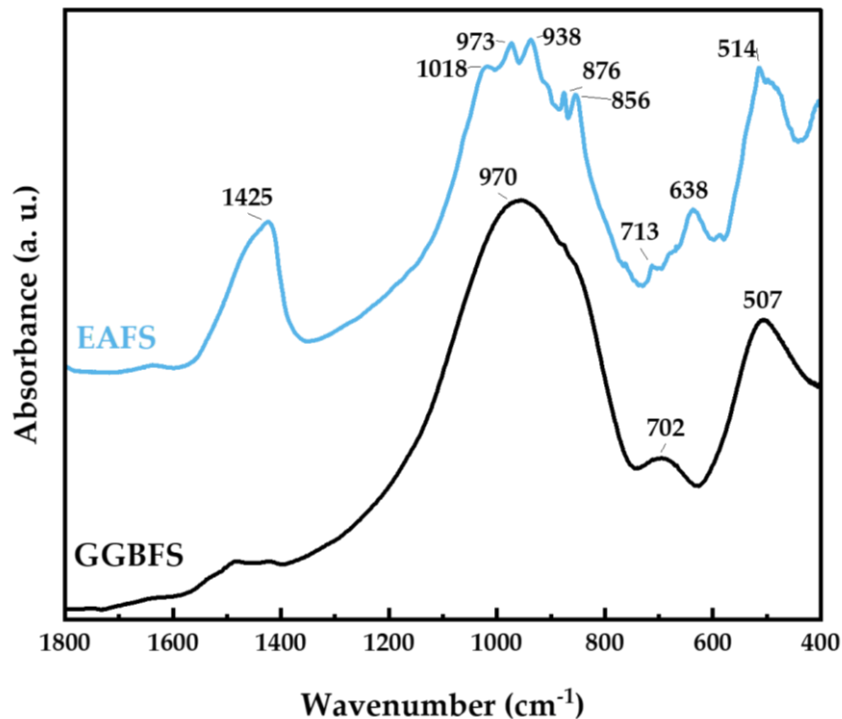


Fig. 5.11: FTIR spectra of precursors GGBFS and EAFS

The EAFS spectrum similarly exhibits these two main bands, at $\sim 1000\text{-}900\text{ cm}^{-1}$ and at $\sim 500\text{ cm}^{-1}$, corroborating that silicates (calcium silicates with Mg and Al) are the most abundant phases, as seen in the XRD in Fig. 5.10. Besides these bands, several well defined and sharp peaks are detected for the crystalline phases present. Peaks at 1425 cm^{-1} , 875 cm^{-1} , 713 cm^{-1} are attributed to calcite, specifically the C-O asymmetric stretching vibration and C-O out-of-plane and in-plane bending [344]. The bands at 638 cm^{-1} and the shoulder at 500 cm^{-1} are due to the Cr(III)-O vibration characteristic of the spinel phase $(\text{Fe, Mg, Al})\text{Cr}_2\text{O}_4$ [345]. The remnant peaks at 1018 cm^{-1} , 973 cm^{-1} , 938 cm^{-1} , 855 cm^{-1} and 587 cm^{-1} are associated with the presence of crystalline åkermanite, merwinite, and wollastonite [346].

A BSE image of a large EAFS particle with distinct greyscale contrast is shown in Fig. 5.12.

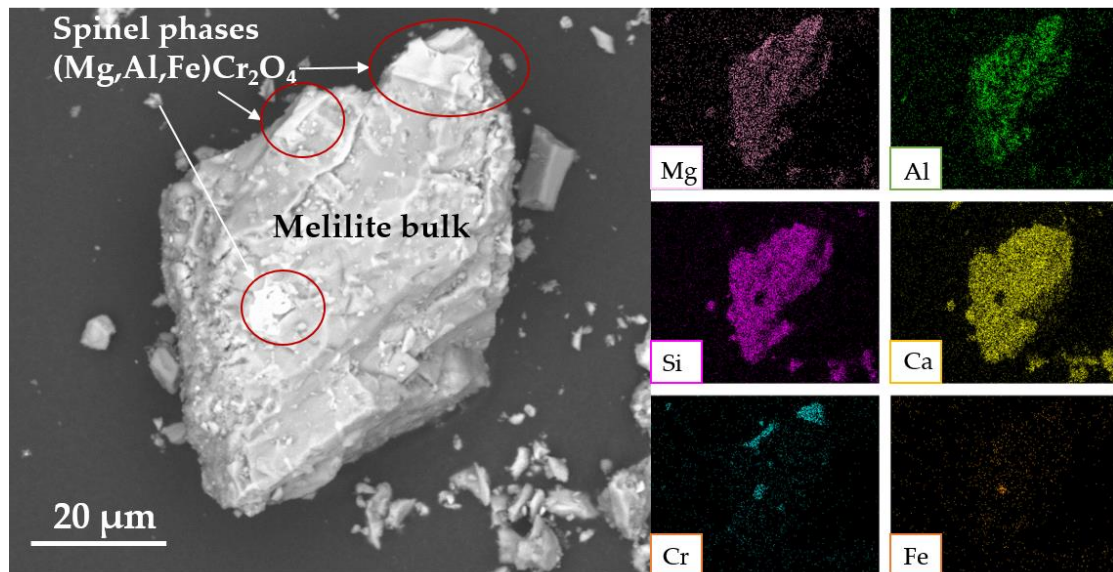


Fig. 5.12: BSE image of a EAFS particle with EDS analysis (from top left: Mg, Al, Si, Ca, Cr, and Fe)

From the EDS elemental map, distinct regions of Cr are observable, which overlap with Mg, Al, and Fe. No Si and Ca are detected within these Cr-rich regions. Primary crystalline phases identified via XRD, åkermanite, and merwinite, have element compositions that include Ca, Si, Mg, and Al, as seen in the bulk of the particle. The

calcium silicates åkermanite, merwinite, and wollastonite are known to have low reactivity in alkaline media [347]. Cr containing spinel phases have also been reported in literature, with the Cr occupying the B-site in the spinel AB_2O_4 with an oxidation state of +3. Strong octahedral Cr-O bonding present in the spinel structure is very resistant towards oxidation to the toxic hexavalent state (Cr(VI)) and resistant to dissolution [337]. The leaching of chromium sometimes poses a serious problem for the utilization of EAFS in binding materials.

Solid precursors (GGBFS and EAFS) were initially dry mixed in a 2 l capacity Hobart mixer for 60 s to achieve a uniform distribution. Standard CEN sand according to EN 196-1 [348] was also added and pre-blended prior to the alkali-activation of mortars. Both precursors and alkaline solution were mixed for 60 s at low speed (140 rpm), then subsequently for 90 s at high speed (285 rpm) to achieve a homogeneous mixture. Alkali-activated mixtures were designed with a constant water/binder (w/b) mass ratio of 0.32, where the binder is defined as the sum of the solid precursors plus dissolved solids in the activator. The alkali solution was prepared 24 h in advance, by mixing sodium hydroxide, sodium silicate, and water to give a modulus (molar ratio of SiO_2/Na_2O) of 1.6 and an alkali-dosage (wt.% of Na_2O with respect to solid precursors) of 5.3 wt. %. The same procedure was used to prepare pastes, except for the sand addition. Five slag-based AACs with varying EAFS replacement levels (0 wt. %, 25 wt. %, 50 wt. %, 75 wt. %, and 100 wt. %) were produced and shown in Table 5.6.

Table 5.6: Mix proportions of the alkali-activated mortars based on GGBFS and EAFS

| Sample | Precursors (wt. %) | | Activator solution | | w/b (mass ratio) | Sand in mortars (wt. %) |
|--------|--------------------|------|---|-----------------------------------|---------------------|-------------------------------|
| | GGBFS | EAFS | Modulus (SiO_2/Na_2O molar ratio) | Alkali-dosage (wt. % Na_2O) | | |
| 100G | 100 | 0 | 1.6 | 5.3 | 0.32 | 275 |
| 25E | 75 | 25 | 1.6 | 5.3 | 0.32 | 275 |
| 50E | 50 | 50 | 1.6 | 5.3 | 0.32 | 275 |
| 75E | 25 | 75 | 1.6 | 5.3 | 0.32 | 275 |
| 100E | 0 | 100 | 1.6 | 5.3 | 0.32 | 275 |

5.2.3 Results and discussion

5.2.3.1 Isothermal calorimetry

The heat evolution and cumulative heat profiles of the alkali-activation reaction of blended GGBFS and EAFS systems are displayed shown in Fig. 5.13 (a) and (b), respectively.

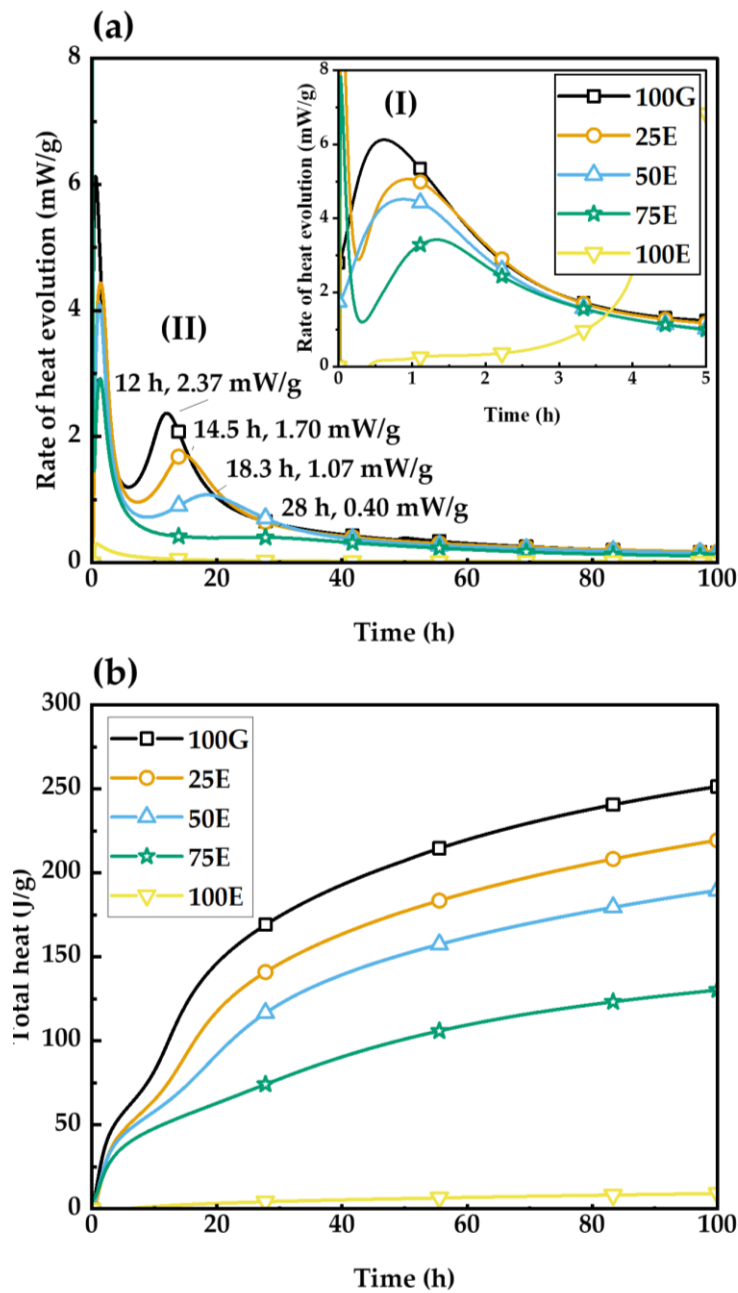


Fig. 5.13: Isothermal calorimetry data for samples 100G, 25E, 50E, 75E, and 100E, measured at 20 °C

One possible classification for the heat evolution of AACs is in five stages described as: pre-induction or dissolution, induction or dormant, acceleration, deceleration, and the steady stage [349] similarly to traditional cement systems, which is usually acceptable for AACs activated with sodium silicates. According to this classification we see a first exothermic peak between 0 to 3 h, identified as a pre-induction peak and representing the contact wetting of the solid precursors with the alkaline activator and initial particle dissolution. The formation of primary C-A-S-H and C-(N)-A-S-H gels begins with the deceleration of the first peak [261], [274], [350]. The intensity of this peak is highest for 100G, decreasing progressively with the addition of EAFS. For the 100E sample, the pre-induction peak is barely detectable due to the lack of reactivity of EAFS in this system. The main contribution to the pre-induction peak comes from the ready dissolution of GGBFS particles. The initial stage of wetting/dissolution of the solid precursors is followed by an induction or dormant period, characterised by a very low, but non-zero rate of heat release in which the dissolution process continues. A second exothermic peak follows the induction period; this is related to the precipitation, nucleation, and growth of reaction products during polycondensation. Within this period a large volume of binding phase, primarily C-A-S-H and C-(N)-A-S-H gels, is formed. 100G has an induction period of about 9 h followed by the second exothermic peak, with a maximum at 12 h. Overall, the 100G sample shows an acceleration in heat release and subsequent deceleration within the space of 30 h. By increasing the replacement level of EAFS, the induction period becomes longer and there is a reduction in the maximum intensity of the second exothermic peak. This extent of reduction follows a linear relationship (with $R^2 = 0.994$) with the GGBFS replacement level: reductions of 28.3 %, 54.8 %, and 83 % were observed for 25 wt. %, 50 wt. %, and 75 wt.% replacements, respectively. This indicates that the reaction of the EAFS during the acceleration-deceleration period is minimal, and with limited influence from any form of filler effect. 100E mixture has negligible exothermic activity overall.

The cumulative heat is shown in Fig. 5.13 (b). Evaluating the total heat released after 100 h of reaction there is a non-linear trend of heat reduction with the GGBFS

replacement (12.7 %, 24.3 %, and 48 % reduction for 25 wt. %, 50 wt. %, and 75 wt.% EAFS, respectively), which indicates that the EAFS is influencing the reaction in these blends to some extent after the initial 20-hour period of the main exothermic peaks. However, 100E has a minimal cumulative exothermic activity of 8 J/g after 100 h, which is attributed to the very limited dissolution of particles. These results suggest the low reactivity of EAFS when included in a blended alkali-activated binder, verifying the potential of EAFS to be used as a filler material. The cumulative heat release of the blended AACs from 20 to 100 h may be enhanced by the filler effect of EAFS which allows a higher space for hydration products and extent of reaction of the remaining GGBFS in these binders.

5.2.3.2 Mini-slump test and setting times

The mini-slump test and setting time results exploring the workability and setting time properties of the tested AACs are shown in Fig. 5.14.

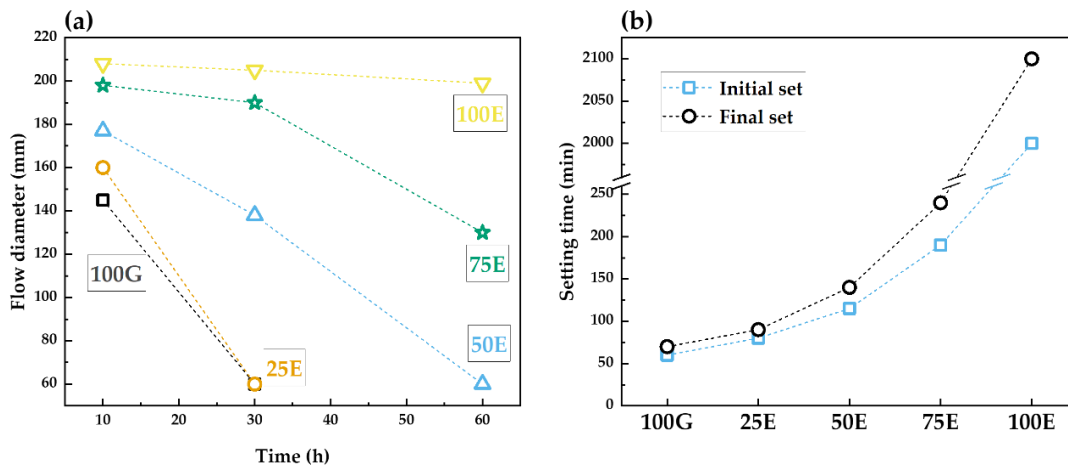


Fig. 5.14: Fresh properties of the AACs based on GGBFS and EAFS: (a) flow diameter over time of the GGBFS-EAFS mixtures; (b) initial and final setting time increasing the replacement level of GGBFS

As can be seen in Fig. 5.14 (a), the initial slump diameter values of the paste mixtures with EAFS vary within the range of 162 - 212 mm (from an initial cone base diameter of 60 mm), while for the 100G mixture a lower slump diameter value of 149 mm is obtained. Using EAFS replacement increases the initial slump values of fresh

mixtures (9 %, 17 %, 36 % and 43 % increase for 25 wt. %, 50 %, 75 % and 100 % EAFS, respectively), despite the higher fineness of the EAFS. This observation may be attributed to the less reactive nature of EAFS, consisting of stable mineral phases which do not show pronounced early reactivity [351]. Similar observations have been reported [342], [343] where the fresh properties of AACs improved with different steel slag additions [343], [351], [352] due to their limited participation in early hydration reactions. Considering that a constant liquid to solid ratio (by mass) was used to produce the paste mixture, using EAFS with a higher density than GGBFS yields a larger liquid to solid volume ratio of the fresh mixture, and consequently higher slump values [342]. As demonstrated in Fig. 5.14 (a), the 100G and 25E paste mixtures showed a drastic loss in the slump values after 30 min, approaching a zero-slump condition (diameter equal to the cone base diameter of 60 mm) at this time due to the intensive early-stage reactions occurring, as illustrated in previous sections. Using higher contents of EAFS reduces the slope of the slump loss curves, highlighting the retardation of early-stage activation reactions of AAC with increasing EAFS replacement, in line with isothermal calorimetry.

The setting time measurements are shown in Fig. 5.14 (b). 100G has the shortest initial setting time of 60 min, with final setting measured after 70 min, which is to be expected with the type and dosage of activator used here [325]. Increasing the replacement of GGBFS with EAFS shows an increase in the initial setting time, by as much as 200 % at 75 wt. % EAFS content. A setting time of over 2000 min is observed for 100E.

5.2.3.3 *X-ray diffraction*

The XRD patterns of the hardened pastes at 2 and 28 days of curing are shown in Fig. 5.15. 100G after 2 days (Fig. 5.15) shows only one crystalline feature which is attributed to calcite (CaCO_3) at $\sim 29^\circ 2\theta$, a product of atmospheric carbonation. Several distinct diffuse humps are detected, at $\sim 29^\circ$, 33° , and $50^\circ 2\theta$ which are related to the formation of C-A-S-H gel phases. Only at later ages in Fig. 5.15 (b), two minor humps at $\sim 12^\circ$ and $56^\circ 2\theta$ are attributed to hydrotalcite-group minerals

(approximately $\text{Mg}_4\text{Al}_2(\text{CO}_3)(\text{OH})_{12}\cdot 3\text{H}_2\text{O}$ PDF #01-089-0460 with variation in Mg/Al ratio and CO_3/OH ratio), resulting from the reaction of the Mg^{2+} present in GGBFS [295]. The broadness and low intensity of these peaks suggests the slow formation of nanoscale hydrotalcite-group crystallites.

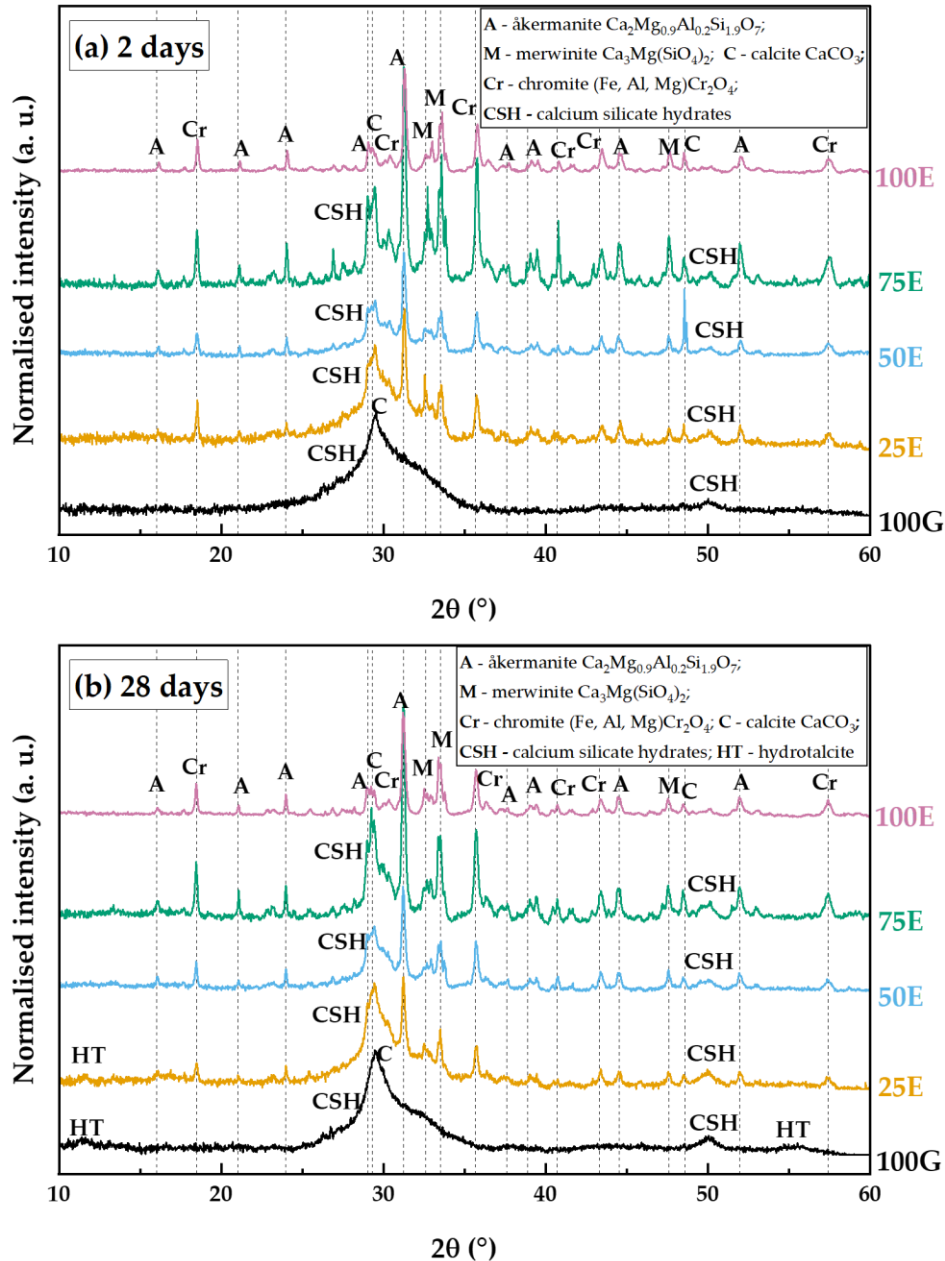


Fig. 5.15: XRD patterns of AACs based on GGBFS and EAFs at 2 days and 28 days of curing. Note that the phases marked as “CSH” will contain alumina and thus are more precisely described as C-A-S-H, but a more concise form of the notation is used in the graphics

When 25 wt.% EAFS is included into the mixture, the crystalline phases åkermanite (A), merwinite (M), and a spinel phase similar to chromite (Cr) are detected, attributed to unreacted EAFS grains. The formation of C-A-S-H gel phases, calcite, and after 28 days, hydrotalcite-group structures, is noted, similar to the case of 100G. A further increase of EAFS content in 50E and 75E causes an increase in intensity of the unreacted crystalline phases, and notably less C-A-S-H gel formation. Calcite formation is detected, whereas hydrotalcite does not appear to be formed from binder blends with 50 % or more EAFS. When increasing the curing time from 2 to 28 days, an increase in the C-A-S-H phase fraction is seen, along with narrowing of the C-A-S-H humps at $\sim 29^\circ 2\theta$ and $\sim 50^\circ 2\theta$, suggesting an increased short-term ordering of the gel [280]. The XRD pattern of 100E is similar to that of the EAFS precursor. C-A-S-H gel phases do not appear to form, underlining the stability of the crystalline phases present in EAFS in alkaline conditions.

5.2.3.4 Fourier-transform infrared spectroscopy

Infrared spectra of the AACs cured for 2 and 28 days are represented in Fig. 5.16.

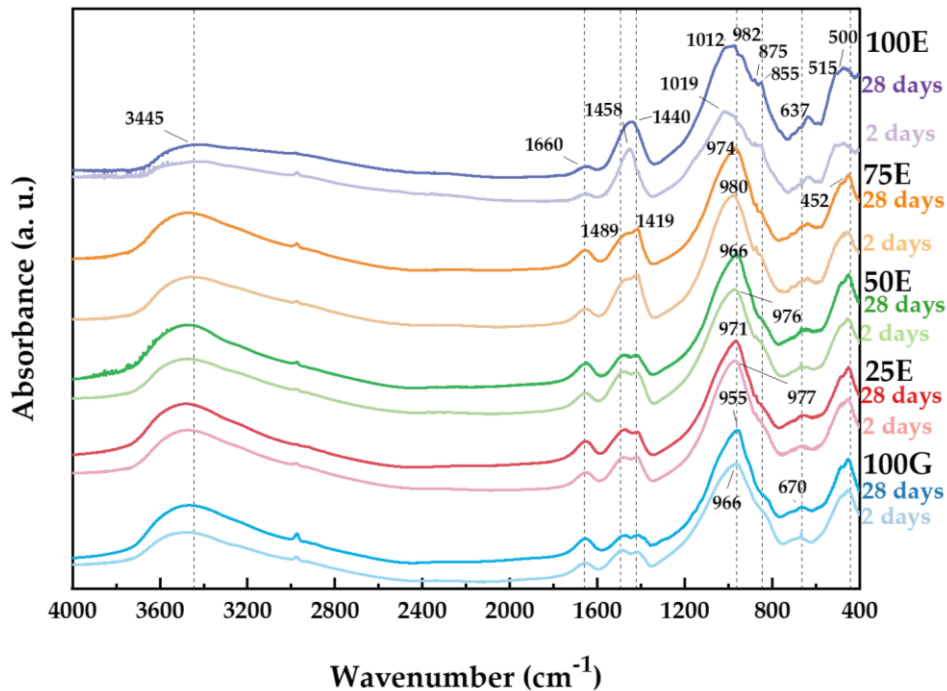


Fig. 5.16: FTIR spectra of AACs based on GGBFS and EAFS at 2 days and 28 days of curing

All AACs studied exhibit absorbance bands at $\sim 3445\text{ cm}^{-1}$, and 1660 cm^{-1} , which are generally assigned to stretching/bending vibrations of O–H groups. These specific bands are typical of weakly bonded water within the structure, which can occur during the formation of hydration products such as C-A-S-H gels. The bands at $1489\text{--}1418\text{ cm}^{-1}$ are due to C-O stretching vibrations and can be attributed to atmospheric carbonation products, such as the calcite identified in some samples by XRD (Fig. 5.15), and also amorphous calcium carbonates [344]. Calcite is also present in the EAFS prior to activation (Fig. 5.10), with corresponding absorbance bands at $875\text{--}713\text{ cm}^{-1}$ detectable in samples with high contents of EAFS, such as 100E and 75E.

The main band at $1200\text{--}800\text{ cm}^{-1}$ is attributed to asymmetric stretching vibrations of Si-O-T bonds (T = tetrahedral Si, Al) [353]. Analysis of this broad band is used to interpret the chain structure of amorphous gel-type phases present, with a distinct narrowing with increased curing time indicating a shift in structural ordering of the gel phase as the polycondensation reaction progresses [280], [301]. This reaction also results in a shift of the band towards lower wavenumbers due to increasing incorporation of tetrahedral Al into the silica network [168]. Both of these behaviours are seen to a varying degree in all samples, with slight peak shifts and narrowing of the Si-O-T band with increasing curing time from 2 to 28 days in all samples. It is interesting to note that the 100E sample, which from phase identification of XRD data is believed to be largely unreactive, shows a slight band shift as evidence of partial gel formation, consistent with the low but non-zero calorimetric response of this sample also. This is supported by a relative increase in O-H band intensity from the emergence of hydration products between 2 and 28 days. Sharp peaks at around $1080\text{--}940\text{ cm}^{-1}$, assigned to åkermanite and merwinite, are more diffuse in character after 28 days, suggesting possible dissolution of calcium magnesium silicate phases and resulting in a weak amorphous gel. Conversely, the bands for the spinel phase (chromite) at 637 cm^{-1} and 500 cm^{-1} remain sharp at all curing times.

5.2.3.5 Scanning electron microscopy

BSE images were collected for 2 and 28-day cured 100G, 50E, and 100E samples. Comparison of Fig. 5.17 (a) and (b) shows a clear evolution of the 100G binding phase between 2 and 28 days of curing. There is an increase in binding phase present, but also a homogenous distribution of angular GGBFS particles still visible within the matrix after 28 days. Sample porosity is also seen to be reduced with increasing curing time.

In the 50E samples, Fig. 5.17 (c) and (d), the EAFS particles can be identified, as well as GGBFS embedded within the binding phase. Some large EAFS particles show internal Z-contrast contrast, indicating compositional inhomogeneity. The composition of various EAFS particles from point EDS analysis (2-5) are shown in Table 5.7. The GGBFS particles show a reaction rim as they dissolve to form the binding phase, as seen in the 28-day specimen in Fig. 5.17 (d). The composition of the reaction rim is noted to be different than that of the bulk gel phase, and is consistent with previous observations of hydrotalcite-group phases becoming formed specifically in this area of the microstructure of alkali-activated BFS-based binders [354]. No reaction rim is seen around EAFS particles, most likely due to their slower dissolution rate compared to GGBFS.

The 100E sample after 2 days curing in Fig. 5.17 forms a highly porous matrix with a weak particle assemblage. Curing for 28 days results in an increased binding phase fraction and reduction in matrix porosity, in agreement with the FTIR data (Fig. 5.16). This confirms that EAFS in alkali-activation can partially form a binding phase from the dissolution of either of the constituent merwinite and åkermanite phases. Engström *et al.* [347] have previously reported the favourable dissolution of merwinite under alkali-activation conditions, and the results presented here are consistent with those findings.

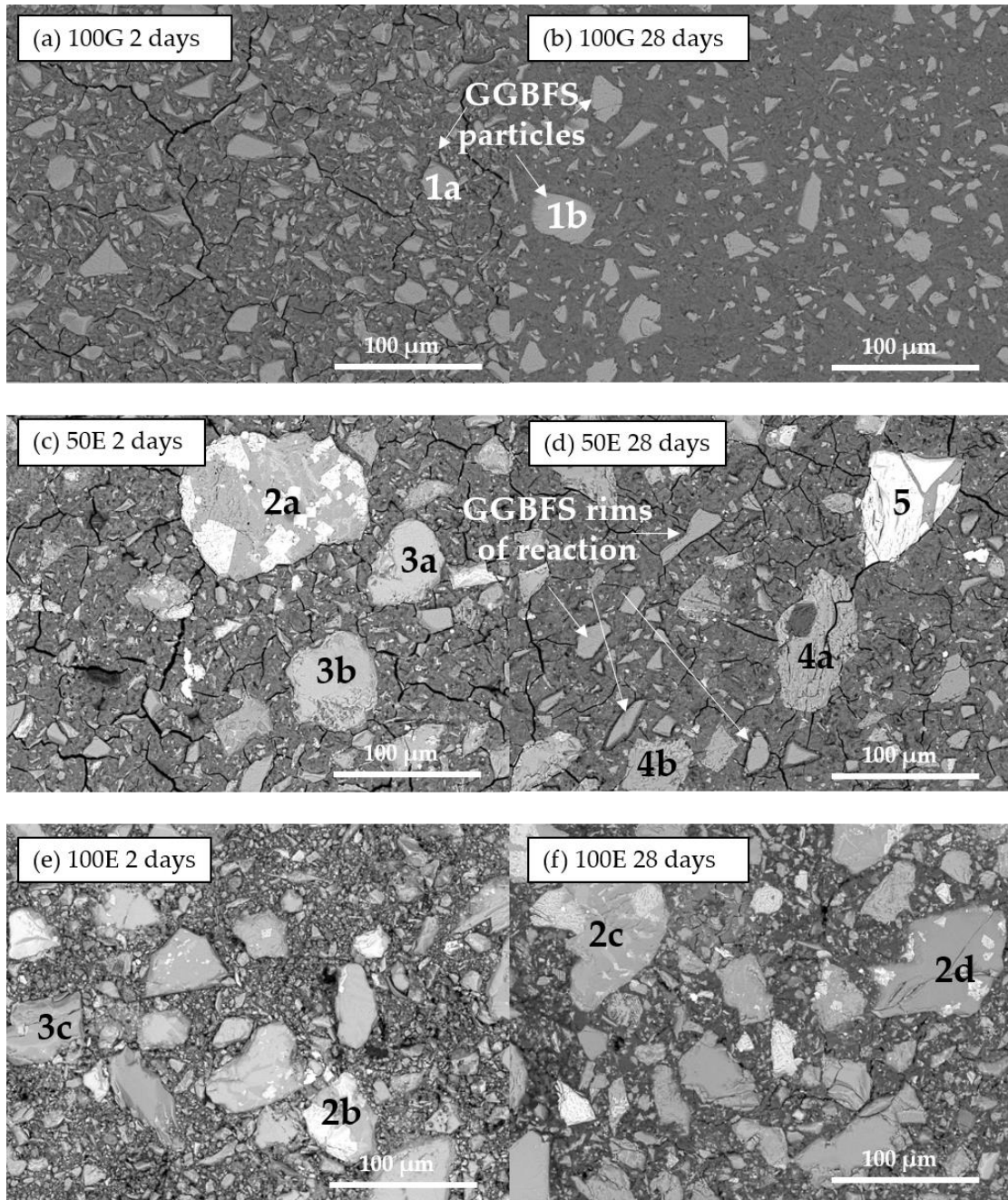


Fig. 5.17: BSE images of alkali-activated pastes based on GGBFS and EAFS after 2 days and 28 days of curing. Compositions of particles numbered 1 to 5 are given in **Table 5.7**.

Energy dispersive spectroscopy (EDS) was used to identify several types of particles (labelled in Fig. 5.17) and to determine their composition, as summarised in Table 5.7. Particle type 1 is associated with GGBFS, while various EAFS particles are distinguished: type 2) the spinel $(\text{Mg,Fe,Al})\text{Cr}_2\text{O}_4$ embedded in a melilite solid

solution phase; type 3) calcium silicate particles with low Mg content, possibly wollastonite or bredigite ($\text{Ca}_7\text{Mg}(\text{SiO}_4)_4$); type 4) merwinite particles; and type 5) iron silicate particles, potentially glassy in nature.

Table 5.7: Compositional EDS analysis of particles of GGBFS and EAFS labelled 1 to 5 in Fig. 5.17, where 1 *a* and *b* are GGBFS particles; 2 *a*, *b*, *c*, and *d* are spinel phases embedded in the melilite solid solution; 3 *a*, *b*, and *c* calcium silicates; 4 *a* and *b* are merwinite particles; and particle 5 is an iron silicate

| (wt. %) | GGBFS particles | | EAFS particles | | | | | | | | | |
|-----------|-----------------|----------|----------------|----------|----------|----------|----------|----------|----------|----------|----------|--------|
| | Type 1 | | Type 2 | | | | Type 3 | | | Type 4 | | Type 5 |
| | <i>a</i> | <i>b</i> | <i>a</i> | <i>b</i> | <i>c</i> | <i>d</i> | <i>a</i> | <i>b</i> | <i>c</i> | <i>a</i> | <i>b</i> | - |
| O | 45.5 | 46.1 | 45.7 | 44.8 | 47.7 | 45.0 | 44.0 | 43.4 | 44.9 | 45.0 | 42.5 | 38.3 |
| Ca | 27.3 | 24.6 | 21.3 | 28.0 | 23.0 | 26.0 | 36.0 | 32.8 | 32.6 | 27.0 | 34.1 | 4.1 |
| Si | 17.3 | 16.8 | 11.9 | 13.8 | 14.0 | 12.4 | 15.0 | 15.3 | 13.8 | 11.3 | 14.1 | 15.1 |
| Al | 5.0 | 4.9 | 2.9 | 1.4 | 2.8 | 5.1 | 1.0 | 2.6 | 0.7 | 0.8 | 0.5 | 2.1 |
| Mg | 3.5 | 4.3 | 3.6 | 4.3 | 2.3 | 3.8 | 1.7 | 2.5 | 5.0 | 14.1 | 6.8 | 0.8 |
| Na | 1.2 | 2.7 | 1.3 | 1.1 | 5.6 | 0.7 | 1.8 | 1.9 | 1.9 | 1.1 | 1.9 | 4.9 |
| Fe | 0.1 | 0.3 | 1.3 | 0.4 | 0.4 | 0.2 | 0 | 0.1 | 0 | 0.5 | 0.1 | 34.4 |
| Cr | 0 | 0.1 | 11.7 | 5.8 | 4.6 | 6.9 | 0.4 | 1.3 | 0.9 | 0.2 | 0 | 0.2 |

5.2.3.6 Mercury intrusion porosimetry

The pore size distributions of 100G and 50E pastes at curing ages of 2 and 28 days, as determined by mercury intrusion porosimetry, are presented in Fig. 5.18. As reported in the literature [300], [355] the pore structure of the AAC matrix can be categorised into three regions: (1) air voids ($> 10 \mu\text{m}$), (2) capillary pores (50 nm - $10 \mu\text{m}$) and (3) gel pores (10 - 50 nm). As shown in Fig. 5.18 (b), the differential pore volume curves are flattened across the capillary pore region and begin to rise within the gel pore region, indicating that the gel pores are the dominant pores within the paste specimen structure. The shapes of the distributions in Fig. 5.18 (b) show only the 50E mixture having a distinct pore size distribution within the explored range of the MIP test, with the 100G sample possibly containing additional pores $< 6.5 \text{ nm}$ that are not probed by this technique. The total porosities of the alkali-activated pastes in the

range of 6.5 nm to 10 μm calculated from the total cumulative pore volumes are given in Table 5.8.

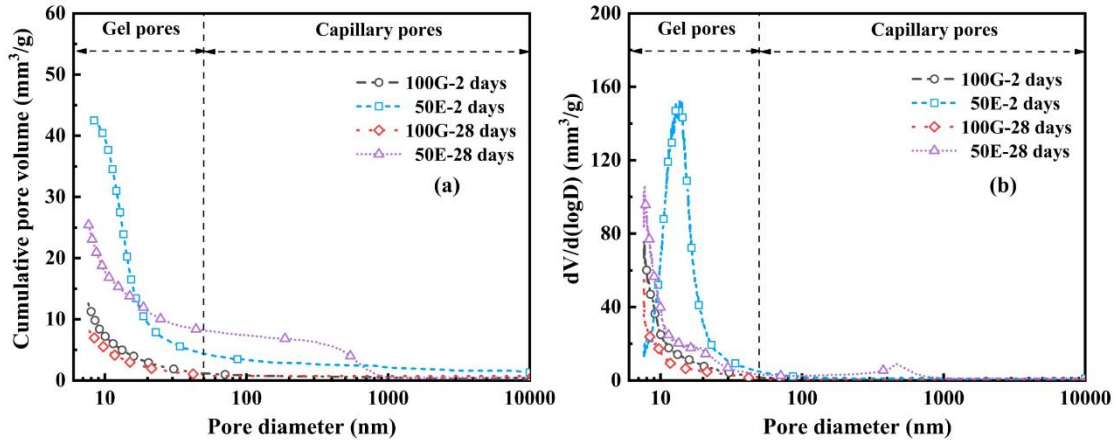


Fig. 5.18: Pore structure of the alkali-activated pastes after 2 days and 28 days: (a) cumulative pore volume and (b) differential pore volume

From the data in in Fig. 5.18 and Table 5.8, blending EAFS with the GGBFS used to produce AACs significantly increases the cumulative pore volume of the paste matrix at both ages tested here, yielding a larger total porosity in the range of 6.5 nm to 10 μm.

Table 5.8: Total porosity of the pastes based on GGBFS and EAFS after 2 days and 28 days of curing

| Mixture | Total porosity (%) | |
|---------|--------------------|---------|
| | 2 days | 28 days |
| 100G | 2.55 | 1.75 |
| 50E | 8.95 | 5.35 |

The porous structure of EAFS pastes arises from the presence of stable crystalline phases that do not participate in the formation of pore-filling gel phases [342], [343], [356]. The exact nature of the gel formed in the matrix is also a factor affecting the pore structure of AACs [171], as each individual type of binding gel promotes a unique pore structure [357].

As seen in Fig. 5.18, with continued curing, the total cumulative pore volume of the paste specimens decreases, reflecting the formation of new gel phases filling remnant pores. This is in agreement with studies reporting increasing density with curing age [270], [342], [356], [358].

5.2.3.7 Strength properties

The compressive and flexural strengths of the alkali-activated mortars after curing for 1, 3, 7, and 28 days are presented in Fig. 5.19. Increasing EAFS replacement results in a reduction in the strength properties of AACs, consistent with the differences in microstructural evolution and binder densification observed in the preceding sections.

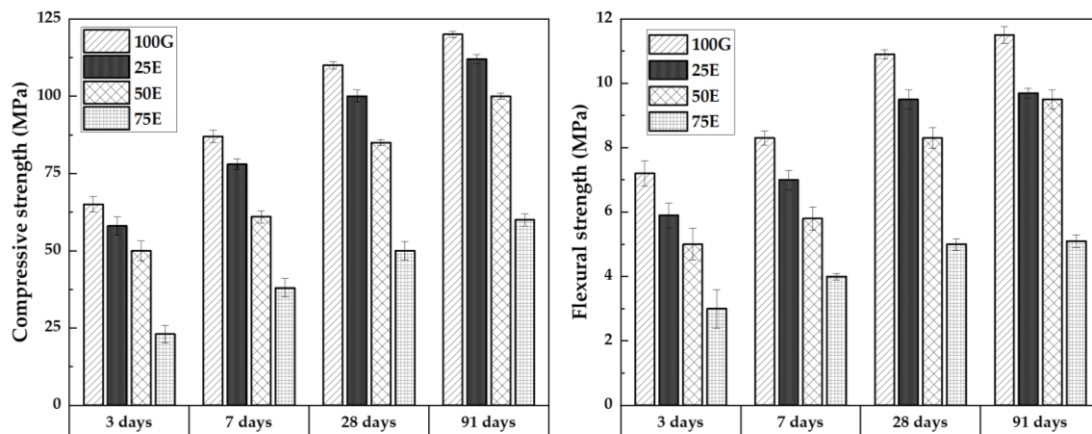


Fig. 5.19: Strength development of alkali-activated mortars based on GGBFS and EAFS: (left) compressive strength and (right) flexural strength. Error bars represent the standard deviation among six replicate specimens (left) and three replicate specimens (right)

This observation also supports the slower structural development seen in the isothermal calorimetry data (Fig. 5.13) for EAFS-containing mixtures. The strength properties of mixtures with up to 50 wt.% EAFS replacements are satisfactory for practical applications. The mixtures with 25 wt.% and 50 wt.% EAFS showed compressive and flexural strengths that were no worse than 30 % below that of 100G.

Therefore, incorporation of up to 50 wt. % EAFS can be achieved without major losses in mechanical properties.

5.2.3.8 Leaching tests

Table 5.9 presents the results obtained by ICP analysis of the leachates collected from monolith immersion tests of 100G and 50E. The results are calculated according to NEN-7345:94 [242] and enables the materials to be classified in categories: C1 when the leaching of potentially hazardous elements is less than the limits specified as U1 for each element respectively, C2 when the leaching is between the levels specified as U1 and U2, and C3 when leaching of one or more elements is greater than U2.

Table 5.9: Results obtained from ICP and calculated following NEN-7345:94 test for samples 100G and 50E, and compared with limit U1

| | As | Ba | Cd | Co | Cr | Cu | Hg | Mo | Ni | Pb | Sb | Se | V | Zn |
|-------------------------------------|------|-----|------|------|------|------|------|------|-----|------|------|------|-----|-----|
| 100G (mg/m ²) | <0.5 | 3.3 | <0.1 | 0.2 | <0.2 | <0.2 | <0.3 | <0.2 | 2.3 | <0.5 | <0.8 | <1.2 | 0.2 | 1.1 |
| 50E (mg/m ²) | <0.5 | 2.1 | <0.1 | <0.1 | <0.2 | <0.2 | <0.3 | 13.6 | 3.3 | <0.5 | <0.8 | <1.2 | 4.0 | 1.4 |
| U1 (mg/m ²) | 40 | 600 | 1 | 25 | 150 | 50 | 0.4 | 15 | 50 | 100 | 3.5 | 3 | 250 | 200 |

All of the values obtained during the leaching tests were below the U1 classification limits for all elements examined, meaning there is no environmental restriction in the usage of these binders according to NEN-7345. Leaching of chromium, which is present in significant quantities in the EAFS, is not detected from the 50E specimen. This confirms the hypothesis that the chromium present in EAFS is stable in the solid spinel phase and satisfactorily immobilised within the alkali-activated binder. The presence of a reducing environment within the binders, due to the presence of sulfide from the GGBFS, is also likely to be beneficial in reducing the leaching of redox-sensitive transition metals [359]. The most problematic heavy metal resulting from the test present in EAFS is molybdenum. The level of 13.6 mg/m² is below U1 in the case of 50E, however, it is possible that this element may prove to be a limiting factor on the use of binders with higher EAFS replacement levels if the U1 value is exceeded

and a C2 classification becomes necessary. However, those samples were not able to be tested for leaching within the scope of the current study.

5.2.4 Conclusions

The use of EAFS in blends with GGBFS for producing alkali-activated slag-based materials has been evaluated via the characterisation of early hydration and fresh, microstructural, and mechanical properties. Based on this analysis the following main conclusions are made:

- 1- Replacing GGBFS with EAFS significantly affects the reaction kinetics, resulting in a significant retarding effect. The dormant period of the heat evolution curve becomes prolonged with higher EAFS replacements, with a suppression in the secondary exothermic peak after dissolution.
- 2- The structural formation of the AACs is retarded with increasing EAFS replacements.
- 3- EAFS improved the workability and setting time of AACs amongst other due to its lower reactivity compared to GGBFS.
- 4- The XRD data indicate that most phases of the EAFS are stable (acting more inert) in alkaline systems, however a small fraction of the EAFS can react to form a weak binding phase as was observed through FTIR and SEM.
- 5- EAFS blending is found to increase the cumulative pore volume of AACs within the range of 6.5 nm to 10 μm , resulting in a more porous structure with coarser pore sizes.
- 6- EAFS replacement gives a general reduction in strength properties, although mortars with up to 50 wt. % EAFS exhibit a satisfactory compressive strength after 28 days of 85 MPa, and corresponding flexural strength of 9.5 MPa.
- 7- Leaching tests highlight this GGBFS/EAFS binder system to be suitable for the immobilisation of heavy metals present within the precursors. All heavy metals detected are well below the U1 limit, meaning that the usage of these binders do not present any environmental restriction (classified as C1). No chromium was detected in the leachates.

5.3 Copper slag (CS) and ternary blends in alkali-activated cements

This section is based on: L. Stefanini, S. Ghorbani, G. De Schutter, S. Matthys, B. Walkley, and J. L. Provis, "Evaluation of copper slag and stainless steel slag as replacements for blast furnace slag in binary and ternary alkali-activated cements," *Journal of Material Science*, vol. 58, no. 31, pp. 12537–12558, 2023, <https://doi:10.1007/s10853-023-08815-7>.

The experimental investigation, data interpretation, and writing of the original draft of this chapter were carried out by L. Stefanini in collaboration with S. Ghorbani, whilst B. Walkley, J. L. Provis G. De Schutter, and S. Matthys provided supervision and revised the draft. Specific tests, such as mini-slump tests, MIP analysis, and compressive and flexural strength testing were conducted at Ghent University by S. Ghorbani.

5.3.1 Introduction

Commonly used alkali-activation precursors such as blast furnace slag and fly ash will soon become less available due to resource competition and may cease to be produced in certain regions. This limitation in future supply is a main driving force for the investigation of alternative precursor sources, such as non-blast furnace slags and non-ferrous slags, to produce alkali-activated binders.

The global production of CS, a smelting by-product from Cu production, is reported to be 46.2 million tonnes in 2018, with 2.20 tonnes of CS produced for every tonne of Cu [94], [103], [360]. Steel slags are also generated in considerable volumes, up to about 300-400 kg of slags for each tonne of stainless steel produced [361], with EAFS being a considerable fraction of this production [362]. EAFS has applications as a road base material [363], [364], as an aggregate in traditional concrete [160], and as a

SCM or filler material for PC blends [365]. EAFS is reported to have a low reactivity and mainly affects workability and setting times, when used in AACs [156], [157], [342]. The use of CS as a SCM and an aggregate for PC has been reported in literature [95], [97], [366], however there is less published work on its use in the production of AACs [104], [360], [367], [368]. Nazer et al [368] reported similar compressive strength values to conventional PC mixtures for a hybrid system including 25 wt. % CS as an SCM, after 91 days. Use of sodium silicate as an activator for CS has been reported to be more effective in terms of strength development compared to sodium hydroxide [360]. Curing CS-based AACs at higher temperatures is also noted to improve the reaction rate of the mixtures [369], [370]. Non-ferrous slags often have high Fe (> 40 wt. %) and Si contents, while inclusion of Ca and Al is generally limited [371]. The amorphous fraction of these non-ferrous slags can be high, depending on cooling conditions after smelting [99], with Fe present in both amorphous and crystalline phases. Crystalline phases containing Fe are usually stable in alkaline media and do not participate in the formation of binding phases [372], whereas amorphous Fe-rich phases may dissolve and have a pronounced effect on the polycondensation reaction [105], [373], [374]. Other vitreous Fe-rich precursors have proven to be suitable for alkali-activation including iron silicate glasses from municipal solid wastes [375], low calcium copper-nickel slags [376], and ferro-nickel slags from electric arc furnaces [211].

The current section investigates the incorporation of CS and EAFS as partial and total replacements for GGBFS in producing AACs. Five binary alkali-activated mixtures with different replacement levels of GGBFS with CS, and three ternary mixtures with both CS and EAFS are activated by a sodium silicate solution. Isothermal calorimetry, setting time, and mini-slump tests are conducted to better understand the fresh-state and early hydration properties. The microstructural development of the resulting alkali-activated binders is characterised using XRD, FTIR, SEM, and MIP techniques. The leaching of heavy metals is also assessed. A hypothesis on the CS inclusions enabling the formation of 'Fe-rich' binding phases together with well-known C-A-S-H gels is proposed.

5.3.2 Materials and methods

Three types of solid precursors were used: GGBFS supplied by Ecocem (Belgium), CS type Koranel 419 supplied by Aurubis Beerse (Belgium), and EAFS type Fillinox 3000 supplied by Orbix (Belgium) to produce AACs. Table 5.10 shows the chemical compositions of the solid precursors identified using XRF. The EAFS used here also contains a high concentration of chromium, well above that which is expected in conventional stainless steel slags [377]. The CS composition is characterised by low CaO content and high Fe₂O₃ content compared to GGBFS.

Table 5.10: Oxide composition (wt. %) of GGBFS, CS, and EAFS as measured with XRF

| Sample | SiO ₂ (%) | CaO (%) | Al ₂ O ₃ (%) | Fe ₂ O ₃ (%) | MgO (%) | SO ₃ (%) | K ₂ O (%) | MnO (%) | Cr ₂ O ₃ (%) | Na ₂ O (%) | ZnO (%) | Others (%) |
|--------|-------------------------|------------|---------------------------------------|---------------------------------------|------------|------------------------|-------------------------|------------|---------------------------------------|--------------------------|------------|---------------|
| GGBFS | 36.4 | 43.5 | 10.7 | 0.3 | 7.0 | 1.4 | - | 0.3 | - | - | - | 0.6 |
| CS | 29.5 | 2.6 | 9.9 | 45.4 | 1.0 | 0.9 | 0.2 | 0.7 | 1.4 | 3.4 | 3.3 | 1.7 |
| EAFS | 28.0 | 44.2 | 6.3 | 2.0 | 4.4 | 0.5 | 0.1 | 2.7 | 9.9 | - | - | 1.9 |

The particle size distributions of the precursor materials are shown in Fig. 5.20.

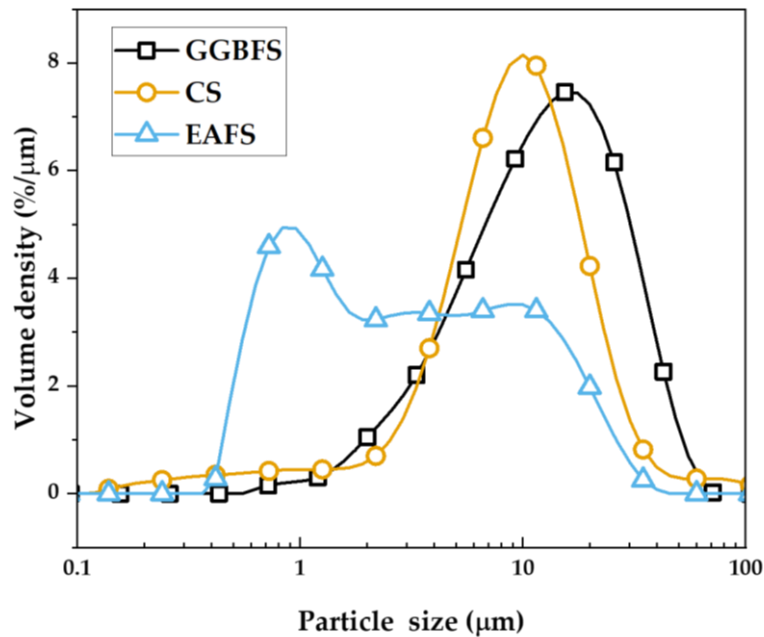


Fig. 5.20: Particle size distributions of GGBFS, CS, and EAFS

The d_{10} , d_{50} and d_{90} values of the solid precursors derived from the particle size distribution curves are given in Table 5.11, along with their measured densities. Both GGBFS and CS materials have similar size distributions with centre at ~ 10 - $11 \mu\text{m}$, whilst EAFS has a multi-modal distribution, centred at $\sim 1 \mu\text{m}$ and $\sim 10 \mu\text{m}$. Inspection of CS and EAFS particles via SEM (Fig. 5.21) shows more regular morphologies compared to the angular-shaped of GGBFS particles.

Table 5.11: Physical properties of solid precursors GGBFS, CS, and EAFS

| Solid precursor | Particle size distribution | | | Specific density g/cm ³ |
|-----------------|----------------------------|----------------------------|----------------------------|---------------------------------------|
| | d_{10} (μm) | d_{50} (μm) | d_{90} (μm) | |
| GGBFS | 1.4 | 8.0 | 23.5 | 2.89 |
| CS | 3.2 | 9.9 | 22.8 | 3.45 |
| EAFS | 0.8 | 3.0 | 15.6 | 3.25 |

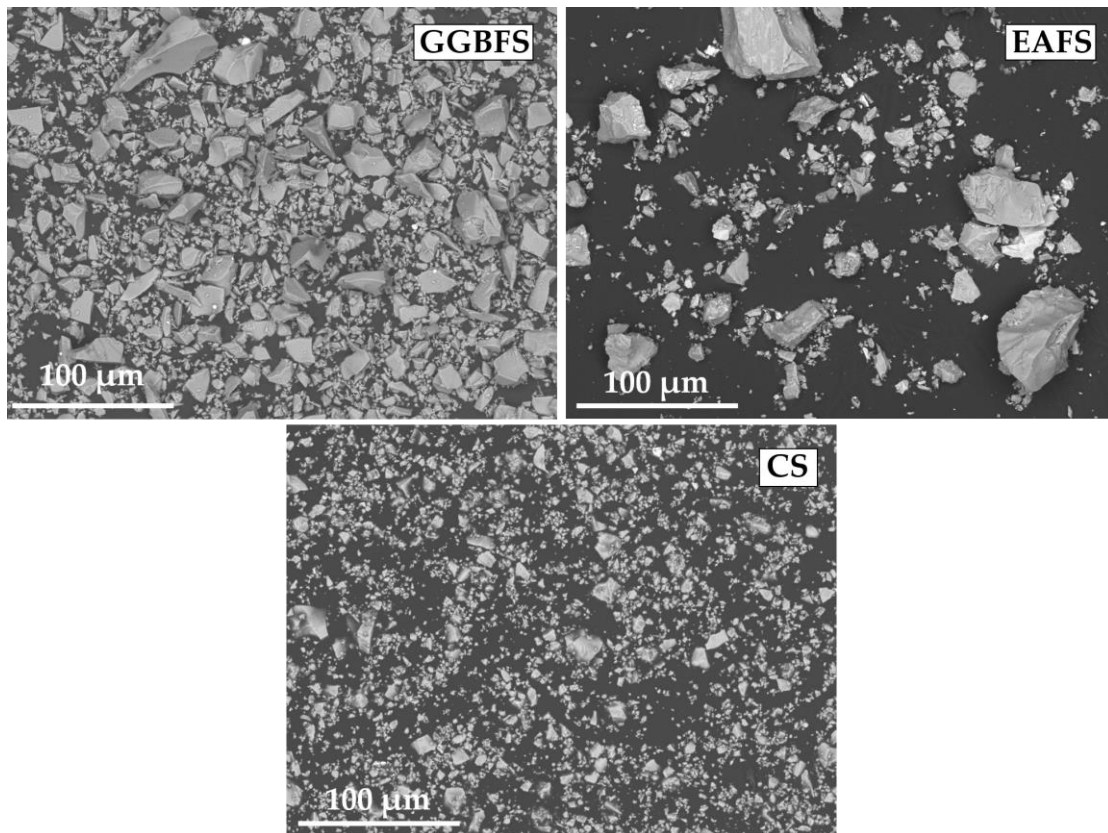


Fig. 5.21: Morphology of solid precursors GGBFS, EAFS, and CS as observed by SEM

Fig. 5.22 shows the XRD patterns of the raw materials. GGBFS and CS are predominantly amorphous, exhibiting a distinctive hump at $\sim 30^\circ 2\theta$.

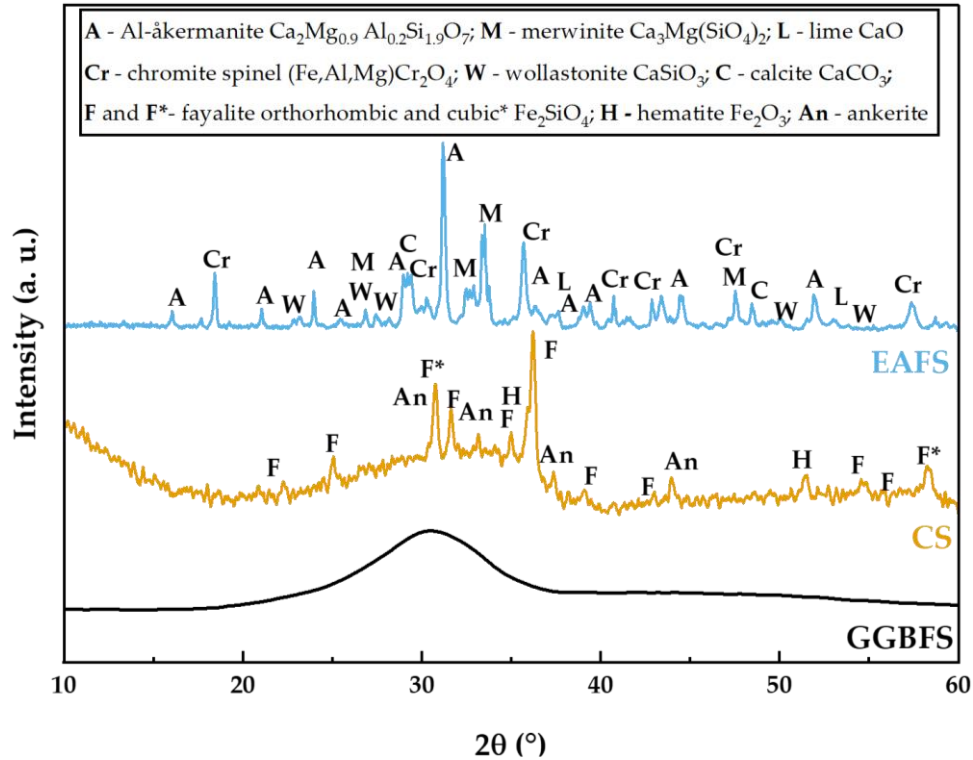


Fig. 5.22: XRD patterns of GGBFS, CS, and EAFS

This hump for CS is broader and is slightly shifted to higher 2θ . Minor crystalline phases are also present, identified as cubic fayalite (Fe_2SiO_4 , PDF #04-017-9804) and orthorhombic fayalite (PDF #00-034-0178), hematite (Fe_2O_3 , PDF #00-056-1302), and ankerite ($\text{Ca}(\text{Fe},\text{Mg},\text{Mn})(\text{CO}_3)_2$, PDF #00-033-0282). The mineral composition defined here is in agreement with several previous studies [101], [103], [360], [378]. The major crystalline phases of EAFS are from the melilite group, mainly åkermanite ($\text{Ca}_2\text{MgSi}_2\text{O}_7$) with a partial Al replacement (åkermanite aluminian, $\text{Ca}_2\text{Mg}_{0.9}\text{Al}_{0.2}\text{Si}_{1.9}\text{O}_7$, PDF# 04-014-4688), and merwinite ($\text{Ca}_3\text{Mg}(\text{SiO}_4)_2$, PDF# 01-086-6219). Minor phases are identified as a mixed spinel phase ($(\text{Fe},\text{Mg},\text{Al})\text{Cr}_2\text{O}_4$ (PDF# 04-016-2691), calcite (CaCO_3 , PDF# 01-086-4272), wollastonite (CaSiO_3 , PDF# 00-027-0088), and traces of free lime (CaO , PDF# 00-037-1497). This EAFS phase assemblage

is consistent with previous studies, albeit highly dependent on the cooling conditions, initial composition, and type of initial scrap used in the EAF, which necessitates a case-by-case study of slag precursors from differing sources. When compared with values presented in literature, the EAFS used in this study has a particularly high chromium content and low Fe content [103], [377], [379].

Fig. 5.23 displays the FTIR spectra of the precursor materials. The GGBFS spectrum shows two major absorption bands between 1000-900 cm^{-1} and at $\sim 500 \text{ cm}^{-1}$ corresponding to Si-O-T (T = tetrahedral Si, Al) asymmetric stretching vibrations (ν_a) and Si-O symmetric stretching vibrations (ν_s), respectively.

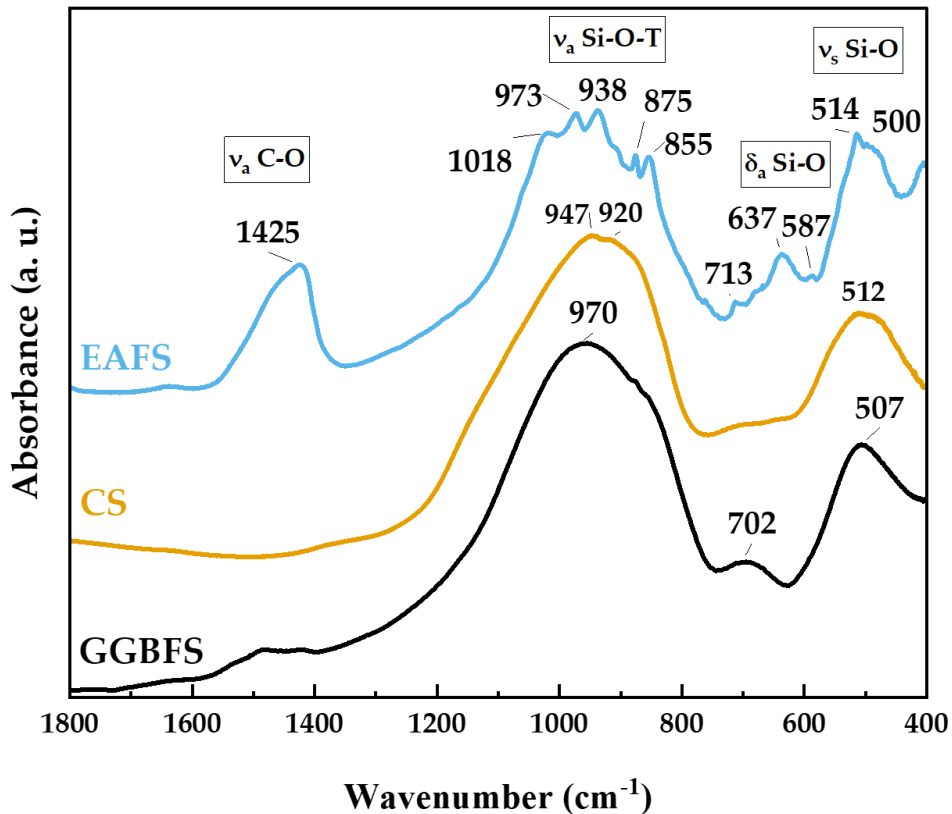


Fig. 5.23: FTIR spectra of the precursors GGBFS, CS, and EAFS

Similar absorption bands at 970-920 cm^{-1} and at $\sim 500 \text{ cm}^{-1}$ are identified in the CS spectrum, in this case the asymmetric stretching vibrations Si-O-T could involve T = Si, Al, and/or Fe^{3+} [380]. The broadness and smoothness of these peaks indicate a

highly amorphous structure consisting predominantly of silicates [381]. The sharper peaks in the CS spectrum at $\sim 947 \text{ cm}^{-1}$ correspond to the vibrational modes of crystalline fayalite [382]. The GGBFS spectrum shows an additional signal at $\sim 700 \text{ cm}^{-1}$, related to symmetric Si-O-Si bond stretching, that is not clearly identified in the CS spectrum. The maximum of the Si-O-T band is located at 970 cm^{-1} for GGBFS and at 947 cm^{-1} for CS. This shift toward lower wavenumbers is indicative of an amorphous network with more highly substituted Si tetrahedra (due to the high Fe^{3+} content) [383].

The EAFS spectrum similarly exhibits these two main bands, between $1000\text{-}900 \text{ cm}^{-1}$ and at $\sim 500 \text{ cm}^{-1}$, corroborating that silicates (calcium silicates with Mg and Al) are the most abundant phases as seen in the XRD in Fig. 5.22. Besides these bands, several well defined and sharp peaks are detected for the crystalline phases present. Peaks at 1425 cm^{-1} , 875 cm^{-1} , 713 cm^{-1} are attributed to calcite, specifically the C-O asymmetric stretching vibration and C-O out-of-plane and in-plane bending [344]. The bands at 638 cm^{-1} and the shoulder at 500 cm^{-1} are due to the Cr(III)-O vibration characteristic of the spinel phase $(\text{Fe, Mg, Al})\text{Cr}_2\text{O}_4$ [345]. The remaining peaks at 1018 cm^{-1} , 973 cm^{-1} , 938 cm^{-1} , 855 cm^{-1} and 587 cm^{-1} are associated with the presence of crystalline åkermanite, merwinite, and wollastonite [346].

The solid precursors (GGBFS, CS, and EAFS) were initially dry mixed for 60 s in a Hobart mixer to homogenise, then sand was added and blended for 60 s into the pre-mixed powders to prepare mortars. The alkali solution was prepared 24 h prior mixing, made of sodium hydroxide, sodium silicate, and water to give a modulus (molar ratio of $\text{SiO}_2/\text{Na}_2\text{O}$ of 1.6, an alkali-dosage (Na_2O wt. %, defined as total mass of Na_2O per 100 g of precursors) of 5.3, and a water binder mass ratio (w/b) = 0.32, where the binder is defined as the sum of the solid precursors plus dissolved solids in the activator. The activator solution was kept constant for all AACs. The precursors and alkaline solution were mixed for 60 s at low speed (140 rpm), then for 90 s at high speed (285 rpm) to achieve a homogeneous mixture. The preparation of pastes followed the same procedure, except for the sand addition. A total of eight

AACs with different replacement levels of GGBFS were produced: five binary mixtures with CS replacement levels of 0 wt.%, 25 wt.%, 50 wt.%, 75 wt.%, 100 wt.%, and three ternary mixtures with 50 wt.% CS, and EAFS inclusions at 15 wt.%, 25 wt.%, and 35 wt.%. The mix proportions of all mixtures, each of which was prepared as paste and mortar specimens, are shown in Table 5.12.

Table 5.12: Mix proportions of the alkali-activated mortars based on GGBFS, CS, and EAFS

| Sample | Precursors (wt. %) | | | Activator solution | | w/b (mass ratio) | Sand in mortars (wt. %) |
|---------|--------------------|-----|------|---|--|---------------------|-------------------------------|
| | GGBFS | CS | EAFS | Modulus (SiO ₂ /Na ₂ O molar ratio) | Alkali-dosage (wt. % Na ₂ O) | | |
| 100G | 100 | 0 | 0 | 1.6 | 5.3 | 0.32 | 275 |
| 25C | 75 | 25 | 0 | 1.6 | 5.3 | 0.32 | 275 |
| 50C | 50 | 50 | 0 | 1.6 | 5.3 | 0.32 | 275 |
| 75C | 25 | 75 | 0 | 1.6 | 5.3 | 0.32 | 275 |
| 50C/15E | 35 | 50 | 15 | 1.6 | 5.3 | 0.32 | 275 |
| 50C/25E | 25 | 50 | 25 | 1.6 | 5.3 | 0.32 | 275 |
| 50C/35E | 15 | 50 | 35 | 1.6 | 5.3 | 0.32 | 275 |
| 100C | 0 | 100 | 0 | 1.6 | 5.3 | 0.32 | 275 |

5.3.3 Results and discussion

5.3.3.1 Isothermal calorimetry

The isothermal calorimetry results for the alkali-activated pastes are shown in Fig. 5.24 (I). The first exothermic peak present for all samples except 100C occurs within the first 3 h of reaction. This initial stage is associated with the wetting and dissolution of solid precursor particles and formation of primary C-A-S-H gels [260], [261]. The 100G sample exhibits the highest intensity for this peak. Specimens with CS inclusion show a decreasing trend in dissolution peak intensity and increasing time delay to its onset. Samples 75C and 50C/25E have similar dissolution peak intensities, however the ternary sample has a delay in the appearance of the dissolution peak, and a convoluted peak shape composed of an initial shoulder peak

merging into a dissolution peak, with a maximum after 1.5 h. Similar behaviour is seen for 50C/35E, which suggests that the origin of the convoluted dissolution peak is due to the differing dissolution rates of GGBFS and EAFS particles in alkaline media, with both of these types of slag showing a notable contribution to the reaction process at early age.

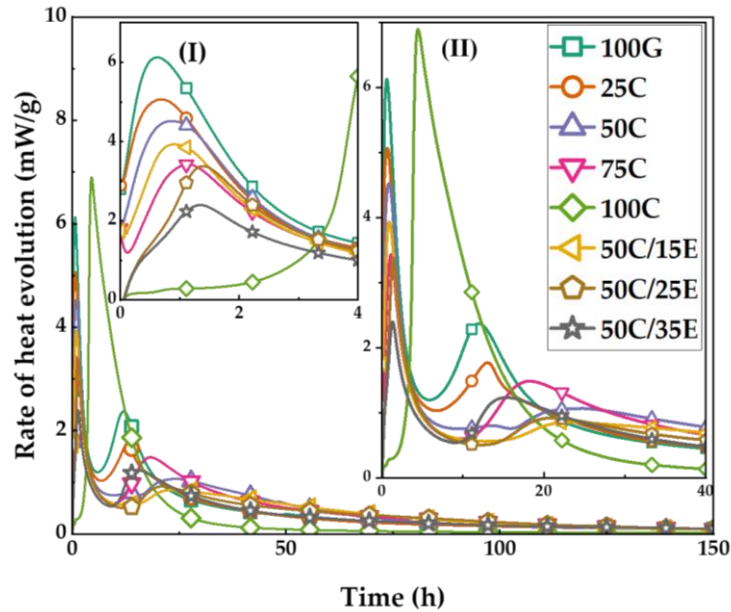


Fig. 5.24: Heat evolution of alkali-activated pastes based on GGBFS, CS, and EAFS at 20 °C

The dissolution peak is followed by a dormant period during which heat release is reduced to a steady state with continuing dissolution [124], [261]. The dormant period is followed by a second exothermic peak Fig. 5.24 (II) which can be fundamentally divided into two segments: acceleration and deceleration. The heat flow signals in both of these segments can also be convoluted in blended binders, resulting in significant peak broadening due to overlapping contributions from individual precursors and their reaction products. The acceleration period is associated with the primary C-A-S-H undergoing precipitation and polymerisation to form a gel structure, while the deceleration period is linked with further gel densification and hardening, and continues until reaching the steady state. This second peak is the most intense in the 100G sample. By comparison, 25C exhibited a delay of 1.3 h, and a 25.7 % reduction in maximum heat flow. Larger GGBFS replacements show a similar reduction in maximum intensity accompanied by peak

broadening. Sample 100C is the exception, exhibiting a delay in dissolution, with no evidence of exothermic activity during the first 3 h. After 3-4 h there is a steep acceleration in the heat release profile of 100C, forming a broad singular peak with a maximum after 4.8 h, and a subsequent deceleration period concluding between 20-30 h. The relatively large peak intensity and delayed onset time in CS-blended binders suggests a distinctly different exothermic behaviour due to the dissolution and reaction of Fe species. Samples with both GGBFS and CS would be expected to have combined calorimetry profiles that consist of both the dissolution and reaction of GGBFS and CS, and any interaction effects between the two materials. This is highlighted in the 50CS mixtures, showing two delayed secondary signals with lower intensity than the 75C mixture, which does not follow the trend based on the higher GGBFS content mixture. The reaction peak in the 75C mixture occurs after a shorter period of time, indicating that CS now dominates the exothermic behaviour, acting to increase the reaction rate. Both 50C and 50C/15E have convoluted signals in which two peaks are distinguishable, indicating that more than one type of exothermic process is taking place. This may be either a delayed dissolution of CS followed by a more conventional polycondensation reaction, or the formation of two distinct gel structures throughout the bulk arising from different gel-forming species, i.e. Ca, Si, Al from GGBFS and Fe, Si, Al from CS. The second peak intensity increases, narrows, and appears earlier in time with further additions of EAFS. This behaviour is unusual for low-reactivity precursor materials and may be explained by the high amount of activator available for the reaction of CS due to the limited content of GGBFS in the systems, rapidly forming gel phases. The subsequent deceleration period is clearly reduced, resulting in quick reaction propagation and hardening of the mixtures.

Fig. 5.25 shows the total cumulative heat profiles of all samples. Two distinct effects can be seen comparing the data of the single precursor mixtures (100G and 100C). The 100C mixture evolves the greatest amount of heat within the first 20 h of reaction followed by a complete cessation of activity thereafter. The 100G mixture shows lower heat evolution after 20 hours, however continues to react up to 150 h, resulting in a greater overall magnitude of heat evolution than the 100C system. Unexpectedly,

the addition of a small amount of GGBFS to a predominately CS system (75C) results in the suppression of early age heat evolution, with continued reactivity seen at later ages, similar to 100G. This could be explained by the GGBFS providing the necessary Ca source for the protracted creation and improvement of the binding phase present in iron silicate systems [105]. Further additions of Ca-rich material decrease the cumulative rate of heat released after 150 hours, suggesting the existence of an optimum in the elemental ratios of the precursors. The inclusion of EAFS into the mixtures manifests mainly as a filler-type effect.

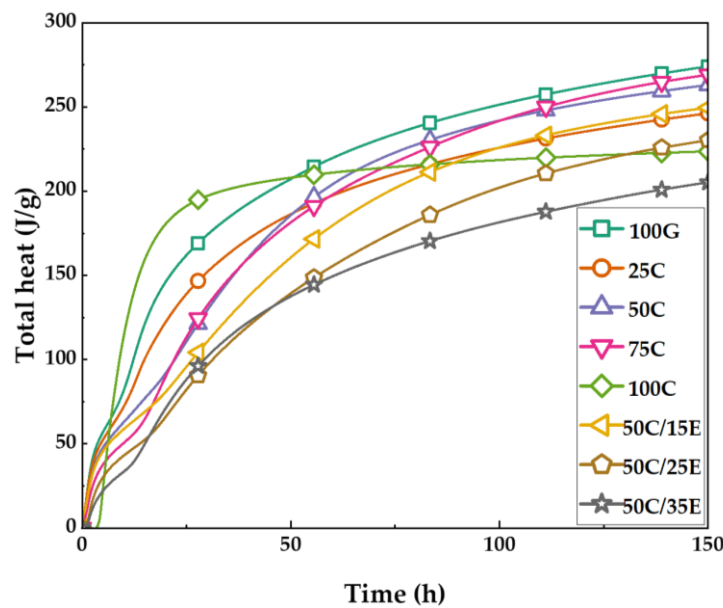


Fig. 5.25: Cumulative heat released by alkali-activated pastes based on GGBFS, CS, and EAFS at 20 °C

5.3.3.2 Mini-slump test and setting times

Fig. 5.26 illustrates the mini-slump test values obtained up to 1 h after mixing, and Vicat initial and final setting time results, for all the alkali-activated pastes investigated. As seen in Fig. 5.26 (a), the solely GGBFS-based mixture has the lowest initial slump flow diameter of 149 mm. All mixtures with CS or EAFS replacements achieve a slump diameter between 153 mm to 185 mm. Additions of both CS and EAFS into GGBFS-based binders have been reported in previous studies to increase the mixture slump [342], [343] despite their small particle sizes (Fig. 5.20).

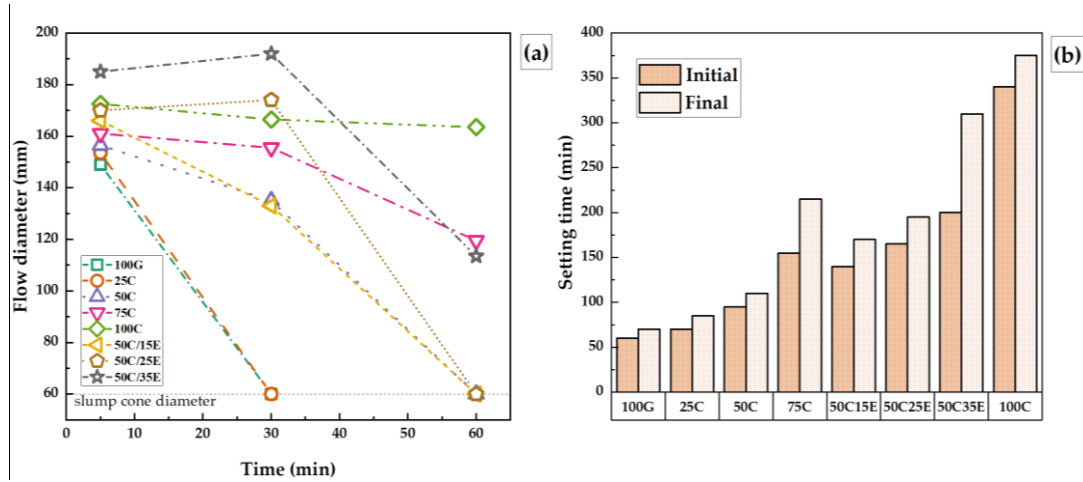


Fig. 5.26: (a) Mini-slump test and (b) setting times results for all alkali-activated pastes based on GGBFS, CS, and EAFS

The general trend in slump values shows an increase with CS inclusion, and when CS is replaced with EAFS, as seen for 50C25E. This is a result of the slow dissolution of CS and low early stage reactivity, as corroborated by the isothermal calorimetry data in Fig. 5.24 where the first exothermic peak occurs after ~ 4 h. Early reactivity of EAFS is even lower due to the large fraction of unreactive minerals present, as shown in Fig. 5.22. Lower angularity of CS and EAFS particles and higher specific density may also increase the slump diameter, considering the higher apparent liquid to solid volume ratio.

After 30 min, the slump values for 100G and 25C mixtures are reduced to a near zero-slump condition, maintaining the cone shape once the mould is removed, suggesting a high early reactivity. For replacement levels of 50 wt.%, and 65 wt.%, (50C and 50C15E) the slump loss is less rapid, but these mixes also reach a zero-slump state at 60 min. For further replacement (75C, 50C25E, and 50C35E) the slump diameter values remain nearly constant during the initial 30 min and decrease only slightly after 1 h. The slump diameter of 100C does not appear to decrease during the first hour of reaction indicating very low early reactivity.

Setting times are reported in Fig. 5.26 (b). Sample 100G begins to set after 60 min, and the completely sets after 70 min, which is considered quick setting. This can be attributed to the high modulus and dosage of the activator solution used in this work. Previous studies have demonstrated that the type and the molar ratio of the activator solution are the main factors that affect the setting time of an AAC [325]. All initial setting times for binary and ternary mixtures vary between 70 min to 200 min, and final setting times between 85 min and 310 min. The progressive inclusion of CS and EAFS results in an increase in the setting time, however sample 75C has a similar initial setting time but a longer setting period than 50C/25E. A divergence in setting period is also seen for 50C/35E. The 100C mixture is the exception, with the setting process starting after 340 min (5.7 h) with a relatively short setting period of 35 min. Overall the setting periods of the binders here are relatively short, indicating the possibility for rapid development of hardened material properties once the point of initial setting has been reached; this is considered a desirable attribute.

A comparison between setting times and heat evolution calorimetric profiles for 100G and 100C mixtures is shown in Fig. 5.27.

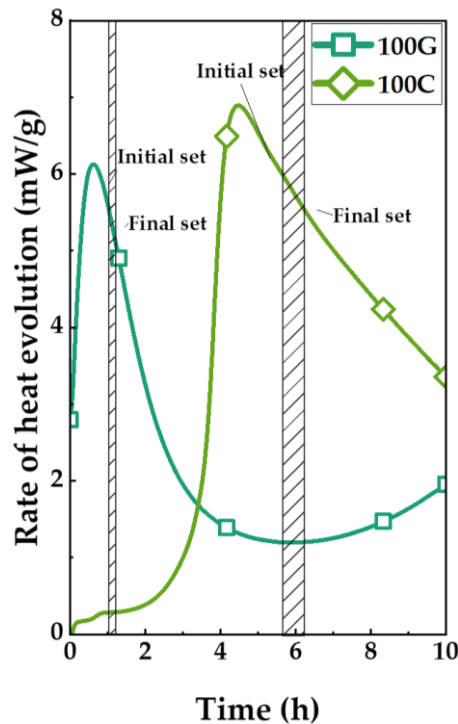


Fig. 5.27: Comparison of setting times and heat evolution profiles for samples 100G and 100C

It can be seen that the setting process starts shortly after the beginning of the deceleration stage of the dissolution peak for 100G. Similarly, for alkali-activated CS the setting process can be seen to coincide with the single peak in the calorimetric profile. The acceleration period may be associated with the delayed dissolution of CS particles. The setting process starts 1 h after the beginning of the deceleration stage, indicating that dissolution, setting, and gel formation and propagation take place sequentially.

5.3.3.3 X-ray diffraction

Fig. 5.28 shows the XRD patterns for 100G, 50C, 50G/15E, and 100C mixtures obtained after 2 days, 28 days, and 91 days of curing.

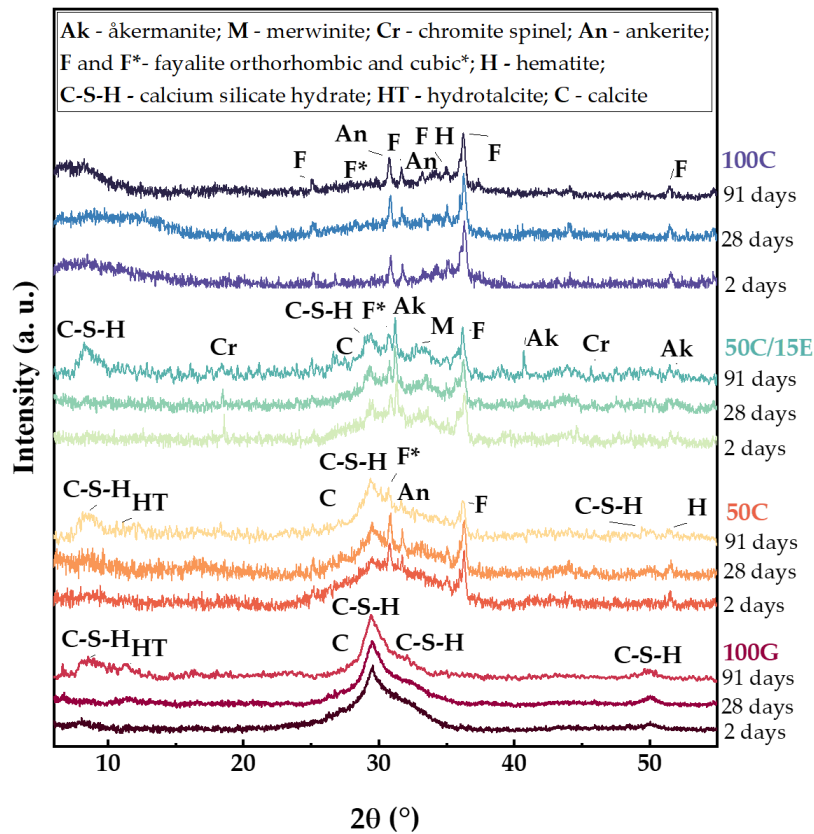


Fig. 5.28: XRD patterns of alkali-activated pastes based on GGBFS, CS, and EAFS after 2 days, 28 days, and 91 days. Note that the phases marked as “CSH” will contain alumina and thus are more precisely described as C-A-S-H, but a more concise form of the notation is used in the graphics

The pattern for alkali-activated GGBFS (100G) shows distinct diffuse peaks (also called “amorphous humps”), between $25\text{--}35^\circ 2\theta$ and at $\sim 50^\circ 2\theta$, indicative of C-A-S-H gel formation [15]. The only crystalline feature seen above the first diffuse peak at $\sim 29^\circ 2\theta$ is identified as calcite, which is a common surface carbonation product. The main time-dependent phase evolution concerns the degree of C-A-S-H formation, with a narrowing of the diffuse peak indicating increased short range ordering, reflecting a higher degree of polymerisation of the gel phase [280]. The presence of hydrotalcite-group phases (HT, approximately $\text{Mg}_4\text{Al}_2(\text{CO}_3)(\text{OH})_{12}\cdot 3\text{H}_2\text{O}$ resembling the mineral quintinite, PDF#01-089-0460), which are expected to form from the dissolution of the large Mg component of GGBFS [285], [328], are not detected in the XRD patterns for specimens cured for less than 28 days. The appearance of a hump at $\sim 12^\circ 2\theta$ in the 100G specimen demonstrates low levels of hydrotalcite formation that can be detected only after 28 days. The broad peak suggests only very small (nanoscale) ordered crystallites of hydrotalcite phases are present [328], [384]. Such slow growth of ordered hydrotalcite structures are attributed to the use of high molar ratio activators (high Si content) which readily form concentrated regions of C-A-S-H gels hindering any further mobility of readily dissolved species, in this case Al, necessary for hydrotalcite formation. This behaviour is also confirmed by the 90-day pattern which shows an identifiable hydrotalcite peak. XRD patterns for 50C show similar trends of calcite and C-A-S-H gel formation, but the further development of these phases is limited after 2 days, and significant hydrotalcite is present only after curing for 91 days. Identification of the narrow intense peaks, originating from the inclusion of CS, found satisfactory agreement with references for the minerals fayalite, ankerite, and hematite. It is believed that these crystalline phases remain stable and do not contribute to the formation of binding phases [385], [386]. The ternary binder 50C/15E, as well as containing the main minerals of CS, also includes the crystalline phases present in EAFS: åkermanite, merwinite and chromite spinel as discussed above, whereas hydrotalcite is not identified due to the limited content of GGBFS in the mixture. EAFS phases also have very low reactivity in alkaline media, as discussed in section 5.2 [342]. Further increasing CS addition results in a suppression in the intensity of

the C-A-S-H hump, indicating a pronounced effect on the overall quantity of C-A-S-H gel formation. This decrease in C-A-S-H gel formation can be attributed to the decrease in readily available Ca within the system, as is noted in the 100C mixture.

5.3.3.4 *Fourier-transform infrared spectroscopy*

The FTIR spectra were recorded after 2 days and 28 days, as presented in Fig. 5.29.

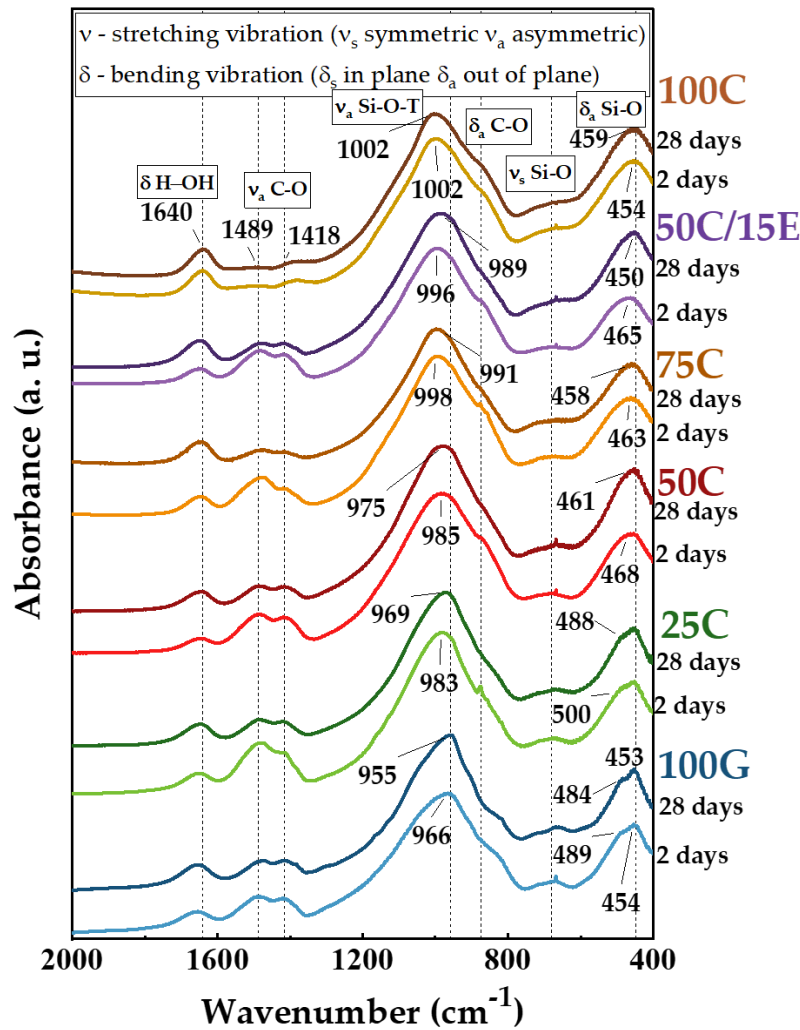


Fig. 5.29: FTIR spectra of AACs based on GGBFS, CS, and EAFS after 2 days and 28 days

The main bands exhibited after alkali-activation are at 1640 cm⁻¹, attributed to O-H bending vibrations. This band is characteristic of weakly adsorbed water molecules captured in remnant bulk porosity or on the surface of the alkali-activated samples,

and can be associated with the presence of products of hydration, i.e. C-A-S-H gels [333], [381]. The peaks at 1489 cm^{-1} and 1418 cm^{-1} correspond to the stretching vibration of O=C=O bonds of the carbonate group (CO_3^{2-}) for poorly crystalline vaterite, aragonite, and/or calcite [330], [331]; calcite was initially present only in EAFS (Fig. 5.22). The appearance of these bands for partially ordered carbonates is due to the reaction between atmospheric carbon dioxide and the surface of the binders. The contribution of carbonation is larger at early ages (2 days of curing), with decreasing band intensity after 28 days. The suppression of these bands in the 100C sample can be explained by the very low Ca content present, allowing for only limited carbonation to occur. The main band located at $1200\text{--}800\text{ cm}^{-1}$ (asymmetric stretching vibrations of Si-O-(Si,Al) bonds) is associated with the degree of polycondensation and resulting formation of silicate gels [67], [387], [388]. This band for the 100G mixture shows a shift to lower wavenumbers with respect to the solid precursors, from 970 cm^{-1} to 966 cm^{-1} after 2 days, and to 955 cm^{-1} after 28 days. This trend is reported in literature to arise from the increased incorporation of Al species, and consequently an increased contribution from Al-O-Si linkages [280]. This peak becomes distinctively narrower and sharper with increasing the curing time, which indicates an increasing degree of polycondensation [280]. Conversely, all other mixtures show a shift towards higher wavenumbers with respect to both the precursors, in accordance with previous literature on CS behaviour [104]–[106], [382]. This is due to the combined effect of increasing silicate content in the gel, and may also related to the oxidation of Fe present in the CS from Fe^{2+} to Fe^{3+} [106], [373]. For increasing CS replacement, the curing time decreases the magnitude of the band shift; between 2 days and 28 days the gap is reduced from 983 cm^{-1} to 969 cm^{-1} for 25C, from 985 cm^{-1} to 975 cm^{-1} for 50C, and from 998 cm^{-1} to 991 cm^{-1} for 75C as the incorporation of Al^{3+} or Fe^{3+} into the gel proceeds. This shift is accompanied by a narrowing/sharpening of the band for 25C mixture, suggesting a higher degree of polymerisation in the gel, whilst a less marked impact can be observed for 50C and 75C mixtures. For the 50C15E specimen, the Si-O stretching vibration also moves toward lower wavenumbers (996 cm^{-1} to 989 cm^{-1}), similarly to 75C, whereas the stretching band for the 100C mixture has already reached its final wavenumber after

2 days of curing with no apparent shift seen between 2 days and 28 days. This suggests a very low rate of ongoing reaction in 100C, with the broad Si-O stretching band centred around 1002 cm^{-1} , in agreement with the calorimetric data (section 5.3.3.1) highlighting activity before 48 h reaching a steady state, with no subsequent strength development noted after the one-day test. The Si-O bending band, at $500\text{-}512\text{ cm}^{-1}$, shifts toward lower wavenumbers with respect to the precursors (Fig. 5.23) after the alkali-activation for all samples, further indicating the network developing through Al and Fe incorporation [389].

5.3.3.5 Scanning electron microscopy

BSE images of AACs at 2 days and 28 days of curing are displayed in Fig. 5.30.

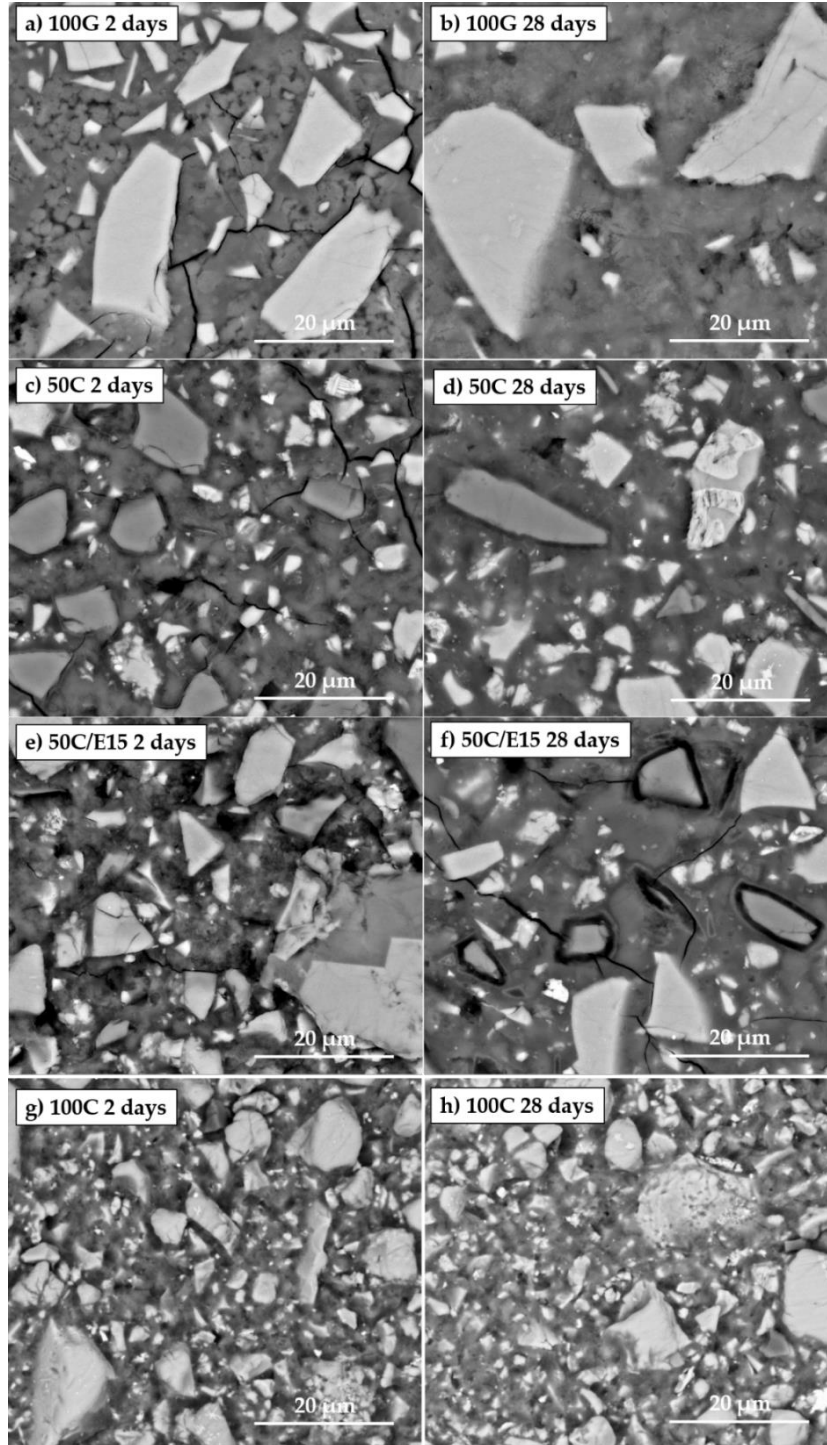


Fig. 5.30: BSE images of samples 100G, 50C, 50C/15E, and 100C after 2 days and 28 days of curing

Several distinctive microstructural features are seen in the 100G 2-day sample (Fig. 5.30 (a)), including large unreacted and/or partially reacted GGBFS particles (light grey) surrounded by a heterogeneous matrix of smaller dissolving GGBFS particles, an initial binder phase (grey), and darker regions identified as porosity. The 100G 28-day specimen (Fig. 5.30 (b)) consists of a highly homogenous dense matrix resulting from the further dissolution of small GGBFS particles and a consequently increased fraction of binding phase present. Large unreacted GGBFS particles persist throughout the matrix.

In the 50C 2-day sample (Fig. 5.30 (c)), we can identify large GGBFS particles and CS particles (white) surrounded by a heterogeneous matrix. There is a clear difference in particle size distribution between the residual GGBFS and CS, linked in part to the high reactivity of small GGBFS particles in forming the initial matrix phase. The contribution of the CS seems to be limited, by comparison of the 2-day and 28-day microstructures. The 50C 28-day microstructure (Fig. 5.30 (d)) shows progressive densification, generating a more compact and homogenous binder with remnant unreacted GGBFS and CS particles. 50C/15E, in addition to the GGBFS and CS particles, also contains large residual particles of EAFS.

The structural evolution and the increase of matrix gel fraction are also considerable when comparing 50C/15E at 2 days and 28 days in Fig. 5.30 (e) and (f), however, some newly formed macropores are noted after 28 days. Even though the porosity is on a much larger length scale, beyond the scope of MIP analysis (see section 5.3.3.6), the effect can be attributed to the high content of stable minerals. The differences between 2-day and 28-day 100C microstructures (Fig. 5.30 (e) and (f)) appears to be minimal. There exists a binding phase, albeit much lower in extent than the specimens with GGBFS, surrounded by unreacted CS particles. The lack of microstructural evolution regarding the dissolution of CS particles between 2 days and 28 days agrees with all data presented.

Evolutions in the chemical composition of alkali-activated specimens 100G, 50C, and 100C with increasing curing time from 2 days to 28 days as analysed by SEM-EDS

are reported in Fig. 5.31, along with the elemental composition of precursors materials, GGBFS and CS. For each sample, ten EDS point scans are taken in homogeneous regions of the bulk to be representative of the gel.

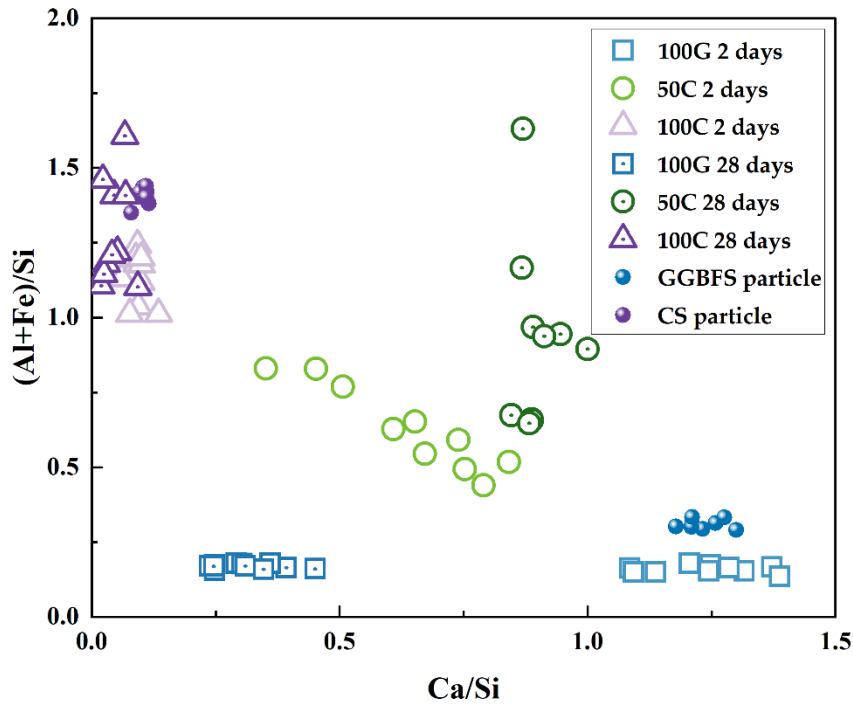


Fig. 5.31: Plot of $(Al+Fe)/Si$ vs Ca/Si mass ratios obtained from EDS analysis of distinctive matrix regions for samples 100G, 50C, and 100C after 2 days and 28 days, along with precursors, GGBFS and CS

The Ca/Si versus $(Al+Fe)/Si$ atomic ratio is identified for each point. 100G after 2 days has Ca/Si ratio in the same range as the raw GGBFS whilst the Al/Si ratio ($Fe \sim 0$ in this sample) is slightly inferior as should be expected with the initial inclusion of Si from the activator. With increased curing time, the Ca/Si ratio shifts towards lower values, caused by the slower dissolution of Si and delayed incorporation of Si in C-A-S-H gels. For both curing times the EDS points are quite clustered together, meaning high consistency in the binder phase.

EDS points describing 50C have a wider spread in their distribution, due to the higher complexity of the system. An increase in both Ca/Si and $(Al+Fe)/Si$ ratios could be possibly identified. This could be due to a delayed incorporation of Fe which

is slowly released by CS. 100C shows minimal change in elemental composition with increase curing time. A minor shift could be identified from raw CS towards lower values of $(Al+Fe)/Si$ ratio, as the Si from the activator becomes included in the gel, followed by a small growth after 28 days, which might be due to subsequent incorporation of Al and Fe.

5.3.3.6 Mercury intrusion porosimetry

Fig. 5.32 illustrates the pore size distributions of the mixtures after 2 days and 28 days of curing. The pore sizes of AACs can be classified as follows: gel pores in the range of 10 to 50 nm, capillary pores between 50 nm to 10 μm , and air voids (which were the pores visible by SEM in section 5.3.3.5) over 10 μm [300]. The dominant type of porosity appears to be in the gel pore range for all AACs. No capillary pores are detected except for sample 50C/35E after 28 days, which exhibits a limited amount of pores ~ 300 nm in size, and 100C with pore sizes around 1 μm .

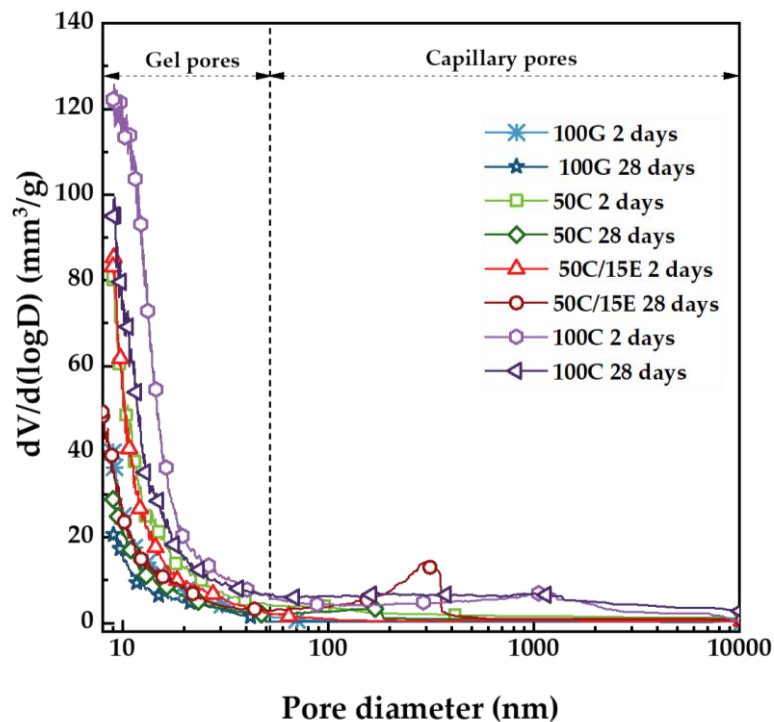


Fig. 5.32: Differential porosity of alkali-activated pastes based on GGBFS, CS, and EAFS after 2 days and 28 days of curing

The total porosities of the AACs calculated from MIP data are given in Table 5.13. For all paste specimens, the total porosity decreases as the curing age continues. This is indicative of densification of the specimens through a gradual reduction of gel pores as new gel phases form [270], [342], [356], [358].

The inclusion of CS results in an initial increase in total porosity after 2 days, as seen for 50C when compared to 100G. After 28 days the total porosity of 50C is reduced by more than 50 %. The inclusion of EAFS appears to be initially beneficial in reducing initial porosity, most likely due to improved particle packing from the differences in precursor particle size distributions [390]. After 28 days the reduction in total porosity of 50C15E is minimal, this is because despite the reduction in gel porosity, a new type of pores has formed in the macro-pore region, as can be seen in Fig. 5.32, denoting a lower degree of structural evolution. This is also associated with the increased content of stable mineral phases in the EAFS that do not take part in any pore-filling reaction [157], [342], [356]. Mix 100C has the highest total porosity, and very little reduction (~ 2 %) is obtained with increasing curing times.

Table 5.13: Total porosity of alkali-activated pastes based on GGBFS, CS, and EAFS, measured by MIP after 2 and 28 days of curing

| Mixture | Total porosity (vol. %) | |
|---------|-------------------------|---------|
| | 2 days | 28 days |
| 100G | 2.55 | 1.75 |
| 50C | 5.95 | 2.80 |
| 50C/15E | 4.95 | 4.00 |
| 100C | 10.90 | 9.00 |

The increase in porosity when replacing GGBFS by other less-reactive slags may also depend on the nature of the gel type [171]. Each individual type of binding gel promotes a distinctive pore structure [357], specifically the main reaction product of GGBFS is C-A-S-H gel, whereas alkali-activated CS forms a low-Ca, Fe-rich aluminosilicate gel [104] which may not be as dense as conventional C-A-S-H gels [391].

5.3.3.7 Strength properties

Fig. 5.33 shows the compressive and flexural strength developed by alkali-activated mortars after 1 days, 3 days, 7 days, and 28 days. Replacing GGBFS with CS and EAFS resulted in an overall reduction of compressive and flexural strength, depending on the degree of replacement. This apparent strength loss is more noticeable when comparing the 1-day specimens, with the difference between 100G and 50C being a reduction by approximately 50 %. This effect has been generally explained in the previous sections by the limited structural evolution and slower kinetics/reactivity of CS and EAFS, compared to GGBFS, during alkali-activation. From the calorimetry data discussed previously (Fig. 5.24), the greater release of heat for the 100G mixture at early ages compared to CS mixtures suggests a more rapid degree of polycondensation and formation of strength-giving phases, hence the large difference in strength properties. The difference in mechanical properties between specimens 100G and 50C becomes minor at later ages, with only a 9 % strength loss in compression and 14 % loss in flexural strength after 28 days of curing even at the high degree of GGBFS replacement used in 50C, suggesting that binders of comparable quality can be produced with 50 % (or maybe further) replacement of GGBFS by alternative slags.

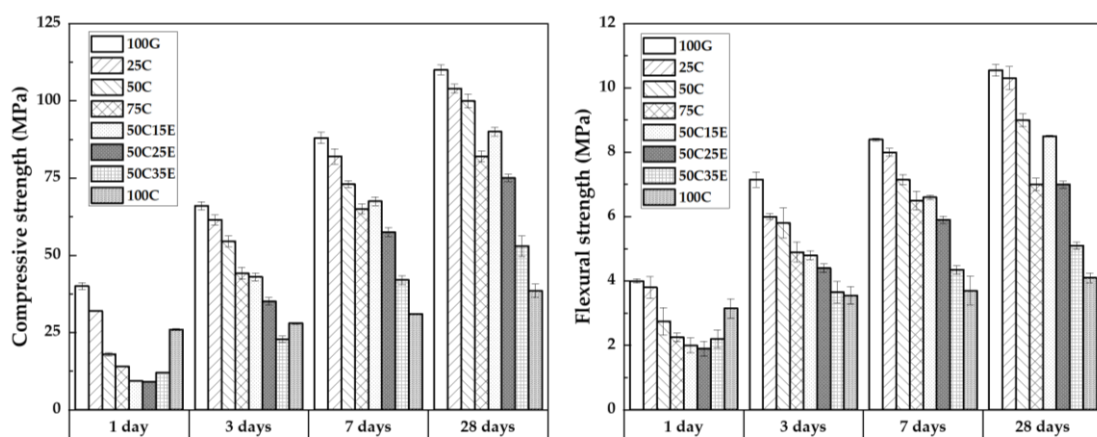


Fig. 5.33: Strength development of alkali-activated mortars based on GGBFS, CS, and EAFS: (left) compressive strength and (right) flexural strength. Error bars represent the standard deviation among six replicate specimens (left) and three replicate specimens (right)

It is interesting to note that between the ternary samples, 50C/35E has the highest 1-day strength, but it reaches the lowest 28-day strength. This can be the result of the high amount of available activator for GGBFS to promptly and fully react during the early stages, followed by a deceleration of the reaction, leading to a lower eventual strength development. This is in agreement with the calorimetry data, and the behaviour is typically seen for filler materials of small particle size as EAFS which allow high availability of activator in the system and additional surface area for the nucleation of hydration products at early ages [296]. Although reaching the lowest strength values among the blended binders after 28 days, 50C/35E still passes 50 MPa in compression and 5 MPa in bending, meaning that it has more than sufficient strength for a wide range of potential practical applications.

The 100C sample shows a remarkable early-age compressive strength of over 20 MPa after 1 day, arising from the formation of strength phases during the first 24 h. This result agrees with the exothermic peak developed within 24 h of reaction seen in the calorimetry data (Fig. 5.24), that is believed to be due to both dissolution of the precursors in an activator-rich environment, and the generation of a binding phase composed primarily of $\text{CaO-FeO-Al}_2\text{O}_3\text{-SiO}_2$ derived from the elements present in the CS. In contrast to GGBFS-based mixtures, the increase in strength after 1 day is near-negligible. This is likely due to the low continuing availability of Ca, resulting in limited C-A-S-H gel formation [392]. Similar findings were reported by Siakati et al. [392], where mixtures at low CaO/FeO molar ratios exhibited a larger extent of reactivity at early age, followed by minimal improvements of mechanical strength over time. Increasing the CaO/FeO ratio was found to inhibit reactivity at early ages, while further improving late age properties through the incorporation of Ca into an iron-phyllosilicate type structure.

5.3.3.8 Leaching tests

Leaching of heavy metals from monolithic specimens was evaluated through ICP analysis of leachates, and the results for samples 100G, 50C, 50C/15E are presented in Table 5.14. The leaching values for each element are calculated following NEN-

7345:94 and each element is categorised as follows: class C1 if the leaching potential of all hazardous elements is below the threshold value specified as U1; class C2 if the leaching value of one or more hazardous elements falls between the threshold values specified as U1 and U2; class C3 when the leaching of any element is above the limit U2.

Table 5.14: Results obtained from ICP and calculated following NEN-7345:94 test [242] for samples 100G and 50C, and 50C/50E, and comparison with limits U1 and U2. Values above these limits are underlined in the table

| Sample (mg/m ²) | As | Ba | Cd | Co | Cr | Cu | Hg | Mo | Ni | Pb | Sb | Se | V | Zn |
|--------------------------------|------|-------|------|-----|------|-------------|------|--------------|-----|------|------|------|------|-------|
| 100G | <0.5 | 3.3 | <0.1 | 0.2 | <0.2 | <0.2 | <0.3 | <0.2 | 2.3 | <0.5 | <0.8 | <1.2 | 0.2 | 1.1 |
| 50C | <0.5 | 0.8 | <0.1 | 1.3 | 0.7 | <u>57.6</u> | <0.3 | <u>120.6</u> | 2.7 | <0.5 | <0.8 | <1.2 | 0.4 | 109.4 |
| 50C/15E | <0.5 | 0.3 | <0.1 | 1.4 | 0.7 | <u>62.2</u> | <0.3 | <u>131.1</u> | 4.2 | <0.5 | <0.8 | <1.2 | 1.5 | 89.3 |
| U1 | 40 | 600 | 1 | 25 | 150 | 50 | 0.4 | 15 | 50 | 100 | 3.5 | 3 | 250 | 200 |
| U2 | 300 | 45000 | 7.5 | 200 | 950 | 350 | 3 | 95 | 350 | 800 | 25 | 20 | 1500 | 1500 |

Sample 100G can be classified as C1 as all of the leaching values obtained are below the U1 limits, meaning that there are no environmental restrictions in the usage of this mixture according to NEN-7345. However, both samples 50C and 50C/15E, containing 50 wt.% CS, have two problematic elements: Cu which in both cases falls into class C2, and Mo which is above the U2 limit and thus places the material into C3, meaning that these binders can have only limited utilisation as construction materials. From the previous section 5.2 we can deduce that both Cu and Mo are leaching from CS only, as blends containing EAFS did not show any issue. Comparing the two binders it can be observed that a higher amount of hazardous elements is immobilised for higher contents of GGBFS, e.g. sample 50G over 50G/15E. It is possible to assume that a modest reduction of CS content in a mixture, in favour of GGBFS, would generate a binder which complies with the standard values by falling within classes C1 or C2. This is also due to the highly reducing environment provided by the sulfide content in GGBFS, known to be beneficial in the reduction of leaching of redox-sensitive transition metals [359]. The test has been performed on

pastes, and it is also possible that a different outcome might be obtained from studies at a concrete level due to the dilution effect of the aggregates.

5.3.4 Conclusions

In this study, the properties of alkali-activated pastes based on CS and EAFSS as partial and total replacements for GGBFS have been investigated.

The findings show that alkali activation of solely CS-based and GGBFS-based mixes result in contrasting calorimetry profiles. Alkali-activated CS exhibits a broad intense heat release peak followed by negligible heat evolution increase, whilst GGBFS-based samples exhibit dissolution and reaction peaks. CS addition result in increased dormant periods and reduced peak intensities. EAFSS acts as a filler, enhancing activator availability per unit mass and reducing dormant periods of ternary mixtures. Both workability and setting times increase with replacement of GGBFS due to the better retention of workability properties promoted by the low early reactivity and dissolution of CS particles, and the stability of mineral phases of EAFSS. XRD analysis reveals that alkali activation of GGBFS generates C-A-S-H gel, disordered hydrotalcite, and calcite, whilst increasing CS replacements their formation is reduced and not detectable for 100 wt. % CS paste in which the calcium content is too low. The crystalline phases of CS and EAFSS remain stable throughout alkali-activation. FTIR spectra of CS-based samples indicates shifts that may be related to the oxidation of Fe^{2+} to Fe^{3+} . All samples show increased incorporation of Al^{3+} or Fe^{3+} over time, except 100% CS which shows minimal change between 2- and 28-day spectra. SEM analysis reveals matrix densification over time, except for alkali-activated 100 wt. % CS. Total porosity initially increases with 50 wt. % CS addition, but after 28 days, the difference from 100 wt. % GGBFS-AAM is minimal. Ternary blends with CS and EAFSS have lower initial porosity than binary blends due to improved particle packing, but develop macroporosity after 28 days due to coarse crystalline phases. Mechanical properties decrease when replacing GGBFS with CS, but the difference diminishes with time. After 28 days, compressive and flexural strength values reach 53 MPa and 5.1 MPa for a sample based on only 15 wt. % GGBFS in a

ternary blend, and 38 MPa and 4.10 MPa for 100 wt. % CS, suggesting that CS is a potential alternative precursor to GGBFS. Leaching tests identify Cu and Mo as problematic elements associated with CS use, potentially limiting GGBFS replacement levels by CS.

Overall, CS can be a suitable precursor in alkali-activation and replacement for GGBFS, whereas EAFSS has proven to be an adequate filler material. The proven reactivity of CS in alkali-activation, as seen in this work and other reported studies on CS, provide a foundation for CS to be utilised as a more sustainable alternative to traditional binders. This study considered the fresh, microstructural and strength properties of CS and ternary binders. Further work is required to characterise other important properties such as durability and late age performance, along with additional investigation on the effects of leaching in mortars and concretes containing CS. This is necessary to ascertain a maximum CS inclusion level that avoids significant leaching of Mo and Cu that would limit the application of CS. The outcomes of this research may further guide sustainable construction practices.

Chapter 6.

Hybrid Binders with Calcium Aluminate Cements (CAC)

This section is based on: L. Stefanini, B. Walkley, and J. L. Provis, "Investigating the retarding effect of CAC in alkali-activated cements," *Frontiers in Materials*, vol. 10. 2023, doi: <https://doi.org/10.3389/fmats.2023.1212177>.

The experimental investigation, data interpretation, and writing of the original draft of this chapter were carried out by L. Stefanini, whilst B. Walkley and J. L. Provis supervised the work and revised the draft.

6.1 Introduction

The Al contained in C-A-S-H and N-A-S-H gels plays a fundamental role in the initial stages of gel formation by increasing the crosslinking of the binding phase [292], [393]. The presence of reactive Al in precursor materials is a requirement to obtain a well-behaving and water-insoluble AAC, driving further investigation into a wide range of reactive Al sources [292], [393]. The need for certain proportions of reactive silica and alumina, essential in designing binders with optimised properties [394], [395], is why CAC appears to offer potential as a reactive Al-rich component for improving alkali-activated formulations by enhancing the reactivity of the mixtures.

Besides the potential as source of reactive alumina, hybrid cements have been shown to enhance binding systems [183], especially providing improved early age properties [184]. PC [180], portlandite ($\text{Ca}(\text{OH})_2$), and CaO can be successfully used as additives in alkali-activation to improve binder properties, including compressive and flexural strength and early age behaviour, whilst allowing a reduction of the

liquid activator concentration as their dissolution increases the pH of the system [179], [185]. As discussed in section 2.4.3.2, there exists several studies on the use of CAC to produce hybrid binders, however the research is not fully exhaustive.

For all these reasons, the focus of the present work is on the development of hybrid systems based on GGBFS and CAC, using sodium silicate activating solutions with varying $\text{SiO}_2/\text{Na}_2\text{O}$ molar ratio, and NaOH as activating solutions. The mechanical properties of the binders are tested with respect to criteria including setting time, workability, and compressive strength, along with microstructural analysis carried out using XRD, FTIR, and SEM-EDS. The results are used to formulate a hypothesis on the underlying reaction mechanisms occurring during the alkali-activation of these blended systems and to evaluate the contribution of CAC as source of additional reactive Al during alkali-activation.

6.2 Materials and methods

A commercial CAC, Secar 51 (containing 51 wt. % alumina) from Imerys (France) and GGBFS from Ecocem (Belgium) were utilised in this section. The physical properties such as densities and d_{10} , d_{50} and d_{90} values for the precursor materials are shown in Table 6.1, whilst the particle distribution curves are illustrated in Fig. 6.1. The chemical compositions of both CAC and GGBFS, are presented in Table 6.2.

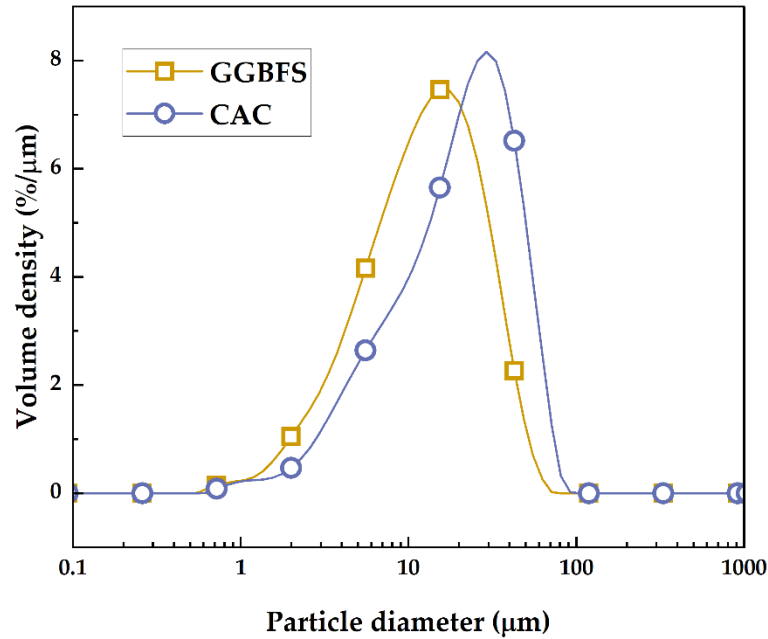


Fig. 6.1: Particle size distribution of GGBFS and CAC

Table 6.1: Density and particle size analysis of GGBFS and CAC

| Sample | Density (g/cm ³) | Particle size analysis (μm) | | |
|--------|---------------------------------|-----------------------------|-----------------|-----------------|
| | | d ₁₀ | d ₅₀ | d ₉₀ |
| GGBFS | 2.9 | 3.8 | 12.7 | 31.0 |
| CAC | 3.0 | 4.6 | 18.7 | 44.8 |

Table 6.2: Oxide composition (wt. %) of GGBFS and CAC as measured with XRF

| Sample | CaO (%) | SiO ₂ (%) | Al ₂ O ₃ (%) | MgO (%) | SO ₃ (%) | TiO ₂ (%) | Fe ₂ O ₃ (%) | MnO 2 (%) | K ₂ O (%) | Na ₂ O (%) | Other (%) |
|--------|------------|-------------------------|---------------------------------------|------------|------------------------|-------------------------|---------------------------------------|--------------|-------------------------|--------------------------|--------------|
| GGBFS | 43.5 | 36.4 | 10.5 | 7.0 | 1.4 | 0.5 | 0.3 | 0.3 | - | - | 0.2 |
| CAC | 38.4 | 4.8 | 50.8 | - | - | 2.0 | 1.8 | - | 0.3 | 0.2 | 1.7 |

Fig. 6.2 presents the XRD patterns of precursors. GGBFS pattern is determined to be predominantly amorphous, exhibiting a very broad peak centred at $\sim 29^\circ 2\theta$. The crystalline phases identified in CAC are monocalcium aluminate ($\text{CaO}\cdot\text{Al}_2\text{O}_3$ or CA, PDF#04-013-0779), gehlenite ($2\text{CaO}\cdot\text{Al}_2\text{O}_3\cdot\text{SiO}_2$ or C_2AS , PDF#01-073-2041), and monocalcium dialuminate ($\text{CaO}\cdot 2\text{Al}_2\text{O}_3$ or CA_2 , PDF#00-007-0082) ().

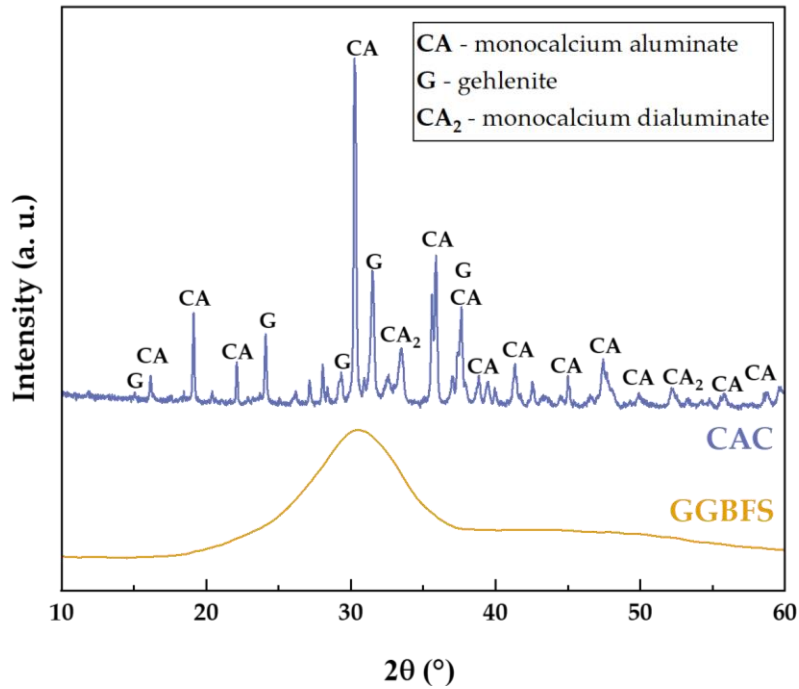


Fig. 6.2: XRD patterns of precursor materials GGBFS and CAC

Mix proportions used for the formulation of hybrid binders of this section are shown in Table 6.3.

Table 6.3: Mix proportions of hybrid pastes with GGBFS and CAC

| Mixture | Precursors (wt. %) | | Activator solution | | | w/b (mass ratio) |
|---------|--------------------|-----|--|--|-------|---------------------|
| | GGBFS | CAC | Modulus (SiO ₂ /Na ₂ O molar ratio) | Alkali-dosage (Na ₂ O wt. %) | NaOH | |
| 0C-a | 100 | 0 | 0.56 | 4.0 | 3.9 g | 0.38 |
| 10C-a | 90 | 10 | 0.56 | 4.0 | 3.9 g | 0.38 |
| 10C-b | 90 | 10 | 0.91 | 4.7 | 4.4 g | 0.38 |
| 0C-c | 100 | 0 | 0 | 5.4 | 4 M | 0.38 |
| 10C-c | 90 | 10 | 0 | 5.4 | 4 M | 0.38 |

Alkali-activated pastes were prepared by mixing GGBFS with 10 wt. % additions of CAC. The activator solution was prepared by mixing NaOH pellets with water, and subsequently adding sodium silicate solution on cooling of the aqueous NaOH

solution. Two activator concentrations were formulated by varying the modulus (molar ratio of $\text{SiO}_2/\text{Na}_2\text{O}$) from 0.56 to 0.91 and the alkali-dosage from 4 to 4.7 (expressed as Na_2O wt. % relative to the precursors, GGBFS and CAC) for activator "a" and activator "b", respectively. Solutions of NaOH were also prepared with a target concentration of 4 M (activator "c"). The water binder mass ratio (w/b) was kept constant to 0.38, where the binder is defined as the sum of the solid precursors plus dissolved solids in the activator. Table 6.3 shows the mix proportions and the respective sample nomenclature used henceforth. The water to binder ratio of 0.38 was maintained the same for all mixes.

6.3 Results and discussion

6.3.1 Isothermal calorimetry

The heat flow profiles of the alkali-activated and hybrid samples are shown in Fig. 6.3 (a). An initial exothermic peak, designated as the pre-induction peak, appears immediately for all samples representing the wetting and dissolution of precursor materials. When GGBFS is activated with a sodium silicate solution of modulus of 0.56 (0C-a) the dissolution peak is followed by a dormant period which ends after ~ 8 h with the beginning of the acceleration period. In contrast, GGBFS activated with 4M NaOH (0C-c) exhibits a very short dormant period with a subsequent acceleration period commencing after 1.5 h. The dormant period dependence on the activator solution is consistent with previous studies [124], [261]. The large second exothermic peak is centred at ~ 15 h and ~ 7 h for 0C-a and 0C-c, respectively, with the acceleration/deceleration stages concluded within the initial 24 h for both mixtures. This exotherm is associated with the precipitation, nucleation, and growth of reaction products, such as C-A-S-H gels during polycondensation [396].

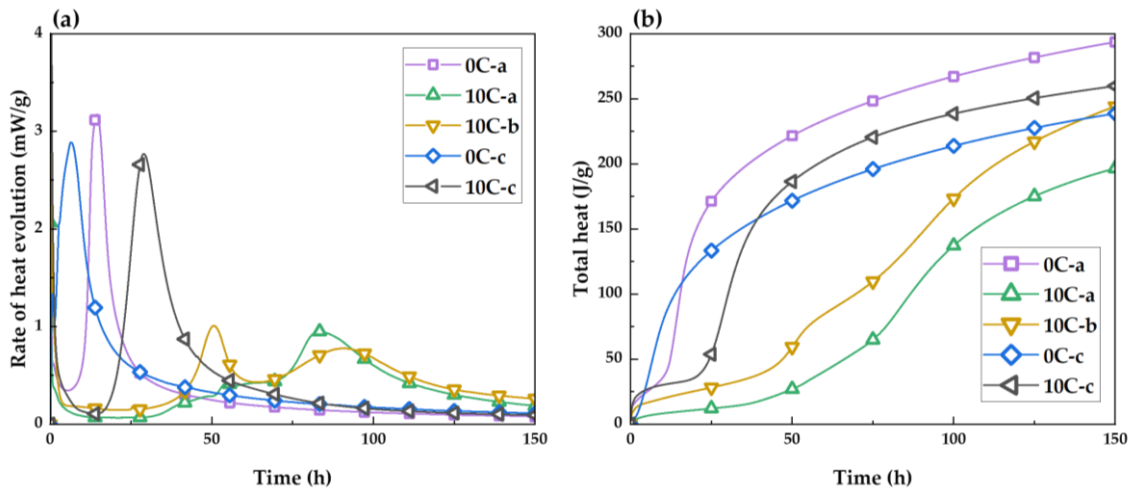


Fig. 6.3: (a) Heat evolution and (b) cumulative heat of alkali-activated and hybrid samples at 20 °C

Hybrid samples activated with sodium silicate and sodium hydroxide, 10C-a and 10C-b, exhibit a markedly different response. Regardless of the activator dosage, the dormant period is prolonged up to ~ 40 h. The 10C-a sample shows several overlapping heat evolution peaks between 35-50 h, resolving into a small narrow peak at ~ 55 h. The appearance of these secondary exothermic peaks may indicate initial gel formation, i.e. progression of the polycondensation reaction. The subsequent induction-like period spans from 55 h to 70 h, after which a visibly suppressed second exothermic peak is apparent with a maximum at ~85 h. The induction period in the 10C-b sample also exceeds 35 h, followed by two more distinct exothermic peaks: a sharp narrow peak at ~ 50 h and a broader peak at ~ 80 h. As seen in the case of 10C-a, the slope of the last peak diminishes after 150 h. The exact designation of individual heat evolution peaks to describe the progress of several concurrent and competing reactions sequences in this multi-component system is difficult, however, it is clear from the data that both the 10C-a and 10C-b systems with the addition of CAC experience a serious retarding effect on the formation kinetics associated with polycondensation, similarly to the delay observed for alkali-activated 100 wt. % CAC [197].

The 10C-c system also exhibits a prolonged dormant period compared with 0C-c. Only after ~ 17 h does the acceleration stage begin and reaction products such as primary C-A-S-H gels form. The acceleration/deceleration period is seen to conclude within 50 h.

6.3.2 Mini-slump test and setting times

Table 6.4 presents mini-slump and setting time test results for all samples. The water/binder mass ratio used in the formulation of the binders was kept constant in order to compare the effects of individual binder components on workability. The addition of CAC results in a decrease in slump flow even though the CAC used in this work has a slightly larger particle size than the GGBFS (see Table 6.1), and literature on the effect of CAC additions on paste flow reports CAC particles having a low tendency to form agglomerates, and thus high mobility in aqueous solutions [201]. The reason behind the reduction in slump flow is due to the high early reactivity of CAC and the prompt formation of aluminate hydrates from the onset of reaction in the alkaline environment. Workability is found to be dependent on the nature of the activator solution, as clearly seen from the comparison between NaOH-activated and sodium silicate-activated pastes [397]. The activator type is a significant factor affecting workability; in particular, the presence of dissolved silicates results in a direct increase in flow by acting as a plasticiser for alkali-activated mixtures [398]. The activator modulus and alkali content can be seen to reduce fresh-state flow, when comparing 10C-a and 10C-b.

Table 6.4: Mini-slump tests and initial and final setting time results for hybrid mixtures based on GGBFS and CAC

| Sample | Mini-slump (mm) | | Setting time (h) | |
|--------|-----------------|--------|------------------|-------|
| | 10 min | 30 min | Initial | Final |
| 0C-a | 105 | 92 | 3.33 | 4.67 |
| 10C-a | 94 | 85 | > 40 | |
| 10C-b | 98 | 82 | > 40 | |
| 0C-c | 96 | 88 | 3.83 | 5.83 |
| 10C-c | 92 | 84 | 8.00 | 12.17 |

Sample 0C-a starts to set after 3.33 h and reaches final setting after 4.67 h. These results show that the common issue of quick setting of AAC has been avoided, if compared to previous results obtained in sections 5.2 and 5.3, giving setting times similar to those of traditional PC binders, confirming the suitability of the activator selected for the control mix 0C-a [399], [400]. The second control formulation, 0C-c, prepared with 4M NaOH has a slightly longer setting time, albeit still less than 6 h to final setting.

Addition of CAC results in a delay in setting times in all cases. Setting times over 40 h were recorded for solutions (a) and (b), made with sodium silicate solutions with different modulus, used in conjunction with CAC. When 4M NaOH is used as activator, type (c), the setting times are still prolonged compared to 0C-c, however set within a reasonable timeframe (< 13 h). These results are consistent with kinetics curves seen in Fig. 6.3. The amount of aluminate hydrate C_3AH_6 formation, which causes a reduction in flow, is not significant enough to trigger the setting process. This may be due to the low mass fraction of CAC in the mixes, which limits the extent of early hydrate formation.

6.3.3 X-ray diffraction

Fig. 6.4 (a) shows the XRD diffraction patterns for control specimens 0C-a after 1 day, 2 days, 7 days, and 28 days. The pattern shows distinct broad humps at $\sim 7^\circ$, $\sim 29^\circ$, and $\sim 35^\circ 2\theta$ indicative of amorphous C-A-S-H gel formation [265]. Minor peaks are due to the formation of a hydrotalcite-group phase (approximately $Mg_4Al_2(CO_3)(OH)_{12} \cdot 3H_2O$, PDF#01-089-0460) which has been observed extensively in alkali-activated slag systems [15], [266], [267]. The formation of crystalline hydrotalcite involves the dissolution of the Mg^{2+} component present within the GGBFS, and can result in enhanced properties of the binder, such as resistance to carbonation and chloride ingress [125], [268]. Calcite ($CaCO_3$, PDF# 01-086-0174) is formed as the main carbonation product, appearing as a sharp peak overlaid on the broad hump at $\sim 29^\circ 2\theta$.

The phase evolution between 1 day and 28 days is minimal. The humps attributed to C-A-S-H are noted to become narrower over time as a result of increased short-range order and improved gel development. The XRD patterns of 10C-a are presented in Fig. 6.4 (b). After 1 day, the peaks at $\sim 30^\circ$ and $\sim 32^\circ 2\theta$ are identified as unreacted CAC phases: calcium monoaluminate (CA), as well as gehlenite (G) which is generally characterised by low reactivity and expected to be stable within the system at ambient temperature during the first stages of reaction [401]. Both CA and G are the major constituents of CAC [186]. Further peaks are referenced to calcium monocarboaluminate (Mc, $C_4A\bar{C}H_{11}$ PDF#00-041-0219), an AFm-like phase likely to be formed from the carbonation of CA hydration products, and aluminate hydrates (C_3AH_6 PDF# 00-024-0217). Meta-stable hexagonal aluminate hydrates (CAH_{10} and C_2AH_8), compounds that conventionally form in the early hydration of CAC, are not observed, suggesting either that in alkaline environments the formation of cubic aluminate hydrate is favoured from the onset of reaction, or that the conversion of the metastable aluminates to cubic aluminate hydrates has very fast kinetics [196], [197], [201], [202]. The formation of AH_3 along with cubic aluminate hydrates is not excluded as a possibility, however this phase is not easily detected in its disordered forms. Both Mc and C_3AH_6 are attributed to the reaction of CA only, whilst the main reaction products of GGBFS alkali-activation (C-A-S-H and hydrotalcite) are not yet observed. This indicates that CAC promptly dissolves and reacts, whilst the dissolution of GGBFS is inhibited. The quick precipitation of reaction products (including C_3AH_6) on the surface of GGBFS grains might be the barrier that affects the dissolution and diffusion of the ions into solution for polycondensation reaction [402] causing a delay in C-A-S-H formation, extended duration of the dormant period in the calorimetry data (Fig. 6.3 (a)) and retarded setting times (Table 6.4). Calcite is formed as carbonation product after 2 days, whilst the intensity of C_3AH_6 is progressively reduced during the following days of curing until it becomes undetectable after 7 days. Early C-A-S-H formation is slow to occur due to the inhibited dissolution of GGBFS. Increased C-A-S-H formation after 7 days is accompanied by the appearance of strätlingite (C_2ASH_8 , PDF# 01-085-8414). Strätlingite crystals are hexagonal AFm-like structured plates incorporating Si, and

therefore can form at relatively early ages if there exists a sufficient source of soluble silica promoted by sodium salts in a moderately alkaline environment [193]. Strätlingite formation is also reported to be favoured with higher Al contents [117], [403], and it is possible that the Al provided by the redissolution of the C_3AH_6 is contributing to this process. The stability and coexistence of strätlingite with C-A-S-H can be confirmed after 28 days [404], [405]. The XRD patterns of 10C-b in Fig. 6.4 (c) include the formation of vaterite ($CaCO_3$ PDF# 01-072-0506) along with C_3AH_6 , while Mc formation is not clearly defined until 28 days (Fig. 6.4 (c)). C_3AH_6 is present in the XRD data until 7 days as C-A-S-H forms slowly, similar to the 10C-a sample, and no peaks referenced to strätlingite are present. The lack of strätlingite is explained by its unfavourable formation at very high pH, in agreement with previous studies [196] whereby strätlingite did not form from CAC in highly alkaline environments. It is hypothesised that as strätlingite requires a readily available source of soluble silica to form, there is insufficient dissolution of silica in the 10C-a sample after 2 days to allow for significant formation of this phase to be detected. All three samples containing CAC show a defined C-A-S-H peak at $\sim 29^\circ 2\theta$ that narrows over time, indicating an increase in short range ordering due to a higher degree of polymerisation of the gel phase [406].

The XRD pattern of 0C-c in Fig. 6.4 (d) contains peaks indexed to hydrotalcite, calcite, C-A-S-H, and also tetracalcium aluminate hydrate (C_4AH_{13}) as a secondary AFm-like phase with major peaks overlapping hydrotalcite peaks. The formation of AFm-like secondary products alongside hydrotalcite has been identified in NaOH-activated GGBFS [113], [122], [407], [408]. The evolution of phases with time is very limited, similar to the 0C-a control sample, meaning that the primary phase assemblage and structures formed since the initial stages of reaction remain stable.

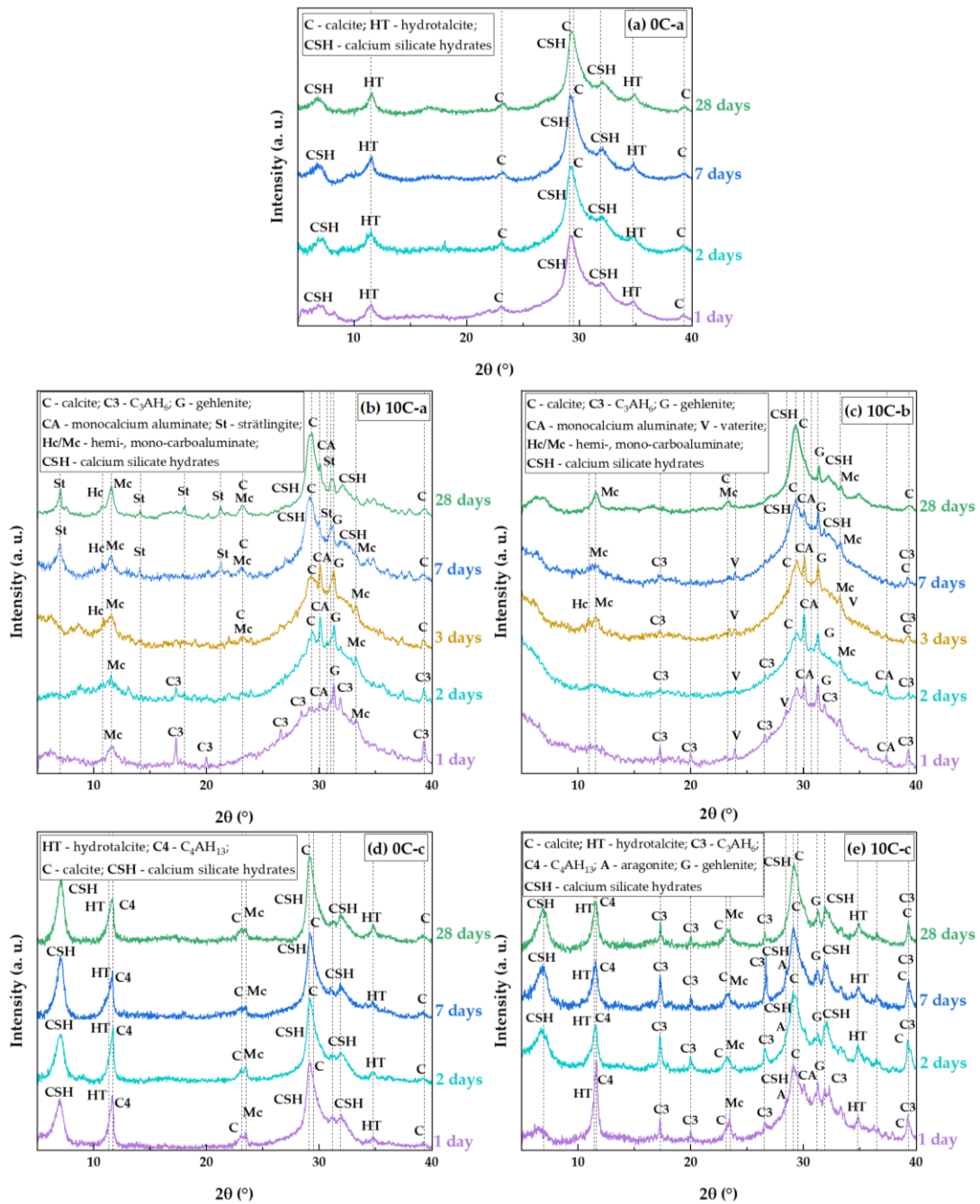


Fig. 6.4: XRD patterns of alkali-activated and hybrid samples from 1 day to 28 days of curing: (a) 0C-a, (b) 10C-a, (c) 10C-b, (d) 0C-c, and (e) 10C-c. Note that the phases marked as “CSH” will contain alumina and thus are more precisely described as C-A-S-H, but a more concise form of the notation is used in the graphics

Fig. 6.4 (e) shows the XRD patterns for 10C-c. Similar to the 0C-c samples, formation of hydrotalcite, calcite, C-A-S-H, and a secondary AFm-like phase is noted. Unreacted CA inclusions are observed from a secondary peak at $\sim 30^\circ 2\theta$ (which disappears after 1 day) and unreacted gehlenite which remains stable throughout

alkali-activation. The identified aragonite peak (CaCO_3 , PDF# 00-041-1475) at $\sim 28^\circ$ represents a secondary carbonation product along with calcite. C_3AH_6 is formed from the onset of reaction, as seen for 10C-a and 10C-b, however remains stable even after 28 days. It is noted that C-A-S-H forms initially, unlike for samples activated with sodium silicate, consistent with the calorimetry data as discussed above which show much less severe inhibition of the dissolution of GGBFS by CAC addition in systems activated by NaOH.

6.3.4 Fourier-transform infrared spectroscopy

Fig. 6.5 shows the FTIR results obtained for alkali-activated and hybrid samples after 2 days and 28 days. The band at 1650 cm^{-1} is due to H-OH bond bending, indicative of weakly bonded water molecules trapped on the surface or in pores within the samples [272], [276]. The bands at $\sim 1490\text{-}1410\text{ cm}^{-1}$ are related to C-O bond stretching and corresponding asymmetric bending at $\sim 900\text{-}820\text{ cm}^{-1}$ [277]–[279], [409]. All samples show modes relating to carbonation products. The major absorption band between $1200\text{-}900\text{ cm}^{-1}$ is associated with asymmetric Si-O-T (T = tetrahedral Si, Al) bond stretching and is significant in understanding the formation of reaction products [168], [201]. It is noted for all binders that after alkali-activation, the Si-O-T band shifts to lower wavenumbers and sharpens. The band is the combination of Si-O-Si asymmetric stretching vibrations with varying Al substitution, resulting in a change in bond stretching contributions. The remaining symmetric Si-O-T bond stretching $\sim 700\text{ cm}^{-1}$ and Si-O-T bond bending $\sim 520\text{-}420\text{ cm}^{-1}$ bands are also considered to include contributions from substituted Al. In general, the major absorption band $\sim 950\text{ cm}^{-1}$ in alkali-activated specimens becomes more narrow and tends to shift to lower wavenumbers after 28 days compared with 2 days [280]. This is reported in the literature to be due to increased incorporation of Al, and the subsequent contribution from Al-O-Si linkages, within which the Al-O bonds are weaker than Si-O [281]. The integrated intensity of the band is also noted to shift to lower wavenumbers due to Al perturbations in local Si-O bonding [282]. This is reflected in both 10C-a and 10C-b samples, where the major bands shift from 976 and

984 cm^{-1} (respectively) to 954 cm^{-1} and 957 cm^{-1} after 28 days, and the shape of the band markedly changes from broad to sharp. The contribution of Si-O symmetric stretching vibrations appears to be larger for samples 0C-c and 10C-c activated with NaOH. Due to the contributions of LDH phases these samples show three distinct bands in the range $\sim 510\text{-}420 \text{ cm}^{-1}$, which are attributed to the Al-O bonds of hydrotalcite, C-A-S-H, and C_4AH_{13} [408], [410]. The bands at $\sim 896 \text{ cm}^{-1}$ and $\sim 590 \text{ cm}^{-1}$ for samples with CAC addition can be attributed to C_3AH_6 . [410].

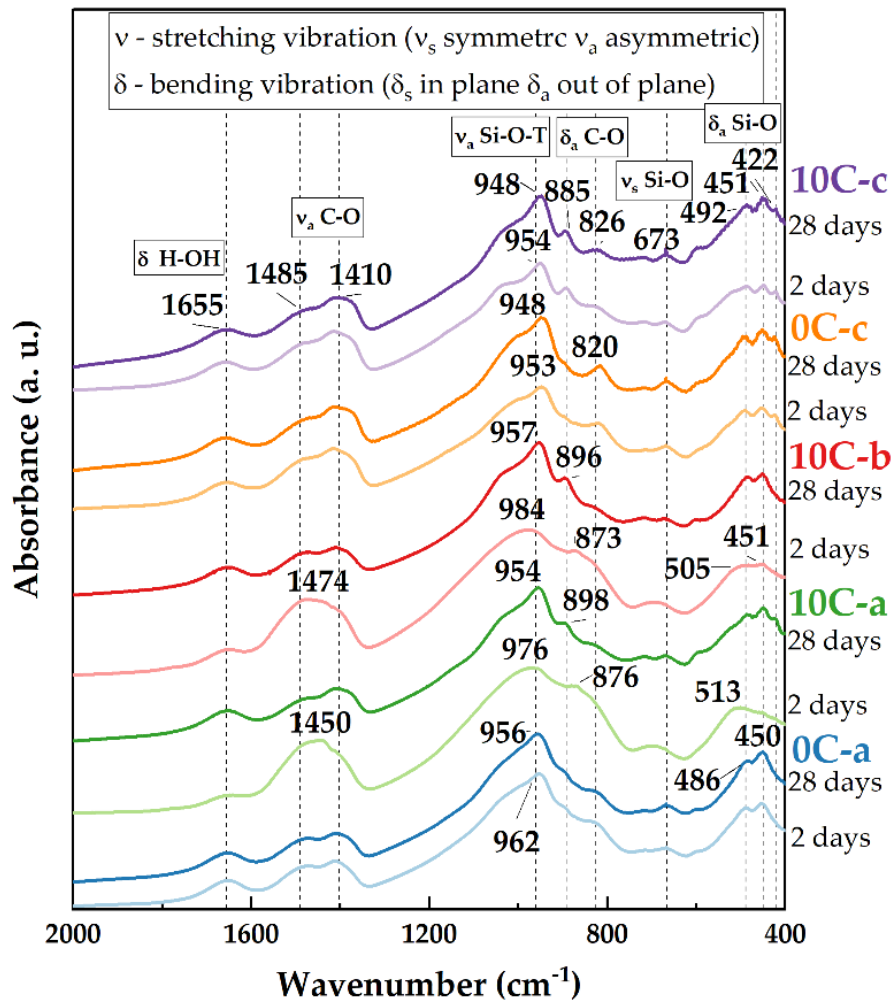


Fig. 6.5: FTIR spectra of alkali-activated and hybrid samples after 2 days and 28 days

6.3.5 Solid-state nuclear magnetic resonance spectroscopy

^{29}Si MAS NMR spectra, deconvolutions, and simulated spectra for the 2-day and 28-day cured samples activated with sodium silicate and NaOH are shown in Fig. 6.7 and Fig. 6.8, respectively. The raw GGBFS spectrum is simulated with one peak centred at isotropic chemical shift, δ_{iso} , = -75 ppm (Fig. 6.6 (a)) and is linearly scaled and included in the simulation of the data for all alkali-activated samples to account for remnant unreacted GGBFS, with the assumption that this lineshape does not change throughout the reaction. The simulated spectrum for GGBFS in this work is consistent with previous studies [411]. Any Si content within CAC is related to the presence of gehlenite, as seen in the XRD data of the precursors (Fig. 6.2).

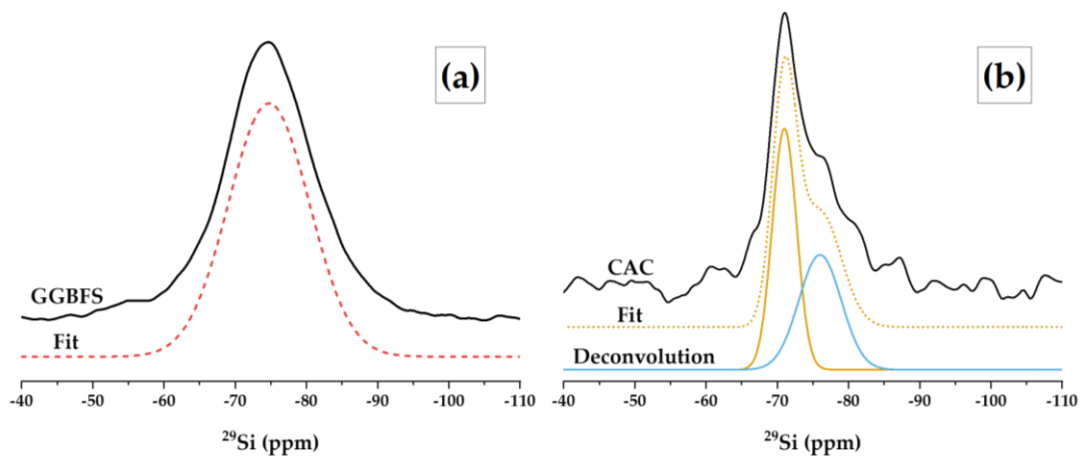


Fig. 6.6: ^{29}Si MAS NMR spectra of precursors (a) GGBFS and (b) CAC

The deconvoluted spectrum in Fig. 6.6 (b) shows Q^0 and Q^1 sites (δ_{iso} = -68 ppm, -71 ppm, -74 ppm, and -78 ppm) as the main Si environments [412], [413]. Table 6.5 gives the deconvolution data for all ^{29}Si MAS NMR spectra and quantification of Q^n environments identified in all samples after 2 days and 28 days of curing.

Resonances at δ_{iso} = -68 ppm and -71 ppm are attributed to Q^0 and Q^1 units of unreacted GGBFS and CAC (Fig. 6.6). Both precursors have terminal and isolated Si groups present [414]. Signals at δ_{iso} = -74 ppm and -78 ppm are attributed to the presence of two different types of Q^1 sites in C-S-H or C-A-S-H gels, which are the main reaction products in all the investigated systems. The assignment of Q^1 sites in

C-A-S-H gel is challenging as each individual unit may be bonded to Si or Al and have Ca^{2+} , Na^+ , or H^+ as balancing cations in various ratios that when combined cause variation in Si chemical shifts. Q^1 is simulated with two peaks in the region between -70 ppm and -80 ppm which are named $\text{Q}^1(\text{I})$ and $\text{Q}^1(\text{II})$ without assigning a specific chemical environment to each one, as a consequence of the complexity of such interactions [285]. Network modifying cations can also affect the chemical environment of $\text{Q}^n(\text{mAl})$ species, increasing the chemical shift, especially for strongly polarising cations such as Ca [415], resulting in additional overlap of the individual $\text{Q}^n(\text{mAl})$ environments. The presence of distorted Al tetrahedra, Al(V), and Al(VI) species in octahedral configurations further complicates peak assignment in the ^{29}Si MAS NMR spectra.

Table 6.5: Quantification of Q^n environments identified in ^{29}Si MAS NMR spectra of alkali-activated and hybrid samples based on GGBFS and CAC after 2 days and 28 days. Estimated uncertainty in site percentages is $\pm 1\%$

| Sample | Isotropic chemical shift, δ_{iso} (ppm) | | | | | | | | GGBFS |
|--------------------|---|------------------------|-------------------------|--------------------------|--------------|--------------------------|--------------------------|-----|-------|
| | Q^0 | $\text{Q}^1(\text{I})$ | $\text{Q}^1(\text{II})$ | $\text{Q}^2(1\text{Al})$ | Q^2 | $\text{Q}^3(1\text{Al})$ | $\text{Q}^4(3\text{Al})$ | | |
| | -71 | -74 | -78 | -81.5 | -84 | -85.5 | -89 | -91 | -74.7 |
| 0Ca 2 days | 1% | 26% | 10% | 3% | 21% | - | 4% | - | 36% |
| 28 days | 1% | 23% | 14% | 2% | 29% | 9% | 4% | 3% | 16% |
| 10Ca 2 days | 1% | - | 9% | 8% | 20% | - | - | - | 61% |
| 28 days | - | 7% | 10% | 12% | 32% | - | - | - | 39% |
| 10Cb 2 days | 5% | 12% | 8% | 9% | 14% | 5% | - | 4% | 43% |
| 28 days | 9% | 9% | 17% | 21% | 9% | 35% | 1% | 1% | 30% |
| 0Cc 2 days | 2% | 8% | 11% | 13% | 11% | 10% | - | - | 44% |
| 28 days | 3% | 5% | 18% | 32% | 12% | 1% | - | - | 29% |
| 10Cc 2 days | 4% | 4% | 18% | 7% | 17% | 9% | - | - | 41% |
| 28 days | 5% | 9% | 20% | 23% | 27% | - | - | - | 17% |

Resonances at $\delta_{\text{iso}} = -81.5$ ppm, -84 ppm, and -85.5 ppm are attributed to $\text{Q}^2(1\text{Al})$ and Q^2 units indicating the formation of an C-A-S-H gel with a tobermorite-type structure. The signals at $\delta_{\text{iso}} = -89$ ppm and -93 ppm are attributed to highly cross-linked $\text{Q}^3(1\text{Al})$ and $\text{Q}^4(3\text{Al})$ environments which overlap within the spectra [16]. These are found in the control sample 0C-a activated with sodium silicate (Fig. 6.7 (b)), whilst not detected in the 0C-c sample activated using NaOH (Fig. 6.8 (b)). This

formation of greater cross-linked C-A-S-H gels when using sodium silicate has been observed in previous studies [112].

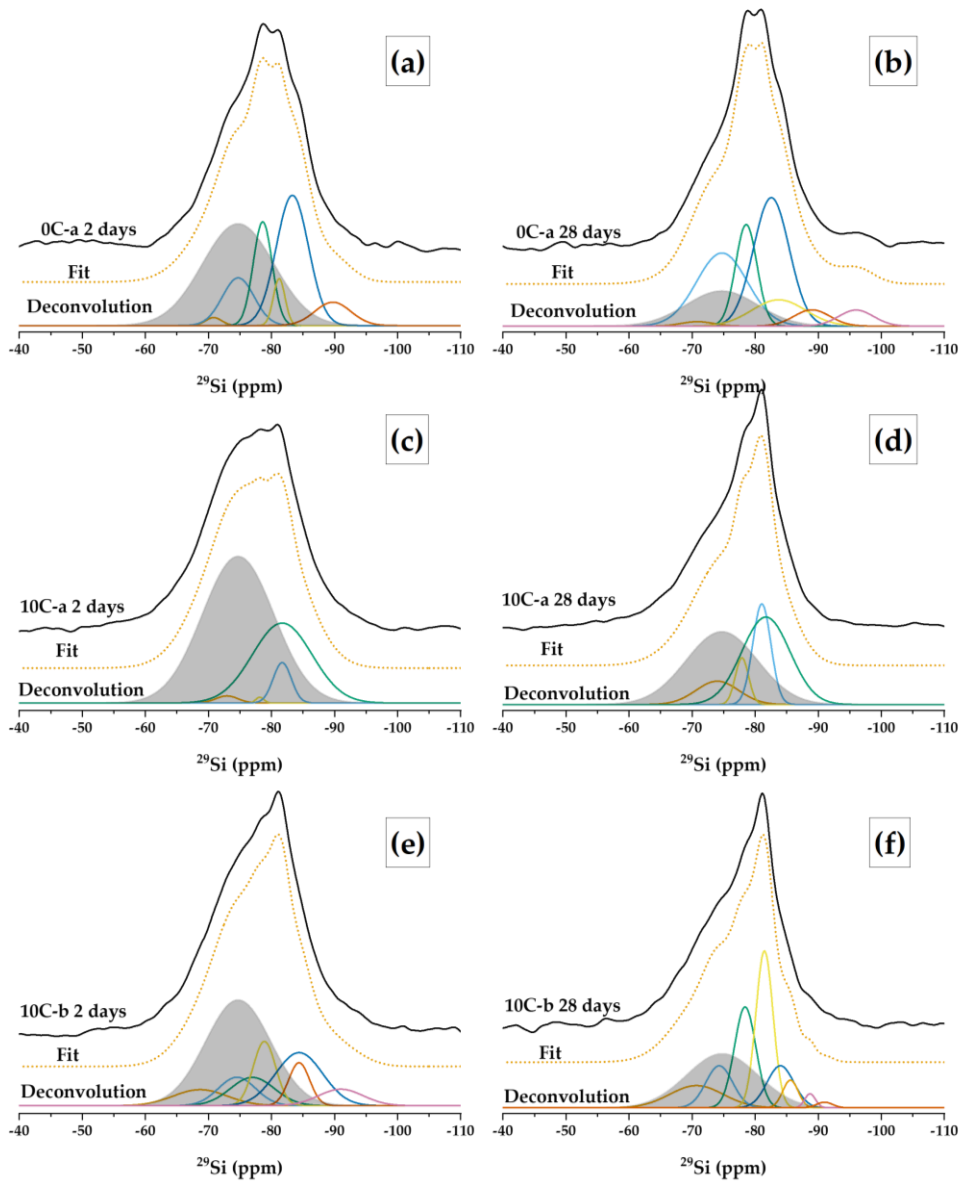


Fig. 6.7: ^{29}Si MAS NMR spectra with fit and deconvolution, of: (a) 0C-a 2 days, (b) 0C-a 28 days, (c) 10C-a 2 days, (d) 10C-a 28 days (e) 10C-b 2 days, and (f) 10C-b 28 days. The grey band represents the contribution of the unreacted GGBFS which is directly scaled from the raw GGBFS spectrum under the assumption of congruent dissolution

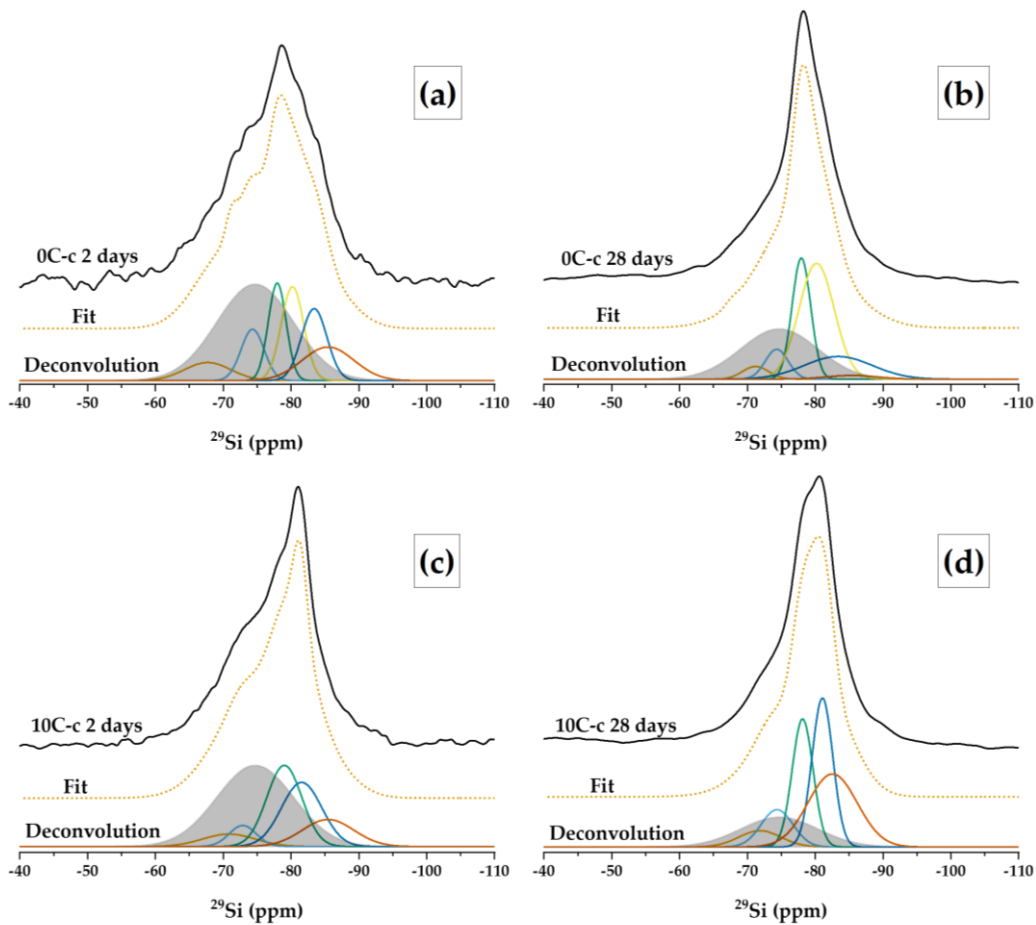


Fig. 6.8: ^{29}Si MAS NMR spectra with fit and deconvolution of samples activated with 4M NaOH: (a) 0C-c 2 days, (b) 0C-c 28 days, (c) 10C-c 2 days, and (d) 10C-c 28 days. The grey band represents the contribution of the unreacted GGBFS which is directly scaled from the raw GGBFS spectrum under the assumption of congruent dissolution

The ^{27}Al MAS NMR spectra for both precursors and pastes are shown in Fig. 6.9. The GGBFS spectrum exhibits one broad resonance spanning between $\delta_{\text{obs}} = 80$ ppm and 40 ppm, centred at $\delta_{\text{obs}} = \sim 63$ ppm, and which is assigned to a distribution of tetrahedral Al environments. There is not a single well-defined Al environment distinguishable within the spectrum due to the amorphous structure of the GGBFS precursor [280], [285] (Fig. 6.9 (a)). The main characteristic of the CAC spectrum is an intense broad signal with centre at $\delta_{\text{obs}} = 81$ ppm, attributed to the presence of tetrahedral Al [415]–[417]. The asymmetry of this peak is due to the convolution of signals assigned to two different CaAl_2O_4 components [415], [416]. A minor signal

between $\delta_{\text{obs}} = 10$ ppm and 13 ppm is associated with the presence of octahedral Al in CAH_{10} , that may appear as a consequence of material weathering [198].

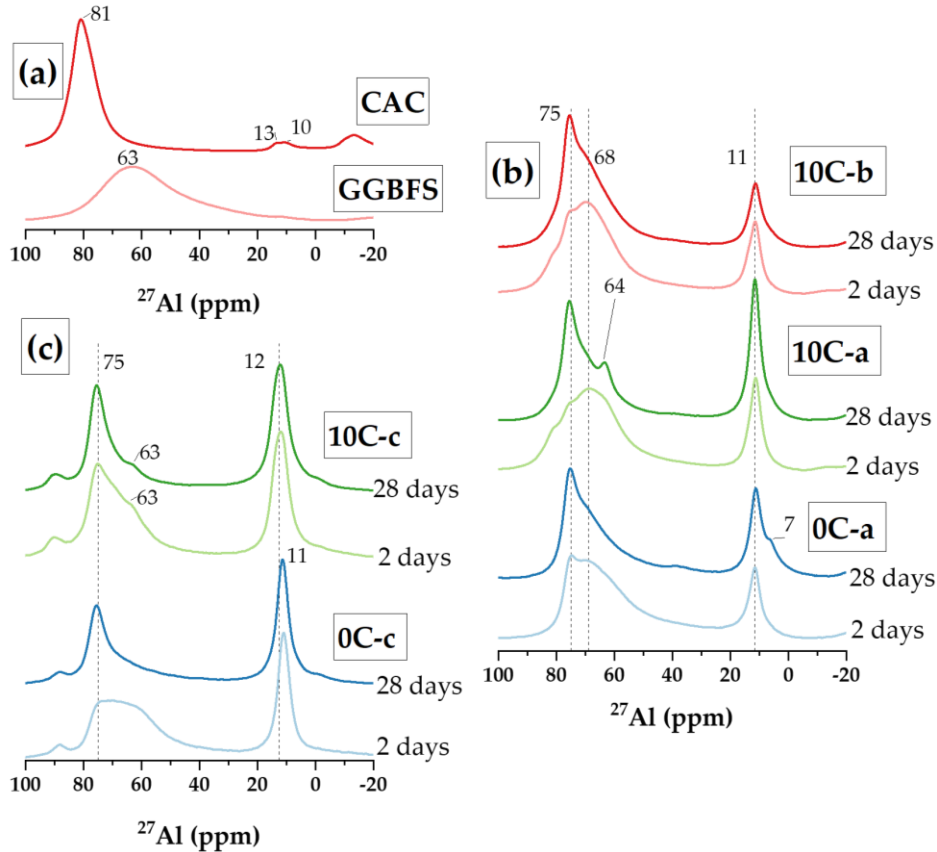


Fig. 6.9: ^{27}Al MAS NMR spectra for (a) alkali-activated and hybrid specimens activated with activator mixtures a and b after 2 days and 28 days, (b) alkali-activated and hybrid specimens activated with 4M NaOH after 2 days and 28 days, and (c) precursor materials GGBFS and CAC

The ^{27}Al NMR spectra for 2-day samples in Fig. 6.9 (b) show a similar broad signal spanning from $\delta_{\text{obs}} = 80$ ppm to 50 ppm assigned to Al in a slightly distorted tetrahedral environment. The sharp peak that appears at $\delta_{\text{obs}} \sim 75$ ppm in the 0C-a 2-day spectrum is not present in either the 10C-a or 10C-b 2-day spectra. This peak is attributed to Al in a well-defined tetrahedral coordination and incorporated in bridging sites, bonded to $\text{Q}^2(1\text{Al})$ sites (also defined as $\text{q}^2(2\text{Si})$) [116], [418]. This resonance becomes more intense and narrower for all samples with increasing curing time, particularly in the 10C-b 28-day spectrum, typical of a well-structured C-A-S-H gel. The resonance at $\delta_{\text{obs}} = 64$ ppm in the 10C-a 28-day spectrum is attributed to

strätlingite formation which is identified from the XRD data (Fig. 6.4 (b)). The narrow resonance at $\delta_{\text{obs}} = \sim 11$ ppm present in all sample spectra is assigned to octahedral Al, found in AFm-like phases. The intensity of this band for the 10C-a 28-day sample is greater than the other samples due to the convolution of responses from both phases and strätlingite [404], [419]. This resonance is also attributed to C_3AH_6 , which is initially present in both 10C-a and 10C-b samples. The shoulder band at $\delta_{\text{obs}} = \sim 7$ ppm in the 0Ca 28-day spectrum may indicate the presence of hydrotalcite-like phase as identified in the XRD data in Fig. 6.4 (a) [407], [420].

The ^{27}Al NMR spectra for the mixtures activated with NaOH solution, 0C-c and 10C-c, (Fig. 6.9 (c)) exhibit two signals related to tetrahedral and octahedral Al environments, respectively. For both samples, intense peaks are found at $\delta_{\text{obs}} = 11$ ppm and 12 ppm. Hydrotalcite, AFm-like phases, and aluminate hydrates as C_3AH_6 (for 10C-c) are associated with this peak, identified from XRD data in Fig. 6.4 (d) and (e). The signal associated with tetrahedral Al environments in 0C-c spectrum evolves with increasing curing time, becoming sharper and narrower, with the main resonance found at $\delta_{\text{obs}} = \sim 75$ ppm attributed to $q^2(2\text{Si})$ environment. The shoulder identified in the 10C-c spectrum at ~ 63 ppm can be attributed to $q^3(3\text{Si})$ due to additional Al incorporation into the gel [198], [284], [294]. This may be attributed to formation of strätlingite as seen for 10C-a 28-day, however strätlingite is not identified from the XRD data of these samples.

6.3.6 Scanning electron microscopy

Fig. 6.10 shows BSE images of all samples after 2 days and 28 days. The initial formation of C-A-S-H gel (grey region) in the 0C-a 2-day sample is seen surrounding partially unreacted GGBFS particles (brighter particles), with apparent porosity identified by the darker regions. Comparison with the sample after 28 days reveals that the 0C-a specimen progressively densifies, generating a more compact binder that appears homogenous, albeit with the persistent inclusion of remnant unreacted GGBFS particles.

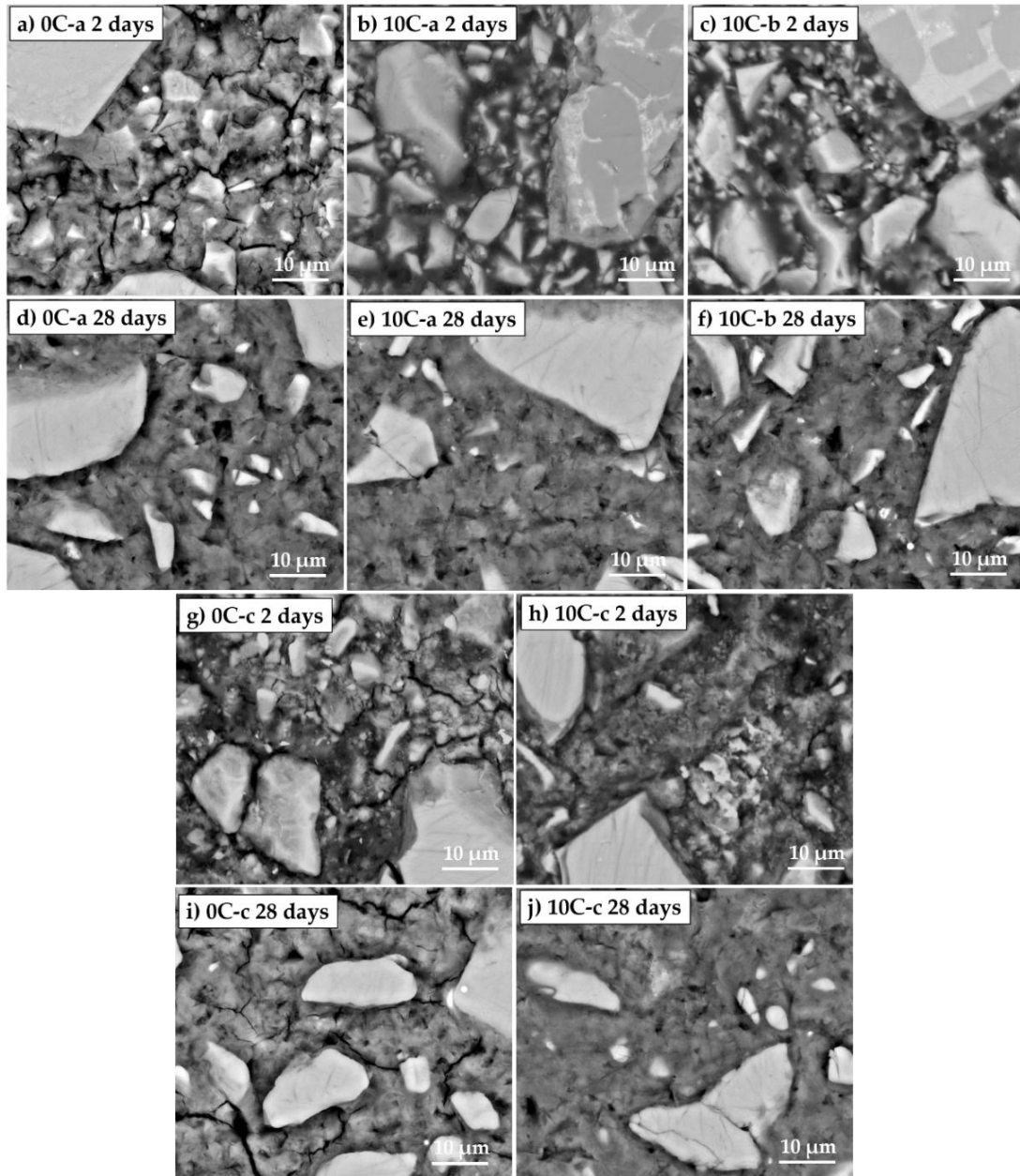


Fig. 6.10: BSE images of alkali-activated and hybrid samples after 2 days and 28 days of curing

The 10C-a and 10C-b 2-day image (Fig. 6.10 (b) and (c)) shows limited matrix gel formation; numerous unreacted small and large GGBFS particles are present with reduced interparticle spacing, resulting in a highly porous binder. Large CAC particles are also present, for which two distinctive areas of different greyscale levels are identified as CA and gehlenite (Fig. 6.11). The change in microstructure of both samples after 28 days (Fig. 6.10 (e) and (f)) is similar to the 0C-a sample with

increased densification and gel phase formation. Most of the small GGBFS particles are dissolved.

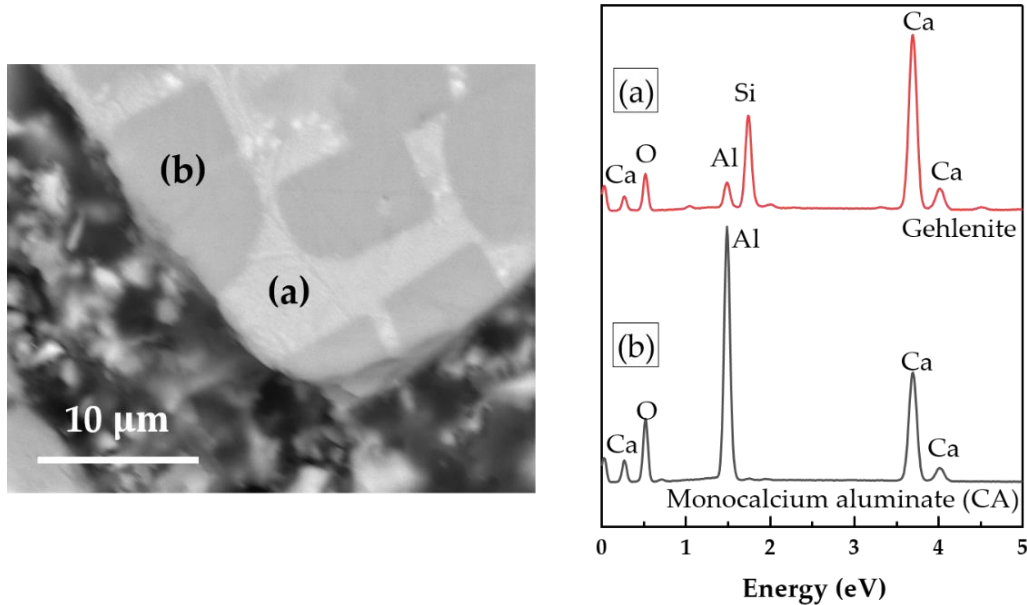


Fig. 6.11: CAC particle (left) and EDS points (a) and (b) identified as gehlenite and CA (right)

Samples 0C-c and 10C0c after 2 days (Fig. 6.10 (g) and (h)) also show prominent unreacted GGBFS particles and are highly heterogeneous composed by distinctive regions with a jagged appearance. The progression of C-A-S-H gel formation is visibly improved after 28 days. The result is similar to the gel formed in sample 0C-a, however the gel formed in 0C-c appears more porous with respect to 10C-c. Changes in the Ca/Si atomic ratios of the binders cured for 2 days and 28 days were determined by SEM-EDS point analysis and are shown in Fig. 6.12. The initial inclusion of CAC results in higher Ca/Si ratios as seen for samples 10C-a and 10C-b, however after 28 days 0C-a, 10C-a, and 10C-b show a reduction of Ca/Si ratio resulting ~ 1.2 as expected in systems activated with sodium silicate. This is due to the further incorporation of Si in C-A-S-H gels as the polycondensation reaction proceeds. The initial dissolution rate of Si with respect to Ca from the precursor materials, in particular GGBFS, is slower than the rapid dissolution of Ca in CAC [266]. For samples activated with NaOH the resulting Ca/Si ratio increases with

increase curing time and is overall higher due to absence of Si in the activator solution.

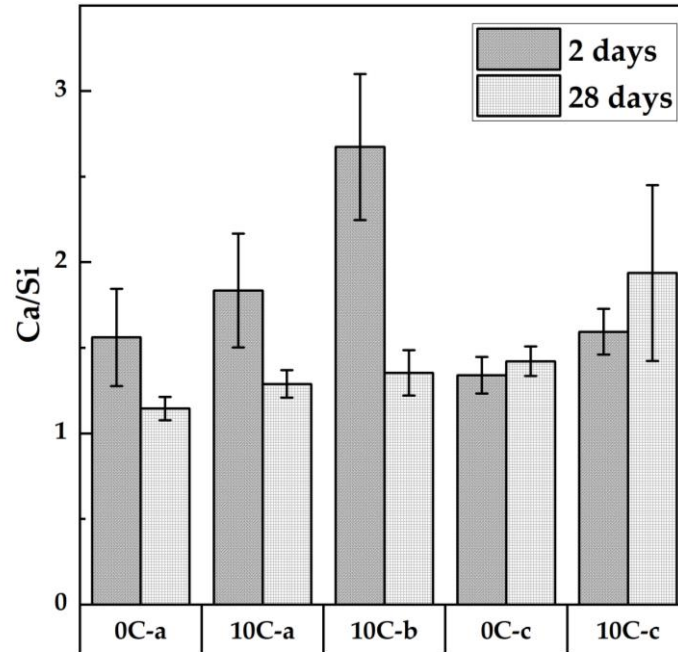


Fig. 6.12: Bulk atomic ratio Ca/Si (as determined by SEM-EDS analysis) for alkali-activated and hybrid samples after 2 days and 28 days of curing

6.3.7 Compressive strength

The 7-day and 28-day compressive strength results for alkali-activated and hybrid samples are displayed in Fig. 6.13. The 10C-a and 10C-b specimens after 7 days exhibit a slightly inferior strength (~ 35 MPa) with respect to the control specimen 0C-a (~ 44 MPa). As seen in the previous sections [reaction kinetics (Fig. 6.3), FTIR (Fig. 6.5), XRD data (Fig. 6.4), and SEM (Fig. 6.10 (b) and (c))], the gel formation reaction during the first few days of curing is partially inhibited by the competitive and concurrent formation of other phases, such as aluminate hydrates C_3AH_6 , AFm-like phases, and strätlingite. These compounds when formed at later stages do not result in diminished mechanical integrity, however their initial formation may prevent the complete dissolution and subsequent reorganisation of slag particles during polycondensation. The increase in compressive strength seen after 28 days,

from 35 MPa to 61 MPa for 10C-a and from 37 MPa to 60 MPa for 10C-b, is considerable. This suggests that whilst formation of additional gel is gradual due to the initially retarded dissolution of Al and Ca sources, it is accompanied by significant AFm-like phases and strätlingite phase formation, which are known to promote the densification of the matrix [192], [195], [401], [421], resulting in a more compact gel structure [198], [199], [201]. Both formulations surpass the 28-day strength developed by the control formulation 0C-a, which is 58 MPa.

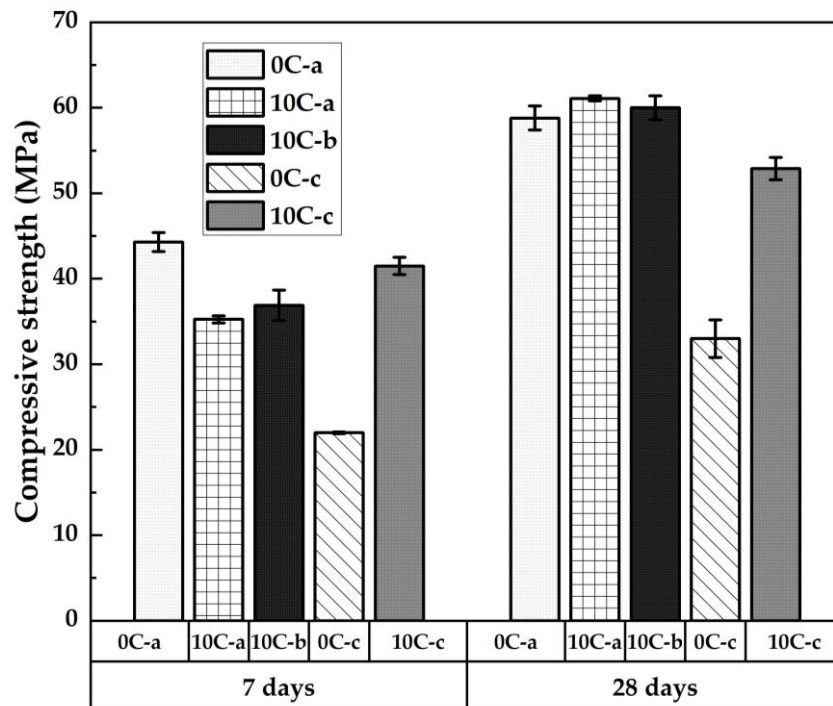


Fig. 6.13: Compressive strength of alkali-activated and hybrid samples after 7 days and 28 days. Error bars represent the standard deviation among three replicate specimens

When using NaOH as an activator the compressive strength developed by the control formulation 0C-c is inferior to that of 0C-a, reaching 22 MPa and 33 MPa after 7 days and 28 days, respectively; these values are consistent with those found in the literature [408], [422]–[424]. In this case the addition of CAC is beneficial as the increase of strength is substantial, surpassing 42 MPa and 52 MPa after 7 days and 28 days. This provides evidence of good incorporation of Al into the binding phases.

6.4 Conclusions

Hybrid systems based on GGBFS with CAC additions, activated with sodium silicate or sodium hydroxide, have been characterised and analysed. The addition of CAC to alkali-activated systems does not result in the formation of the conventional CAC hydration products, such as CAH_{10} , C_2AH_8 , and AH_3 , reported in literature [186].

The conversion issue related to the use of CAC in traditional concrete mixes is avoided, as a direct consequence of alkali-activation resulting in differing reaction sequences. The addition of 10 wt. % of CAC to alkali-activated binders has a strong impact, especially in the early stages of reaction; it retards the dissolution of GGBFS and consequently the polycondensation reaction of the main strength contributing phase, C-A-S-H gel.

Reaction kinetics and setting time show a delay of up to 50 h when 10% CAC is included in mixtures activated with sodium silicate. NaOH activated binders with CAC additions show a minimal delay. The workability is reduced with CAC addition.

Phase evolution studied by XRD revealed that when CAC is included in the mixture, aluminate hydrate C_3AH_6 is formed along with carboaluminate hydrate phases from the onset of reaction, and the formation of C-A-S-H gel is delayed. C_3AH_6 is reduced over time and strätlingite is formed depending on activator dosage and pH. When NaOH is used as an activator the formation of AFm-like phases along with hydrotalcite-group phase is recorded. C-A-S-H gel forms from an early age (1 day) along with C_3AH_6 , which in this case remains stable over time, and strätlingite does not form. FTIR data confirm the retardation in C-A-S-H gel formation when sodium silicate is used as an activator for GGBFS with CAC additions.

From the comparison of sodium silicate activated CAC/GGBFS blends, the highest activator modulus results in larger, even if still limited, amounts of GGBFS reacting at early age as revealed by ^{29}Si MAS NMR analysis. After 28 days, the C-A-S-H gel formed with CAC additions has higher Al incorporation. BSE images taken at 2 days

and 28 days exhibit the clear evolution of gel phases obtained for control samples and hybrid samples activated with NaOH, whilst the 2-day images of 10C-a and 10C-b show an unformed binding phase. The final gel obtained after 28 days has a similar composition for all samples.

Compressive strength of hybrid samples is slightly lower than those solely based on GGBFS at early ages, but surpasses it after 28 days, reaching 60 MPa. NaOH-activated GGBFS has inferior strength development compared to when using sodium silicate, but in this case the addition of CAC is beneficial, as the strength increases by almost 50 %.

The addition of CAC in alkali-activated GGBFS-based binders seems promising when NaOH is used as an activator, whilst, for silicate-activated systems, the prolonged setting time poses practical challenges despite the high final strength achieved by these materials. The overall efficacy of adding CAC to alkali-activated GGBFS-based binders may depend on the specific application and the type of activator used.

Chapter 7

Conclusions and Suggestions for Further Work

The design of AACs with maximised recycled content can bring significant environmental benefits. This study focuses on the replacement of GGBFS with four classes of unconventional precursors, specifically five calcined waste clays sourced from a kaolin mine, Imerys (UK), non-blast furnace slags, such as BOFS, ArcelorMittal (Belgium), EAFS, Orbix (Belgium), and CS from Aurubis Beerse (Belgium). The results of this study indicates that alkali-activation allows a larger utilisation and valorisation of wastes if compared with traditional PC-based materials. Specific findings of this study are illustrated below.

Particle morphology and amorphous phase fraction are deemed the major criteria for selecting the most suitable calcined waste clay, collected from the side extraction of a kaolin mine in Cornwall, UK, in blends with GGBFS. The five calcined clay samples exhibit distinct platelet-like morphologies characteristic of common clays. A replacement level of 30 wt. % of GGBFS is found to be the upper usage limit of calcined clays in these types of alkali-activated blends with GGBFS. The amorphous phase fraction is known to underpin the reactivity of the calcined clay during alkali-activation, whilst most mineral phases are found to remain chemically stable throughout. Calcined clays with minimal amorphous phase fractions have poor reactivity and are adjudged unsuitable as a direct precursor replacement, being more suited as a filler material. The best calcined clay blend consisting of 20 wt. % calcined clay achieves a reduction in porosity compared to solely GGBFS-based alkali-activated cement, and an increased final compressive strength value of 70 MPa (using

an activator with molar ratio $\text{SiO}_2/\text{Na}_2\text{O} = 1.2$ and $\% \text{Na}_2\text{O} = 5.2$) after 28 days, qualifying it for use in high strength applications.

BOFS samples from the ArcelorMittal steelmaking plant in Zelzate (Belgium), are found to contain a significant phase fraction of portlandite ($\text{Ca}(\text{OH})_2$), due to weathering by storage outside, from XRD analysis. All free lime (f-CaO), commonly present in conventional BOFS sources and limiting its application in construction due to detrimental expansion during hydration, appears to be converted to portlandite. The high content of portlandite in this material is exploited as a potential reaction accelerator in GGBFS blends. GGBFS and BOFS blends activated with sodium silicate show improved reaction kinetics with increasing BOFS content up to 30 wt.%. The relatively highly alkaline medium (molar ratio $\text{SiO}_2/\text{Na}_2\text{O} = 0.56$ and $\% \text{Na}_2\text{O} = 4$) is noted not to favour the complete reaction of all portlandite present. Using sodium carbonate as an activator with reduced alkalinity ($\text{pH} < 12$) maintains favourable reaction kinetics, setting and hardening after just 1 day whilst consuming most of portlandite contained in the BOFS precursor since the initial stage of reaction. The beneficial fresh properties achieved highlight the viability of sodium carbonate as a sustainable low-cost activator for BOFS and GGBFS blends.

EAFS in blended GGBFS cement results in a retardation of reaction kinetics with increasing replacements. EAFS consists of predominantly crystalline phases that show good chemical stability and the inclusion of harmful metal species (especially high chromium content) that are subject to strict leaching controls. Only a weak binding phase is identified from FTIR and SEM analysis for 100 wt. % EAFS. The predominant crystalline phase, merwinite ($\text{Ca}_3\text{Mg}(\text{SiO}_4)_3$), is believed to slowly dissolve in the alkaline media to form a minimal amount of C-A-S-H gel phase. The lack of contribution from EAFS in acting as a source for gel formation, requiring the usage of high activator dosages, is seen by a general decrease in overall compressive strength. On using a higher activator modulus and dosage (molar ratio $\text{SiO}_2/\text{Na}_2\text{O} = 1.6$ and $\% \text{Na}_2\text{O} = 5.3$), up to 50 wt. % EAFS blended with GGBFS exhibits a compressive strength value of 85 MPa and corresponding flexural strength of 9.5

MPa after 28 days. Leaching tests carried out on EAFS blends show heavy metal values well below the environmental limit, with no chromium detected in any leachates.

CS is found to have good reactivity in alkaline media due to the large amorphous iron-silicates phase fraction and can be classified as a direct precursor material. The investigation of CS and GGBFS blended systems shows a delay in reaction kinetics, with an improvement in fresh properties, better retention of workability, and longer setting times. The paste with 100 wt. % CS exhibits a delay in dissolution up to 3.5 h, with an intense convoluted dissolution-polycondensation peak apparent in the heat evolution profile. XRD data indicate that the major crystalline phases present in CS are chemically stable, however the significant amorphous fraction is believed to be activated to give an Fe-rich binding phase. The inclusion of 50 wt. % CS results in only a minor reduction in compressive and flexural strengths compared to 100 wt. % GGBFS cement, surpassing 100 MPa and 9 MPa respectively (using an activator with molar ratio $\text{SiO}_2/\text{Na}_2\text{O} = 1.6$ and $\% \text{Na}_2\text{O} = 5.3$) after 28 days. 100 wt. % CS develops a remarkable 1-day compressive strength of 23 MPa, with a minor increase, thereafter, reaching 38 MPa after 28 days. This lack of substantial strength improvement at later ages is elucidated from both FTIR and SEM analysis, highlighting only minor changes in gel development after 2 days. It is believed that the lack of further development is related to the low availability of Ca in the precursor material and could be alleviated by blending with Ca-rich additives. CS can be classified as a useful precursor for replacing GGBFS in the production of alkali-activated cements.

The expectation of producing high early strength from the addition of CAC, as seen in conventional CAC hydration behaviour, was originally postulated as a way to reduce initial activator doses for alkali-activated cements. Unexpectedly, the results obtained by blending GGBFS with CAC additions exhibit the converse trend: a delay of up to 3-4 days in reaction kinetics is seen in 10 wt. % CAC blends. This retarding effect is more pronounced in systems with higher alkalinity, by increasing the

molarity of the sodium hydroxide activator solution and with the inclusion of sodium silicates. It is believed that the dissolution of CAC occurs rapidly before the GGBFS component, forming cubic aluminate hydrates (C_3AH_6) from the onset of reaction which inhibit the further dissolution of GGBFS. Further work is required to elucidate the dominant reaction mechanism.

Identifying suitable waste materials may require case-by-case analysis, and a systematic methodology that includes materials characterisation, experimental formulation, binder characterisation, and final evaluation is now needed. This can lead, however, to a future simplified process of designing novel binders with tailored properties while increasing the fundamental understanding of AACs.

Several aspects should also be considered to advance the understanding of alkali-activation technology. Firstly, it would be essential to explore the specific surface area of precursors and their Blaine fineness to gain additional insights into reactivity. This investigation will shed light on how finer particles can enhance the efficiency of the reaction with alkaline solutions, resulting in faster setting times, increased strength and packing, and potential improved durability of alkali-activated materials. Additionally, studies focusing on alkali-activation of calcined clays as sole systems, rather than blended systems, are needed to better understand their unique properties and potential advantages. Exploring alternative methods for waste clay activation beyond calcination, such as mechanochemical activation, should be considered, especially given the substantial muscovite content.

Further research should focus on characterising other fundamental properties of all the considered AACs, such as long-term durability and late-age performance, across all systems. Comparisons with upscaling formulations will provide valuable information on the scalability and practicality of these systems in real-world applications. Additionally, investigating the effects of leaching in mortars and concretes containing CS will contribute to a comprehensive understanding of their behaviour in various conditions. By addressing these aspects, future research can pave the way for more

sustainable and effective alkali-activated materials and alternative precursors in the construction industry.

In conclusion, the use of waste materials as alternative precursors for AACs is a promising strategy for achieving sustainable construction practices, and the incorporation of waste-derived precursors in the production of AACs not only reduces the demand for virgin materials but also reduces the environmental impact of the construction industry by diverting waste from landfills and reducing CO₂ emissions. Furthermore, the use of waste materials in the production of alkali-activated cements can potentially create a market for waste materials, thereby incentivising their proper disposal and management.

References

- [1] UNFCCC, “The Paris Agreement,” 2015. doi: 10.1126/science.ns-2.26.131.
- [2] IPCC, “Global Warming of 1.5 °C,” 2019. [Online]. Available: <https://www.ipcc.ch/sr15/>.
- [3] J. M. Uratani and S. Griffiths, “A forward looking perspective on the cement and concrete industry: Implications of growth and development in the Global South,” *Energy Res. Soc. Sci.*, vol. 97, no. 102972, 2023, doi: <https://doi.org/10.1016/j.erss.2023.102972>.
- [4] S. Dhar, M. Pathak, and P. R. Shukla, “Transformation of India’s steel and cement industry in a sustainable 1.5 °C world,” *Energy Policy*, vol. 137, no. 111104, 2020, doi: <https://doi.org/10.1016/j.enpol.2019.111104>.
- [5] C. Tan, X. Yu, and Y. Guan, “A technology-driven pathway to net-zero carbon emissions for China’s cement industry,” *Appl. Energy*, vol. 325, no. 119804, 2022, doi: <https://doi.org/10.1016/j.apenergy.2022.119804>.
- [6] M. Yetano Roche, “Built for net-zero: analysis of long-term greenhouse gas emission pathways for the Nigerian cement sector,” *J. Clean. Prod.*, vol. 383, no. 135446, 2023, doi: <https://doi.org/10.1016/j.jclepro.2022.135446>.
- [7] E. Hache, M. Simoën, G. S. Seck, C. Bonnet, A. Jabberi, and S. Carcanague, “The impact of future power generation on cement demand: An international and regional assessment based on climate scenarios,” *Int. Econ.*, vol. 163, pp. 114–133, 2020, doi: <https://doi.org/10.1016/j.inteco.2020.05.002>.
- [8] S. A. Miller, A. Horvath, and P. J. M. Monteiro, “Readily implementable techniques can cut annual CO₂ emissions from the production of concrete by over 20%,” *Environ. Res. Lett.*, vol. 11, no. 074029, 2016, doi: 10.1088/1748-9326/11/7/074029.

- [9] P. J. M. Monteiro, S. A. Miller, and A. Horvath, "Towards sustainable concrete," *Nat. Mater.*, vol. 16, no. 7, pp. 698–699, 2017, doi: 10.1038/nmat4930.
- [10] S. A. Miller, G. Habert, R. J. Myers, and J. T. Harvey, "Achieving net zero greenhouse gas emissions in the cement industry via value chain mitigation strategies," *One Earth*, vol. 4, no. 10, pp. 1398–1411, 2021, doi: <https://doi.org/10.1016/j.oneear.2021.09.011>.
- [11] I. H. Shah, S. A. Miller, D. Jiang, and R. J. Myers, "Cement substitution with secondary materials can reduce annual global CO₂ emissions by up to 1.3 gigatons," *Nat. Commun.*, vol. 13, no. 1, pp. 1–11, 2022, doi: 10.1038/s41467-022-33289-7.
- [12] A. Fernández Jiménez, V. Ramesh, T. Terai, A. Palomo, and K. Ikeda, "Synthesis and thermal behavior of different aluminosilicate gels," *J. Non. Cryst. Solids*, vol. 352, pp. 2061–2066, 2006, doi: 10.1016/j.jnoncrysol.2006.03.037.
- [13] M. Criado, A. Palomo, and A. Fernández-Jiménez, "Alkali activation of fly ashes. Part 1: Effect of curing conditions on the carbonation of the reaction products," *Fuel*, vol. 84, no. 16, pp. 2048–2054, 2005, doi: <https://doi.org/10.1016/j.fuel.2005.03.030>.
- [14] S.-D. Wang, X.-C. Pu, K. L. Scrivener, and P. L. Pratt, "Alkali-activated slag cement and concrete: a review of properties and problems," *Adv. Cem. Res.*, vol. 7, no. 27, pp. 93–102, 1995, doi: 10.1680/adcr.1995.7.27.93.
- [15] S.-D. Wang and K. L. Scrivener, "Hydration products of alkali activated slag cement," *Cem. Concr. Res.*, vol. 25, no. 3, pp. 561–571, 1995, doi: [https://doi.org/10.1016/0008-8846\(95\)00045-E](https://doi.org/10.1016/0008-8846(95)00045-E).
- [16] R. J. Myers, S. A. Bernal, R. San Nicolas, and J. L. Provis, "Generalized structural description of calcium–sodium aluminosilicate hydrate gels: the cross-linked substituted tobermorite model," *Langmuir*, vol. 29, no. 17, pp.

- 5294–5306, 2013, doi: 10.1021/la4000473.
- [17] P. Duxson, J. L. Provis, G. C. Lukey, and J. S. J. van Deventer, “The role of inorganic polymer technology in the development of ‘green concrete,’” *Cem. Concr. Res.*, vol. 37, no. 12, pp. 1590–1597, 2007, doi: <https://doi.org/10.1016/j.cemconres.2007.08.018>.
- [18] T. Bakharev, J. G. Sanjayan, and Y.-B. Cheng, “Sulfate attack on alkali-activated slag concrete,” *Cem. Concr. Res.*, vol. 32, no. 2, pp. 211–216, 2002, doi: [https://doi.org/10.1016/S0008-8846\(01\)00659-7](https://doi.org/10.1016/S0008-8846(01)00659-7).
- [19] A. Van Riessen, W. Rickard, and J. Sanjayan, “15 - Thermal properties of geopolymers,” in *Geopolymers*, J. L. Provis and J. S. J. van Deventer, Eds. Woodhead Publishing, 2009, pp. 315–342.
- [20] J. L. Provis *et al.*, “Chapter 2. Historical Aspects and Overview,” in *Alkali Activated Materials: State-of-the-Art Report, RILEM TC 224-AAM*, J. L. Provis and J. S. J. van Deventer, Eds. RILEM/Springer, Dordrecht, 2014, pp. 11–57.
- [21] World Commission on Environment and Development, *The Brundtland Report: “Our Common Future,”* vol. 4, no. 1. Oxford University Press, 1987.
- [22] M. Garside, “Cement production worldwide from 1995 to 2022 (in billion metric tons),” *US Geological Survey*, 2023. <https://www.statista.com/statistics/1087115/global-cement-production-volume/> (accessed Jan. 31, 2023).
- [23] J. G. J. . Oliver, G. Janssens-Maenhout, M. Muntean, and J. A. H. W. Peters, “Trends in global CO₂ emissions.” PBL Publishers, The Hague, 2016.
- [24] R. M. Andrew, “Global CO₂ emissions from cement production, 1928 – 2017,” *Earth Syst. Sci. Data*, vol. 10, no. 4, pp. 1–20, 2021.
- [25] M. Roser and L. Rodés-Guirao, “Future population growth,” *Our World in Data*. 2013, Accessed: Feb. 07, 2023. [Online]. Available:

<https://ourworldindata.org/future-population-growth#>.

- [26] E. Gartner and H. Hirao, "A review of alternative approaches to the reduction of CO₂ emissions associated with the manufacture of the binder phase in concrete," *Cem. Concr. Res.*, vol. 78, pp. 126–142, 2015, doi: 10.1016/j.cemconres.2015.04.012.
- [27] L. Coppola *et al.*, "Binders alternative to Portland cement and waste management for sustainable construction," *J. Appl. Biomater. Funct. Mater.*, vol. 16, no. 3, pp. 186–202, 2018, doi: 10.1177/2280800018782845.
- [28] Jasper Whiting, "Manufacture of cement - US Patent US544706A," 1895.
- [29] H. Kuhl, "Slag cement and process of making the same - US Patent US900939A," 1908.
- [30] A. O. Purdon, "The action of alkalis on blast-furnace slag," *J. Soc. Chem. Ind.*, vol. 59, no. 9, pp. 191–202, 1940.
- [31] V. D. Glukhovskiy, "Soil silicates, their properties, technology and manufacturing and fields of application," Ph.D thesis, Kiev Civil Engineering Institute, Kiev, 1965.
- [32] C. Shi, D. Roy, and P. Krivenko, *Alkali-Activated Cements and Concretes*. Taylor & Francis, London, 2006.
- [33] J. Davidovits, "Mineral polymers and methods of making them - US Patent 4349386," U. S. Patent 4,349,386, 1982.
- [34] J. Davidovits, *Geopolymer Chemistry and Applications*. Institut Géopolymère, Saint-Quentin, 2008.
- [35] P. G. Malone, C. J. Randall, and T. Kirkpatrick, "Potential application of alkali-activated aluminosilicate binders in military operations," Houston, U.S. Army Corps of Engineers, 1985.

- [36] T. B. Husbands, P. G. Malone, and L. D. Wakeley, "Performance of concretes proportioned with Pyrament blended cement," Vicksburg, U.S. Army Corps of Engineers, 1994.
- [37] T. Gourley, "Geopolymers in Australia," *J. Aust. Ceram. Soc.*, vol. 50, pp. 102–110, 2014.
- [38] J. L. Provis, "Alkali-activated materials," *Cem. Concr. Res.*, vol. 114, pp. 40–48, 2018, doi: 10.1016/j.cemconres.2017.02.009.
- [39] J. L. Provis and J. S. J. van Deventer, *Alkali-Activated Materials, State-of-the-Art Report, RILEM TC 224-AAM*. RILEM/Springer, Dordrecht, 2014.
- [40] EPA, "11.6 Portland Cement Manufacturing," *Mineral Products Industry*. 2020.
- [41] L. Barcelo, "Cement and carbon emissions," *Mater. Struct.*, vol. 47, no. 6, pp. 1055–1065, 2014, doi: 10.1617/s11527-013-0114-5.
- [42] J. S. Damtoft, J. Lukasik, D. Herfort, D. Sorrentino, and E. M. Gartner, "Sustainable development and climate change initiatives," *Cem. Concr. Res.*, vol. 38, no. 2, pp. 115–127, 2008, doi: <https://doi.org/10.1016/j.cemconres.2007.09.008>.
- [43] U. S. Geological Survey, "Mineral Commodity Summaries," 2019.
- [44] G. Habert and C. Ouellet-Plamondon, "Recent update on the environmental impact of geopolymers," *RILEM Tech. Lett.*, vol. 1, pp. 17–23, 2016, doi: 10.21809/rilemtechlett.2016.6.
- [45] C. Ouellet-Plamondon and G. Habert, "Life cycle assessment (LCA) of alkali-activated cements and concretes," in *Handbook of Alkali-Activated Cements, Mortars and Concretes*, F. Pacheco-Torgal, J. A. Labrincha, C. Leonelli, A. Palomo, and P. Chindapasirt, Eds. Woodhead Publishing, 2015, pp. 663–686.
- [46] G. Habert, J. B. d'Espinose de Lacaillerie, and N. Roussel, "An environmental

- evaluation of geopolymers based concrete production: reviewing current research trends," *J. Clean. Prod.*, vol. 19, no. 11, pp. 1229–1238, 2011, doi: <https://doi.org/10.1016/j.jclepro.2011.03.012>.
- [47] P. Van den Heede and N. De Belie, "Environmental impact and life cycle assessment (LCA) of traditional and 'green' concretes: Literature review and theoretical calculations," *Cem. Concr. Compos.*, vol. 34, no. 4, pp. 431–442, 2012, doi: <https://doi.org/10.1016/j.cemconcomp.2012.01.004>.
- [48] P. Duxson, A. Fernández-Jiménez, J. L. Provis, G. C. Lukey, A. Palomo, and J. S. J. Van Deventer, "Geopolymer technology: The current state of the art," *J. Mater. Sci.*, vol. 42, no. 9, pp. 2917–2933, 2007, doi: 10.1007/s10853-006-0637-z.
- [49] E. U. von Weizsäcker, K. Hargroves, M. Smith, C. Desha, and P. Stasinopoulos, *Factor Five: Transforming the Global Economy through 80 % Improvements in Resource Productivity*. Earthscan Routledge, 2009.
- [50] E. M. McGuire, J. L. Provis, P. Duxson, and R. Crawford, "Geopolymer concrete is there an alternative and viable technology in the concrete sector which reduces carbon emissions," *Proceedings of Concrete 2011: Building a Sustainable Future*. Perth, 2011.
- [51] A. Heath, K. Paine, and M. McManus, "Minimising the global warming potential of clay based geopolymers," *J. Clean. Prod.*, vol. 78, pp. 75–83, 2014, doi: 10.1016/j.jclepro.2014.04.046.
- [52] B. C. McLellan, R. P. Williams, J. Lay, A. van Riessen, and G. D. Corder, "Costs and carbon emissions for geopolymer pastes in comparison to ordinary portland cement," *J. Clean. Prod.*, vol. 19, no. 9, pp. 1080–1090, 2011, doi: <https://doi.org/10.1016/j.jclepro.2011.02.010>.
- [53] I. Bianco, B. Ap Dafydd Tomos, and R. Vinai, "Analysis of the environmental impacts of alkali-activated concrete produced with waste glass-derived silicate activator – A LCA study," *J. Clean. Prod.*, vol. 316, no. 128383, 2021, doi:

<https://doi.org/10.1016/j.jclepro.2021.128383>.

- [54] P. Duxson and J. Provis, "Designing precursors for geopolymer cements," *J. Am. Ceram. Soc.*, vol. 91, pp. 3864–3869, 2008, doi: 10.1111/j.1551-2916.2008.02787.x.
- [55] B. Lothenbach, K. Scrivener, and R. D. Hooton, "Supplementary cementitious materials," *Cem. Concr. Res.*, vol. 41, no. 12, pp. 1244–1256, 2011, doi: 10.1016/j.cemconres.2010.12.001.
- [56] R. J. Kirkpatrick, "MAS NMR spectroscopy of minerals and glasses," *Spectrosc. Methods Mineral. Geol.*, vol. 18, pp. 341–403, 1988.
- [57] W. Loewenstein, "The distribution of aluminum in the tetrahedra of silicates and aluminates," *Am. Mineral.*, vol. 39, no. 1–2, pp. 92–96, 1954.
- [58] B. Walkley, G. J. Rees, R. San Nicolas, J. S. J. Van Deventer, J. V. Hanna, and J. L. Provis, "New structural model of hydrous sodium aluminosilicate gels and the role of charge-balancing extra-framework Al," *J. Phys. Chem. C*, vol. 122, no. 10, pp. 5673–5685, 2018, doi: 10.1021/acs.jpcc.8b00259.
- [59] J. L. Provis, G. C. Lukey, and J. S. J. van Deventer, "Do geopolymers actually contain nanocrystalline zeolites? A reexamination of existing results," *Chem. Mater.*, vol. 17, no. 12, pp. 3075–3085, 2005, doi: 10.1021/cm050230i.
- [60] S. Onutai, J. Sato, and T. Osugi, "Possible pathway of zeolite formation through alkali activation chemistry of metakaolin for geopolymer–zeolite composite materials: ATR-FTIR study," *J. Solid State Chem.*, vol. 319, no. 123808, 2023, doi: <https://doi.org/10.1016/j.jssc.2022.123808>.
- [61] F. Lolli, H. Manzano, J. L. Provis, M. C. Bignozzi, and E. Masoero, "Atomistic simulations of geopolymer models: The impact of disorder on structure and mechanics," *ACS Appl. Mater. Interf.*, vol. 10, no. 26, pp. 22809–22820, 2018, doi: 10.1021/acsami.8b03873.

- [62] P. Rožek, M. Król, and W. Mozgawa, "Geopolymer-zeolite composites: A review," *J. Clean. Prod.*, vol. 230, pp. 557–579, 2019, doi: <https://doi.org/10.1016/j.jclepro.2019.05.152>.
- [63] J. L. Provis and J. S. J. van Deventer, "Geopolymerisation kinetics. 2. Reaction kinetic modelling," *Chem. Eng. Sci.*, vol. 62, pp. 2318–2329, 2007, doi: [10.1016/j.ces.2007.01.028](https://doi.org/10.1016/j.ces.2007.01.028).
- [64] H. Rahier, J. Wastiels, M. Biesemans, R. Willlem, G. Van Assche, and B. Van Mele, "Reaction mechanism, kinetics and high temperature transformations of geopolymers," *J. Mater. Sci.*, vol. 42, no. 9, pp. 2982–2996, 2007, doi: [10.1007/s10853-006-0568-8](https://doi.org/10.1007/s10853-006-0568-8).
- [65] I. Garcia-Lodeiro, A. Palomo, and A. Fernández-Jiménez, "2 - An overview of the chemistry of alkali-activated cement-based binders," in *Handbook of Alkali-Activated Cements, Mortars and Concretes*, F. Pacheco-Torgal, J. A. Labrincha, C. Leonelli, A. Palomo, and P. Chindapasirt, Eds. Oxford: Woodhead Publishing, 2015, pp. 19–47.
- [66] P. Duxson, J. L. Provis, G. C. Lukey, S. W. Mallicoat, W. M. Kriven, and J. S. J. Van Deventer, "Understanding the relationship between geopolymer composition, microstructure and mechanical properties," *Colloids Surfaces A Physicochem. Eng. Asp.*, vol. 269, no. 1–3, pp. 47–58, 2005, doi: [10.1016/j.colsurfa.2005.06.060](https://doi.org/10.1016/j.colsurfa.2005.06.060).
- [67] M. Criado, A. Fernández-Jiménez, and A. Palomo, "Alkali activation of fly ash: Effect of the SiO₂/Na₂O ratio: Part I: FTIR study," *Micropor. Mesopor. Mater.*, vol. 106, no. 1, pp. 180–191, 2007, doi: <https://doi.org/10.1016/j.micromeso.2007.02.055>.
- [68] G. Le Saoût, M. Ben Haha, F. Winnefeld, and B. Lothenbach, "Hydration degree of alkali-activated slags: a ²⁹Si NMR study," *J. Am. Ceram. Soc.*, vol. 94, no. 12, pp. 4541–4547, 2011, doi: <https://doi.org/10.1111/j.1551->

2916.2011.04828.x.

- [69] J. L. Provis, P. Duxson, G. C. Lukey, and J. S. J. van Deventer, "Statistical thermodynamic model for Si/Al ordering in amorphous aluminosilicates," *Chem. Mater.*, vol. 17, no. 11, pp. 2976–2986, 2005, doi: 10.1021/cm050219i.
- [70] F. Pacheco-Torgal, Z. Abdollahnejad, A. F. Camões, M. Jamshidi, and Y. Ding, "Durability of alkali-activated binders: A clear advantage over Portland cement or an unproven issue?," *Constr. Build. Mater.*, vol. 30, pp. 400–405, 2012, doi: 10.1016/j.conbuildmat.2011.12.017.
- [71] A. Z. Khalifa *et al.*, "Advances in alkali-activation of clay minerals," *Cem. Concr. Res.*, vol. 132, no. 106050, 2020, doi: 10.1016/j.cemconres.2020.106050.
- [72] C. Tournassat, I. C. Bourg, C. I. Steefel, and F. Bergaya, "Chapter 1 - Surface Properties of Clay Minerals," in *Natural and Engineered Clay Barriers*, vol. 6, C. Tournassat, C. I. Steefel, I. C. Bourg, and F. B. T.-D. in C. S. Bergaya, Eds. Elsevier, 2015, pp. 5–31.
- [73] R. H. Worden *et al.*, "Chlorite in sandstones," *Earth-Science Rev.*, vol. 204, p. 103105, 2020, doi: <https://doi.org/10.1016/j.earscirev.2020.103105>.
- [74] C. He, E. Makovicky, and B. Osbæck, "Thermal stability and pozzolanic activity of raw and calcined mixed-layer mica/smectite," *Appl. Clay Sci.*, vol. 17, no. 3, pp. 141–161, 2000, doi: [https://doi.org/10.1016/S0169-1317\(00\)00011-9](https://doi.org/10.1016/S0169-1317(00)00011-9).
- [75] C. Kuenzel, L. J. Vandeperre, S. Donatello, A. R. Boccaccini, and C. Cheeseman, "Ambient temperature drying shrinkage and cracking in metakaolin-based geopolymers," *J. Am. Ceram. Soc.*, vol. 95, no. 10, pp. 3270–3277, 2012, doi: <https://doi.org/10.1111/j.1551-2916.2012.05380.x>.
- [76] W. Smykatz-Kloss, K. Heide, and W. Klinke, "Chapter 11 - Applications of Thermal Methods in The Geosciences," in *Handbook of Thermal Analysis and*

- Calorimetry, Applications to Inorganic and Miscellaneous Materials*, vol. 2, M. E. Brown and P. K. Gallagher, Eds. Elsevier Science B.V., 2003, pp. 451–593.
- [77] N. Msinjili, G. Gluth, P. Sturm, N. Vogler, and H.-C. Kühne, “Comparison of calcined illitic clays (brick clays) and low-grade kaolinitic clays as supplementary cementitious materials,” *Mater. Struct.*, vol. 52, 2019, doi: 10.1617/s11527-019-1393-2.
- [78] B. F. Bohor, “High-temperature phase development in illitic clays,” *Clays Clay Miner.*, vol. 12, no. 1, pp. 233–246, 1963, doi: 10.1346/CCMN.1963.0120125.
- [79] P. M. Nigay, T. Cutard, and A. Nzihou, “The impact of heat treatment on the microstructure of a clay ceramic and its thermal and mechanical properties,” *Ceram. Int.*, vol. 43, no. 2, pp. 1747–1754, 2017, doi: 10.1016/j.ceramint.2016.10.084.
- [80] S. Hollanders, R. Adriaens, J. Skibsted, Ö. Cizer, and J. Elsen, “Pozzolanic reactivity of pure calcined clays,” *Appl. Clay Sci.*, vol. 132–133, pp. 552–560, 2016, doi: 10.1016/j.clay.2016.08.003.
- [81] R. Fernandez, F. Martirena, and K. L. Scrivener, “The origin of the pozzolanic activity of calcined clay minerals: A comparison between kaolinite, illite and montmorillonite,” *Cem. Concr. Res.*, vol. 41, no. 1, pp. 113–122, 2011, doi: 10.1016/j.cemconres.2010.09.013.
- [82] E. Kłosek-Wawrzyn, J. Małolepszy, and P. Murzyn, “Sintering behavior of kaolin with calcite,” *Procedia Eng.*, vol. 57, pp. 572–582, 2013, doi: 10.1016/j.proeng.2013.04.073.
- [83] C. E. White, J. L. Provis, T. Proffen, D. P. Riley, and J. S. J. Van Deventer, “Density functional modeling of the local structure of kaolinite subjected to thermal dehydroxylation,” *J. Phys. Chem. A*, vol. 114, no. 14, pp. 4988–4996, 2010, doi: 10.1021/jp911108d.

- [84] C. E. White, J. L. Provis, T. Proffen, and J. S. J. van Deventer, "Molecular Mechanisms Responsible for the Structural Changes Occurring During Geopolymerization: Multiscale Simulation," *AIChE J.*, vol. 59, no. 7, pp. 2241–2253, 2012, doi: 10.1002/aic.
- [85] J. L. Provis, P. Duxson, and J. S. J. van Deventer, "The role of particle technology in developing sustainable construction materials," *Adv. Powder Technol.*, vol. 21, no. 1, pp. 2–7, 2010, doi: <https://doi.org/10.1016/j.appt.2009.10.006>.
- [86] R. Pouhet and M. Cyr, "Formulation and performance of flash metakaolin geopolymer concretes," *Constr. Build. Mater.*, vol. 120, pp. 150–160, 2016, doi: 10.1016/j.conbuildmat.2016.05.061.
- [87] R. San Nicolas, M. Cyr, and G. Escadeillas, "Characteristics and applications of flash metakaolins," *Appl. Clay Sci.*, vol. 83–84, pp. 253–262, 2013, doi: 10.1016/j.clay.2013.08.036.
- [88] R. Pouhet, M. Cyr, and R. Bucher, "Influence of the initial water content in flash calcined metakaolin-based geopolymer," *Constr. Build. Mater.*, vol. 201, pp. 421–429, 2019, doi: 10.1016/j.conbuildmat.2018.12.201.
- [89] S. Salvador, "Pozzolanic properties of flash-calcined kaolinite: A comparative study with soak-calcined products," *Cem. Concr. Res.*, vol. 25, no. 1, pp. 102–112, 1995, doi: [https://doi.org/10.1016/0008-8846\(94\)00118-I](https://doi.org/10.1016/0008-8846(94)00118-I).
- [90] S. Lawther, A. McIntosh, S. Nanukuttan, J. L. Provis, and M. Soutsos, "Understanding the microstructure of alternative binder systems - banahCEM, a metakaolin based geopolymer.," 2016.
- [91] H. Peng, C. Cui, Z. Liu, C. Cai, and Y. Liu, "Synthesis and reaction mechanism of an alkali-activated metakaolin-slag composite system at room temperature," *J. Mater. Civ. Eng.*, vol. 31, no. 4018345, 2019, doi: 10.1061/(ASCE)MT.1943-5533.0002558.

- [92] R. Siddique and J. Klaus, "Influence of metakaolin on the properties of mortar and concrete: A review," *Appl. Clay Sci.*, vol. 43, no. 3–4, pp. 392–400, 2009, doi: 10.1016/j.clay.2008.11.007.
- [93] M. Garside, "Refinery production of copper worldwide from 2000 to 2021," *Statista*, 2022. <https://www.statista.com/statistics/254917/total-global-copper-production-since-2006/> (accessed Mar. 18, 2023).
- [94] B. Gorai, R. K. Jana, and Premchand, "Characteristics and utilisation of copper slag—a review," *Resour. Conserv. Recycl.*, vol. 39, no. 4, pp. 299–313, 2003, doi: 10.1016/S0921-3449(02)00171-4.
- [95] C. Shi, C. Meyer, and A. Behnood, "Utilization of copper slag in cement and concrete," *Resour. Conserv. Recycl.*, vol. 52, no. 10, pp. 1115–1120, 2008, doi: <https://doi.org/10.1016/j.resconrec.2008.06.008>.
- [96] A. K. Biswas and W. G. Davenport, "Chapter 4 - Matte Smelting," in *Extractive Metallurgy of Copper*, Pergamon, 1994, pp. 74–99.
- [97] B. M. Mithun and M. C. Narasimhan, "Performance of alkali activated slag concrete mixes incorporating copper slag as fine aggregate," *J. Clean. Prod.*, vol. 112, pp. 837–844, 2016, doi: <https://doi.org/10.1016/j.jclepro.2015.06.026>.
- [98] M. Khanzadi and A. Behnood, "Mechanical properties of high-strength concrete incorporating copper slag as coarse aggregate," *Constr. Build. Mater.*, vol. 23, no. 6, pp. 2183–2188, 2009, doi: <https://doi.org/10.1016/j.conbuildmat.2008.12.005>.
- [99] N. M. Piatak, M. B. Parsons, and R. R. Seal, "Characteristics and environmental aspects of slag: A review," *Appl. Geochemistry*, vol. 57, pp. 236–266, 2015, doi: <https://doi.org/10.1016/j.apgeochem.2014.04.009>.
- [100] Y. Jiang, T.-C. Ling, C. Shi, and S.-Y. Pan, "Characteristics of steel slags and their use in cement and concrete—A review," *Resour. Conserv. Recycl.*, vol. 136,

- pp. 187–197, 2018, doi: <https://doi.org/10.1016/j.resconrec.2018.04.023>.
- [101] Y. Fan, B. Zhang, J. Song, V. Volski, G. Vandenbosch, and M. Guo, “An innovated application of reutilize copper smelter slag for cement-based electromagnetic interference composites,” *Sci. Rep.*, vol. 8, no. 1, pp. 1–7, 2018, doi: [10.1038/s41598-018-34680-5](https://doi.org/10.1038/s41598-018-34680-5).
- [102] A. Peys, “Inorganic polymers from CaO-FeO-SiO₂ slags. Processing, reaction mechanism and molecular structure,” Ph.D. thesis, KU Leuven, Leuven, 2018.
- [103] M. A. Gómez-Casero, L. Pérez-Villarejo, P. J. Sánchez-Soto, and D. Eliche-Quesada, “Comparative study of alkali activated cements based on metallurgical slags, in terms of technological properties developed,” *Sustain. Chem. Pharm.*, vol. 29, no. 100746, 2022, doi: <https://doi.org/10.1016/j.scp.2022.100746>.
- [104] A. Peys, A. P. Douvalis, V. Hallet, H. Rahier, B. Blanpain, and Y. Pontikes, “Inorganic polymers from CaO-FeO_x-SiO₂ slag: the start of oxidation of Fe and the formation of a mixed valence binder,” *Front. Mater.*, vol. 6, no. 212, pp. 1–10, 2019.
- [105] C. Siakati, A. P. Douvalis, P. Ziogas, A. Peys, and Y. Pontikes, “Impact of the solidification path of FeO_x-SiO₂ slags on the resultant inorganic polymers,” *J. Am. Ceram. Soc.*, vol. 103, no. 3, pp. 2173–2184, 2020, doi: [10.1111/jace.16869](https://doi.org/10.1111/jace.16869).
- [106] S. Onisei, A. P. Douvalis, A. Malfliet, A. Peys, and Y. Pontikes, “Inorganic polymers made of fayalite slag: On the microstructure and behavior of Fe,” *J. Am. Ceram. Soc.*, vol. 101, no. 6, pp. 2245–2257, 2018, doi: [10.1111/jace.15420](https://doi.org/10.1111/jace.15420).
- [107] S. Simon, G. J. G. Gluth, A. Peys, S. Onisei, D. Banerjee, and Y. Pontikes, “The fate of iron during the alkali-activation of synthetic (CaO-)FeO_x-SiO₂ slags: An Fe K-edge XANES study,” *J. Am. Ceram. Soc.*, vol. 101, no. 5, pp. 2107–2118, 2018, doi: <https://doi.org/10.1111/jace.15354>.

- [108] C. E. White, L. L. Daemen, M. Hartl, and K. Page, "Intrinsic differences in atomic ordering of calcium (alumino)silicate hydrates in conventional and alkali-activated cements," *Cem. Concr. Res.*, vol. 67, pp. 66–73, 2015, doi: <https://doi.org/10.1016/j.cemconres.2014.08.006>.
- [109] I. G. Richardson and G. W. Groves, "Microstructure and microanalysis of hardened cement pastes involving ground granulated blast-furnace slag," *J. Mater. Sci.*, vol. 27, no. 22, pp. 6204–6212, 1992, doi: 10.1007/BF01133772.
- [110] R. J. Myers, S. A. Bernal, and J. L. Provis, "A thermodynamic model for C-(N-)A-S-H gel: CNASH_{ss}. Derivation and validation," *Cem. Concr. Res.*, vol. 66, pp. 27–47, 2014, doi: 10.1016/j.cemconres.2014.07.005.
- [111] H. F. W. Taylor, "Nanostructure of CSH: Current status," *Adv. Cem. Based Mater.*, vol. 1, no. 1, pp. 38–46, 1993, doi: 10.1016/1065-7355(93)90006-A.
- [112] F. Puertas, M. Palacios, H. Manzano, J. S. Dolado, A. Rico, and J. Rodríguez, "A model for the C-A-S-H gel formed in alkali-activated slag cements," *J. Eur. Ceram. Soc.*, vol. 31, no. 12, pp. 2043–2056, 2011, doi: <https://doi.org/10.1016/j.jeurceramsoc.2011.04.036>.
- [113] J. I. Escalante-García, A. F. Fuentes, A. Gorokhovskiy, P. E. Fraire-Luna, and G. Mendoza-Suarez, "Hydration products and reactivity of blast-furnace slag activated by various alkalis," *J. Am. Ceram. Soc.*, vol. 86, no. 12, pp. 2148–2153, 2003, doi: 10.1111/j.1151-2916.2003.tb03623.x.
- [114] D. Damidot, B. Lothenbach, D. Herfort, and F. P. Glasser, "Thermodynamics and cement science," *Cem. Concr. Res.*, vol. 41, no. 7, pp. 679–695, 2011, doi: 10.1016/j.cemconres.2011.03.018.
- [115] B. Lothenbach, T. Matschei, G. Möschner, and F. P. Glasser, "Thermodynamic modelling of the effect of temperature on the hydration and porosity of Portland cement," *Cem. Concr. Res.*, vol. 38, no. 1, pp. 1–18, 2008, doi: 10.1016/j.cemconres.2007.08.017.

- [116] I. G. Richardson, A. R. Brough, R. Brydson, G. W. Groves, and C. M. Dobson, "Location of aluminum in substituted calcium silicate hydrate (C-S-H) gels as determined by ^{29}Si and ^{27}Al NMR and EELS," *J. Am. Ceram. Soc.*, vol. 76, no. 9, pp. 2285–2288, 1993, doi: <https://doi.org/10.1111/j.1151-2916.1993.tb07765.x>.
- [117] R. J. Myers, B. Lothenbach, S. A. Bernal, and J. L. Provis, "Thermodynamic modelling of alkali-activated slag cements," *Appl. Geochemistry*, vol. 61, pp. 233–247, 2015, doi: <https://doi.org/10.1016/j.apgeochem.2015.06.006>.
- [118] J. L. Provis and S. A. Bernal, "Geopolymers and related alkali-activated materials," *Annu. Rev. Mater. Res.*, vol. 44, no. 1, pp. 299–327, 2014, doi: [10.1146/annurev-matsci-070813-113515](https://doi.org/10.1146/annurev-matsci-070813-113515).
- [119] World Steel Association, "World crude steel production from 2012 to 2021," *Statista*, 2022. <https://www.statista.com/statistics/267264/world-crude-steel-production/?locale=en> (accessed Mar. 16, 2023).
- [120] World Steel Association, "Steel industry co-products," 2021. [Online]. Available: <https://worldsteel.org/publications/fact-sheets/>.
- [121] I. Z. Yildirim and M. Prezzi, "Chemical, mineralogical, and morphological properties of steel slag," *Adv. Civ. Eng.*, vol. 2011, no. 463638, 2011, doi: [10.1155/2011/463638](https://doi.org/10.1155/2011/463638).
- [122] K. Gong and C. E. White, "Impact of chemical variability of ground granulated blast-furnace slag on the phase formation in alkali-activated slag pastes," *Cem. Concr. Res.*, vol. 89, pp. 310–319, 2016, doi: <https://doi.org/10.1016/j.cemconres.2016.09.003>.
- [123] B. Tailing and J. Brandstetr, "Present state and future of alkali-activated slag concretes," in *American Concrete Institute, ACI Special Publication*, 1989, vol. SP-114, pp. 1519–1545, doi: [10.14359/1873](https://doi.org/10.14359/1873).
- [124] M. Ben Haha, B. Lothenbach, G. Le Saout, and F. Winnefeld, "Influence of slag

- chemistry on the hydration of alkali-activated blast-furnace slag — Part I: Effect of MgO,” *Cem. Concr. Res.*, vol. 41, no. 9, pp. 955–963, 2011, doi: <https://doi.org/10.1016/j.cemconres.2011.05.002>.
- [125] S. A. Bernal *et al.*, “MgO content of slag controls phase evolution and structural changes induced by accelerated carbonation in alkali-activated binders,” *Cem. Concr. Res.*, vol. 57, pp. 33–43, 2014, doi: <https://doi.org/10.1016/j.cemconres.2013.12.003>.
- [126] C.-L. Hwang, D.-H. Vo, V.-A. Tran, and M. D. Yehualaw, “Effect of high MgO content on the performance of alkali-activated fine slag under water and air curing conditions,” *Constr. Build. Mater.*, vol. 186, pp. 503–513, 2018, doi: <https://doi.org/10.1016/j.conbuildmat.2018.07.129>.
- [127] C. Shi, “Steel slag—Its production, processing, characteristics, and cementitious properties,” *J. Mater. Civ. Eng.*, vol. 16, no. 3, pp. 230–236, 2004, doi: 10.1061/(asce)0899-1561(2004)16:3(230).
- [128] C. Pellegrino, F. Faleschini, and C. Meyer, “2 - Recycled materials in concrete,” in *Developments in the Formulation and Reinforcement of Concrete*, 2nd Edit., S. Mindess, Ed. Woodhead Publishing, 2019, pp. 19–54.
- [129] H. Yi, G. Xu, H. Cheng, J. Wang, Y. Wan, and H. Chen, “An overview of utilization of steel slag,” *Procedia Environ. Sci.*, vol. 16, pp. 791–801, 2012, doi: [10.1016/j.proenv.2012.10.108](https://doi.org/10.1016/j.proenv.2012.10.108).
- [130] Q. Wang and P. Yan, “Hydration properties of basic oxygen furnace steel slag,” *Constr. Build. Mater.*, vol. 24, no. 7, pp. 1134–1140, 2010, doi: <https://doi.org/10.1016/j.conbuildmat.2009.12.028>.
- [131] H. Motz and J. Geiseler, “Products of steel slags an opportunity to save natural resources,” *Waste Manag.*, vol. 21, no. 3, pp. 285–293, 2001, doi: [https://doi.org/10.1016/S0956-053X\(00\)00102-1](https://doi.org/10.1016/S0956-053X(00)00102-1).

- [132] Y.-C. Ding, T.-W. Cheng, P.-C. Liu, and W.-H. Lee, "Study on the treatment of BOF slag to replace fine aggregate in concrete," *Constr. Build. Mater.*, vol. 146, pp. 644–651, 2017, doi: <https://doi.org/10.1016/j.conbuildmat.2017.04.164>.
- [133] H. Yue, S. Hua, H. Qian, X. Yao, Y. Gao, and F. Jiang, "Investigation on applicability of spherical electric arc furnace slag as fine aggregate in superplasticizer-free 3D printed concrete," *Constr. Build. Mater.*, vol. 319, no. 126104, 2022, doi: <https://doi.org/10.1016/j.conbuildmat.2021.126104>.
- [134] N. Rojas, M. Bustamante, P. Muñoz, K. Godoy, and V. Letelier, "Study of properties and behavior of concrete containing EAF slag as coarse aggregate," *Dev. Built Environ.*, no. 100137, 2023, doi: <https://doi.org/10.1016/j.dibe.2023.100137>.
- [135] P. Sukmak, G. Sukmak, P. De Silva, S. Horpibulsuk, S. Kassawat, and A. Suddeepong, "The potential of industrial waste: Electric arc furnace slag (EAF) as recycled road construction materials," *Constr. Build. Mater.*, vol. 368, no. 130393, 2023, doi: <https://doi.org/10.1016/j.conbuildmat.2023.130393>.
- [136] V. J. Ferreira *et al.*, "Evaluation of the steel slag incorporation as coarse aggregate for road construction: technical requirements and environmental impact assessment," *J. Clean. Prod.*, vol. 130, pp. 175–186, 2016, doi: <https://doi.org/10.1016/j.jclepro.2015.08.094>.
- [137] A. Santamaría, V. Ortega-López, M. Skaf, J. A. Chica, and J. M. Manso, "The study of properties and behavior of self compacting concrete containing electric arc furnace slag (EAFS) as aggregate," *Ain Shams Eng. J.*, vol. 11, no. 1, pp. 231–243, 2020, doi: <https://doi.org/10.1016/j.asej.2019.10.001>.
- [138] M. Mastali *et al.*, "Using carbonated BOF slag aggregates in alkali-activated concretes," *Materials (Basel)*, vol. 12, no. 8, p. 1288, 2019, doi: [10.3390/ma12081288](https://doi.org/10.3390/ma12081288).
- [139] K. Sun, X. Peng, S. H. Chu, S. Wang, L. Zeng, and G. Ji, "Utilization of BOF

- steel slag aggregate in metakaolin-based geopolymer," *Constr. Build. Mater.*, vol. 300, no. 124024, 2021, doi: <https://doi.org/10.1016/j.conbuildmat.2021.124024>.
- [140] A. Amani, A. M. Ramezani-pour, and M. Palassi, "Investigation on the sustainable use of electric arc furnace slag aggregates in eco-friendly alkali-activated low fineness slag concrete as a green construction composite," *J. Clean. Prod.*, vol. 307, no. 127257, 2021, doi: <https://doi.org/10.1016/j.jclepro.2021.127257>.
- [141] M. H. Lai, J. Zou, B. Yao, J. C. M. Ho, X. Zhuang, and Q. Wang, "Improving mechanical behavior and microstructure of concrete by using BOF steel slag aggregate," *Constr. Build. Mater.*, vol. 277, no. 122269, 2021, doi: <https://doi.org/10.1016/j.conbuildmat.2021.122269>.
- [142] E. K. Anastasiou, A. Liapis, and M. Papachristoforou, "Life cycle assessment of concrete products for special applications containing EAF slag," *Procedia Environ. Sci.*, vol. 38, pp. 469–476, 2017, doi: <https://doi.org/10.1016/j.proenv.2017.03.138>.
- [143] D. Mombelli, C. Mapelli, S. Barella, C. Di Cecca, G. Le Saout, and E. Garcia-Diaz, "The effect of microstructure on the leaching behaviour of electric arc furnace (EAF) carbon steel slag," *Process Saf. Environ. Prot.*, vol. 102, pp. 810–821, 2016, doi: <https://doi.org/10.1016/j.psep.2016.05.027>.
- [144] S. Kourounis, S. Tsivilis, P. E. Tsakiridis, G. D. Papadimitriou, and Z. Tsibouki, "Properties and hydration of blended cements with steelmaking slag," *Cem. Concr. Res.*, vol. 37, no. 6, pp. 815–822, 2007, doi: <https://doi.org/10.1016/j.cemconres.2007.03.008>.
- [145] M. Frías, J. San-José, and I. Vegas, "Steel slag aggregate in concrete: the effect of ageing on potentially expansive compounds," *Mater. Constr.*, vol. 60, no. 297, pp. 33–46, 2010.

- [146] Q. Song, M.-Z. Guo, L. Wang, and T.-C. Ling, "Use of steel slag as sustainable construction materials: A review of accelerated carbonation treatment," *Resour. Conserv. Recycl.*, vol. 173, no. 105740, 2021, doi: <https://doi.org/10.1016/j.resconrec.2021.105740>.
- [147] G. Albertsson, L. Teng, F. Engstrom, and S. Seetharaman, "Effect of the heat treatment on the chromium partition in CaO-MgO-SiO₂-Cr₂O₃ synthetic slags," *Metall. Mater. Trans. B*, vol. 44, pp. 1586–1597, 2013, doi: 10.1007/s11663-013-9939-0.
- [148] G. Albertsson, F. Engstrom, and L. Teng, "Effect of the heat treatment on the chromium partition in Cr-containing industrial and synthetic slags," *Steel Res. Int.*, vol. 85, no. 10, pp. 1418–1431, 2014, doi: 10.1002/srin.201300231.
- [149] D. Mombelli, C. Mapelli, S. Barella, A. Gruttadauria, G. Le Saout, and E. Garcia-Diaz, "The efficiency of quartz addition on electric arc furnace (EAF) carbon steel slag stability," *J. Hazard. Mater.*, vol. 279C, pp. 586–596, 2014, doi: 10.1016/j.jhazmat.2014.07.045.
- [150] J. Deja, "Immobilization of Cr⁶⁺, Cd²⁺, Zn²⁺ and Pb²⁺ in alkali-activated slag binders," *Cem. Concr. Res.*, vol. 32, no. 12, pp. 1971–1979, 2002, doi: [https://doi.org/10.1016/S0008-8846\(02\)00904-3](https://doi.org/10.1016/S0008-8846(02)00904-3).
- [151] L. Muhmood, S. Vitta, and D. Venkateswaran, "Cementitious and pozzolanic behavior of electric arc furnace steel slags," *Cem. Concr. Res.*, vol. 39, no. 2, pp. 102–109, 2009, doi: <https://doi.org/10.1016/j.cemconres.2008.11.002>.
- [152] L. Kriskova *et al.*, "Effect of mechanical activation on the hydraulic properties of stainless steel slags," *Cem. Concr. Res.*, vol. 42, pp. 778–788, 2012, doi: 10.1016/j.cemconres.2012.02.016.
- [153] Q. Zhao, J. Stark, E. Freyburg, and M. Zhou, "Steam and autoclave treatments on structure characteristics of steel slag," *Adv. Mater. Res.*, vol. 356–360, pp. 1919–1927, 2011.

- [154] Q. Guangren, D. Sun, J.-H. Tay, and L. Zhenyu, "Hydrothermal reaction and autoclave stability of Mg bearing RO phase in steel slag," *Br. Ceram. Trans.*, vol. 101, pp. 159–164, 2002, doi: 10.1179/096797802225003415.
- [155] B. Huo, B. Li, S. Huang, C. Chen, Y. Zhang, and N. Banthia, "Hydration and soundness properties of phosphoric acid modified steel slag powder," *Constr. Build. Mater.*, vol. 254, no. 119319, 2020, doi: <https://doi.org/10.1016/j.conbuildmat.2020.119319>.
- [156] W. Song *et al.*, "Efficient use of steel slag in alkali-activated fly ash-steel slag-ground granulated blast furnace slag ternary blends," *Constr. Build. Mater.*, vol. 259, no. 119814, 2020, doi: <https://doi.org/10.1016/j.conbuildmat.2020.119814>.
- [157] E. Furlani *et al.*, "Synthesis and characterization of geopolymers containing blends of unprocessed steel slag and metakaolin: The role of slag particle size," *Ceram. Int.*, vol. 44, no. 5, pp. 5226–5232, 2018, doi: <https://doi.org/10.1016/j.ceramint.2017.12.131>.
- [158] A. Elkhachine, N. Khachani, M. Saadi, and A. Diouri, "Mineralogy at early age of alkali activated mortar based on binary additions of limestone quarry dust and electric arc furnace slag," *Mater. Today Proc.*, vol. 58, pp. 1566–1572, 2022, doi: <https://doi.org/10.1016/j.matpr.2022.03.459>.
- [159] W. Yang, Y. Xue, S. Wu, Y. Xiao, and M. Zhou, "Performance investigation and environmental application of basic oxygen furnace slag – Rice husk ash based composite cementitious materials," *Constr. Build. Mater.*, vol. 123, pp. 493–500, 2016, doi: <https://doi.org/10.1016/j.conbuildmat.2016.07.051>.
- [160] S. Monosi, M. L. Ruello, and D. Sani, "Electric arc furnace slag as natural aggregate replacement in concrete production," *Cem. Concr. Compos.*, vol. 66, pp. 66–72, 2016, doi: <https://doi.org/10.1016/j.cemconcomp.2015.10.004>.
- [161] G. Liu, H. Rong, and J. Wang, "Valorization of converter steel slag in

- sustainable mortars by a combined alkali and carbonation activation," *J. Clean. Prod.*, vol. 370, no. 133519, 2022, doi: <https://doi.org/10.1016/j.jclepro.2022.133519>.
- [162] A. S. Reddy, R. K. Pradhan, and S. Chandra, "Utilization of Basic Oxygen Furnace (BOF) slag in the production of a hydraulic cement binder," *Int. J. Miner. Process.*, vol. 79, no. 2, pp. 98–105, 2006, doi: <https://doi.org/10.1016/j.minpro.2006.01.001>.
- [163] J. Hou, Q. Liu, J. Liu, and Q. Wu, "Material Properties of Steel Slag-Cement Binding Materials Prepared by Precarbonated Steel Slag," *J. Mater. Civ. Eng.*, vol. 30, no. 9, 2018, doi: 10.1061/(asce)mt.1943-5533.0002370.
- [164] N. Kabay, N. Miyan, and H. Özkan, "Basic oxygen furnace and ground granulated blast furnace slag based alkali-activated pastes: Characterization and optimization," *J. Clean. Prod.*, vol. 327, no. 129483, 2021, doi: <https://doi.org/10.1016/j.jclepro.2021.129483>.
- [165] P. L. Lopez Gonzalez, R. M. Novais, J. A. Labrincha, B. Blanpain, and Y. Pontikes, "Modifications of basic-oxygen-furnace slag microstructure and their effect on the rheology and the strength of alkali-activated binders," *Cem. Concr. Compos.*, vol. 97, pp. 143–153, 2019, doi: <https://doi.org/10.1016/j.cemconcomp.2018.12.013>.
- [166] I. García Lodeiro, D. E. Macphee, A. Palomo, and A. Fernández-Jiménez, "Effect of alkalis on fresh C–S–H gels. FTIR analysis," *Cem. Concr. Res.*, vol. 39, no. 3, pp. 147–153, 2009, doi: <https://doi.org/10.1016/j.cemconres.2009.01.003>.
- [167] I. García Lodeiro, A. Fernández-Jimenez, A. Palomo, and D. E. Macphee, "Effect on fresh C-S-H gels of the simultaneous addition of alkali and aluminium," *Cem. Concr. Res.*, vol. 40, no. 1, pp. 27–32, 2010, doi: <https://doi.org/10.1016/j.cemconres.2009.08.004>.
- [168] I. García-Lodeiro, A. Fernández-Jiménez, M. T. Blanco, and A. Palomo, "FTIR

- study of the sol–gel synthesis of cementitious gels: C–S–H and N–A–S–H,” *J. Sol-Gel Sci. Technol.*, vol. 45, no. 1, pp. 63–72, 2008, doi: 10.1007/s10971-007-1643-6.
- [169] S. A. Bernal, J. L. Provis, V. Rose, and R. Mejía De Gutiérrez, “High-resolution X-ray diffraction and fluorescence microscopy characterization of alkali-activated slag-metakaolin binders,” *J. Am. Ceram. Soc.*, vol. 96, no. 6, pp. 1951–1957, 2013, doi: <https://doi.org/10.1111/jace.12247>.
- [170] I. Garcia-Lodeiro, A. Palomo, A. Fernández-Jiménez, and D. E. MacPhee, “Compatibility studies between N-A-S-H and C-A-S-H gels. Study in the ternary diagram $\text{Na}_2\text{O}-\text{CaO}-\text{Al}_2\text{O}_3-\text{SiO}_2-\text{H}_2\text{O}$,” *Cement and Concrete Research*, vol. 41, no. 9, pp. 923–931, 2011, doi: 10.1016/j.cemconres.2011.05.006.
- [171] I. Ismail, S. A. Bernal, J. L. Provis, R. San Nicolas, S. Hamdan, and J. S. J. van Deventer, “Modification of phase evolution in alkali-activated blast furnace slag by the incorporation of fly ash,” *Cem. Concr. Compos.*, vol. 45, pp. 125–135, 2014, doi: <https://doi.org/10.1016/j.cemconcomp.2013.09.006>.
- [172] C. K. Yip and J. S. J. van Deventer, “Microanalysis of calcium silicate hydrate gel formed within a geopolymeric binder,” *J. Mater. Sci.*, vol. 38, no. 18, pp. 3851–3860, 2003, doi: 10.1023/A:1025904905176.
- [173] C. K. Yip, G. C. Lukey, and J. S. J. van Deventer, “The coexistence of geopolymeric gel and calcium silicate hydrate at the early stage of alkaline activation,” *Cem. Concr. Res.*, vol. 35, no. 9, pp. 1688–1697, 2005, doi: DOI:101016/jcemconres200410042.
- [174] C. K. Yip, G. C. Lukey, J. L. Provis, and J. S. J. van Deventer, “Effect of calcium silicate sources on geopolymerisation,” *Cem. Concr. Res.*, vol. 38, no. 4, pp. 554–564, 2008, doi: 10.1016/j.cemconres.2007.11.001.
- [175] I. Garcia-Lodeiro, A. Palomo, and A. Fernández-Jiménez, “2 - An overview of the chemistry of alkali-activated cement-based binders,” in *Handbook of Alkali-*

- Activated Cements, Mortars and Concretes*, F. Pacheco-Torgal, J. A. Labrincha, C. Leonelli, A. Palomo, and P. Chindapasirt, Eds. Woodhead Publishing, Oxford, 2015, pp. 19–47.
- [176] I. García-Lodeiro, O. Maltseva, Á. Palomo, and A. Fernández-Jiménez, “Cimenturi hibride alcaline. Partea I: Fundamente,” *Rev. Rom. Mater. Rom. J. Mater.*, vol. 42, no. 4, pp. 330–335, 2012.
- [177] L. Arnout, G. Beersaerts, M. Liard, D. Lootens, and Y. Pontikes, “Valorising slags from non-ferrous metallurgy into hybrid cementitious binders: mix design and performance,” *Waste and Biomass Valorization*, vol. 12, no. 8, pp. 4679–4694, 2021, doi: 10.1007/s12649-020-01322-9.
- [178] A. Palomo, A. Fernández-Jiménez, G. Kovalchuk, L. M. Ordoñez, and M. C. Naranjo, “OPC-fly ash cementitious systems: study of gel binders produced during alkaline hydration,” *J. Mater. Sci.*, vol. 42, no. 9, pp. 2958–2966, 2007, doi: 10.1007/s10853-006-0585-7.
- [179] I. García-Lodeiro, A. Fernández-Jiménez, and A. Palomo, “Variation in hybrid cements over time. Alkaline activation of fly ash–portland cement blends,” *Cem. Concr. Res.*, vol. 52, pp. 112–122, 2013, doi: <https://doi.org/10.1016/j.cemconres.2013.03.022>.
- [180] S. Alahrache, F. Winnefeld, J.-B. Champenois, F. Hesselbarth, and B. Lothenbach, “Chemical activation of hybrid binders based on siliceous fly ash and Portland cement,” *Cem. Concr. Compos.*, vol. 66, pp. 10–23, 2016, doi: <https://doi.org/10.1016/j.cemconcomp.2015.11.003>.
- [181] Z. Bian, G. Jin, and T. Ji, “Effect of combined activator of $\text{Ca}(\text{OH})_2$ and Na_2CO_3 on workability and compressive strength of alkali-activated ferronickel slag system,” *Cem. Concr. Compos.*, vol. 123, no. 104179, 2021, doi: <https://doi.org/10.1016/j.cemconcomp.2021.104179>.
- [182] L. Qing, S. Shaokang, J. Zhen, W. Junxiang, and L. Xianjun, “Effect of CaO on

- hydration properties of one-part alkali-activated material prepared from tailings through alkaline hydrothermal activation," *Constr. Build. Mater.*, vol. 308, no. 124931, 2021, doi: <https://doi.org/10.1016/j.conbuildmat.2021.124931>.
- [183] A. Palomo, P. Monteiro, P. Martauz, V. Bilek, and A. Fernandez-Jimenez, "Hybrid binders: A journey from the past to a sustainable future (opus caementicium futurum)," *Cem. Concr. Res.*, vol. 124, no. 105829, 2019, doi: <https://doi.org/10.1016/j.cemconres.2019.105829>.
- [184] I. Garcia-Lodeiro, A. Fernandez-Jimenez, and A. Palomo, "Hydration kinetics in hybrid binders: Early reaction stages," *Cem. Concr. Compos.*, vol. 39, pp. 82–92, 2013, doi: <https://doi.org/10.1016/j.cemconcomp.2013.03.025>.
- [185] V. Bocullo, D. Vaičiukynienė-Palubinskaitė, A. Kantautas, R. Borg, and C. Briguglio, "Alkaline activation of hybrid cements binders based on industrial by-products," *J. Sustain. Archit. Civ. Eng.*, vol. 19, no. 2, pp. 65–73, 2017, doi: [10.5755/j01.sace.19.2.17836](https://doi.org/10.5755/j01.sace.19.2.17836).
- [186] J. H. Ideker, K. L. Scrivener, H. Fryda, and B. Touzo, "12 - Calcium Aluminate Cements," in *Lea's Chemistry of Cement and Concrete*, 5th Edit., P. C. Hewlett and M. Liska, Eds. Butterworth-Heinemann, 2019, pp. 537–584.
- [187] W. Ding, Y. He, L. Lu, F. Wang, and S. Hu, "Mechanical property and microstructure of quaternary phase paste blended with metakaolin," *Cem. Concr. Compos.*, vol. 118, no. 103934, 2021, doi: <https://doi.org/10.1016/j.cemconcomp.2021.103934>.
- [188] M. C. G. Juenger, F. Winnefeld, J. L. Provis, and J. H. Ideker, "Advances in alternative cementitious binders," *Cem. Concr. Res.*, vol. 41, no. 12, pp. 1232–1243, 2011, doi: <https://doi.org/10.1016/j.cemconres.2010.11.012>.
- [189] S. M. Bushnell-Watson and J. H. Sharp, "On the cause of the anomalous setting behaviour with respect to temperature of calcium aluminate cements," *Cem. Concr. Res.*, vol. 20, no. 5, pp. 677–686, 1990, doi: <https://doi.org/10.1016/0008->

8846(90)90002-F.

- [190] N. Y. Mostafa, Z. I. Zaki, and O. H. Abd Elkader, "Chemical activation of calcium aluminate cement composites cured at elevated temperature," *Cem. Concr. Compos.*, vol. 34, no. 10, pp. 1187–1193, 2012, doi: 10.1016/j.cemconcomp.2012.08.002.
- [191] A. H. López, J. L. G. Calvo, J. G. Olmo, S. Petit, and M. C. Alonso, "Microstructural evolution of calcium aluminate cements hydration with silica fume and fly ash additions by scanning electron microscopy, and mid and near-infrared spectroscopy," *J. Am. Ceram. Soc.*, vol. 91, no. 4, pp. 1258–1265, 2008, doi: 10.1111/j.1551-2916.2008.02283.x.
- [192] H. J. Yang, K. Y. Ann, and M. S. Jung, "Development of strength for calcium aluminate cement mortars blended with GGBS," *Adv. Mater. Sci. Eng.*, vol. 2019, no. 9896012, 2019, doi: 10.1155/2019/9896012.
- [193] J. Ding, Y. Fu, and J. J. Beaudoin, "Strätlingite formation in high alumina cement - silica fume systems: Significance of sodium ions," *Cem. Concr. Res.*, vol. 25, no. 6, pp. 1311–1319, 1995, doi: [https://doi.org/10.1016/0008-8846\(95\)00124-U](https://doi.org/10.1016/0008-8846(95)00124-U).
- [194] J. Ding, Y. Fu, and J. J. Beaudoin, "Study of hydration mechanisms in the high alumina cement - sodium silicate system," *Cem. Concr. Res.*, vol. 26, no. 5, pp. 799–804, 1996, doi: [https://doi.org/10.1016/S0008-8846\(96\)85017-4](https://doi.org/10.1016/S0008-8846(96)85017-4).
- [195] H. G. Midgley and P. Bhaskara Rao, "Formation of stratlingite, $2\text{CaO}\cdot\text{SiO}_2\cdot\text{Al}_2\text{O}_3\cdot 8\text{H}_2\text{O}$, in relation to the hydration of high alumina cement," *Cem. Concr. Res.*, vol. 8, no. 2, pp. 169–172, 1978, doi: [https://doi.org/10.1016/0008-8846\(78\)90005-4](https://doi.org/10.1016/0008-8846(78)90005-4).
- [196] A. Fernández-Jiménez, T. Vázquez, and A. Palomo, "Effect of sodium silicate on calcium aluminate cement hydration in highly alkaline media: A microstructural characterization," *J. Am. Ceram. Soc.*, vol. 94, no. 4, pp. 1297–

- 1303, 2011, doi: 10.1111/j.1551-2916.2010.04242.x.
- [197] C. Pastor, A. Fernández-Jiménez, T. Vázquez, and Á. Palomo, "Hidratación del cemento de aluminato de calcio en condiciones de muy elevada alcalinidad," *Mater. Construcción*, vol. 59, no. 293, 2009, doi: 10.3989/mc.2009.42407.
- [198] K. Arbi, A. Palomo, and A. Fernández-Jiménez, "Alkali-activated blends of calcium aluminate cement and slag/diatomite," *Ceram. Int.*, vol. 39, no. 8, pp. 9237–9245, 2013, doi: 10.1016/j.ceramint.2013.05.031.
- [199] A. Fernández-Jiménez, A. Palomo, T. Vazquez, V. Ramesh, T. Terai, and K. Ikeda, "Alkaline activation of blends of metakaolin and calcium aluminate," *J. Am. Ceram. Soc.*, vol. 91, pp. 1231–1236, 2008, doi: 10.1111/j.1551-2916.2007.02002.x.
- [200] L. Carrasco, A. Fernández-Gimenez, and Á. Palomo, "Alkali activation of 'Pozzolan-calcium aluminate cement' mixtures," *Proceedings of the 12th ICCM*. Montreal, 2007.
- [201] M. Vafaei and A. Allahverdi, "Influence of calcium aluminate cement on geopolymerization of natural pozzolan," *Constr. Build. Mater.*, vol. 114, pp. 290–296, 2016, doi: 10.1016/j.conbuildmat.2016.03.204.
- [202] L. Reig, L. Soriano, M. V Borrachero, J. Monzó, and J. Payá, "Influence of calcium aluminate cement (CAC) on alkaline activation of red clay brick waste (RCBW)," *Cem. Concr. Compos.*, vol. 65, pp. 177–185, 2016, doi: <https://doi.org/10.1016/j.cemconcomp.2015.10.021>.
- [203] Y. F. Cao, Z. Tao, Z. Pan, and R. Wuhrer, "Effect of calcium aluminate cement on geopolymer concrete cured at ambient temperature," *Constr. Build. Mater.*, vol. 191, pp. 242–252, 2018, doi: 10.1016/j.conbuildmat.2018.09.204.
- [204] S. A. Bernal, E. D. Rodríguez, A. P. Kirchheim, and J. L. Provis, "Management

- and valorisation of wastes through use in producing alkali-activated cement materials," *J. Chem. Technol. Biotechnol.*, vol. 91, no. 9, pp. 2365–2388, 2016, doi: 10.1002/jctb.4927.
- [205] M. Criado, X. Ke, J. L. Provis, and S. A. Bernal, "7 - Alternative inorganic binders based on alkali-activated metallurgical slags," in *Sustainable and Nonconventional Construction Materials using Inorganic Bonded Fiber Composites*, H. Savastano Jr, J. Fiorelli, and S. F. dos Santos, Eds. Woodhead Publishing, 2017, pp. 185–220.
- [206] J. Bollen, F. Hanrot, A. Deruwe, J. Domas, and A. Marquina, "Slags valorization in the EU: tapping the full potential," in *6th International Slag Valorisation Symposium*, 2019, pp. 35–41.
- [207] Y. Pontikes and A. Malfliet, "Slag valorisation as a contribution to zero-waste metallurgy," *J. Sustain. Metall.*, vol. 2, pp. 1–2, 2016.
- [208] C. Shi and J. Qian, "High performance cementing materials from industrial slags – a review," *Resour. Conserv. Recycl.*, vol. 29, no. 3, pp. 195–207, 2000.
- [209] S. Caijun and L. Yinyu, "Investigation on some factors affecting the characteristics of alkali-phosphorus slag cement," *Cem. Concr. Res.*, vol. 19, no. 4, pp. 527–533, 1989, doi: [https://doi.org/10.1016/0008-8846\(89\)90004-5](https://doi.org/10.1016/0008-8846(89)90004-5).
- [210] T. Yang, Z. Zhang, H. Zhu, X. Gao, C. Dai, and Q. Wu, "Re-examining the suitability of high magnesium nickel slag as precursors for alkali-activated materials," *Constr. Build. Mater.*, vol. 213, pp. 109–120, 2019, doi: <https://doi.org/10.1016/j.conbuildmat.2019.04.063>.
- [211] K. Komnitsas, D. Zaharaki, and V. Perdikatsis, "Geopolymerisation of low calcium ferronickel slags," *J. Mater. Sci.*, vol. 42, no. 9, pp. 3073–3082, 2007, doi: 10.1007/s10853-006-0529-2.
- [212] I. Maragkos, I. P. Giannopoulou, and D. Papias, "Synthesis of ferronickel slag-

- based geopolymers," *Miner. Eng.*, vol. 22, no. 2, pp. 196–203, 2009, doi: <https://doi.org/10.1016/j.mineng.2008.07.003>.
- [213] T. C. Alex *et al.*, "Utilization of zinc slag through geopolymerization: Influence of milling atmosphere," *Int. J. Miner. Process.*, vol. 123, pp. 102–107, 2013, doi: <https://doi.org/10.1016/j.minpro.2013.06.001>.
- [214] S. Onisei *et al.*, "Synthesis of inorganic polymers using fly ash and primary lead slag," *J. Hazard. Mater.*, vol. 205–206, pp. 101–110, 2012, doi: <https://doi.org/10.1016/j.jhazmat.2011.12.039>.
- [215] S. Kumar, P. García Triñanes, A. Teixeira-Pinto, and M. Bao, "Development of alkali activated cement from mechanically activated silico-manganese (SiMn) slag," *Cem. Concr. Compos.*, vol. 40, pp. 7–13, 2013, doi: [10.1016/j.cemconcomp.2013.03.026](https://doi.org/10.1016/j.cemconcomp.2013.03.026).
- [216] S. K. Nath, N. S. Randhawa, and S. Kumar, "A review on characteristics of silico-manganese slag and its utilization into construction materials," *Resour. Conserv. Recycl.*, vol. 176, no. 105946, 2022, doi: [10.1016/j.resconrec.2021.105946](https://doi.org/10.1016/j.resconrec.2021.105946).
- [217] J. Chen, H. Chen, P. Xiao, and L. Zhang, "A study on complex alkali-slag environmental concrete," in *International Workshop on Sustainable Development and Concrete Technology*, 2004, no. 299.
- [218] S. Fernando, C. Gunasekara, D. W. Law, M. C. M. Nasvi, S. Setunge, and R. Dissanayake, "Life cycle assessment and cost analysis of fly ash–rice husk ash blended alkali-activated concrete," *J. Environ. Manage.*, vol. 295, no. 113140, 2021, doi: <https://doi.org/10.1016/j.jenvman.2021.113140>.
- [219] G. F. Huseien *et al.*, "Synergism between palm oil fuel ash and slag: Production of environmental-friendly alkali activated mortars with enhanced properties," *Constr. Build. Mater.*, vol. 170, pp. 235–244, 2018, doi: <https://doi.org/10.1016/j.conbuildmat.2018.03.031>.

- [220] M. A. Salih, N. Farzadnia, A. A. Abang Ali, and R. Demirboga, "Development of high strength alkali activated binder using palm oil fuel ash and GGBS at ambient temperature," *Constr. Build. Mater.*, vol. 93, pp. 289–300, 2015, doi: <https://doi.org/10.1016/j.conbuildmat.2015.05.119>.
- [221] V. N. Castaldelli *et al.*, "Use of slag/sugar cane bagasse ash (SCBA) blends in the production of alkali-activated materials," *Materials (Basel)*, vol. 6, no. 8, pp. 3108–3127, 2013, doi: 10.3390/ma6083108.
- [222] T. Hertel and Y. Pontikes, "Geopolymers, inorganic polymers, alkali-activated materials and hybrid binders from bauxite residue (red mud) – Putting things in perspective," *J. Clean. Prod.*, vol. 258, no. 120610, 2020, doi: 10.1016/j.jclepro.2020.120610.
- [223] D. Zaharaki, M. Galetakis, and K. Komnitsas, "Valorization of construction and demolition (C&D) and industrial wastes through alkali activation," *Constr. Build. Mater.*, vol. 121, pp. 686–693, 2016, doi: <https://doi.org/10.1016/j.conbuildmat.2016.06.051>.
- [224] K. König, K. Traven, M. Pavlin, and V. Ducman, "Evaluation of locally available amorphous waste materials as a source for alternative alkali activators," *Ceram. Int.*, vol. 47, no. 4, pp. 4864–4873, 2021, doi: <https://doi.org/10.1016/j.ceramint.2020.10.059>.
- [225] M. H. Samarakoon, P. G. Ranjith, W. Hui Duan, A. Haque, and B. K. Chen, "Extensive use of waste glass in one-part alkali-activated materials: Towards sustainable construction practices," *Waste Manag.*, vol. 130, pp. 1–11, 2021, doi: <https://doi.org/10.1016/j.wasman.2021.04.060>.
- [226] A. Bagheri and S. Moukannaa, "A new approach to the reuse of waste glass in the production of alkali-activated materials," *Clean. Eng. Technol.*, vol. 4, no. 100212, 2021, doi: <https://doi.org/10.1016/j.clet.2021.100212>.
- [227] M. A. Longhi, E. D. Rodríguez, S. A. Bernal, J. L. Provis, and A. P. Kirchheim,

- “Valorisation of a kaolin mining waste for the production of geopolymers,” *J. Clean. Prod.*, vol. 115, pp. 265–272, 2016, doi: <https://doi.org/10.1016/j.jclepro.2015.12.011>.
- [228] Y. Luna Galiano, C. Fernández Pereira, and J. Vale, “Stabilization/solidification of a municipal solid waste incineration residue using fly ash-based geopolymers,” *J. Hazard. Mater.*, vol. 185, no. 1, pp. 373–381, 2011, doi: <https://doi.org/10.1016/j.jhazmat.2010.08.127>.
- [229] J. Liu, L. Hu, L. Tang, and J. Ren, “Utilisation of municipal solid waste incinerator (MSWI) fly ash with metakaolin for preparation of alkali-activated cementitious material,” *J. Hazard. Mater.*, vol. 402, no. 123451, 2021, doi: <https://doi.org/10.1016/j.jhazmat.2020.123451>.
- [230] L. Zheng, C. Wang, W. Wang, Y. Shi, and X. Gao, “Immobilization of MSWI fly ash through geopolymerization: effects of water-wash,” *Waste Manag.*, vol. 31, no. 2, p. 311–317, 2011, doi: [10.1016/j.wasman.2010.05.015](https://doi.org/10.1016/j.wasman.2010.05.015).
- [231] H.-Y. Hu *et al.*, “Comparison of CaO’s effect on the fate of heavy metals during thermal treatment of two typical types of MSWI fly ashes in China,” *Chemosphere*, vol. 93, 2013, doi: [10.1016/j.chemosphere.2013.05.077](https://doi.org/10.1016/j.chemosphere.2013.05.077).
- [232] S. Amiralian, M. A. Budihardjo, A. Chegenizadeh, and H. Nikraz, “Study of scale effect on strength characteristic of stabilised composite with sewage sludge – Part B : Critical investigation,” *Constr. Build. Mater.*, vol. 80, pp. 346–350, 2015, doi: [10.1016/j.conbuildmat.2015.01.070](https://doi.org/10.1016/j.conbuildmat.2015.01.070).
- [233] M. Smol, J. Kulczycka, A. Henclik, K. Gorazda, and Z. Wzorek, “The possible use of sewage sludge ash (SSA) in the construction industry as a way towards a circular economy,” *J. Clean. Prod.*, vol. 95, pp. 45–54, 2015, doi: <https://doi.org/10.1016/j.jclepro.2015.02.051>.
- [234] F. Gervais, A. Blin, D. Massiot, J. P. Coutures, M. H. Chopinet, and F. Naudin, “Infrared reflectivity spectroscopy of silicate glasses,” *J. Non. Cryst. Solids*, vol.

- 89, no. 3, pp. 384–401, 1987, doi: [https://doi.org/10.1016/S0022-3093\(87\)80280-6](https://doi.org/10.1016/S0022-3093(87)80280-6).
- [235] L. Wadsö, “Operational issues in isothermal calorimetry,” *Cem. Concr. Res.*, vol. 40, no. 7, pp. 1129–1137, 2010, doi: 10.1016/j.cemconres.2010.03.017.
- [236] Z. Tan, S. A. Bernal, and J. L. Provis, “Reproducible mini-slump test procedure for measuring the yield stress of cementitious pastes,” *Mater. Struct.*, vol. 50, no. 6, pp. 1–12, 2017, doi: 10.1617/s11527-017-1103-x.
- [237] British Standards Institution, “BS EN 196-3:2016 Methods of testing cement - Part 3: Determination of setting times and soundness.” 2016.
- [238] R. Snellings *et al.*, “RILEM TC-238 SCM recommendation on hydration stoppage by solvent exchange for the study of hydrate assemblages,” *Mater. Struct.*, vol. 51, no. 172, 2018, doi: 10.1617/s11527-018-1298-5.
- [239] ASTM C109/C109M-20, “Standard test method for compressive strength of hydraulic cement mortars.” 2020.
- [240] British Standards Institution, “BS EN 1015-11:2019, Methods of test for mortar for masonry.” 2019.
- [241] Q. Zeng, K. Li, T. Fen-Chong, and P. Dangla, “Analysis of pore structure, contact angle and pore entrapment of blended cement pastes from mercury porosimetry data,” *Cem. Concr. Compos.*, vol. 34, no. 9, pp. 1053–1060, 2012, doi: <https://doi.org/10.1016/j.cemconcomp.2012.06.005>.
- [242] Nederlands Normalisatie-Instituut, “NEN-7345:94 Leaching characteristics of solid earthy and stony building and waste materials - Leaching tests - Determination of the leaching of inorganic components from buildings and monolithic waste materials with the diffusion test.” 1994.
- [243] J. Skibsted and R. Snellings, “Reactivity of supplementary cementitious materials (SCMs) in cement blends,” *Cem. Concr. Res.*, vol. 124, no. 105799,

- 2019, doi: 10.1016/j.cemconres.2019.105799.
- [244] F. Souayfan, E. Roziere, C. Justino, M. Paris, D. Deneele, and A. Loukili, "Comprehensive study on the reactivity and mechanical properties of alkali-activated metakaolin at high H₂O/Na₂O ratios," *Appl. Clay Sci.*, vol. 231, no. 106758, 2023, doi: <https://doi.org/10.1016/j.clay.2022.106758>.
- [245] X. Liu *et al.*, "Thermal stability and microstructure of metakaolin-based geopolymer blended with rice husk ash," *Appl. Clay Sci.*, vol. 196, no. 105769, 2020, doi: <https://doi.org/10.1016/j.clay.2020.105769>.
- [246] J. Yang, L. Xu, H. Wu, J. Jin, and L. Liu, "Microstructure and mechanical properties of metakaolin-based geopolymer composites containing high volume of spodumene tailings," *Appl. Clay Sci.*, vol. 218, no. 106412, 2022, doi: <https://doi.org/10.1016/j.clay.2022.106412>.
- [247] J. L. Provis, "4 - Activating solution chemistry for geopolymers," in *Geopolymers: Structures, Processing, Properties and Industrial Applications*, J. L. Provis and J. S. J. van Deventer, Eds. Woodhead Publishing, 2009, pp. 50–71.
- [248] C. Li, H. Sun, and L. Li, "A review: The comparison between alkali-activated slag (Si+Ca) and metakaolin (Si+Al) cements," *Cem. Concr. Res.*, vol. 40, no. 9, pp. 1341–1349, 2010, doi: <https://doi.org/10.1016/j.cemconres.2010.03.020>.
- [249] D. S. Perera, O. Uchida, E. R. Vance, and K. S. Finnie, "Influence of curing schedule on the integrity of geopolymers," *J. Mater. Sci.*, vol. 42, no. 9, pp. 3099–3106, 2007, doi: 10.1007/s10853-006-0533-6.
- [250] J. J. Thomas and H. M. Jennings, "Changes in the size of pores during shrinkage (or expansion) of cement paste and concrete," *Cem. Concr. Res.*, vol. 33, no. 11, pp. 1897–1900, 2003, doi: [https://doi.org/10.1016/S0008-8846\(03\)00167-4](https://doi.org/10.1016/S0008-8846(03)00167-4).
- [251] S. A. Bernal, R. Mejía De Gutiérrez, and J. L. Provis, "Engineering and

- durability properties of concretes based on alkali-activated granulated blast furnace slag/metakaolin blends," *Constr. Build. Mater.*, vol. 33, pp. 99–108, 2012, doi: 10.1016/j.conbuildmat.2012.01.017.
- [252] Y.-M. Liew, C.-Y. Heah, A. B. Mohd Mustafa, and H. Kamarudin, "Structure and properties of clay-based geopolymer cements: A review," *Prog. Mater. Sci.*, vol. 83, pp. 595–629, 2016, doi: <https://doi.org/10.1016/j.pmatsci.2016.08.002>.
- [253] E. Ferraz, S. Andrejkovičová, W. Hajjaji, A. L. Velosa, A. S. Silva, and F. Rocha, "Pozzolanic activity of metakaolins by the French standard of the modified Chappelle test: A direct methodology," *Acta Geodyn. Geomater.*, vol. 12, no. 3, pp. 289–298, 2015, doi: 10.13168/AGG.2015.0026.
- [254] French Standard, "Chappelle test modified," *NF 18-513 Annexe A*. 2012.
- [255] F. Avet, R. Snellings, A. Alujas Diaz, M. Ben Haha, and K. Scrivener, "Development of a new rapid, relevant and reliable (R3) test method to evaluate the pozzolanic reactivity of calcined kaolinitic clays," *Cem. Concr. Res.*, vol. 85, pp. 1–11, 2016, doi: <https://doi.org/10.1016/j.cemconres.2016.02.015>.
- [256] British Standards Institution, "BS EN 197-1:2011: Cement Composition, specifications and conformity criteria for common cements." 2019.
- [257] H. Paiva, A. Velosa, P. Cachim, and V. M. Ferreira, "Effect of metakaolin dispersion on the fresh and hardened state properties of concrete," *Cem. Concr. Res.*, vol. 42, no. 4, pp. 607–612, 2012, doi: 10.1016/j.cemconres.2012.01.005.
- [258] M. H. Derkani *et al.*, "Mechanisms of dispersion of metakaolin particles via adsorption of sodium naphthalene sulfonate formaldehyde polymer," *J. Colloid Interface Sci.*, vol. 628, pp. 745–757, 2022, doi: <https://doi.org/10.1016/j.jcis.2022.07.166>.
- [259] Y. Kocak, "Effects of metakaolin on the hydration development of Portland–

- composite cement," *J. Build. Eng.*, vol. 31, no. 101419, 2020, doi: <https://doi.org/10.1016/j.jobbe.2020.101419>.
- [260] S. A. Bernal, R. San Nicolas, J. S. J. van Deventer, and J. L. Provis, "Alkali-activated slag cements produced with a blended sodium carbonate/sodium silicate activator," *Adv. Cem. Res.*, vol. 28, no. 4, pp. 262–273, 2016, doi: 10.1680/jadcr.15.00013.
- [261] Y. Zuo and G. Ye, "Preliminary interpretation of the induction period in hydration of sodium hydroxide/silicate activated slag," *Materials (Basel)*, vol. 13, no. 21, pp. 1–19, 2020, doi: 10.3390/ma13214796.
- [262] A. Buchwald, R. Tatarin, and D. Stephan, "Reaction progress of alkaline-activated metakaolin-ground granulated blast furnace slag blends," *J. Mater. Sci.*, vol. 44, no. 20, pp. 5609–5617, 2009, doi: 10.1007/s10853-009-3790-3.
- [263] A. Machowska, Z. Kledyński, I. Wilińska, and B. Pacewska, "A study of the early hydration processes and properties of fly ash-slag binders," *Bull. Mater. Sci.*, vol. 42, no. 5, 2019, doi: 10.1007/s12034-019-1886-1.
- [264] F. Collins and J. G. Sanjayan, "Early age strength and workability of slag pastes activated by NaOH and Na₂CO₃," *Cem. Concr. Res.*, vol. 28, no. 5, pp. 655–664, 1998, doi: [https://doi.org/10.1016/S0008-8846\(98\)00025-8](https://doi.org/10.1016/S0008-8846(98)00025-8).
- [265] E. Tajuelo Rodriguez, K. Garbev, D. Merz, L. Black, and I. G. Richardson, "Thermal stability of C-S-H phases and applicability of Richardson and Groves' and Richardson C-(A)-S-H(I) models to synthetic C-S-H," *Cem. Concr. Res.*, vol. 93, pp. 45–56, 2017, doi: <https://doi.org/10.1016/j.cemconres.2016.12.005>.
- [266] B. Walkley, R. San Nicolas, M. A. Sani, S. A. Bernal, J. S. J. van Deventer, and J. L. Provis, "Structural evolution of synthetic alkali-activated CaO-MgO-Na₂O-Al₂O₃-SiO₂ materials is influenced by Mg content," *Cem. Concr. Res.*, vol. 99, pp. 155–171, 2017, doi: 10.1016/j.cemconres.2017.05.006.

- [267] R. J. Myers, S. A. Bernal, and J. L. Provis, "Phase diagrams for alkali-activated slag binders," *Cem. Concr. Res.*, vol. 95, pp. 30–38, 2017, doi: <https://doi.org/10.1016/j.cemconres.2017.02.006>.
- [268] O. Kayali, M. S. H. Khan, and M. Sharfuddin Ahmed, "The role of hydrotalcite in chloride binding and corrosion protection in concretes with ground granulated blast furnace slag," *Cem. Concr. Compos.*, vol. 34, no. 8, pp. 936–945, 2012, doi: <https://doi.org/10.1016/j.cemconcomp.2012.04.009>.
- [269] J. Sun and Z. Chen, "Effect of silicate modulus of water glass on the hydration of alkali-activated converter steel slag," *J. Therm. Anal. Calorim.*, vol. 138, no. 1, pp. 47–56, 2019, doi: [10.1007/s10973-019-08146-3](https://doi.org/10.1007/s10973-019-08146-3).
- [270] K. Gao *et al.*, "Effects SiO₂/Na₂O molar ratio on mechanical properties and the microstructure of nano-SiO₂ metakaolin-based geopolymers," *Constr. Build. Mater.*, vol. 53, pp. 503–510, 2014, doi: [10.1016/j.conbuildmat.2013.12.003](https://doi.org/10.1016/j.conbuildmat.2013.12.003).
- [271] B. T. Poe, P. F. McMillan, C. A. Angell, and R. K. Sato, "Al and Si coordination in SiO₂-Al₂O₃ glasses and liquids: A study by NMR and IR spectroscopy and MD simulations," *Chem. Geol.*, vol. 96, no. 3, pp. 333–349, 1992, doi: [https://doi.org/10.1016/0009-2541\(92\)90063-B](https://doi.org/10.1016/0009-2541(92)90063-B).
- [272] T. Uchino, T. Sakka, and M. Iwasaki, "Interpretation of hydrated states of sodium silicate glasses by infrared and raman analysis," *J. Am. Ceram. Soc.*, vol. 74, no. 2, pp. 306–313, 1991, doi: [10.1111/j.1151-2916.1991.tb06880.x](https://doi.org/10.1111/j.1151-2916.1991.tb06880.x).
- [273] M. A. Longhi, E. D. Rodríguez, B. Walkley, Z. Zhang, and A. P. Kirchheim, "Metakaolin-based geopolymers: Relation between formulation, physicochemical properties and efflorescence formation," *Compos. Part B Eng.*, vol. 182, no. 107671, 2020, doi: <https://doi.org/10.1016/j.compositesb.2019.107671>.
- [274] Z. Zhang, H. Wang, J. L. Provis, F. Bullen, A. Reid, and Y. Zhu, "Quantitative kinetic and structural analysis of geopolymers. Part 1. The activation of

- metakaolin with sodium hydroxide," *Thermochim. Acta*, vol. 539, pp. 23–33, 2012, doi: <https://doi.org/10.1016/j.tca.2012.03.021>.
- [275] J. Ojima, "Determining of crystalline silica in respirable dust samples by infrared spectrophotometry in the presence of interferences," *J. Occup. Health*, vol. 45, no. 2, pp. 94–103, 2003, doi: 10.1539/joh.45.94.
- [276] C. Y. Heah *et al.*, "Study on solids-to-liquid and alkaline activator ratios on kaolin-based geopolymers," *Constr. Build. Mater.*, vol. 35, pp. 912–922, 2012, doi: 10.1016/j.conbuildmat.2012.04.102.
- [277] W. K. W. Lee and J. S. J. van Deventer, "The effects of inorganic salt contamination on the strength and durability of geopolymers," *Colloids Surfaces A Physicochem. Eng. Asp.*, vol. 211, no. 2, pp. 115–126, 2002, doi: [https://doi.org/10.1016/S0927-7757\(02\)00239-X](https://doi.org/10.1016/S0927-7757(02)00239-X).
- [278] M. A. Trezza and A. E. Lavat, "Analysis of the system $3\text{CaO}\cdot\text{Al}_2\text{O}_3\text{-CaSO}_4\cdot 2\text{H}_2\text{O}\text{-CaCO}_3\text{-H}_2\text{O}$ by FT-IR spectroscopy," *Cem. Concr. Res.*, vol. 31, no. 6, pp. 869–872, 2001, doi: [https://doi.org/10.1016/S0008-8846\(01\)00502-6](https://doi.org/10.1016/S0008-8846(01)00502-6).
- [279] A. Hidalgo, J. L. García, M. C. Alonso, L. Fernández, and C. Andrade, "Microstructure development in mixes of calcium aluminate cement with silica fume or fly ash," *J. Therm. Anal. Calorim.*, vol. 96, no. 2, pp. 335–345, 2009, doi: 10.1007/s10973-007-8439-3.
- [280] B. Walkley *et al.*, "Phase evolution of C-(N)-A-S-H/N-A-S-H gel blends investigated via alkali-activation of synthetic calcium aluminosilicate precursors," *Cem. Concr. Res.*, vol. 89, pp. 120–135, 2016.
- [281] M. Król, P. Rożek, D. Chlebda, and W. Mozgawa, "Influence of alkali metal cations/type of activator on the structure of alkali-activated fly ash – ATR-FTIR studies," *Spectrochim. Acta - Part A Mol. Biomol. Spectrosc.*, vol. 198, pp. 33–37, 2018, doi: 10.1016/j.saa.2018.02.067.

- [282] A. Allahverdi and F. Škvára, "Nitric acid attack on hardened paste of geopolymeric cements," *Ceram.-Silik.*, vol. 45, no. 4, pp. 143–149, 2001.
- [283] B. Walkley, A. Kashani, M. A. Sani, T. D. Ngo, and P. Mendis, "Examination of alkali-activated material nanostructure during thermal treatment," *J. Mater. Sci.*, vol. 53, no. 13, pp. 9486–9503, 2018, doi: 10.1007/s10853-018-2270-z.
- [284] S. D. Wang and K. L. Scrivener, "²⁹Si and ²⁷Al NMR study of alkali-activated slag," *Cem. Concr. Res.*, vol. 33, no. 5, pp. 769–774, 2003, doi: 10.1016/S0008-8846(02)01044-X.
- [285] S. A. Bernal *et al.*, "Gel nanostructure in alkali-activated binders based on slag and fly ash, and effects of accelerated carbonation," *Cem. Concr. Res.*, vol. 53, pp. 127–144, 2013, doi: 10.1016/j.cemconres.2013.06.007.
- [286] B. Walkley, X. Ke, J. L. Provis, and S. A. Bernal, "Activator anion influences the nanostructure of alkali-activated slag cements," *J. Phys. Chem. C*, vol. 125, no. 37, pp. 20727–20739, 2021, doi: 10.1021/acs.jpcc.1c07328.
- [287] K. J. D. Mackenzie, I. W. M. Brown, C. M. Cardile, and R. H. Meinhold, "The thermal reactions of muscovite studied by high-resolution solid-state ²⁹Si and ²⁷Al NMR," *J. Mater. Sci.*, vol. 22, no. 7, pp. 2645–2654, 1987, doi: 10.1007/BF01082158.
- [288] D. H. Brouwer, "9.06 - Applications of silicon-29 NMR spectroscopy," in *Comprehensive Inorganic Chemistry III*, 3rd Edit., J. Reedijk and K. Poepelmeier, Eds. Oxford: Elsevier, 2023, pp. 107–137.
- [289] R. Oestrike, W. Yang, R. J. Kirkpatrick, R. L. Hervig, A. Navrotsky, and B. Montez, "High-resolution ²³Na, ²⁷Al and ²⁹Si NMR spectroscopy of framework aluminosilicate glasses," *Geochim. Cosmochim. Acta*, vol. 51, no. 8, pp. 2199–2209, 1987, doi: 10.1016/0016-7037(87)90269-9.
- [290] S. Guggenheim, Y. H. Chang, and A. F. Koster Van Groos, "Muscovite

- dehydroxylation: high-temperature studies.," *Am. Mineral.*, vol. 72, no. 5–6, pp. 537–550, 1987.
- [291] V. Hanykýř, J. Ederová, Z. Trávníček, J. Šrank, and J. Doubek, "Isothermal dehydroxylation of muscovite mica," *Thermochim. Acta*, vol. 93, pp. 517–520, 1985, doi: [https://doi.org/10.1016/0040-6031\(85\)85130-3](https://doi.org/10.1016/0040-6031(85)85130-3).
- [292] R. J. Myers, S. A. Bernal, J. D. Gehman, J. S. J. van Deventer, and J. L. Provis, "The role of Al in cross-linking of alkali-activated slag cements," *J. Am. Ceram. Soc.*, vol. 98, no. 3, pp. 996–1004, Mar. 2015, doi: <https://doi.org/10.1111/jace.13360>.
- [293] J. Schneider, M. A. Cincotto, and H. Panepucci, "²⁹Si and ²⁷Al high-resolution NMR characterization of calcium silicate hydrate phases in activated blast-furnace slag pastes," *Cem. Concr. Res.*, vol. 31, no. 7, pp. 993–1001, 2001, doi: [https://doi.org/10.1016/S0008-8846\(01\)00530-0](https://doi.org/10.1016/S0008-8846(01)00530-0).
- [294] B. Walkley and J. L. Provis, "Solid-state nuclear magnetic resonance spectroscopy of cements," *Mater. Today Adv.*, vol. 1, no. 100007, 2019, doi: <https://doi.org/10.1016/j.mtadv.2019.100007>.
- [295] M. Ben Haha, B. Lothenbach, G. Le Saout, and F. Winnefeld, "Influence of slag chemistry on the hydration of alkali-activated blast-furnace slag — Part II: Effect of Al₂O₃," *Cem. Concr. Res.*, vol. 42, no. 1, pp. 74–83, 2012, doi: <https://doi.org/10.1016/j.cemconres.2011.08.005>.
- [296] T. Oey, A. Kumar, J. W. Bullard, N. Neithalath, and G. Sant, "The filler effect: The influence of filler content and surface area on cementitious reaction rates," *J. Am. Ceram. Soc.*, vol. 96, no. 6, pp. 1978–1990, 2013, doi: [10.1111/jace.12264](https://doi.org/10.1111/jace.12264).
- [297] P. Duxson, J. L. Provis, G. C. Lukey, F. Separovic, and J. S. J. van Deventer, "²⁹Si NMR study of structural ordering in aluminosilicate geopolymer gels," *Langmuir*, vol. 21, no. 7, pp. 3028–3036, 2005, doi: [10.1021/la047336x](https://doi.org/10.1021/la047336x).

- [298] M. Mantovani, A. Escudero, and A. I. Becerro, "Application of ^{29}Si and ^{27}Al MAS NMR spectroscopy to the study of the reaction mechanism of kaolinite to illite/muscovite," *Clays Clay Miner.*, vol. 57, no. 3, pp. 302–310, 2009, doi: 10.1346/CCMN.2009.0570303.
- [299] F. Souayfan, E. Rozière, M. Paris, D. Deneele, A. Loukili, and C. Justino, " ^{29}Si and ^{27}Al MAS NMR spectroscopic studies of activated metakaolin-slag mixtures," *Constr. Build. Mater.*, vol. 322, no. 126415, 2022, doi: <https://doi.org/10.1016/j.conbuildmat.2022.126415>.
- [300] Y. Ma, J. Hu, and G. Ye, "The pore structure and permeability of alkali activated fly ash," *Fuel*, vol. 104, pp. 771–780, 2013, doi: <https://doi.org/10.1016/j.fuel.2012.05.034>.
- [301] S. A. Bernal, J. L. Provis, V. Rose, and R. Mejía De Gutierrez, "Evolution of binder structure in sodium silicate-activated slag-metakaolin blends," *Cem. Concr. Compos.*, vol. 33, no. 1, pp. 46–54, 2011, doi: 10.1016/j.cemconcomp.2010.09.004.
- [302] T. S. Naidu, C. M. Sheridan, and L. D. van Dyk, "Basic oxygen furnace slag: Review of current and potential uses," *Miner. Eng.*, vol. 149, no. 106234, 2020, doi: <https://doi.org/10.1016/j.mineng.2020.106234>.
- [303] "World Steel Association Yearbook," 2018. <https://worldsteel.org/steel-topics/statistics/steel-statistical-yearbook/>.
- [304] K. L. Scrivener and R. J. Kirkpatrick, "Innovation in use and research on cementitious material," *Cem. Concr. Res.*, vol. 38, no. 2, pp. 128–136, 2008, doi: <https://doi.org/10.1016/j.cemconres.2007.09.025>.
- [305] G. L. F. Benachio, M. do C. D. Freitas, and S. F. Tavares, "Circular economy in the construction industry: A systematic literature review," *J. Clean. Prod.*, vol. 260, no. 121046, 2020, doi: <https://doi.org/10.1016/j.jclepro.2020.121046>.

- [306] A. Fernández-Jiménez, N. Cristelo, T. Miranda, and Á. Palomo, "Sustainable alkali activated materials: Precursor and activator derived from industrial wastes," *J. Clean. Prod.*, vol. 162, pp. 1200–1209, 2017, doi: <https://doi.org/10.1016/j.jclepro.2017.06.151>.
- [307] A. T. M. Marsh, A. P. M. Velenturf, and S. A. Bernal, "Circular economy strategies for concrete: implementation and integration," *J. Clean. Prod.*, vol. 362, no. 132486, 2022, doi: 10.1016/j.jclepro.2022.132486.
- [308] N. Zhang, L. Wu, X. Liu, and Y. Zhang, "Structural characteristics and cementitious behavior of basic oxygen furnace slag mud and electric arc furnace slag," *Constr. Build. Mater.*, vol. 219, pp. 11–18, 2019, doi: 10.1016/j.conbuildmat.2019.05.156.
- [309] Y. Kong, P. Wang, and S. Liu, "Microwave pre-curing of Portland cement-steel slag powder composite for its hydration properties," *Constr. Build. Mater.*, vol. 189, pp. 1093–1104, 2018, doi: 10.1016/j.conbuildmat.2018.09.088.
- [310] M. Deng, D. Hong, X. Lan, and M. Tang, "Mechanism of expansion in hardened cement pastes with hard-burnt free lime," *Cem. Concr. Res.*, vol. 25, no. 2, pp. 440–448, 1995, doi: [https://doi.org/10.1016/0008-8846\(95\)00030-5](https://doi.org/10.1016/0008-8846(95)00030-5).
- [311] Y. Xue, S. Wu, H. Hou, and J. Zha, "Experimental investigation of basic oxygen furnace slag used as aggregate in asphalt mixture," *J. Hazard. Mater.*, vol. 138, no. 2, pp. 261–268, 2006, doi: <https://doi.org/10.1016/j.jhazmat.2006.02.073>.
- [312] S. Pathak, R. Choudhary, A. Kumar, and D. T. Damena, "Feasibility assessment of the use of basic oxygen furnace slag in open graded asphalt courses," *Int. J. Pavement Res. Technol.*, vol. 12, no. 6, pp. 664–673, 2019, doi: 10.1007/s42947-019-0079-2.
- [313] C. Kambole, P. Paige-Green, W. K. Kupolati, J. M. Ndambuki, and A. O. Adeboje, "Basic oxygen furnace slag for road pavements: A review of material characteristics and performance for effective utilisation in southern Africa,"

- Constr. Build. Mater.*, vol. 148, pp. 618–631, 2017, doi: <https://doi.org/10.1016/j.conbuildmat.2017.05.036>.
- [314] T. A. Branca *et al.*, “Investigation of (BOF) Converter slag use for agriculture in europe,” *Metall. Res. Technol.*, vol. 111, no. 3, pp. 155–167, 2014, doi: 10.1051/metal/2014022.
- [315] T. Zhang, Q. Yu, J. Wei, J. Li, and P. Zhang, “Preparation of high performance blended cements and reclamation of iron concentrate from basic oxygen furnace steel slag,” *Resour. Conserv. Recycl.*, vol. 56, no. 1, pp. 48–55, 2011, doi: <https://doi.org/10.1016/j.resconrec.2011.09.003>.
- [316] T. Sithole, F. Okonta, and N. Freeman, “Mechanical properties and structure of fly ash modified basic oxygen furnace slag based geopolymer masonry blocks,” *J. Solid Waste Technol. Manag.*, vol. 46, pp. 372–383, 2020, doi: 10.5276/JSWTM/2020.372.
- [317] A. M. Humad, K. Habermehl-Cwirzen, and A. Cwirzen, “Effects of fineness and chemical composition of blast furnace slag on properties of alkali-activated binder,” *Materials (Basel)*, vol. 12, no. 20, 2019, doi: 10.3390/ma12203447.
- [318] M. Ibrahim and M. Maslehuiddin, “An overview of factors influencing the properties of alkali-activated binders,” *J. Clean. Prod.*, vol. 286, no. 124972, 2021, doi: <https://doi.org/10.1016/j.jclepro.2020.124972>.
- [319] B. Yuan, Q. L. Yu, and H. J. H. Brouwers, “Time-dependent characterization of Na₂CO₃ activated slag,” *Cem. Concr. Compos.*, vol. 84, pp. 188–197, 2017, doi: <https://doi.org/10.1016/j.cemconcomp.2017.09.005>.
- [320] A. Adesina, “Influence of various additives on the early age compressive strength of sodium carbonate activated slag composites: An overview,” *J. Mech. Behav. Mater.*, vol. 29, no. 1, pp. 106–113, 2020, doi: 10.1515/jmbm-2020-0011.

- [321] S. A. Bernal, J. L. Provis, R. J. Myers, R. San Nicolas, and J. S. J. van Deventer, "Role of carbonates in the chemical evolution of sodium carbonate-activated slag binders," *Mater. Struct.*, vol. 48, no. 3, pp. 517–529, 2014, doi: 10.1617/s11527-014-0412-6.
- [322] S. A. Bernal, "Advances in near-neutral salts activation of blast furnace slags," *RILEM Tech. Lett.*, vol. 1, pp. 39–44, 2016.
- [323] J. Wang, X. Lyu, L. Wang, X. Cao, Q. Liu, and H. Zang, "Influence of the combination of calcium oxide and sodium carbonate on the hydration reactivity of alkali-activated slag binders," *J. Clean. Prod.*, vol. 171, pp. 622–629, 2018, doi: <https://doi.org/10.1016/j.jclepro.2017.10.077>.
- [324] X. Ke, S. A. Bernal, and J. L. Provis, "Controlling the reaction kinetics of sodium carbonate-activated slag cements using calcined layered double hydroxides," *Cem. Concr. Res.*, vol. 81, pp. 24–37, 2016, doi: <https://doi.org/10.1016/j.cemconres.2015.11.012>.
- [325] A. Fernández-Jiménez and F. Puertas, "Effect of activator mix on the hydration and strength behaviour of alkali-activated slag cements," *Adv. Cem. Res.*, vol. 15, no. 3, pp. 126–136, 2003, doi: 10.1680/adcr.13.3.115.39288.
- [326] A. Kashani, J. L. Provis, G. G. Qiao, and J. S. J. van Deventer, "The interrelationship between surface chemistry and rheology in alkali activated slag paste," *Constr. Build. Mater.*, vol. 65, pp. 583–591, 2014, doi: <https://doi.org/10.1016/j.conbuildmat.2014.04.127>.
- [327] A. Fernandez-Jimenez and F. Puertas, "Setting of alkali-activated slag cement. Influence of activator nature," *Adv. Cem. Res.*, vol. 13, no. 3, pp. 115–121, 2001, doi: 10.1680/adcr.13.3.115.39288.
- [328] I. G. Richardson, A. R. Brough, G. W. Groves, and C. M. Dobson, "The characterization of hardened alkali-activated blast-furnace slag pastes and the nature of the calcium silicate hydrate (C-S-H) phase," *Cem. Concr. Res.*, vol. 24,

- no. 5, pp. 813–829, 1994, doi: 10.1016/0008-8846(94)90002-7.
- [329] I. Ismail, S. A. Bernal, J. L. Provis, S. Hamdan, and J. S. J. van Deventer, “Microstructural changes in alkali activated fly ash/slag geopolymers with sulfate exposure,” *Mater. Struct.*, vol. 46, no. 3, pp. 361–373, 2013, doi: 10.1617/s11527-012-9906-2.
- [330] F. Puertas, M. Palacios, and T. Vázquez, “Carbonation process of alkali-activated slag mortars,” *J. Mater. Sci.*, vol. 41, no. 10, pp. 3071–3082, 2006, doi: 10.1007/s10853-005-1821-2.
- [331] N. Li, N. Farzadnia, and C. Shi, “Microstructural changes in alkali-activated slag mortars induced by accelerated carbonation,” *Cem. Concr. Res.*, vol. 100, pp. 214–226, 2017, doi: <https://doi.org/10.1016/j.cemconres.2017.07.008>.
- [332] G. C. Jones and B. Jackson, *Infrared Transmission Spectra of Carbonate Minerals*. Springer, Dordrecht, 1993.
- [333] P. Yu, R. J. Kirkpatrick, B. Poe, P. F. McMillan, and X. Cong, “Structure of calcium silicate hydrate (C-S-H): near-, mid-, and far-infrared spectroscopy,” *J. Am. Ceram. Soc.*, vol. 82, no. 3, pp. 742–748, 1999, doi: <https://doi.org/10.1111/j.1151-2916.1999.tb01826.x>.
- [334] B. Das, S. Prakash, P. S. R. Reddy, and V. N. Misra, “An overview of utilization of slag and sludge from steel industries,” *Resour. Conserv. Recycl.*, vol. 50, no. 1, pp. 40–57, 2007, doi: 10.1016/j.resconrec.2006.05.008.
- [335] M. Češnovar, K. Traven, B. Horvat, and V. Ducman, “The potential of ladle slag and electric arc furnace slag use in Synthesizing alkali activated materials; the influence of curing on mechanical properties,” *Materials (Basel)*, vol. 12, no. 7, 2019, doi: 10.3390/ma12071173.
- [336] M. Ozturk, M. B. Bankir, O. S. Bolukbasi, and U. K. Sevim, “Alkali activation of electric arc furnace slag: Mechanical properties and micro analyzes,” *J.*

- Build. Eng.*, vol. 21, pp. 97–105, 2019, doi: <https://doi.org/10.1016/j.jobe.2018.10.005>.
- [337] W. Li and X. Xue, “Effect of cooling regime on phase transformation and chromium enrichment in stainless-steel slag,” *Ironmak. Steelmak.*, vol. 46, no. 7, pp. 642–648, 2019, doi: 10.1080/03019233.2018.1436890.
- [338] H. Zhang, C. Wei, and J. Dong, “Inhibition Kinetics of Chromium Leaching by Calcite Coating on the Surface of Stainless Steel Slag via the Gas–Solid Accelerated Carbonation Process,” *Waste and Biomass Valorization*, vol. 12, no. 1, pp. 475–485, 2021, doi: 10.1007/s12649-020-00988-5.
- [339] F. Faleschini, M. A. Fernández-Ruíz, M. A. Zanini, K. Brunelli, C. Pellegrino, and E. Hernández-Montes, “High performance concrete with electric arc furnace slag as aggregate: Mechanical and durability properties,” *Constr. Build. Mater.*, vol. 101, pp. 113–121, 2015, doi: <https://doi.org/10.1016/j.conbuildmat.2015.10.022>.
- [340] M. Pasetto, A. Baliello, G. Giacomello, and E. Pasquini, “Sustainable solutions for road pavements: A multi-scale characterization of warm mix asphalts containing steel slags,” *J. Clean. Prod.*, vol. 166, pp. 835–843, 2017, doi: <https://doi.org/10.1016/j.jclepro.2017.07.212>.
- [341] J. Rosales, F. Agrela, J. L. Díaz-López, and M. Cabrera, “Alkali-activated stainless steel slag as a cementitious material in the manufacture of self-compacting concrete,” *Materials (Basel)*, vol. 14, no. 14, 2021, doi: 10.3390/ma14143945.
- [342] W. Song *et al.*, “Effect of steel slag on fresh, hardened and microstructural properties of high-calcium fly ash based geopolymers at standard curing condition,” *Constr. Build. Mater.*, vol. 229, no. 116933, 2019, doi: <https://doi.org/10.1016/j.conbuildmat.2019.116933>.
- [343] N. You, B. Li, R. Cao, J. Shi, C. Chen, and Y. Zhang, “The influence of steel slag

- and ferronickel slag on the properties of alkali-activated slag mortar," *Constr. Build. Mater.*, vol. 227, no. 116614, 2019, doi: <https://doi.org/10.1016/j.conbuildmat.2019.07.340>.
- [344] L. Addadi, S. Raz, and S. Weiner, "Taking advantage of disorder: amorphous calcium carbonate and its roles in biomineralization," *Adv. Mater.*, vol. 15, no. 12, pp. 959–970, 2003, doi: <https://doi.org/10.1002/adma.200300381>.
- [345] M. Stefanescu, M. Barbu, T. Vlase, P. Barvinschi, L. Barbu-Tudoran, and M. Stoia, "Novel low temperature synthesis method for nanocrystalline zinc and magnesium chromites," *Thermochim. Acta*, vol. 526, no. 1, pp. 130–136, 2011, doi: <https://doi.org/10.1016/j.tca.2011.09.005>.
- [346] E. V. Kalinkina, A. M. Kalinkin, W. Forsling, and V. N. Makarov, "Sorption of atmospheric carbon dioxide and structural change of Ca and Mg silicate minerals during grinding II. Enstatite, åkermanite and wollastonite," *Int. J. Miner. Process.*, vol. 61, no. 4, pp. 289–299, 2001, doi: [10.1016/S0301-7516\(00\)00038-7](https://doi.org/10.1016/S0301-7516(00)00038-7).
- [347] F. Engström, D. Adolfsson, C. Samuelsson, Å. Sandström, and B. Björkman, "A study of the solubility of pure slag minerals," *Miner. Eng.*, vol. 41, pp. 46–52, 2013, doi: <https://doi.org/10.1016/j.mineng.2012.10.004>.
- [348] British Standards Institution, "BS EN 196-1-2016, Methods of testing cement Part 1: Determination of strength," 2016.
- [349] K. L. Scrivener and A. Nonat, "Hydration of cementitious materials, present and future," *Cem. Concr. Res.*, vol. 41, no. 7, pp. 651–665, 2011, doi: <https://doi.org/10.1016/j.cemconres.2011.03.026>.
- [350] C. Shi and R. L. Day, "A calorimetric study of early hydration of alkali-slag cements," *Cem. Concr. Res.*, vol. 25, no. 6, pp. 1333–1346, 1995, doi: [https://doi.org/10.1016/0008-8846\(95\)00126-W](https://doi.org/10.1016/0008-8846(95)00126-W).

- [351] M. Salman *et al.*, "Cementitious binders from activated stainless steel refining slag and the effect of alkali solutions," *J. Hazard. Mater.*, vol. 286, pp. 211–219, 2015, doi: <https://doi.org/10.1016/j.jhazmat.2014.12.046>.
- [352] Q. Wang, J. Yang, and P. Yan, "Cementitious properties of super-fine steel slag," *Powder Technol.*, vol. 245, pp. 35–39, 2013, doi: <https://doi.org/10.1016/j.powtec.2013.04.016>.
- [353] N. V. Chukanov and A. D. Chervonnyi, *Infrared Spectra of Minerals and Related Inorganic Compounds*. Springer, Cham, 2016.
- [354] B. Li, Q. Li, and W. Chen, "Spatial zonation of a hydrotalcite-like phase in the inner product of slag: New insights into the hydration mechanism," *Cem. Concr. Res.*, vol. 145, no. 106460, 2021, doi: <https://doi.org/10.1016/j.cemconres.2021.106460>.
- [355] Z. Zhang, L. Li, X. Ma, and H. Wang, "Compositional, microstructural and mechanical properties of ambient condition cured alkali-activated cement," *Constr. Build. Mater.*, vol. 113, pp. 237–245, 2016, doi: <https://doi.org/10.1016/j.conbuildmat.2016.03.043>.
- [356] R. Cao, B. Li, N. You, Y. Zhang, and Z. Zhang, "Properties of alkali-activated ground granulated blast furnace slag blended with ferronickel slag," *Constr. Build. Mater.*, vol. 192, pp. 123–132, 2018, doi: <https://doi.org/10.1016/j.conbuildmat.2018.10.112>.
- [357] J. L. Provis, R. J. Myers, C. E. White, V. Rose, and J. S. J. van Deventer, "X-ray microtomography shows pore structure and tortuosity in alkali-activated binders," *Cem. Concr. Res.*, vol. 42, no. 6, pp. 855–864, 2012, doi: <https://doi.org/10.1016/j.cemconres.2012.03.004>.
- [358] Sindhunata, J. S. J. van Deventer, G. C. Lukey, and H. Xu, "Effect of curing temperature and silicate concentration on fly-ash-based geopolymerization," *Ind. Eng. Chem. Res.*, vol. 45, no. 10, pp. 3559–3568, 2006, doi:

10.1021/ie051251p.

- [359] J. Zhang, J. L. Provis, D. Feng, and J. S. J. van Deventer, "The role of sulfide in the immobilization of Cr(VI) in fly ash geopolymers," *Cem. Concr. Res.*, vol. 38, no. 5, pp. 681–688, 2008, doi: <https://doi.org/10.1016/j.cemconres.2008.01.006>.
- [360] Z. Yan, Z. Sun, J. Yang, H. Yang, Y. Ji, and K. Hu, "Mechanical performance and reaction mechanism of copper slag activated with sodium silicate or sodium hydroxide," *Constr. Build. Mater.*, vol. 266, no. 120900, 2021, doi: <https://doi.org/10.1016/j.conbuildmat.2020.120900>.
- [361] Z. Huaiwei and H. Xin, "An overview for the utilization of wastes from stainless steel industries," *Resour. Conserv. Recycl.*, vol. 55, no. 8, pp. 745–754, 2011, doi: <https://doi.org/10.1016/j.resconrec.2011.03.005>.
- [362] I. Lancellotti, F. Piccolo, K. Traven, M. Češnovar, V. Ducman, and C. Leonelli, "Alkali activation of metallurgical slags: Reactivity, chemical behavior, and environmental assessment," *Materials (Basel)*, vol. 14, no. 3, pp. 1–19, 2021, doi: [10.3390/ma14030639](https://doi.org/10.3390/ma14030639).
- [363] F. Özalp, "Effects of electric arc furnace (EAF) slags on mechanical and permeability properties of paving stone, kerb and concrete pipes," *Constr. Build. Mater.*, vol. 329, no. 127159, 2022, doi: <https://doi.org/10.1016/j.conbuildmat.2022.127159>.
- [364] L.-A. Esther, L.-G. Pedro, I.-V. Irune, and F. Gerardo, "Comprehensive analysis of the environmental impact of electric arc furnace steel slag on asphalt mixtures," *J. Clean. Prod.*, vol. 275, no. 123121, 2020, doi: <https://doi.org/10.1016/j.jclepro.2020.123121>.
- [365] M. R. Keymanesh, H. Ziari, H. Zalnezhad, and M. Zalnezhad, "Mix design and performance evaluation of microsurfacing containing electric arc furnace (EAF) steel slag filler," *Constr. Build. Mater.*, vol. 269, no. 121336, 2021, doi: <https://doi.org/10.1016/j.conbuildmat.2020.121336>.

- [366] R. S. Edwin, E. Gruyaert, and N. De Belie, "Valorization of secondary copper slag as aggregate and cement replacement in ultra-high performance concrete," *J. Build. Eng.*, vol. 54, no. 104567, 2022, doi: <https://doi.org/10.1016/j.jobe.2022.104567>.
- [367] J. Kuterasińska and A. Król, "Mechanical properties of alkali-activated binders based on copper slag," *Archit. Civ. Eng. Environ.*, vol. 8, pp. 61–67, 2015.
- [368] A. Nazer, J. Payá, M. V. Borrachero, and J. Monzó, "Use of ancient copper slags in Portland cement and alkali activated cement matrices," *J. Environ. Manage.*, vol. 167, pp. 115–123, 2016, doi: <https://doi.org/10.1016/j.jenvman.2015.11.024>.
- [369] J. Singh and S. P. Singh, "Development of alkali-activated cementitious material using copper slag," *Constr. Build. Mater.*, vol. 211, pp. 73–79, 2019, doi: <https://doi.org/10.1016/j.conbuildmat.2019.03.233>.
- [370] S. Ahmari, K. Parameswaran, and L. Zhang, "Alkali activation of copper mine tailings and low-calcium flash-furnace copper smelter slag," *J. Mater. Civ. Eng.*, vol. 27, no. 6, Jun. 2015, doi: 10.1061/(ASCE)MT.1943-5533.0001159.
- [371] R. K. Dhir, J. de Brito, R. Mangabhai, and C. Q. Lye, *Sustainable Construction Materials: Copper Slag*. Woodhead Publishing, 2016.
- [372] Y. Pontikes *et al.*, "Slags with a high Al and Fe content as precursors for inorganic polymers," *Appl. Clay Sci.*, vol. 73, pp. 93–102, 2013, doi: <https://doi.org/10.1016/j.clay.2012.09.020>.
- [373] A. Peys, C. E. White, H. Rahier, B. Blanpain, and Y. Pontikes, "Alkali-activation of CaO-FeO_x-SiO₂ slag: Formation mechanism from in-situ X-ray total scattering," *Cem. Concr. Res.*, vol. 122, pp. 179–188, 2019, doi: <https://doi.org/10.1016/j.cemconres.2019.04.019>.
- [374] A. Adediran, J. Yliniemi, and M. Illikainen, "Development of sustainable alkali-activated mortars using Fe-rich fayalitic slag as the sole solid

- precursor," *Front. Built Environ.*, vol. 7, pp. 1–12, 2021.
- [375] P. R. Monich, A. R. Romero, D. Höllen, and E. Bernardo, "Porous glass-ceramics from alkali activation and sinter-crystallization of mixtures of waste glass and residues from plasma processing of municipal solid waste," *J. Clean. Prod.*, vol. 188, pp. 871–878, 2018, doi: <https://doi.org/10.1016/j.jclepro.2018.03.167>.
- [376] A. M. Kalinkin *et al.*, "Geopolymerization behavior of Cu – Ni slag mechanically activated in air and in CO₂ atmosphere," *Int. J. Miner. Process.*, vol. 112–113, pp. 101–106, 2012, doi: 10.1016/j.minpro.2012.05.001.
- [377] P. T. Teo *et al.*, "Assessment of electric arc furnace (EAF) steel slag waste's recycling options into value added green products: A review," *Metals (Basel)*, vol. 10, no. 10, pp. 1–21, 2020, doi: 10.3390/met10101347.
- [378] T. C. Phiri, P. Singh, and A. N. Nikoloski, "The potential for copper slag waste as a resource for a circular economy: A review – Part II," *Miner. Eng.*, vol. 172, no. 107150, 2021, doi: 10.1016/j.mineng.2021.107150.
- [379] N.-E. Menad, N. Kana, A. Seron, and N. Kanari, "New EAF slag characterization methodology for strategic metal recovery," *Materials (Basel)*, vol. 14, no. 6, 2021, doi: 10.3390/ma14061513.
- [380] S. Zhang *et al.*, "A novel strategy for harmlessness and reduction of copper smelting slags by alkali disaggregation of fayalite (Fe₂SiO₄) coupling with acid leaching," *J. Hazard. Mater.*, vol. 402, no. 123791, 2021, doi: <https://doi.org/10.1016/j.jhazmat.2020.123791>.
- [381] W. K. W. Lee and J. S. J. van Deventer, "Use of infrared spectroscopy to study geopolymerization of heterogeneous amorphous aluminosilicates," *Langmuir*, vol. 19, no. 21, pp. 8726–8734, 2003, doi: 10.1021/la026127e.
- [382] A. Peys, C. E. White, D. Olds, H. Rahier, B. Blanpain, and Y. Pontikes,

- “Molecular structure of CaO–FeO_x–SiO₂ glassy slags and resultant inorganic polymer binders,” *J. Am. Ceram. Soc.*, vol. 101, no. 12, pp. 5846–5857, 2018, doi: 10.1111/jace.15880.
- [383] K. N. Dalby and P. L. King, “A new approach to determine and quantify structural units in silicate glasses using micro-reflectance Fourier-transform infrared spectroscopy,” *Am. Mineral.*, vol. 91, no. 11–12, pp. 1783–1793, 2006, doi: 10.2138/am.2006.2075.
- [384] H. Ye and A. Radlińska, “Carbonation-induced volume change in alkali-activated slag,” *Constr. Build. Mater.*, vol. 144, pp. 635–644, 2017, doi: <https://doi.org/10.1016/j.conbuildmat.2017.03.238>.
- [385] A. Adediran, J. Yliniemi, and M. Illikainen, “Fayalite slag as binder and aggregate in alkali-activated materials—interfacial transition zone study,” *Proceedings of 1st International Conference on Smart Materials for Sustainable Construction—SMASCO 2019*. Luleå, 2019, doi: 10.3390/proceedings2019034001.
- [386] A. Nikolov, “Alkali and acid activated geopolymers based on iron-silicate fines - by-product from copper industry,” *Mach. Technol. Mater.*, vol. 14, no. 1, pp. 37–39, 2020.
- [387] A. Hajimohammadi, J. L. Provis, and J. S. J. Van Deventer, “Effect of alumina release rate on the mechanism of geopolymer gel formation,” *Chem. Mater.*, vol. 22, no. 18, pp. 5199 – 5208, 2010, doi: 10.1021/cm101151n.
- [388] A. Fernández-Jiménez and A. Palomo, “Mid-infrared spectroscopic studies of alkali-activated fly ash structure,” *Micropor. Mesopor. Mater.*, vol. 86, no. 1–3, pp. 207–214, 2005, doi: 10.1016/j.micromeso.2005.05.057.
- [389] M. M. Hasan, M. A. Rhamdhani, M. Al Hossaini Shuva, and G. A. Brooks, “Study of the structure of FeO_x-CaO-SiO₂-MgO and FeO_x-CaO-SiO₂-MgO-Cu₂O-PdO slags relevant to urban ores processing through Cu smelting,”

- Metals (Basel)*., vol. 10, no. 1, pp. 1–23, 2020, doi: 10.3390/met10010078.
- [390] D. Bondar, S. Nanukuttan, J. L. Provis, and M. Soutsos, “Efficient mix design of alkali activated slag concretes based on packing fraction of ingredients and paste thickness,” *J. Clean. Prod.*, vol. 218, pp. 438–449, 2019, doi: <https://doi.org/10.1016/j.jclepro.2019.01.332>.
- [391] B. Walkley, X. Ke, O. Hussein, and J. L. Provis, “Thermodynamic properties of sodium aluminosilicate hydrate (N-A-S-H),” *Dalton Trans.*, vol. 50, no. 39, pp. 13968–13984, 2021, doi: 10.1039/d1dt02202d.
- [392] C. Siakati, A. P. Douvalis, V. Hallet, A. Peys, and Y. Pontikes, “Influence of CaO/FeO ratio on the formation mechanism and properties of alkali-activated Fe-rich slags,” *Cem. Concr. Res.*, vol. 146, no. 106466, 2021, doi: 10.1016/j.cemconres.2021.106466.
- [393] A. Fernández-Jiménez, A. Palomo, I. Sobrados, and J. Sanz, “The role played by the reactive alumina content in the alkaline activation of fly ashes,” *Micropor. Mesopor. Mater.*, vol. 91, no. 1, pp. 111–119, 2006, doi: <https://doi.org/10.1016/j.micromeso.2005.11.015>.
- [394] D. Khale and R. Chaudhary, “Mechanism of geopolymerization and factors influencing its development: A review,” *J. Mater. Sci.*, vol. 42, no. 3, pp. 729–746, 2007, doi: 10.1007/s10853-006-0401-4.
- [395] O. Abdelrahman and N. Garg, “Impact of Na/Al ratio on the extent of alkali-activation reaction: Non-linearity and diminishing returns,” *Front. Chem.*, vol. 9, pp. 1–15, 2022, doi: 10.3389/fchem.2021.806532.
- [396] A. R. Brough and A. Atkinson, “Sodium silicate-based, alkali-activated slag mortars: Part I. Strength, hydration and microstructure,” *Cem. Concr. Res.*, vol. 32, no. 6, pp. 865–879, 2002, doi: [https://doi.org/10.1016/S0008-8846\(02\)00717-2](https://doi.org/10.1016/S0008-8846(02)00717-2).

- [397] X. Dai, S. Aydin, M. Yücel, K. Lesage, and G. De Schutter, "Early age reaction, rheological properties and pore solution chemistry of NaOH-activated slag mixtures," *Cem. Concr. Compos.*, vol. 133, no. 104715, 2022, doi: 10.1016/j.cemconcomp.2022.104715.
- [398] F. G. Collins and J. G. Sanjayan, "Workability and mechanical properties of alkali activated slag concrete," *Cem. Concr. Res.*, vol. 29, no. 3, pp. 455–458, 1999, doi: [https://doi.org/10.1016/S0008-8846\(98\)00236-1](https://doi.org/10.1016/S0008-8846(98)00236-1).
- [399] L. Hertwig and K. Holschemacher, "Setting time and strength monitoring of alkali-activated cement mixtures by ultrasonic testing," *Materials (Basel)*, vol. 1889, no. 14, 2021.
- [400] K. Sasaki, K. Kurumisawa, and K. Ibayashi, "Effect of retarders on flow and strength development of alkali-activated fly ash/blast furnace slag composite," *Constr. Build. Mater.*, vol. 216, pp. 337–346, 2019, doi: <https://doi.org/10.1016/j.conbuildmat.2019.05.022>.
- [401] G. Puerta-Falla *et al.*, "The influence of slightly and highly soluble carbonate salts on phase relations in hydrated calcium aluminate cements," *J. Mater. Sci.*, vol. 51, no. 12, pp. 6062–6074, 2016, doi: 10.1007/s10853-016-9912-9.
- [402] Z. Sun and A. Vollpracht, "Isothermal calorimetry and in-situ XRD study of the NaOH activated fly ash, metakaolin and slag," *Cem. Concr. Res.*, vol. 103, pp. 110–122, 2018, doi: <https://doi.org/10.1016/j.cemconres.2017.10.004>.
- [403] B. Lothenbach and A. Gruskovnjak, "Hydration of alkali-activated slag: Thermodynamic modelling," *Adv. Cem. Res.*, vol. 19, no. 2, pp. 81–92, 2007, doi: 10.1680/adcr.2007.19.2.81.
- [404] S. Kwan, J. LaRosa, and M. W. Grutzeck, "²⁹Si and ²⁷Al MASNMR study of strätlingite," *J. Am. Ceram. Soc.*, vol. 78, no. 7, pp. 1921–1926, 1995, doi: <https://doi.org/10.1111/j.1151-2916.1995.tb08910.x>.

- [405] M. U. Okoronkwo and F. P. Glasser, "Stability of strätlingite in the CASH system," *Mater. Struct.*, vol. 49, no. 10, pp. 4305–4318, 2016, doi: 10.1617/s11527-015-0789-x.
- [406] R. Maddalena, K. Li, P. A. Chater, S. Michalik, and A. Hamilton, "Direct synthesis of a solid calcium-silicate-hydrate (C-S-H)," *Constr. Build. Mater.*, vol. 223, pp. 554–565, 2019, doi: <https://doi.org/10.1016/j.conbuildmat.2019.06.024>.
- [407] F. Bonk, J. Schneider, M. A. Cincotto, and H. Panepucci, "Characterization by multinuclear high-resolution NMR of hydration products in activated blast-furnace slag pastes," *J. Am. Ceram. Soc.*, vol. 86, no. 10, pp. 1712–1719, 2003, doi: 10.1111/j.1151-2916.2003.tb03545.x.
- [408] K. Gijbels, Y. Pontikes, P. Samyn, S. Schreurs, and W. Schroeyers, "Effect of NaOH content on hydration, mineralogy, porosity and strength in alkali/sulfate-activated binders from ground granulated blast furnace slag and phosphogypsum," *Cem. Concr. Res.*, vol. 132, no. 106054, 2020, doi: 10.1016/j.cemconres.2020.106054.
- [409] F. B. Reig, J. V. G. Adelantado, and M. C. M. M. Moreno, "FTIR quantitative analysis of calcium carbonate (calcite) and silica (quartz) mixtures using the constant ratio method . Application to geological samples," *Talanta*, vol. 58, pp. 811–821, 2002.
- [410] M. Horgnies, J. Chen, and C. Bouillon, "Overview of the use of Fourier transformed infrared spectroscopy to study cementitious materials," *WIT Trans. Eng. Sci.*, vol. 77, pp. 251–262, 2013, doi: 10.2495/MC130221.
- [411] R. Tänzer, A. Buchwald, and D. Stephan, "Effect of slag chemistry on the hydration of alkali-activated blast-furnace slag," *Mater. Struct.*, vol. 48, no. 3, pp. 629–641, 2014, doi: 10.1617/s11527-014-0461-x.
- [412] A. R. Allu *et al.*, "Understanding the formation of $\text{CaAl}_2\text{Si}_2\text{O}_8$ in melilite-based

- glass-ceramics: Combined diffraction and spectroscopic studies," *ACS Omega*, vol. 2, no. 9, pp. 6233–6243, 2017, doi: 10.1021/acsomega.7b00598.
- [413] J. F. Stebbins and X. Xue, "15. NMR Spectroscopy of Inorganic Earth Materials," in *Spectroscopic Methods in Mineralogy and Material Sciences*, G. Henderson, D. Neuville, and R. Downs, Eds. De Gruyter, Berlin, 2014, pp. 605–654.
- [414] P. Florian, E. Veron, T. F. G. Green, J. R. Yates, and D. Massiot, "Elucidation of the Al/Si ordering in gehlenite $\text{Ca}_2\text{Al}_2\text{SiO}_7$ by combined ^{29}Si and ^{27}Al NMR spectroscopy/quantum chemical calculations," *Chem. Mater.*, vol. 24, no. 21, pp. 4068–4079, 2012, doi: 10.1021/cm3016935.
- [415] P. Pena, J. M. Rivas Mercury, A. H. de Aza, X. Turrillas, I. Sobrados, and J. Sanz, "Solid-state ^{27}Al and ^{29}Si NMR characterization of hydrates formed in calcium aluminate–silica fume mixtures," *J. Solid State Chem.*, vol. 181, no. 8, pp. 1744–1752, 2008, doi: <https://doi.org/10.1016/j.jssc.2008.03.026>.
- [416] C. E. Hughes *et al.*, "Exploiting in-situ solid-state NMR spectroscopy to probe the early stages of hydration of calcium aluminate cement," *Solid State Nucl. Magn. Reson.*, vol. 99, pp. 1–6, 2019, doi: 10.1016/j.ssnmr.2019.01.003.
- [417] X. Cong and R. J. Kirkpatrick, "Hydration of calcium aluminate cements: a solid-state ^{27}Al NMR study," *J. Am. Ceram. Soc.*, vol. 76, no. 2, pp. 409–416, 1993, doi: <https://doi.org/10.1111/j.1151-2916.1993.tb03799.x>.
- [418] G. K. Sun, J. F. Young, and R. J. Kirkpatrick, "The role of Al in C–S–H: NMR, XRD, and compositional results for precipitated samples," *Cem. Concr. Res.*, vol. 36, no. 1, pp. 18–29, 2006, doi: <https://doi.org/10.1016/j.cemconres.2005.03.002>.
- [419] Z. Dai, T. T. Tran, and J. Skibsted, "Aluminum incorporation in the C–S–H phase of white Portland cement–metakaolin blends studied by ^{27}Al and ^{29}Si MAS NMR spectroscopy," *J. Am. Ceram. Soc.*, vol. 97, no. 8, pp. 2662–2671,

- 2014, doi: <https://doi.org/10.1111/jace.13006>.
- [420] M. D. Andersen, H. J. Jakobsen, and J. Skibsted, "Incorporation of aluminum in the calcium silicate hydrate (C-S-H) of hydrated Portland cements: a high-field ^{27}Al and ^{29}Si MAS NMR investigation," *Inorg. Chem.*, vol. 42, no. 7, pp. 2280–2287, 2003, doi: 10.1021/ic020607b.
- [421] C. Gosselin, E. Gallucci, and K. Scrivener, "Influence of self heating and Li_2SO_4 addition on the microstructural development of calcium aluminate cement," *Cem. Concr. Res.*, vol. 40, no. 10, pp. 1555–1570, 2010, doi: <https://doi.org/10.1016/j.cemconres.2010.06.012>.
- [422] S. Aydin and B. Baradan, "Effect of activator type and content on properties of alkali-activated slag mortars," *Compos. Part B Eng.*, vol. 57, pp. 166–172, 2014, doi: 10.1016/j.compositesb.2013.10.001.
- [423] S. Sasui, G. Kim, J. Nam, T. Koyama, and S. Chansomsak, "Strength and microstructure of class-C fly ash and GGBS blend geopolymer activated in NaOH & $\text{NaOH} + \text{Na}_2\text{SiO}_3$," *Materials (Basel)*, vol. 13, no. 1, 2019, doi: 10.3390/ma13010059.
- [424] I. Hakem Aziz, M. Mustafa Al Bakri Abdullah, M. Arif Anuar Mohd Salleh, and A. Victor Sandu, "The incorporation of sodium hydroxide (NaOH) concentration and CaO-Si components on ground granulated blast furnace slag geopolymers," *IOP Conf. Ser. Mater. Sci. Eng.*, vol. 864, no. 1, 2020, doi: 10.1088/1757-899X/864/1/012005.

Publications, Conferences, and Awards

Journal publications

- 1) L. Stefanini, B. Walkley, J. L. Provis, “Valorisation of calcined clays from waste sources in alkali-activated cements” – under review.
- 2) L. Stefanini, B. Walkley, J. L. Provis, “Sodium carbonate-activated slag cements using basic oxygen furnace (BOF) slag as an additive” – under review.
- 3) S. Ghorbani, L. Stefanini, Y. Sun, B. Walkley, J. L. Provis, G. De Schutter, and S. Matthys, “Characterisation of alkali-activated stainless steel slag and blast-furnace slag cements,” *Cement and Concrete Composites*, vol. 143, no. 105230, 2023, doi: <https://doi.org/10.1016/j.cemconcomp.2023.105230>.
- 4) L. Stefanini, B. Walkley, and J. L. Provis, “Investigating the retarding effect of CAC in alkali-activated cements,” *Frontiers in Materials*, vol. 10, 2023, doi: <https://doi.org/10.3389/fmats.2023.1212177>.
- 5) L. Stefanini, S. Ghorbani, G. De Schutter, S. Matthys, B. Walkley, and J. L. Provis, “Evaluation of copper slag and stainless steel slag as replacements for blast furnace slag in binary and ternary alkali-activated cements,” *Journal of Materials Science*, vol. 58, no. 31, pp. 12537–12558, 2023, <https://doi.org/10.1007/s10853-023-08815-7>.
- 6) S. Ghorbani, L. Stefanini, B. Sun, B. Walkley, J. L. Provis, and S. Matthys, “Microstructural and durability analysis of ternary alkali-activated concretes made from copper slag, EAFS, and GGBFS” – in preparation.

Conferences contributions

- 1) L. Stefanini, B. Walkley, and J. L. Provis, (2021), “A suitability study on alkali-activated materials based on waste calcined clays and BOF slag”, *presented online at the 75th RILEM Annual Week and International Conference on Advances in Sustainable Construction Materials*, Mérida, Yucatán, México.
- 2) L. Stefanini, B. Walkley, and J. L. Provis, (2022), “Investigating the retarding effect of CAC in alkali-activation of blast-furnace slag based binders”, *presented online at the 76th RILEM Annual Week and International Conference on Regeneration and Conservation of Structures (ICRCS 2022)*, Kyoto, Japan.
- 3) L. Stefanini, B. Walkley, and J. L. Provis, (2022), “Alkali-activation of blended copper slag and blast-furnace slag cements”, *presented at the XXX International Materials Research Congress (IMRC22) and International Conference on Advanced Materials (ICAM22)*, Cancún, Quintana Roo, México.
- 4) L. Stefanini, B. Walkley, and J. L. Provis, (2022), “Evaluation of the reactivity of EAF slag in alkali-activated systems blended with GGBFS”, *presented at the 41st Cement and Concrete Science Conference*, Leeds, United Kingdom.
- 5) L. Stefanini, B. Walkley, and J. L. Provis, (2022), “Characterisation of calcined waste clays and utilisation in alkali-activated blends with GGBFS”, *presented at the 42nd Cement and Concrete Science Conference*, London, United Kingdom.

Additionally, I had the chance to participate as a delegate of The University of Sheffield at the COP27 United Nations Climate Change Conference, Sharm El-Sheik, Egypt, (2022). After which I was invited to a panel discussion on “COP27 Reflections and actions” at the *ECR Net Zero Conference*, Manchester, United Kingdom (2022).

Awards

- 1) SMEA Professional Development Fund 2021, *Sheffield Metallurgical & Engineering Association (SMEA)*, issued on 11/05/2021.
- 2) IOM3 Grant to Support Knowledge Exchange 2022, *Institute of Materials, Minerals and Mining (IOM3)*, issued on 01/08/2022.
- 3) Shortlisted finalist for the “Adam Neville PhD Prize for Cement and Concrete 2022” at the *Neville Centre of Excellence in Cement and Concrete Engineering Symposium* held on 08/12/2022